Synthesis and Photophysical Properties of Functional Tetracoordinate Boron Containing Organic Compounds

Sanchita Shah

A thesis submitted for the partial fulfillment of the
Degree of Doctor of Philosophy

Institute of Nano Science and Technology
Knowledge city, Sector 81, SAS Nagar 140306, Punjab, India.

Indian Institute of Science Education and Research Mohali
Knowledge city, Sector 81, SAS Nagar, Manauli PO, Mohali,140306, Punjab, India.

June 2023

Dedicated to

My Parents

and

Husband

Declaration

The work presented in this thesis has been carried out by me under the guidance of Prof. Prakash P. Neelakandan at the Institute of Nano Science and Technology (INST), Mohali. This work has not been submitted in part or in full for a degree, a diploma, or a fellowship to any other university or institute. Whenever contributions of others are involved, every effort is made to indicate this clearly, with due acknowledgement of collaborative research and discussions. This thesis is a bonafide record of original work done by me and all sources listed within have been detailed in the bibliography.

Sanchita Shah

In my capacity as the supervisor of the candidate's thesis work, I certify that the above statements by the candidate are true to the best of my knowledge.

Prakash P. Neelakandan

Acknowledgement

First of all, I bow in reverence to the Almighty for providing enough patience, courage, and zeal that helped me accomplish my Ph.D. thesis work.

At this moment of accomplishment, I would like to express my deep sense of gratitude to my esteemed supervisor ***Prof. Prakash P. Neelakandan****, for his continuous guidance, encouragement and motivation even through the toughest of days, leading to the successful completion of this work. I am extremely thankful to him for giving me the freedom to pursue my research interests and simultaneously keeping me on the right track. He has constantly encouraged me to push my limits further and it is indeed a rare privilege to work under his esteemed guidance.*

I would also like to thank the members of my Ph.D. monitoring committee ***Prof. Debabrata Patra*** *and* ***Prof. Sharmishtha Sinha*** *for their valuable time, insightful comments, and encouragement.*

I am thankful to ***Prof. Amitava Patra****, Director INST, for providing excellent infrastructure to carry out our research work. My special thanks to the founder Director of INST,* ***Prof. A. K. Ganguli****, and ex-officiating Director,* ***Prof. H.N. Ghosh****, and the esteemed Faculty of INST for the guidance and affectionate conversation during this course of time.*

I would like to express my sincere thanks to ***Dr. Nidhi Tyagi and Dr. Neeraj Naithani*** *for their support during the tenure of this work.*

The expression of my gratitude would be incomplete without thanking my lab mates ***Dr. Praveen****,* ***Dr Khalid****,* ***Dr. Atikur****,* ***Parvati****,* ***Ayushi****,* ***Hemant, Suman, Puneet****,* ***Prodipta, Priyanka, Kanchan, Kiran, Ajay and others*** *for the cordial company and regular help they provided in the lab.*

*Account of my journey in INST would never be complete without a special mention of **Dr. Anjana Sharma, Parvati Marandi** and **Dr. Shefali Sartalia** who made this journey really beautiful and memorable for me. I am blessed to have well-wishers and friends in my life, who have seen me and supported me through all my bitter-sweet phases. I am specially thankful to my friends **Dr. Kiran Bharadwaj, Anjana Kamal and Tanya Goel** for their unparalleled love and motivation throughout.*

I would also like to thank all the other people whom I may not be able to mention here, but I thoroughly acknowledge their love, support and guidance.

*I take this opportunity to thank my **Parents** for their never-ending love and support. My simple expression of thanks to them does not seem sufficient as their contribution and efforts are uncountable. I am very grateful to my husband **Akshay Jaitly** for being the most wonderful partner and for being my mentor and friend through all these years. You all are the light of my life and I could not be any more blessed. Last but not the least I am very grateful to my sister **Rachita** and my brother **Suchit** for being my pillar of strength.*

Finally in all the most humble submission, I again thank the Almighty for the countless blessings bestowed upon me.

Sanchita Shah

ABBREVIATIONS

ACQ	Aggregation-caused quenching
AFM	Atomic force microscopy
AIE	Aggregation-induced emission
BODIPY	Boron Dipyrromethene
CT	Charge transfer
CO	Carbon monoxide
CORMs	CO Releasing Molecules
DCM	Dichloromethane
DHN	1,5-Dihydroxynaphthalene
DMF	Dimethylformamide
DMSO	Dimethyl sulfoxide
DPBF	1,3-diphenylisobenzofuran
FA	Formic acid
GC	Gas chromatography
HOMO	Highest occupied molecular orbital
HRMS	High resolution mass spectrometry
ICT	Intramolecular charge transfer
IC	Internal Conversion
ICPMS	Inductively coupled plasma mass spectrometry
IR	Infrared
ISC	Intersystem Crossing

LbL	Layer-by-Layer
LUMO	Lowest unoccupied molecular orbital
m.p.	Melting point
NMR	Nuclear magnetic resonance
OLEDs	Organic light-emitting diodes
ORTEP	Oak Ridge Thermal Ellipsoid Plot
PAA	Polyacrylic acid
PDT	Photodynamic therapy
PEI	Polyethyleneimine
PL	Photoluminescence
PMMA	Polymethylmethacrylate
PS	Photosensitizer
ROS	Reactive oxygen species
TEA	Triethylamine
TFA	Trifluoroacetic acid
TLC	Thin layer chromatography
UV	Ultraviolet
VR	Vibration relaxation

ABSTRACT

Over the past few decades, exploring pathways to access the triplet excited states of organic chromophores has been an appealing area of research. In this regard, tetracoordinate boron containing organic compounds have emerged as a fascinating class of luminescent molecules and photosensitizers. Overlap of the empty *p*-orbital of boron with π- conjugated core in tetracoordinate boron containing organic compounds leads to the delocalization of the electron cloud and planarization of the π-systems thereby resulting in interesting photophysical properties. Boron coordination also results in red shifted absorption and emission as compared to the corresponding chelating units.

BODIPYs are renowned boron containing fluorescent dyes with strong and tuneable absorption in the visible region, high thermal and photo-stability and exceptional fluorescence quantum yields, and they have been turned into efficient triplet photosensitizers by appropriate design strategy with strong absorption in the visible to NIR region. A major drawback with BODIPYs is low reactions yields and the precise reaction conditions that are necessary for their synthesis. This issue could be overcome by chelating boron to simple organic ligands. Among them, N,O-chelated salicylideneimine-boron difluoride complexes, popularly known as boranils, are interesting as they can be easily synthesized in good yields via one pot synthesis using simple, commercially available starting materials like amines and aldehydes. This methodology enables the synthesis of a wide variety of molecules whose properties can be easily tuned across the entire range of electromagnetic spectrum with suitable derivatisation. While they are popularly known for their luminescence properties, their photosensitisation properties are largely unexplored to date.

Considering these facts, this thesis dissertation is devoted to the design and synthesis of novel tetracoordinate boron-containing organic compounds with the objective of tuning their photophysical properties through systematic variations in their chemical structures. Chapter 1 discusses the importance of triplet states and photosensitized generation of singlet oxygen for applications in various fields. An extensive overview of BODIPYs as photosensitizers has been presented from the literature. Common strategies adopted to achieve populated triplet states with a special focus on halogenation and transition metal complex incorporation in BODIPYs are also discussed. We have also thrown some light on the structural features and the associated photophysical properties of a few boranil derivatives.

Chapter 2 describes the synthesis and characterization of appropriately functionalized BODIPY and boranil derivatives. The compounds synthesized include various boron difluoride complexes ranging from heavy metal and transition metal complex incorporated BODIPYs **A-C** to N,O-chelated salicylideneimine boron difluoride complexes **D-G** to diiodosalicylideneimine-boron difluoride functionalized polyethyleneimine **H**.

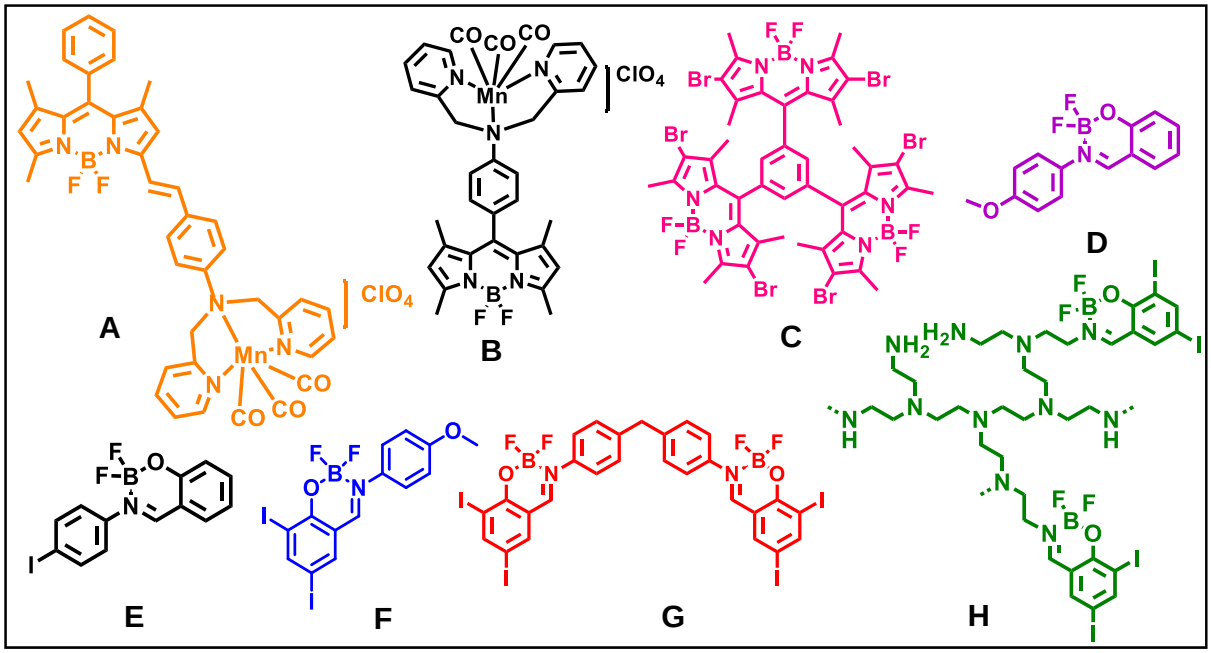

Chapter 3 discusses the photophysical properties of these compounds with respect to their absorption, emission and singlet oxygen generation abilities and our results underline the importance of appropriate functionalisation on the BODIPY/boranil skeletons. The ease of synthetic functionalization at meso and pyrrolic positions of the BODIPY resulted in diverse structural and photophysical features. High CO release efficiency along with singlet oxygen generation under biologically relevant visible light were obtained from single component photoCORMs **A** and **B** whereas the peculiar structure of hexabrominated BODIPY **C** exhibited drastic changes in the luminescence and photosensitizing abilities upon aggregation. On the other hand, the boranil derivatives typically exhibited bright emission in the blue region with good photostabilities and high singlet oxygen generation quantum yields.

Chapter 4 focuses on the potential applications of the synthesized molecules for degradation of water contaminants, as antimicrobial coatings and as antibacterial photodynamic agents. BODIPY complexes **A** and **B** were incorporated into non-woven fabrics using PMMA and the fabrics showed excellent biocompatibility to l929 cell lines and were strongly cytotoxic to c6 cancer cell lines and *E. coli* bacteria under light exposure. PMMA films incorporating the iodo-functionalized boranil **G** were capable of serving as a reusable heterogeneous medium for the photosensitized degradation of organic water pollutants. Furthermore, multilayer nanofilms incorporating boron-functionalized polymer **H** grown inside the surface of the glass vials generated reactive oxygen species upon exposure to visible light. The coated glass vials showed exceptional anti-microbial action against both gram-positive and gram-negative bacteria, functioning as self-cleaning vials.

Content

Chapter 1

Photosensitization properties of tetracoordinate boron compounds: An overview

1.1. Introduction

Triplet excited states are of great importance to scientists working in areas of photochemistry, photodynamic therapy, electroluminescence, photocatalysis, photovoltaics, triplet-triplet annihilation upconversion processes and molecular logic gates[1–5]. The triplet states are composed of even-electron species with same spin multiplicities possessing paramagnetic character[6]. These can be obtained from singlet excited states via non-radiative process of intersystem crossing (ISC, discussed in Section 1.2). Long lifetimes obtained with the excitons have the ability to overcome the hindrances inflicted by short exciton diffusion lengths, thereby successfully finding practical applications in material science.

While triplet excited states have helped achieve ultralong room-temperature phosphorescent materials to construct economic display devices, they are also potential intermediates in major photochemical transformations[7–9]. Molecules which exhibit high triplet quantum yields and sluggish triplet decay modes are often preferably chosen for organic reactions such as [2+2] cycloadditions[10] and in photodynamic therapy. Due to the increasing significance of triplet excited states over multiple domains, developing novel in organic chromophores with exciting properties and unravelling the underlying excited state mechanisms is essential. The major pathways adopted by photoexcited species to generate triplet states include heavy atom induced ISC[11–13], ISC through vibronic coupling[14,15], singlet fission mediated triplet formation[16,17], plasmon-molecule coupling[18,19]and twisting induced triplet population[20,21].

1.2. Singlet oxygen: A direct consequence of photosensitization

Generation of singlet oxygen ($^1O_2$) is a direct consequence of triplet state formation. It has applications in diverse fields like photo-oxidation, DNA damage and photodynamic therapy[22,23]. Photosensitized generation of singlet oxygen presents itself as a straightforward, easy and controllable method that only requires oxygen, light, and a photosensitizer that can absorb the light to generate singlet oxygen from molecular oxygen. Transition between the

ground state (S_0) and singlet excited state (S_n) occurs upon light excitation. The S_n state subsequently relaxes to the lowest excited singlet state, S_1 of the sensitizer following which either relaxation to the ground state, S_0 takes place or the process of ISC generates the triplet states. The longer lifetime of triplet state relative to singlet state allows the excited triplet state to react either via type I or type II mechanism. According to type I mechanism, there occurs hydrogen atom abstraction or electron transfer between the excited sensitizer and a substrate leading to free radicals. On the other hand, type II mechanism involves the generation of singlet oxygen via energy transfer between the excited photosensitizer and molecular oxygen. Following equations illustrate the type II mechanism:

$$P(S_0) \xrightarrow{h\nu} P(S_1) \xrightarrow{k_{ISC}} P(T_1)$$

$$P(T_1) + {}^3O_2 \xrightarrow{k_{en}} P(S_0) + {}^1O_2$$

Wherein P stands for photosensitizer, S_0 is the singlet ground state, T_1 represents the first triplet excited state, k_{ISC} is the rate of intersystem crossing and k_{en} represents the rate constant for the energy transfer process.

Mechanism of singlet oxygen generation. Jablonski diagram[6,24] further illustrates these processes wherein the electronic states are arranged horizontally in the increasing order of spin multiplicity and vertically in the order of increasing energy. Figure 1.1 shows light absorption by the photosensitizer which gets excited to the singlet excited state. Vibrational relaxation is the first method wherein the excess vibrational energy is dissipated to the vibrational modes until the lowest energy vibrational level of the electronic state is achieved. This process of vibrational relaxation takes place on a very fast time scale of 10^{-12} to 10^{-10} s.

Another process is the non-radiative transition between two states that contain same spin multiplicity known as internal conversion (IC). Molecule in the high energy singlet excited states relax to lower lying singlet states and dissipate energy by the process of IC. Vibrational relaxation quickly follows IC enabling the molecule reach lowest vibrational level of that electronic state. IC of the high lying singlet excited states proceeds very fast on a timescale of 10^{-11} to 10^{-9} s as they are closely spaced. On the contrary, as the low-lying energy states S_0 and S_1 have wider energy difference, IC occurs on a comparative sluggish timescale and hence other processes such as fluorescence, intersystem crossing begin to compete.

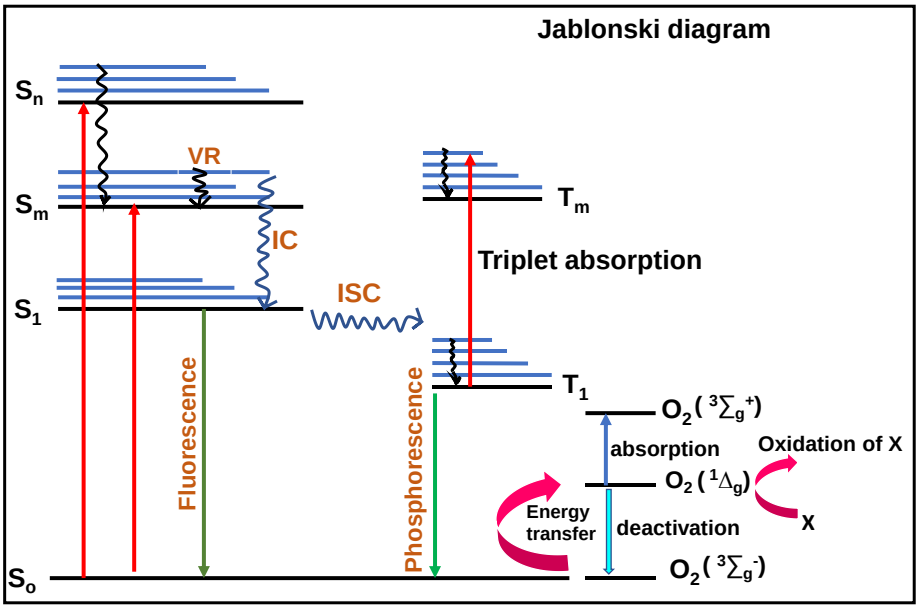

Figure 1.1. Schematic representation of Jablonski diagram and various associated pathways.

Fluorescence is another important property that arises from the radiative transition between the electronic states of same spin multiplicity. Upon photoexcitation, the electrons in the ground state get excited to high energy states where they dwell for a very short timescale. As they relax to the ground state, energy is released as a photon. As a result of the occurrence of competitive processes, some energy gets lost and light with higher wavelength and lower energy is released as a photon relative to the light absorbed. Fluorescence occurs on a time scale of 10^{-10} to 10^{-7} s and takes place from the lowest lying vibrational level of the first excited singlet state to the ground state. The loss of energy before the occurrence of fluorescence comes into picture in accordance with Kasha's rule which states that luminescence only occurs in appreciable yields from the lowest excited state of a given multiplicity. On the other hand, an alternative pathway to fluorescence and IC is intersystem crossing (ISC) that occurs from S_1 to T_1 state thereby pertaining to the electronic states of different spin multiplicities. The molecule undergoes vibrational relaxation to the ground vibrational level of T_1 quickly after ISC takes place. The ISC transition is a forbidden one because of the conservation of spin angular momentum. It becomes weakly allowed because of the spin orbit coupling between spin angular momentum and orbital angular momentum. ISC competes with other de-excitation pathways from S_1 like fluorescence and internal conversion which are more feasible in simple organic molecules. Hence ISC is too slow a process to hold significance for simple organic molecules. As a consequence of ISC, the triplet state is populated and photon emission occurs from T_1 to S_0 state. This radiative transition between the two electronic states of different spin

multiplicities i.e. from the first triplet excited state to the ground singlet state leads to phosphorescence. Phosphorescence is a forbidden process and is weakly allowed via spin orbit coupling. It occurs on a larger time scale contrary to fluorescence, with typical values ranging from 10^{-6} to 10 s. This long lifetime of the triplet state gives it sufficient time to transfer its energy to the molecular oxygen (O_2), which is in its triplet state in its ground state. The process of energy transfer results in the formation of singlet oxygen ($^1O_2$).

Two low lying singlet excited states exist in molecular oxygen above the triplet state namely,$^1\Delta_g$ (95 kJ mol^{-1}) and $^1\sum_g^+$ (158 kJ mol^{-1}). Electronic structure of these states differ from each other by the placement of π-antibonding orbitals. The first excited state, $^1\Delta_g$ has the following molecular orbital configuration: [KK $(2\sigma_g)^2$ $(2\ \sigma_u)^2$ $(3\sigma_g)^2(1\pi_u)^4$ $(1\pi_g^+)$ $(1\pi_{-g}^+)$] The illustration of the orbital assignment for the triplet state, first excited state and second excited state for molecular oxygen is shown in Figure 1.2. Since the transition from $^1\Delta_g$ to $^3\sum_g^-$ is a spin forbidden process, the first singlet excited state of molecular oxygen tends to be a relatively long-lived species. The second excited state of molecular oxygen descends to the first excited state via a spin allowed transition as a result of which $^3\sum_g^+$ is a short-lived species. The radiative lifetimes for O_2 ($^1\Delta_g$) and O_2 ($^3\sum_g^+$) are found to be 45 minutes and 7-12 s in the gaseous state and 10^{-6}-10^{-3} s and 10^{-9}-10^{-11} s in solution state respectively. The metastability of the $^1\Delta_g$ state enables the emission for the $^1\Delta_g \Leftrightarrow {}^3\sum_g^+$ transition to be recorded at 1270 nm despite being a spin and symmetry forbidden.

Singlet oxygen generation efficiency can be quantified via singlet oxygen quantum yield, ϕ_Δ which indicates the ability of a photosensitizer to generate singlet oxygen. ϕ_Δ is a number between 0 and 1 wherein 1 represents 100% efficiency. An ideal case shows that every single photon that is absorbed yields one molecule of singlet oxygen. There are many methods developed to determine the quantum yield for singlet oxygen generation. Some direct determination methods include time resolved near-infrared luminescence and time resolved thermal lensing (TRTL). The NIR emission peak obtained at 1270 nm of $^1\Delta_g$ allows it to be monitored directly via NIR luminescence. Indirect methods include mostly chemical trapping methods via singlet oxygen scavengers such as of 1,3-diphenylisobenzofuran (DPBF), dihydroxynapthalene (DHN), p-nitrodimethylaniline (RNO) etc[25,26]. The chemical trapping methods do not involve any sophisticated instrumentation and can be observed via simple UV spectrophotometer.

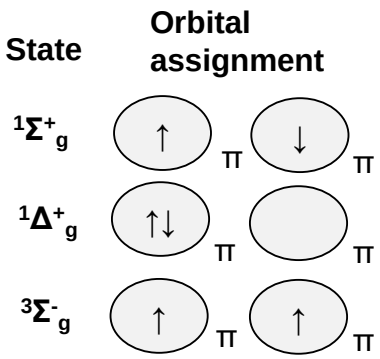

Figure 1.2. Representation of the triplet and singlet excited states of molecular oxygen.

1.3. Applications of photosensitized generation of singlet oxygen

Because of the versatile nature of singlet oxygen and its high degree of stereoselectivity, singlet oxygen has gained special interest over past many decades. Interaction between a photosensitizer with molecular oxygen takes place via an energy transfer process, generating singlet oxygen which further reacts with a substrate and oxidizes it. Photosensitized generation of singlet oxygen has found applications as an important reagent in organic synthesis, for wastewater treatment and photodynamic therapy.

1.3.1. Organic chemical synthesis

Singlet oxygen has found potential applications in the synthesis of important intermediates, drugs, and fine chemicals[22,27]. Most olefins, dienes and sulphides react with singlet oxygen to produce the corresponding dioxetane or allylic hydroperoxides, endoperoxides or sulfoxides, respectively. Among various heterocycles, furans preferentially react with singlet oxygen to yield a range of products that are used as building blocks for drug discovery and natural product chemistry[28,29]. Reaction of furans with singlet oxygen leads to formation of butanolide which serves as an important step in synthesis of many natural products and explored in ionic liquids (ILs)[30]. Upon in situ production by photosynthetic organisms, it can also be involved in multi-steps or induce domino reactions of a particular synthetic pathway. Bis-furan precursors could be a representative example of similar system wherein they participated in singlet oxygen mediated super cascade reaction to produce ABCD ring skeleton of some pectenotoxins[31–33]. Furthermore, insertion of singlet oxygen into the α-CH bond of aliphatic and cyclic ethers has been found to generate hydroperoxides and corresponding lactones under extremely mild conditions of room temperature and ambient pressure with 40-90% yields and outstanding site selectivity[34]. Generally, singlet oxygen is

reactive towards specific groups such as olefins, dienes, sulphides and amines and in presence of suitable reaction conditions its high reactivity and selectivity opens ways of huge variety of synthetic applications. Many endoperoxides have also been synthesised using singlet oxygen from suitable dienes in good yields with efficient photosensitisers. Based on the reaction conditions, the endoperoxides further convert to other products such as 4,5-epoxy-2-penten-1-one, 1,3-dihydroxy-2-cyclopentene, or 3-hydroxy-2-cyclopentenone[35]. Hence, $^1O_2$ has been successfully introduced into a range of organic substrates leading to important products for synthetic organic chemistry.

1.3.2. Wastewater treatment

Use of light, especially solar light, stands an economic solution to complicated environment related problems. Contribution of singlet oxygen towards photooxidation of warfare agents, wastewater pollutants and industrial byproducts is fairly established. Phenol and its derivatives represent a range of toxic compounds extensively found in paper and dye manufacturing industries, oil refineries etc[36]. The photooxidation of phenols has been explored with conventional photosensitizers such as Eosin, Rose Bengal, Methylene blue, Riboflavin, Zn(II) tetraphenylporphyrin etc. Similarly, singlet oxygen assisted oxidation of sulphide salts to sulphates in aqueous solution also holds importance in wastewater treatment as sulphides are toxic industrial byproducts[35]. There are also reports demonstrating the combustion application of singlet oxygen in treating hazardous halogenated pollutants like polychlorinated biphenyls (PCBs) polychlorinated dibenzodioxins (PCDDs) and furans (PCDFs)[37]. Because atmospheric oxidation of these environmental pollutants has negligible kinetic feasibility, commonly adopted measures involve energy demanding source incineration of contaminated materials at high temperatures which usually goes upto 850 °C. Singlet oxygen promises an alternative low-energy strategy of degrading PCDDs which are potent environmental pollutants. In this regard, singlet oxygen mediated photooxidation of polycyclic and halogenated aromatic hydrocarbons is also a thermodynamically and kinetically feasible process that takes place through 1,2-cycloaddition reaction pathway leading to the formation of dioxetane products via diradical intermediate channels. This process required relatively lesser enthalpy of around 100 kJ/mol compared to high temperature incineration which requires ~350 kJ/mol[27]. Furthermore, many water-borne pathogens also undergo photocatalytic inactivation with singlet oxygen. In this regard, Kohn and Nelson[38] showed that the inactivation of pathogens took place in high yields and was independent of the influence of dissolved oxygen and pH variation in the range of 6.5 to 9.3. Neves et al.[39] used porphyrins

as photosensitizers for singlet oxygen assisted photo-treatment of sewage plant water contaminated with micropollutant pharmaceuticals like metoprolol. 90% degradation of metoprolol was successfully conducted within 12 hours via singlet oxygen, as illustrated by HPLC studies. In another report, porphyrin was immobilised on silica support and used as a heterogeneous medium to decontaminate wastewater. Lyubimenko et al.[40] also presented a combination of poly(vinylidene fluoride) (PVDF) membrane with a Pd-porphyrin based photosensitiser to generate a photocatalytic hybrid material membrane for efficient removal (83%) of a model pollutant, methylene blue in a photochemical membrane reactor. Liu and co-workers[41] encapsulated nanoscale TiO_2 within carbon nanotubes and the resulting composite showed high photocatalytic activity with singlet oxygen towards the transformation of highly toxic Sb(III) to the less toxic Sb(V).

1.3.3. Photodynamic therapy for cancer treatment

Photodynamic therapy has gained huge attention ever since its inception because of its non-invasiveness, good selectivity and effectiveness. The combination of light, photosensitizer and reactive oxygen species leads to the production of cytotoxic agents such as singlet oxygen, superoxide, hydroxyl radical, peroxides etc. ultimately causing tumour cell death. Photodynamic therapy involves photodynamic effect which can be defined as a biological damage that occurs when molecular oxygen, a photosensitizer and a UV, visible or infrared light are simultaneously present.

In addition of the ease of synthesis, an ideal photosensitizer should absorb strongly in the phototherapeutic region, exhibit negligible dark toxicity, be capable of deep tissue penetration, have good pharmacokinetic behaviour i.e. high selectivity for tumor tissue, be easily eliminated from the body, have a constant composition with long shelf life and a high triplet quantum yield with efficient energy transfer to produce singlet oxygen in good yields. First generation photosensitisers like hematoporphyrin derivative (HpD) and photofrin II had a complex composition of active components and had many disadvantages like low selectivity for tumor tissues, skin photosensitivity and weak absorption in red region making it difficult to treat deep tumors. Despite the synthesis difficulties, most prevailing photosensitizers (PSs) that are studied in clinical trials over past decades are still cyclic tetrapyrrole derivatives including porphyrins (Photofrin and protoporphyrin IX), chlorins (temoporfin) and bacteriochlorins (verteporfin)[42]. While these are extremely biocompatible, most of them show weak absorption in the phototherapeutic window (650-900 nm) and have low singlet oxygen quantum yields owing to their tendency to aggregate at high concentrations or in aqueous solutions.

Development of nonporphyrin-based photosensitizers has hence attracted the interests of scientists and many were developed including phthalocyanine (ZnPc), phenothiazinium (Methylene Blue and Toluidine Blue), cyanine (Merocyanine 540), squarine (SQDI) and xanthenes (Rose Bengal) derivatives[43]. Most of these PSs face dark toxicity issues along with photobleaching. In this regard, phenothiazinium-based PSs are observed to show low light-to-dark toxicity ratios, conventional cyanine-based PSs show poor photostability, and squaraine-based photosensitizers generally are structurally unstable because of their high aggregate-forming tendencies. These observations further motivated scientists to develop advanced photosensitizers that possess all desired properties discussed for an ideal photosensitizer. In this regard, BODIPYs as photosensitizers are indeed promising because of their structural robustness, ease of synthesis and functionalization, low dark toxicity, good solubility in huge range of solvents, high singlet oxygen quantum yield and interesting and tunable photophysics[2,44,45].

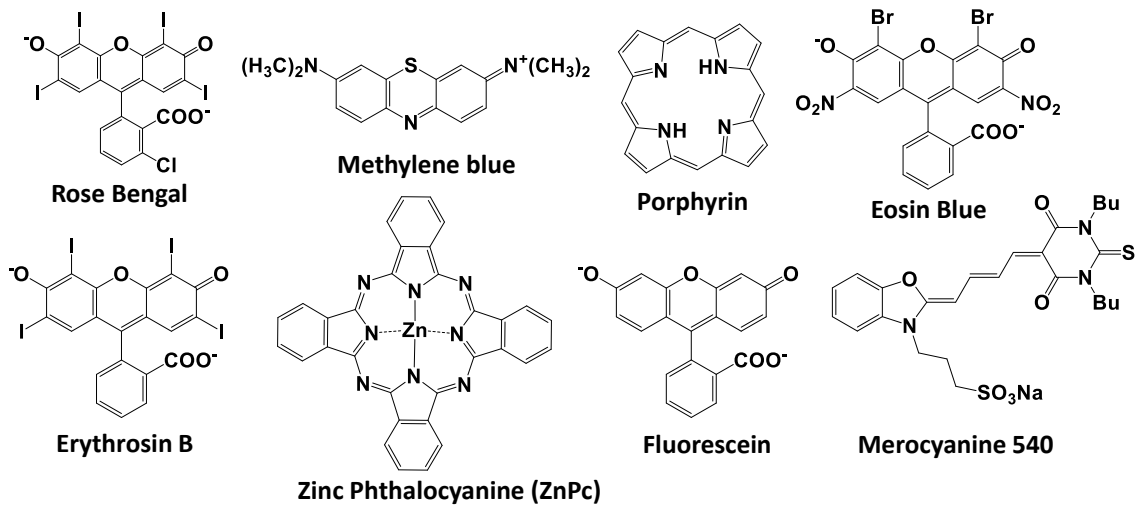

Figure 1.3. Examples of some conventionally known photosensitizers.

1.4. Choice of a robust ligand for efficient photosensitization: Tetracoordinate boron compounds

Typical fluorescent dyes usually lack effective intersystem crossing to the triplet manifold. Hence the process of ISC can be induced through a number of ways like heavy atom substitution, excitonic couplings, or through specially arranged configurations. The interplay between the various excited state phenomenon such as fluorescence, intersystem crossings, non-radiative relaxations, photoinduced electron transfer and energy transfers via bonds as well as space has the ability to tune the process of photosensitization. Appropriately designed and

substituted molecules can act as efficient photosensitizers. Some conventionally known photosensitizers are porphyrins, methylene blue, eosin blue, erythrosin B, fluorescein, zinc phthalocyanine etc. (Figure 1.3). While they are already known and studied in past decades, most of them suffer from issues like photobleaching or dark cytotoxicity.

Choice of a suitable chromophore plays a very crucial role for successfully designing organic photosensitizers as the factors like ease of derivatization, photostability and photophysical parameters hold significant importance. Concerning this aspect, tetracoordinate boron containing compounds are of particular interest owing to their robust structure, interesting photophysics, good molar absorptivity, good photostability and ease of functionalization[46–49]. They have been extensively employed in synthetic chemistry as reagents and catalysts and as luminescent organic materials. Even though tricoordinate boron complexes are already known and largely studied, they usually suffer from air and moisture sensitivity as tri-coordinate boron is coordinatively unsaturated. On the other hand, tetracoordinate boron compounds are highly robust and stable towards air and moisture due to saturated coordination.

Boron with an electronic configuration of $1s^2\ 2s^2\ 2p^1$ and atomic number 5 is an element in group 13 with three valence electrons and two vacant p orbitals. A π-conjugated organic skeleton can be attached to the boron centre to achieve trigonal planar or tetrahedral organoboron compounds. The π-electron cloud of electron rich organic molecules can delocalise over the vacant p-orbitals of boron thereby enabling intramolecular delocalization, rigidifying the π-conjugated skeleton and stabilising it further. Introducing the tetracoordinated boron enhances the planarity of the conjugated skeleton thereby enhancing the charge transfer properties. It is observed that the lowest occupying molecular orbital (LUMO) energy level is also lowered after complexation with boron and hence we observe a bathochromically shifted absorption and emission spectra. The selection of the ligands as well as appropriate substitution on either the ligands or boron can tune the photophysical aspects of these compounds.

The chelating ligands often have a negative charge or carry electron rich hetero atoms like O or N sites while the fluoride or aryl substituents on boron ensure overall charge neutrality of the resulting molecule. There are various chelation modes and sites usually coming from moieties like pyridine, thiazole, quinoline, pyrazine, imidazole, isoquinoline, pyrrole etc. Majorly, these compounds consist of N,N-, O,O-, N,O- and some tritopic ligands as schematically demonstrated. The N,N- , N,O- or O,O- ligands configurationally lock the four coordinate boron atom (Figure 1.4). Out of these, BODIPYs have gained special attention over last decade and hence need no major introduction.

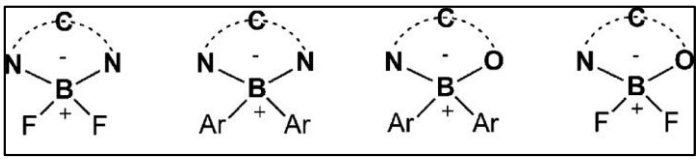

Figure 1.4. Illustration of various chelation modes with boron (III) analogues.

1.4.1. BODIPYs

The most exploited category of tetracoordinate boron compounds are BODIPYs that have attracted special interests from scientists working in areas from photovoltaics to dye-sensitised solar cells, from bioimaging applications to photodynamic therapy and from sensing to light harvesting arrays and photovoltaics[48,50–52]. 4,4-Difluoro-4-bora-3a,4a-diaza-s-indacene, or BODIPY, is also commonly referred to as "porphyrin's little sister". This category of fluorescent dyes consists of a dipyrromethene framework that is complexed to a disubstituted boron unit. The dipyrromethene unit contains two pyrrole units linked via a methine bridge in between. Upon complexation with boron difluoride, the cis-trans isomerization of the dipyrromethene is prevented and a rigidified π-conjugated skeleton is obtained rendering planarity to the overall molecule. They show robust photophysical properties like strong visible/red/NIR light absorption, high fluorescence quantum yield, good photostability and easy functionalization of the core. The systematic numbering of the BODIPY core is represented in Figure 1.5. Positions 3 and 5 are known as alpha positions while 1, 2, 6 and 7 are referred to as the beta positions. The position 8- is the meso position while the fluoride atoms are connected to the boron center at 4,4' positions leaving it to an approximate tetrahedral geometry.

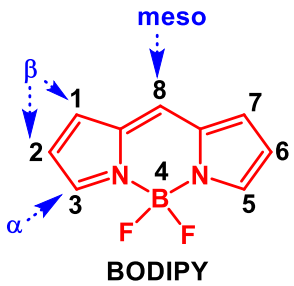

Figure 1.5. Representation of the BODIPY core with IUPAC numberings.

One very interesting property of BODIPY chromophore is facile functionalization that facilitates easy tuning of the associated photophysical parameters like absorption, emission, redox properties, hydrophilicity and excited state behaviour. Since there is scope for suitable

derivatization on BODIPY, they have been employed as efficient photosensitizers. BODIPY based triplet photosensitizers have found applications in photocatalysis, photodynamic therapy, triplet-triplet upconversion and so on. As already discussed, intersystem crossing is a straightforward strategy to generate triplet excited state via $S_1 \rightarrow T_1$ non-radiative transition and introduction of heavy atoms and transition metal atoms onto the chromophoric skeleton can efficiently lead to efficient photosensitization.

1.4.1.1. Heavy atom effect

1.4.1.1.1. Halogenated BODIPYs

Enhancing the spin orbit coupling with heavy atom effect is the most extensively used method to facilitate ISC in BODIPYs. Nagano and co-workers[53] in 2005 prepared the first iodinated BODIPY **1** as a photosensitizing agent that showed strong visible light absorption (ε = 110 000 M^{-1} cm^{-1} at 535 nm) and a red shift of 30 nm in absorption spectrum than the heavy-atom-free 1,3,5,7-tetramethylBODIPY (ε =120 000 M^{-1} cm^{-1} at 502 nm). Furthermore, it also exhibited 1.6-fold better photosensitising ability and improved photostability relative to Rose Bengal. Significant amount of killing of HeLa cells was also observed via photoirradiation of **1**. Hence without losing the unique BODIPY characteristics, a BODIPY fluorophore was transformed into a novel photosensitizer using heavy atom effect.

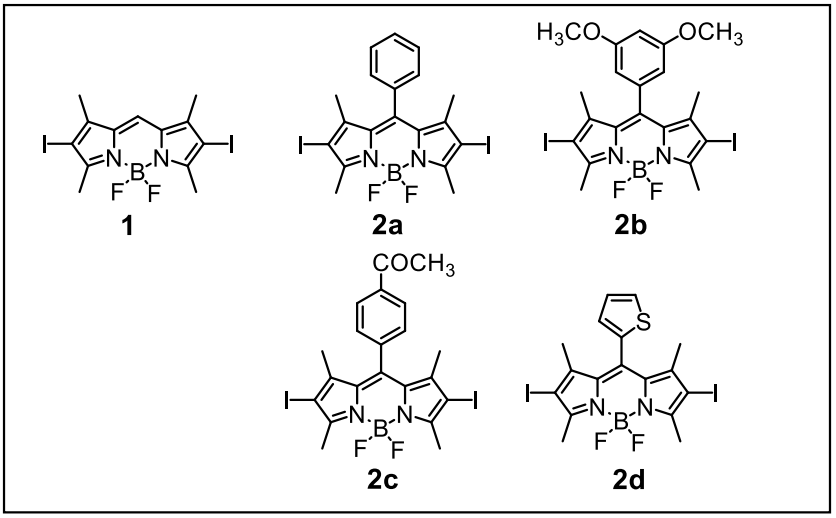

Figure 1.6. Structures of molecules **1** and **2**.

Furthermore, a series of 2,6-diiodo BODIPYs **2a-d** with phenyl and thienyl derivatives on meso positions were synthesized by Vicente and co-workers[54]. These 2,6-diiodo-BODIPYs

showed at least a 7-fold enhancement in photocytotoxicity (IC_{50} = 3.5–28 μM at 1.5 J/cm^2) than the corresponding non-iodinated BODIPYs, and their singlet oxygen quantum yields were in the range of 0.02 to 0.76 in dichloromethane. Relative to hematoporphyrin, a known PDT agent, **3** showed 4-fold better photosensitizing ability for the generation of $^1O_2$[55]. As the bromo atoms were substituted on the phenyl units present on the periphery instead of the π-conjugated skeleton, the $^1O_2$ generation ability was drastically reduced. This further validated the observation that the frontier molecular orbitals and the heavy atoms have to be in close proximity in order to obtain high ISC efficiency.

Ramaiah and co-workers[56] reported an iodinated azaBODIPY **4** as a triplet photosensitizing agent with an absorption maximum at 666 nm (ε = 69900 M^{-1} cm^{-1}) and the singlet oxygen quantum yield of 0.7 relative to methylene blue (0.52). High triplet quantum yield of 78% was obtained which was the highest obtained for aza-BODIPY derivatives to date. Thienyl fused BODIPYs **5** with a thiophene moiety fused into the BODIPY skeleton further pushed the absorption to 730 nm with higher molar absorptivity coefficients (ε= 89000–200000 M^{-1}cm^{-1}) and emission maximum to 750 nm and beyond[57].

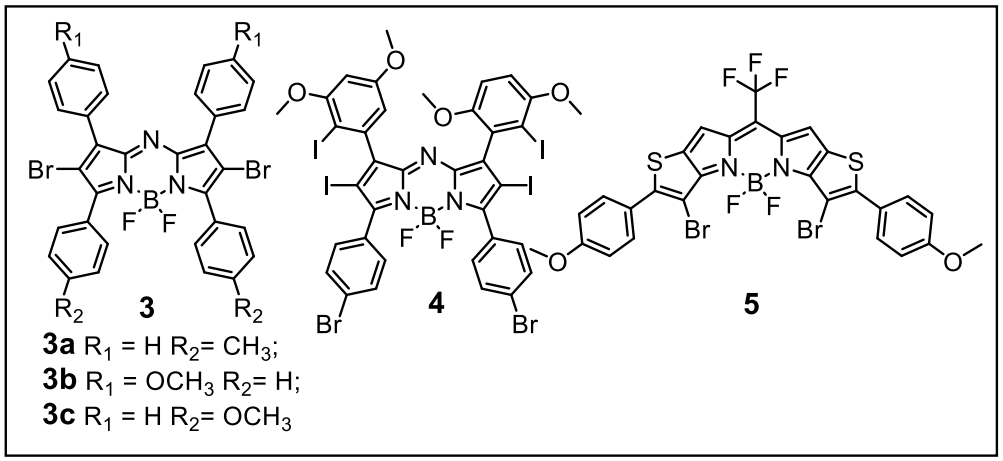

Figure 1.7. Structures of molecules **3**-**5**.

Motivated with the feasible absorption tuning of the BODIPY derivatives with the help of heavy atoms, Zhao and co-workers reported a number of iodo-BODIPY derivatives **6a-f** as triplet photosensitizers and achieved wide range of photophysical properties as mentioned in table T1.1 Via homo and hetero-couplings between different BODIPY derivatives, BODIPY dimers **6c** and **6e** were reported[58]. It is interesting to note that long-lived triplet excited states with triplet lifetimes, τ_T of up to 57.2 μs were obtained at room temperature with these organic photosensitizers. Furthermore, significant amount of upconversion (ϕ_{UC} up to 6.1%) was

obtained in solution state as well as in polymeric films using perylene or 1-chloro-9,10-bis(phenylethynyl) anthracene (1CBPEA) as the triplet acceptors.

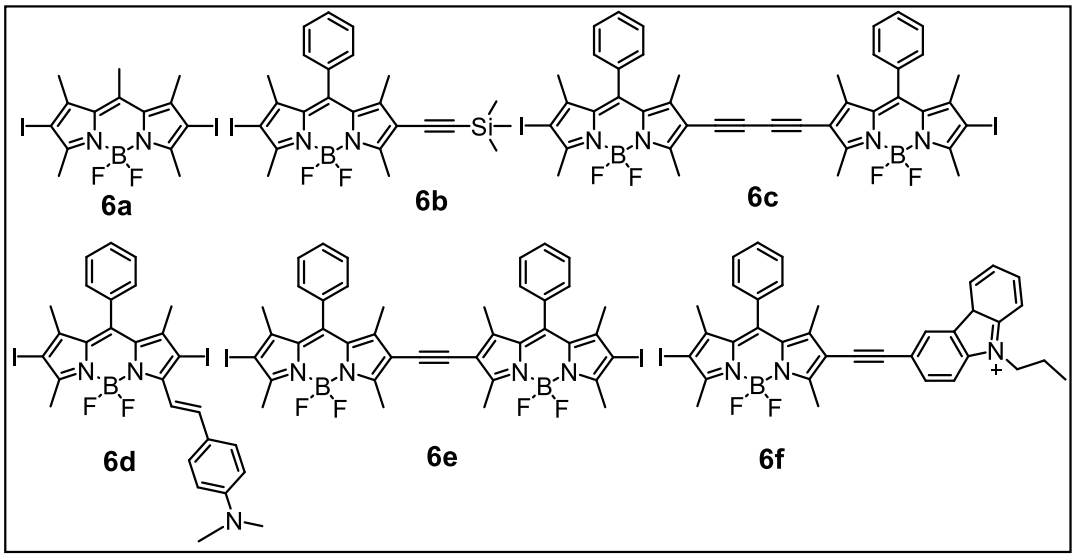

Figure 1.8. Structures of molecules **6a-f.**

Table 1.1. Photophysical parameters of compounds **6a-f.**

	λ_{abs}	λ_{em}	ϕ_F	ε_b	τ_F (ns)	τ_T (μs)	ΔE (T_1-S_0) (nm)	ϕ_{ISC}
6a	529	552	2.7	8.90	0.13	57.1	826	0.973
6b	539	563	7.54	7.8	0.42	57.2	829	0.922
6c	576	623	18.0	10.5	0.42	26.9	893	0.895
6d	629	706	7.28	9.5	1.40	4.0	1075	0.905
6e	575/618	646	9.09/8.95	9.3	0.57	47.0	865	0.907
6f	557	631	5.94	4.6	0.37	54.6	878	0.954

The direct influence of the number of halogen atoms and the positions opted for halogenation on ISC efficiency has been an area of interest for scientists working in these areas. In this regard, a regioselective stepwise bromination on pyrrolic unsubstituted BODIPYs was achieved with liquid bromine. A series of mono- to hexabromoBODIPYs **7a-d** were reported[59] and it was observed that substitution of the first bromine atom at 2- position dramatically increased the triplet quantum yield (ϕ_T) from ~0 to 39%. Similarly, as the number of bromine atoms were increased to two, four and six, there was a regular increase observed with the ϕ_T

values to 0.46, 0.50 and 0.66, respectively in toluene. Fairly long triplet lifetimes of 43, 39, 36 and 26 μs were observed for **7a-d** respectively. It is deduced that the bromination at 2,6-positions of the BODIPY chromophore causes a more significant impact on photosensitization ability while the other positions exhibit only a slight increase in singlet oxygen quantum yield.

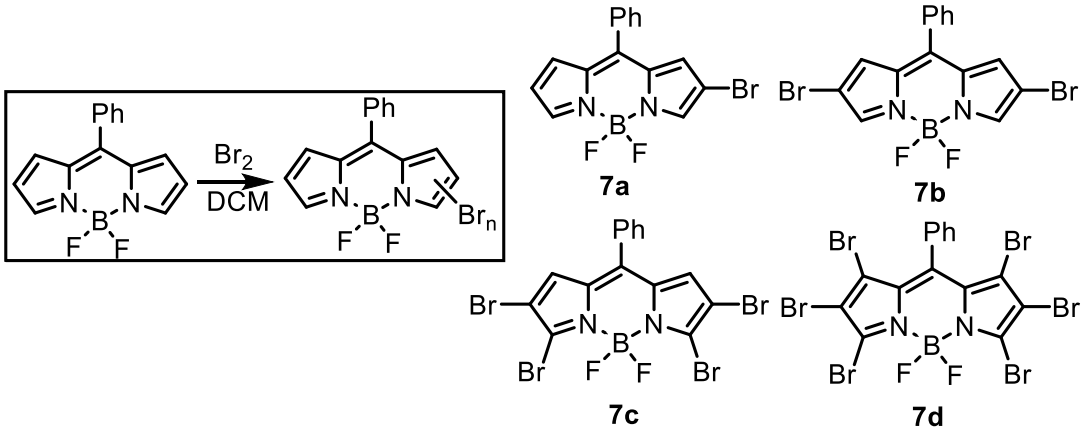

Figure 1.9. Structures of molecules **7a-d.**

Similarly, various oligoiodoBODIPY systems **8a-c** have also been constructed using similar methodology[60]. As the iodine atoms were increased, the absorption maxima gradually shifted from 548 to 563 nm and further to 581 nm. The singlet oxygen quantum yields were quite similar for these iodinated BODIPYs and were found to be 0.83, 0.86, and 0.87 respectively relative to Rose Bengal. This observation is in good accordance with the previous report on oligobromoBODIPY systems wherein heavy atom substitution at 2,6- positions of BODIPY led to drastic improvement in photosensitising ability and introduction of bromines at 3- , 5- position only slightly increased the singlet oxygen efficiency.

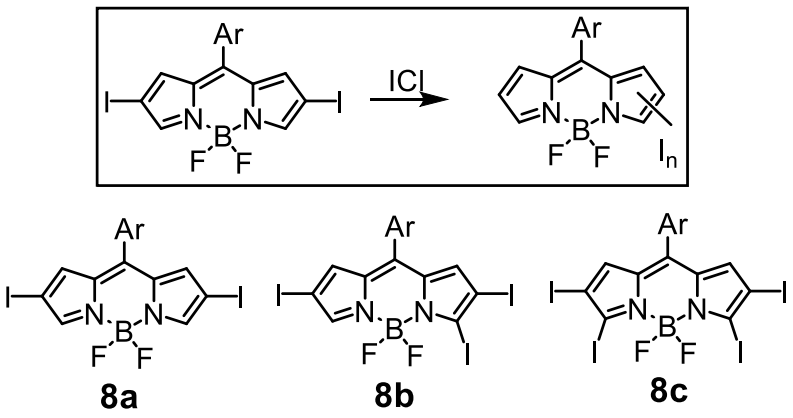

Figure 1.10. Structures of molecules **8a-c.**

Zhao et al[61] reported a photosensitizer **9** consisting of polygalactose-functionalized BODIPY which exhibited high water solubility and selectively detected and killed pathogens over normal cells. It was able to selectively attach to P. aeruginosa over normal cells causing effective pathogen ablation via singlet oxygen. Over 90% of the biofilm formation produced by P. aeruginosa was inhibited by the photosensitizer.

Dong and co-workers[62] have developed NIR absorbing azaBODIPY derivatives **10a-b** with bromine substituents that showed absorption maxima at 683 nm with a high singlet oxygen quantum yield of ϕ_Δ = 0.84. After encapsulation of the photosensitizer with polyethylene glycol–folic acid (PEG–FA) and polyethylene glycol–triphenylphosphonium (PEG–TPP), the nanoparticles from **10a** were obtained with good efficiency of singlet oxygen generation and efficient hyperthermia (40%) under light irradiation. Similarly, the iodinated aza-BODIPY **10b** displays an absorption spectrum at 658 nm and feeble fluorescence at 714 nm alongside very high singlet oxygen generation efficiency (ϕ_Δ = 0.92 in PBS). Nanoparticles prepared from **10b** via self-assembly absorbs in the NIR region and displays high photothermal conversion efficiency (37.9 %) with excellent singlet oxygen generation. Dong and co-workers[63] also reported a NIR aza-BODIPY based photosensitizer **11** with 2-pyridone functional group for image-guided PDT. The diiodo-substituted aza-BODIPY absorbs at 586 nm in DCM but when transformed into NPs via self-assembly with an amphiphilic polymer DSPE-mPEG2000 showed an absorption ranging from 530 nm to 680 nm. Reversible transformation between 2-pyridone moiety and its endoperoxide form rendered the molecule with non-stop $^1O_2$ generation. The nanoparticles are biocompatible and exhibited high photothermal conversion efficiency of 35.7% with excellent and continuous $^1O_2$ generation. They selectively localised at the tumour site through enhanced permeability and retention (EPR) effect and caused efficient inhibition of tumour growth (93.4% inhibition) via photothermal assisted photodynamic therapy without any observable side effects.

PEG-BDP **12** was prepared by Yan and co-workers[64] that exhibited excellent photocytotoxicity to HepG2 and 4T1 cell lines when irradiated with 660 nm light. It acted as a photosensitiser and exhibited good imaging abilities both in vitro and in vivo. **12** self-assembled into micelles and showed good cellular uptake, prolonged blood circulation and preferential accumulation at tumour site. The tumour growth was inhibited and supressed to negligible volume upon irradiation without any noticeable side-effects. The singlet oxygen quantum yield (ϕ) was calculated to be 0.59 for **12** and 0.76 for its free and non-PEGylated form.

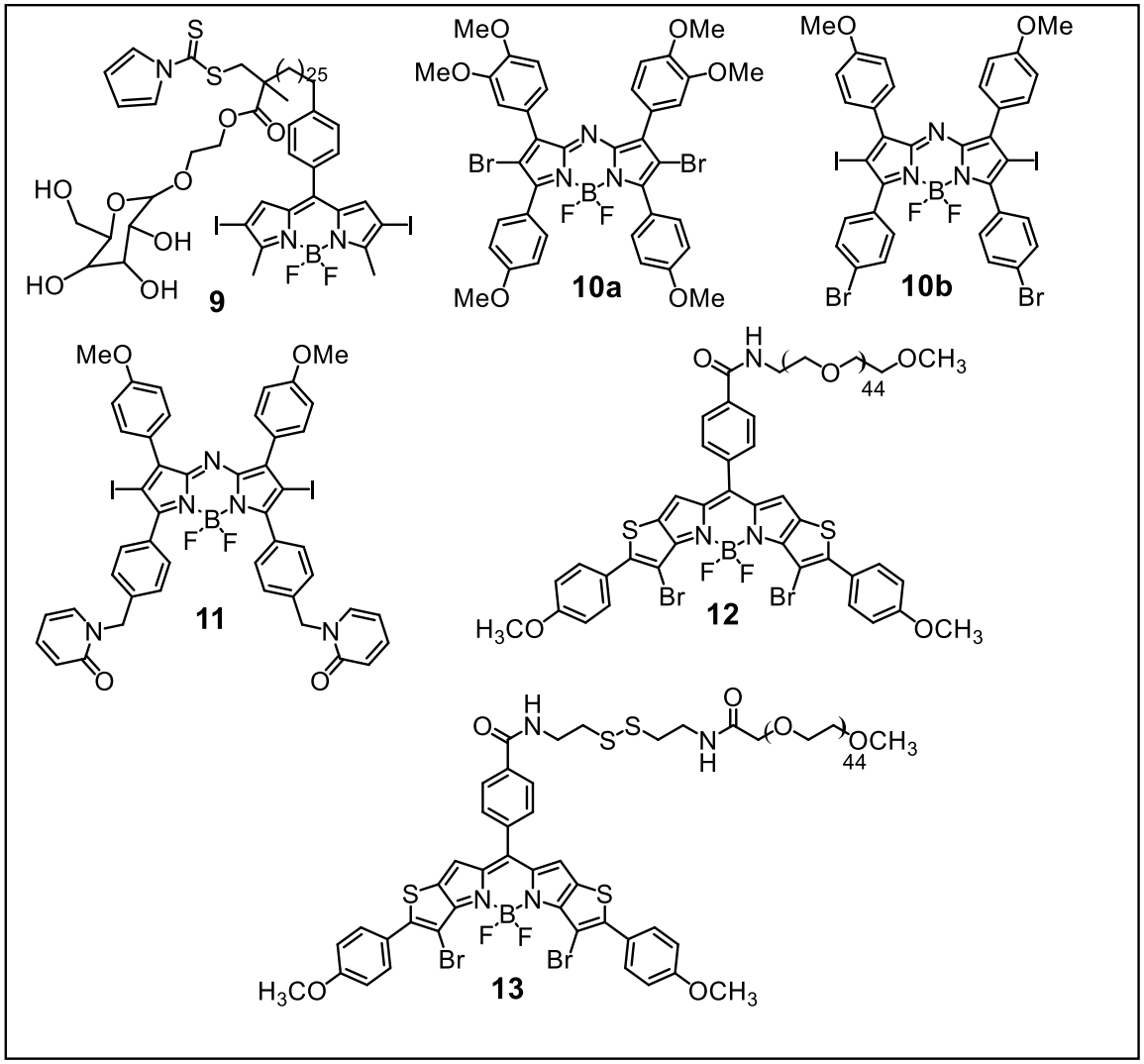

Figure 1.11. Structures of molecules **9-13.**

Yan and co-workers[65] followed similar strategies to develop a redox-responsive PEGylated BODIPY prodrug **13** that contained a disulfide bond which connected the hydrophobic photosensitizer with hydrophilic PEG. The polymeric nanoparticles prepared via self-assembly possessed uniform sizes of about 110 nm that supported prolonged blood circulation and in vivo tumour accumulation along with stronger NIR fluorescence as compared to free molecule. After internalization by cancer cells, release of free photosensitiser took place through cleavage of the disulfide bond triggered in presence of high cellular GSH concentration. 81.9% of the tumour volume was reduced with the nanoparticles under 660 nm laser irradiation.

1.4.1.1.2. 3,5-Styryl substituted haloBODIPYs

Akkaya and co-workers reported post-synthetic functionalization on BODIPY chromophore via Knoevenagel condensation. This methodology uses the acidic methyl substituent at 3,5- positions on BODIPY to introduce aromatic skeletons onto the chromophores with tuning the aromatic aldehydes. It renders long wavelength absorption, intense fluorescence emission, water solubility and good targeting properties. A series of novel water soluble haloBODIPYs have been reported that exhibit absorption in range of 635-725 nm. Ng and co-workers[66] studied the cellular uptake properties, subcellular localization and photocytotoxicity of the iodinated BODIPYs **14** and **15a-b**. In vitro photodynamic activities against HT29 human colorectal carcinoma cells demonstrate that impressive photocytotoxicity with an IC_{50} value as low as 7 nM was obtained for **15a** which specifically localised in the endoplasmic reticulum of cells and caused cell apoptosis upon irradiation. Mono-styryl-BODIPY **16a** designed by Vicente and co-workers[67] absorbed strongly at 636 nm in DMSO and showed high dark toxicity/photocytotoxicity ratio of 74. It preferentially localised in the endoplasmic reticulum and mitochondria with the ability to act as photosensitiser. It was observed that the symmetric di-styryl BODIPY counterparts showed negligible phototoxicity. It was attributed to the unsymmetrical structure of mono-styryl BODIPYs which facilitated cellular uptake and specific binding to intracellular proteins. Furthermore, NIR absorbing triphenylamine grafted BODIPY based photosensitiser **17**[68] showed a decent singlet oxygen generation efficiency of 35%. Its nanoparticles prepared via nanoprecipitation showed efficient photothermal conversion efficiency of 52.6% and induced significant apoptosis of osteosarcoma cells with 808 nm laser illumination alongside exhibiting low dark cytotoxicity. The nanoparticles could accumulate in tumour tissue in 6 hours and had the ability to inhibit the migration of osteosarcoma cells thereby ruling out the possibility of tumour metastasis.

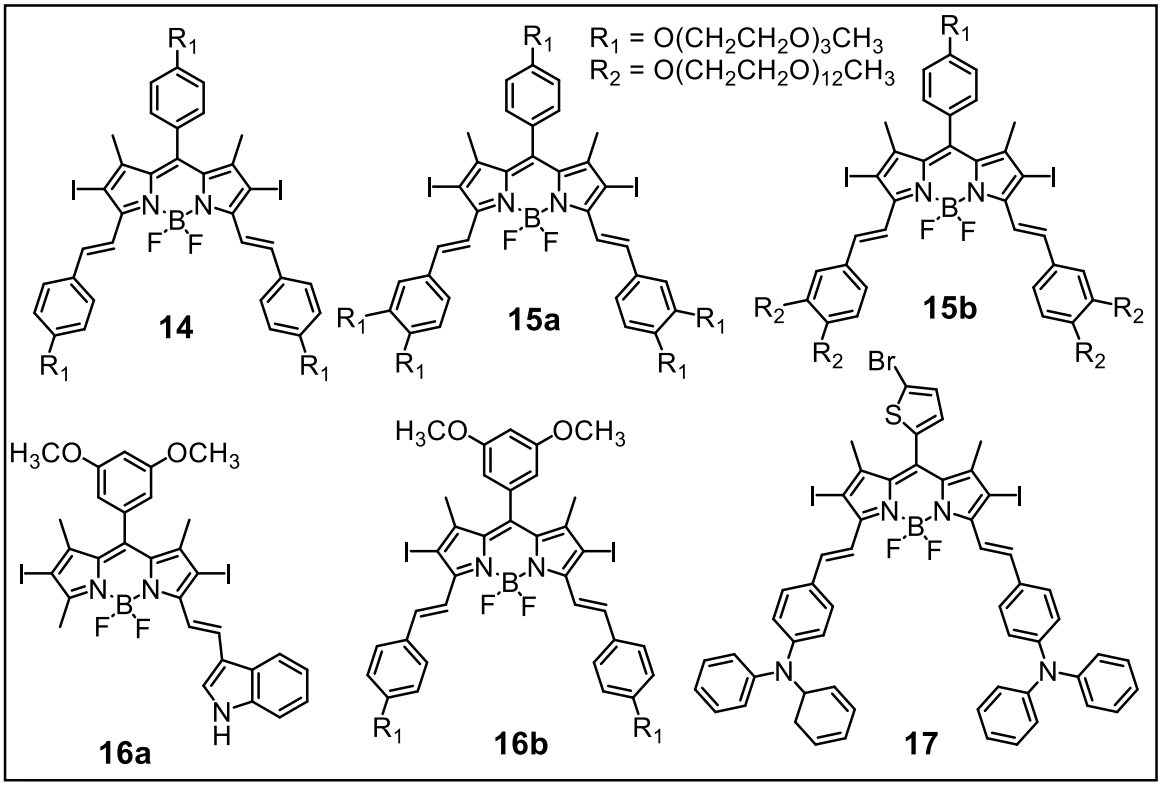

Figure 1.12. Structures of molecules **14-17.**

Dong, Zhang and co-workers[69] reported an anthracene functionalized BODIPY derivative with efficient singlet oxygen trapping and releasing ability for synergistic photothermal and photodynamic therapy. BODIPY **18** with absorption maxima at 628 nm and the singlet oxygen yield of 0.70 in dichloromethane consisted of an anthracene moiety that trapped the $^1O_2$ species in presence of light to form endoperoxide while the endoperoxide in dark went back to regenerate the anthracene moiety via thermal cyclo-reversion thereby generating singlet oxygen. Hence the photodynamic process continued under dark and light conditions. The water solubility of the molecule was improved by preparing nanoparticles using DSPE-PEG-2000 which showed good photothermal conversion efficiency (η = 38.9%) and outstanding biocompatibility with negligible side effects. Low half inhibitory concentration (IC_{50}) of 6.29 μg/mL was obtained on HeLa cells with the NPs. In vivo fluorescence imaging guided phototherapy indicates inhibition in the tumour growth under laser irradiation with no side effects on normal tissues.

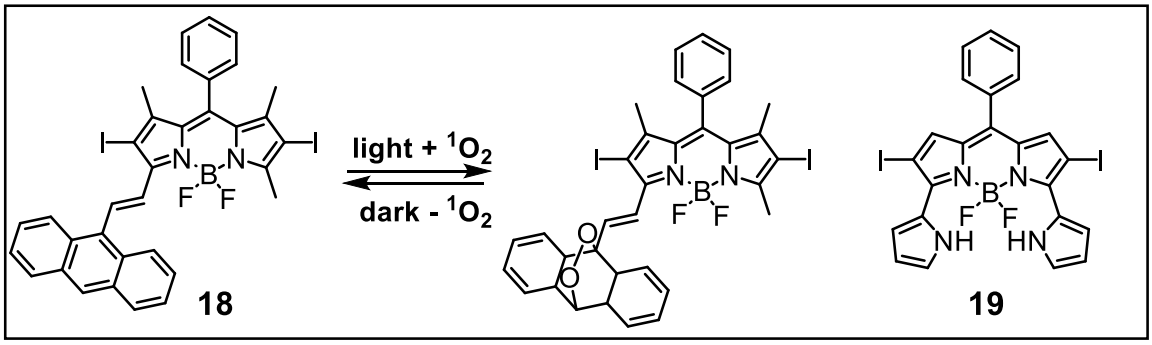

Figure 1.13. Structures of molecules **18-19.**

1.4.1.1.3. 3,5-Pyrrole substituted haloBODIPYs

Yan, Hao and co-workers [70] reported iodinated derivatives of 3,5-pyrrole-substituted BODIPY **19** whose polymeric micellar nanoparticles were prepared upon encapsulation with biocompatible amphiphilic peptide PEG-PLys. The resulting NPs possess good water compatibility, an intense 671 nm NIR absorption and a high singlet oxygen quantum yield (ϕ_Δ = 0.80 in ACN). In vivo PDT results show that the NPs exhibited good tumor targeting and killing abilities (IC_{50} = 0.60 μg/mL or 0.93 μM) on HepG2 cells. Jiao and co-workers reported a regioselective aromatic substitution reaction on some previously reported oligobromoBODIPYs. High reactivity of 3,5-dibromo-BODIPYs led to efficient reaction between 2,3,5,6-tetrabromoBODIPY and 1,2,3,5,6,7-hexabromoBODIPY with pyrrole, leading to substitution at 3,5- positions. Resulting molecules **20a-d** were 3,5-pyrrole substituted bromoBODIPYs[71]. The overall π-conjugation of the chromophore was extended after derivatization with pyrrole which is electron rich in nature. On the other hand, bromo substituents at 2,6- and 3,5- positions ensured good intersystem crossing. Bromotetrapyrroles **20a-b** absorbed strongly around 620 nm while **20c-d** ensured 700 nm absorption, better photostability than methylene blue, singlet oxygen quantum yields of 0.23 and 0.39 in benzene, respectively. As part of control experiments, alkyl substituents on uncoordinated 3,5-pyrroles further shifted the absorption and emission bathochromically but they lowered singlet oxygen generating efficiency and fluorescence quantum yields of these dyes. The molecules incorporated electron rich pyrroles via extended π-conjugation at 3,5-positions to facilitate NIR absorption, emission and efficient intersystem crossing due to the presence of bromines at various positions.

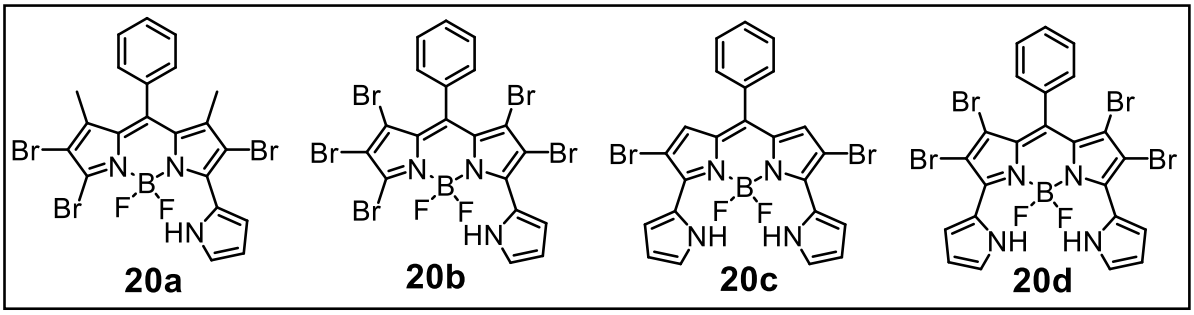

Figure 1.14. Structures of molecules **20a-d.**

1.4.1.1.4. Conjugation of BODIPY core to transition-metal complexes

Introduction of transition metal ions in close proximity to a chromophore offers an interesting strategy to generate triplet excited states. This methodology offers a great promise to photoactivate an otherwise inactive molecule and convert it to a triplet photosensitizer through direct metalation leading to broadband absorption spectrum and controlled kinetics of the intersystem crossing. In this regard, Zhao and co-workers[72] reported a series of complex conjugated BODIPYs **21a-b** wherein the meso-phenyl or β-pyrrolic positions of BODIPY were functionalised with Ir(III)-bipyridine complexes. Relative to the meso positioned BODIPY **21a**, the β-Ir(III)-bipyridine conjugated BODIPY generated singlet oxygen more efficiently with ϕ_Δ = 0.97, 2 fold more than the BODIPY complex **21a.** Complexes **21a** and **21b** showed more pronounced absorption (ε = 71 400 M^{-1} cm^{-1} at 499 nm and 83 000 M^{-1} cm^{-1} at 527 nm, respectively than the BODIPY devoid iridium complex **21c** which weakly absorbs in visible region (ε < 4790 M^{-1} cm^{-1}). Furthermore, while **21c** gave a short triplet state lifetime of 0.35 μs, **21a** and **21b** gave BODIPY-localised triplet lifetime of 23.7 and 87.2 μs respectively. Hence it is concluded that extended conjugation of the BODIPY at the 3,5-positons vastly affects the resulting photophysical parameters. **21a** and **21b** also acted as triplet photosensitiser for triplet-triplet annihilation upconversion with the upconversion yields of 1.2 and 2.8% respectively. **21b** also exhibited room-temperature phosphorescence at 742 nm.

Similarly Ortizand and co-workers[72] reported the biscyclometalated Ir(III) complexes using BODIPY as ancillary ligand directly grafted to acetylacetonate. The resulting complexes **22a-b** show high absorption coefficients at 517 and 594 nm respectively, moderately good fluorescence quantum yields of 0.08 and 0.22 and yield high efficiency of singlet oxygen generation (ϕ_Δ = 0.86, 0.6 in ACN respectively on visible light illumination). Both complexes exhibited similar spectral signature in nanosecond time-resolved transient absorption spectra and a triplet lifetime of ~10 μs was found for both complexes in non-aerated solutions which

was ascribed to the lowest-lying BODIPY-centered triplet state. These complexes internalised into HeLa cells with low dark toxicity, consistent fluorescence response and high photoinduced cytotoxicity.

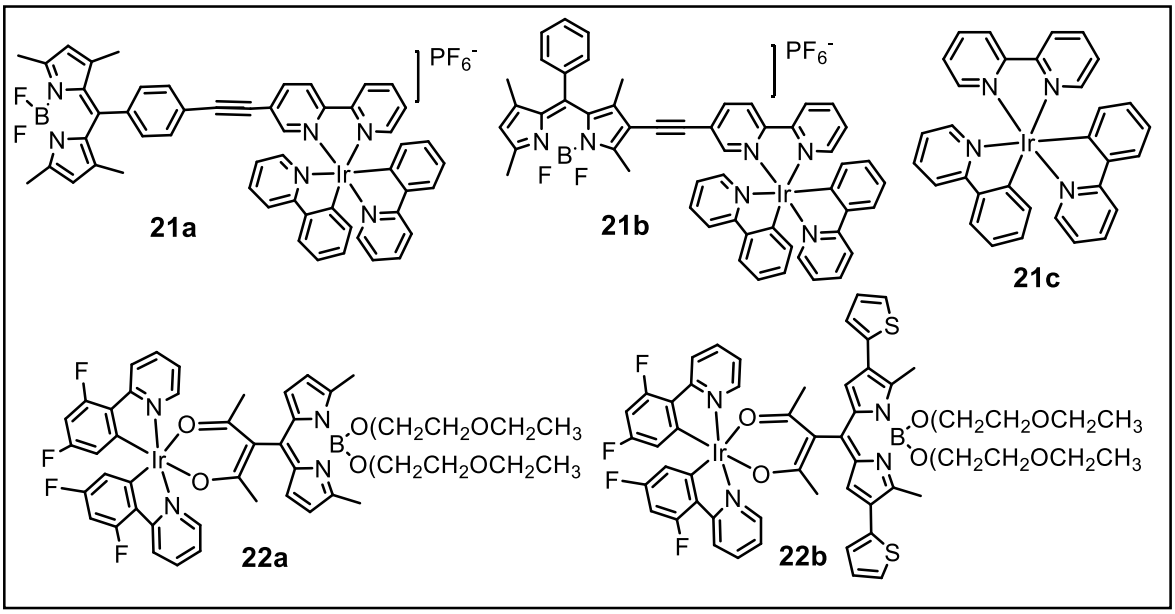

Figure 1.15. Structures of molecules **21-22.**

Furthermore, Ru(II) and Ir(III) containing bimetallic complexes **23a-b** wherein the BODIPY was covalently attached as a bridge to the coordinated bipyridine ligands via acetylene linkers were found to be efficient triplet photosensitizers[73]. Both absorbed strongly in the visible region around 570 nm with high molar absorption coefficients of the order of 10^5 $dm^{-3}mol^{-1}$ cm^{-1}. As the triplet state had a strong intraligand feature alongside some contribution from the metal centers, exceptionally long triplet lifetimes of 1316 and 630.7 μs were found for **23a** and **23b** respectively. Significantly high upconversion quantum yields of 19.1 and 25.5% were respectively obtained for the bimetallic complexes **23a** and **23b** in presence of 9,10–diphenylanthracene (DPA) as an acceptor. They showed singlet oxygen quantum yields of 79 and 75% in acetonitrile and easily penetrated into the cytosol killing most population of the cancer cells upon 600 nm laser illumination.

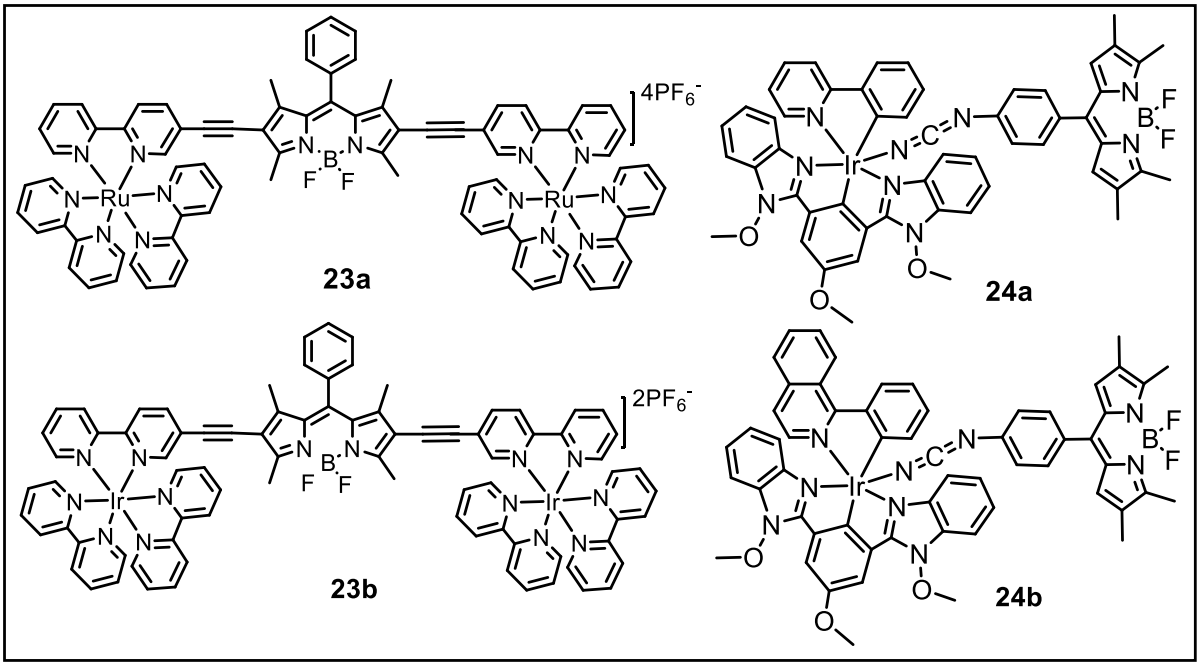

Figure 1.16. Structures of molecules **23-24.**

Tabrizi and co-workers[74] designed two cyclometalated Ir(III) complexes **24a-b** which yielded high ϕ_Δ of 79% and 92% respectively. The binding mode to ct DNA was found to be mainly non-covalent in nature via intercalation. Upon exposure to 500 nm light, complexes **24a** and **24b** displayed 73 and 84% cleavage of SC pUC19 DNA to its nicked circular form respectively due to the formation of $^1O_2$ as reactive species to contribute in the cleavage process. The complexes also showed god cellular uptake and efficient photocytotoxicity in HeLa cell lines with IC_{50} values of 0.78 and 0.53 μM at 10 J/cm^2 of light dose, respectively. Furthermore, exceptional thioredoxin reductase (TrxR)- inhibitory action was observed by these complexes in comparison with auranofin, an extensively known positive TrxR inhibitor constituting a gold phosphine complex.

Direct metalation of BODIPYs with Pt(II) and Au(I) also presents itself a great promise to yield BODIPY based efficient triplet photosensitizers. According to a report published by Zhao and co-workers[75], direct tethering of Pt(II) coordination centre to the π-core of the BODIPY chromophore enhanced the heavy atom effect of the Pt(II) atoms. The designed BODIPY based complexes **25a-b** showed strong absorption maxima ranging from 500 to 640 nm and high singlet oxygen generation efficiency (with singlet oxygen generation quantum yields of 0.70-0.80 in toluene). Complexes **25a** and **25b** acted as efficient photosensitizers for triplet-triplet annihilation upconversion and were excited with red light at 635nm to yield upconverted emission peaks at 447 nm. Long triplet lifetimes of 63.13 and 94.18 μs were found

for complexes **25a** and **25b** respectively. Nanosecond time-resolved transient absorption spectroscopy indicated the distribution of the triplet excited state of **25a** over both the peripheral BODIPY units. However, in the case of **25b**, triplet state was restricted to the centrally placed BODIPY ligand. Furthermore, these complexes also exhibited delayed fluorescence property with lifetimes of 43.8 and 111 μs for **25a** and **25b** respectively. Delayed fluorescence is a property that is rarely observed for transition metal complexes and herein its presence was attributed to the presence of long-lived triplet excited states. These complexes also acted as multi-wavelength activatable photosensitizers for triplet-triplet annihilation upconversion using perylenebisimide (PBI) as triplet energy acceptor. Kinetics of intersystem crossing in similar complexes **25c-e** containing different coordination profiles wherein the Pt(II) atom was directly connected to the π cloud of the BODIPY or to the meso positions of the BODIPYs varied by 4 folds[76]. While intersystem crossing rate constant, $k_{ISC} = 4.23 \times 10^{10}$ s^{-1} and singlet oxygen quantum yield, $\phi_{\Delta} = 37$ % were obtained for **25c**, complex **25d** showed the corresponding values of 9.89×10^{9} s^{-1} and 26%. Similarly, complex **25e** showed efficient singlet oxygen generation, $\phi_{\Delta} = 75\%$ and high triplet state quantum yield, $\phi_{T} = 0.91$ in toluene, pointing towards efficient intersystem crossing in the system. Ultrafast intramolecular singlet energy transfer was observed for **25e** with the rate constant, $k_{FRET} = 2.6 \times 10^{11}$ s^{-1}, intersystem crossing rate constant, $k_{ISC} = 1.92 \times 10^{10}$ s^{-1} and long lived-triplet state lifetime of 54.1 μs. Hence the Pt(II) complexes exhibited broadband visible light absorption, resonance energy transfer, and facilitated funnelling of the excitation energy into the ligand via efficient intersystem crossing.

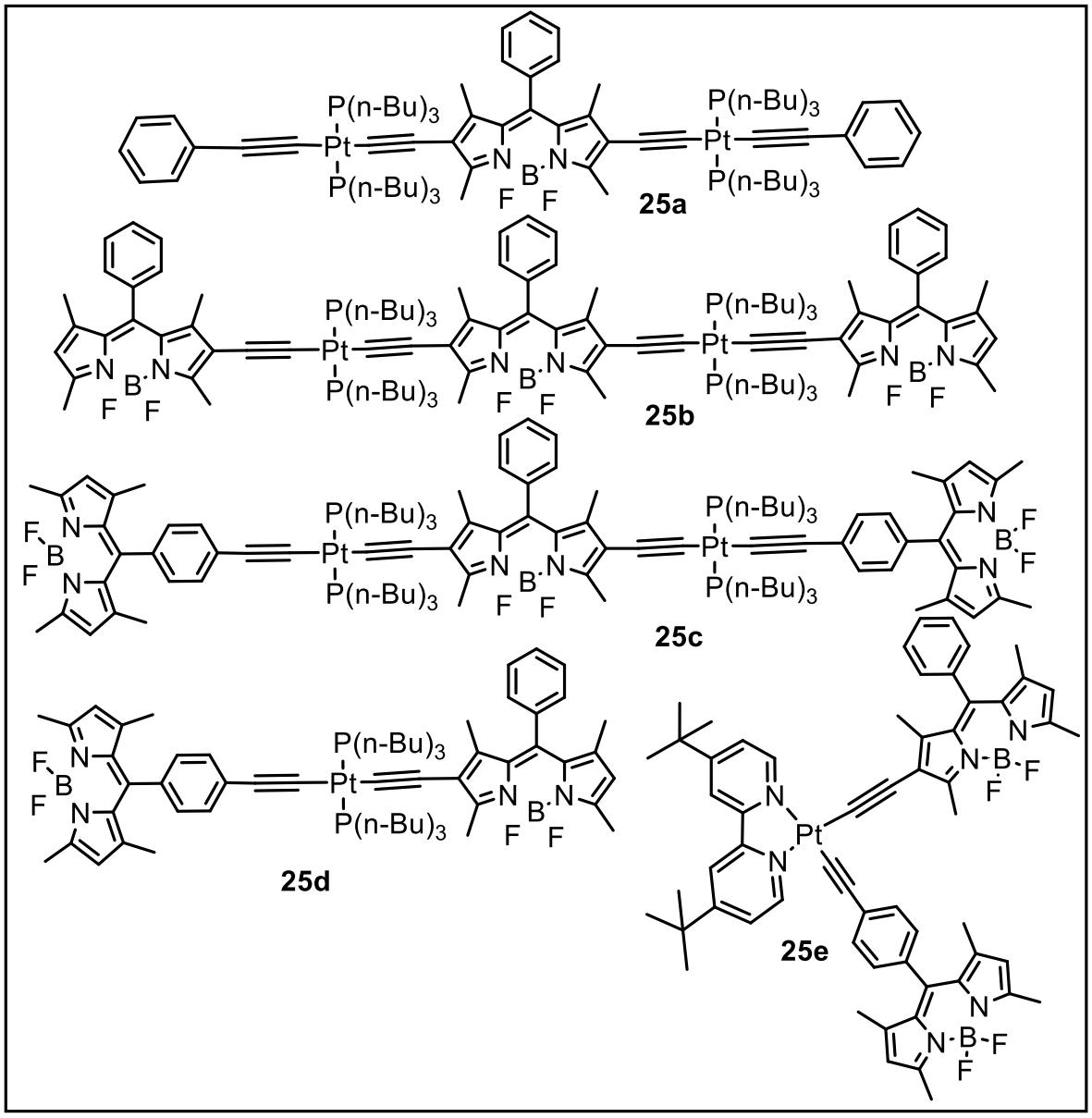

Figure 1.17. Structures of molecules **25a-e.**

Emrullahoğlu and coworkers[77] also explored direct metalation of BODIPY with Au(I) which converted an otherwise photoinactive BODIPY to an efficient photosensitiser to yield **26** wherein PPh_3-Au(I) acted as a spin converter. It was anticipated that incorporation of −LAu(I) into the alkynyl skeleton of BODIPY core could facilitate intersystem crossing owing to heavy atom effect of Au(I). The complex showed high singlet oxygen generation efficiency (ϕ_Δ = 0.84 in DCM) and excellent photocytotoxic activity against A549 cancer cell lines (EC_{50} = 2.5 nM) under 525 nm light for 30 min. On a similar note, Chakravarty *et. al*[78] designed a complex **27** that which exhibited broadband NIR absorption with a maximum at 715 nm in 10% DMSO-DMEM and singlet oxygen quantum yield (ϕ_Δ) of 58%. It showed remarkable

photocytotoxicity under red light illumination towards cervical HeLa, lung cancer A549 and breast cancer MCF-7 cells (IC_{50}: 2.3−24.7 μM in light) with negligible dark toxicity (IC_{50} > 100 μM). The complex localised in the mitochondria of cell, as depicted via confocal microscopy measurements. The binuclear platinum(II) BODIPY complex, reported by Chakravarty and co-workers also exhibited significant lysosomal localization and efficient apoptotic photodynamic therapy effects against HeLa cervical cancer, A549 lung cancer, and MDA-MB231 cancer cell lines, while showcasing truly nontoxic behavior in the HPL1D immortalized lung epithelial normal cells.

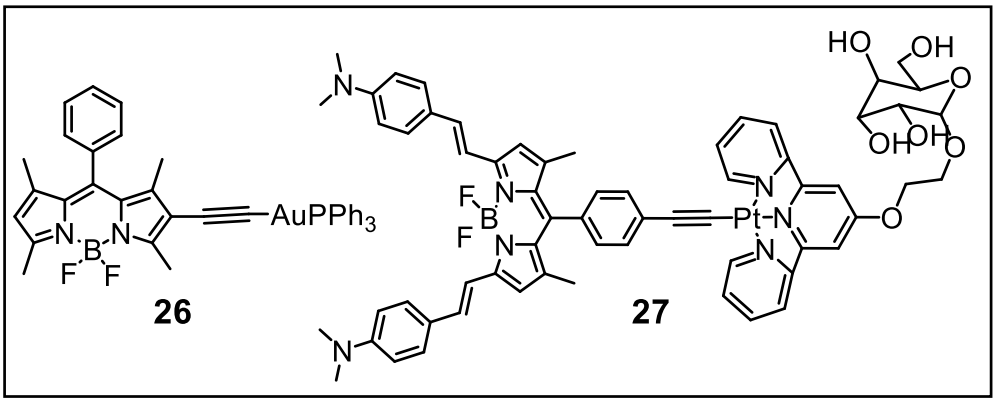

Figure 1.18. Structures of molecules **26-27.**

BODIPY-containing Ru(II) complexes[79] **28a-b** were designed wherein the acetylide linkers were installed onto the meso-phenyl moieties which supposedly opted an orthogonal geometry towards the dipyrromethene core of BODIPY. The absorption maxima for both obtained at 523 nm is attributed to the BODIPY core and at low temperature (77K), fluorescence was observed at 536 nm alongside a band at 774 nm which was attributed to the phosphorescence emission which was further confirmed by the long triplet state lifetime (50 ms) and mega Stokes shift. In comparison, Ru(II) terpyridine coordination center in absence of the BODIPY moiety gave a lifetime in range of few hundred picoseconds.

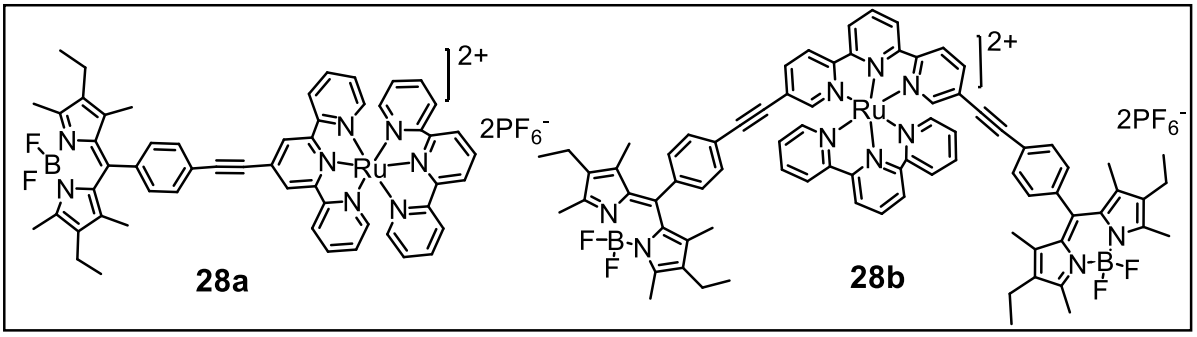

Figure 1.19. Structures of molecules **28a-b.**

In N^N^N Pt(II) acetylide complex **29**, Pt(II) terpyridine chromophore has been connected to a BODIPY subunit and the resulting multichromophore yielded an absorption maximum at 523 nm with a decent fluorescence quantum yield of 0.27[80]. It was concluded that Pt(II) chromophore played a necessary role in order to achieve low temperature phosphorescence in **29.** Energy transfer between the ^{3}MLCT state to the BODIPY centered triplet state was the key phenomenon that enhanced the radiative rate constant of the triplet state of BODIPY via enhanced spin-orbit coupling thereby allowing efficient intersystem crossing and consequent phosphorescence from the BODIPY subunit. Long lifetime of 74 ms was achieved at 77 K with complex **29** at 777 nm. As an attempt to attain maximized heavy atom effect in BODIPY containing Pt(II) complexes, another structural motif **30** was prepared wherein the Pt(II) atoms are directly coordinated to the π-conjugated BODIPY skeleton[81]. This successfully maximised the heavy atom effect, and the associated intersystem crossing as the electrons in the frontier molecular orbitals could easily to move to the vicinity of Pt(II) atoms. Complex **30** showed a drastically different and intense absorption and emission profile relative to the free ethynyl BODIPY ligand with the maxima at 574 nm. The complexes exhibited dual emission at 660 and 770 nm and the first triplet excited state was majorly localised on the BODIPY moiety at ^{3}IL state. Room temperature long lived phosphorescence at 770 nm was observed with a lifetime of 128.4 ms and quantum yield, ϕ_P of 3.5%. Furthermore, owing to the long triplet lifetimes and good light harvesting capability of the complex **30,** triplet-triplet annihilation upconversion was observed with an upconversion quantum yield of 5.2% using perylene as triplet energy acceptor. Strong visible light absorption and long-lived triplet states make these molecules attractive candidates for applications in photovoltaics, photocatalysis and upconversions.

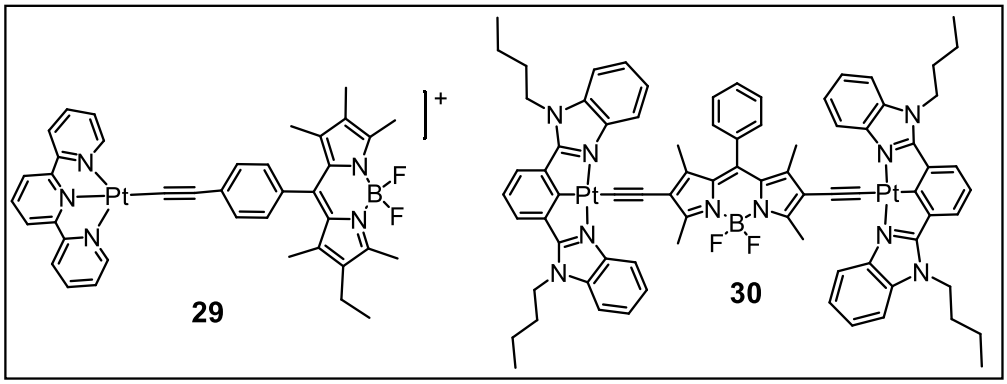

Figure 1.20. Structures of molecules **29**-**30.**

1.4.1.2. Plasmon-Molecule Interaction in Photodynamic Therapy

Plasmonic metal nanoparticles placed in close proximity to organic photosensitiser have demonstrated intense light absorption in NIR region and efficient $^1O_2$ generation ability[19]. This is attributed to plasmon-molecular resonance coupling which takes place when a chromophore is placed in vicinity of plasmonic metal nanoparticles. Consequently, hybrid states are produced which have spectral properties quite different from those of the individual components. AuNPs have found the most extensive applications in PDT amongst all metallic nanoparticles because of localised surface plasmon resonance, LSPR which involves heating of AuNPs upon absorption of a particular wavelength of light by the surface. LSPR allows fast and efficient energy transfer from Au metal surface to molecular oxygen to generate singlet oxygen thus inducing PDT effect. AuNPs can exist in many sizes and shapes such as nanorods, nanocages, nanostars, nanoflower etc. Plasmon-molecule interactions have found applications as ultrafast switches, bistable devices, modulators, sensors, photocatalysts and biological imaging agents[82–85]. Geddes and co-workers reported that the singlet oxygen quantum yield of organic photosensitisers could be enhanced via surface plasmon couplings[86]. Singlet oxygen generation with Rose Bengal depended on the theoretical electric field enhancement or increased absorption of the photosensitizer when present in close proximity of metallic nanoparticles. Similarly, Chen and co-workers showed that an electrostatically bound gold nanorod-chlorin e6 system had strong plasmon resonance coupling which resulted into enhanced singlet oxygen generation and killed cancer cells[87]. In another report, Wu and co-workers[88] reported that plasmon resonance energy transfer (PRET) occuring from plasmonic nanoparticles to photosensitiser led to plasmon quenching dips which is known to enhance $^1O_2$ generation. PS chlorin e6 with AuNR was used as a model system for this study. When an overlap occurred between the localized surface plasmon resonance (LSPR) band of Au NR

with the Q band of Ce6, and the separation between Ce6 and the Au NR lied within the acting distance of PRET, consequently considerable amount of quenching dip in the LSPR band was observed. Plasmon-molecule interactions have also exhibited PDT driven antimicrobial activity. In this regard, Zhang and co-workers[89] reported that the singlet oxygen generation was increased by up to three-fold upon resonance coupling between the surface plasmon of silver nanoparticles and photosensitizers. The nanohybrid systems killed both gram-positive and gram-negative bacteria efficiently in comparison to the individual components. Heyne and co-workers[90] showed enhanced $^1O_2$ generation with silica-coated silver nanocubes coupled with Rose Bengal photosensitiser. The system was employed for the photodynamic killing of Gram-positive bacteria, *S* aureus, and Gram-negative bacteria, *E.* Coli. Similarly, when the surface plasmons on metal nanoparticles couple with the electronic states of organic chromophores, hybrid states are generated with special photophysical properties.

Rahman and co-workers demonstrated that plasmon-molecule coupling in gold−BODIPY nanocomposites effectively caused singlet oxygen production for PDT applications[91]. Furthermore, in another report[92] they showed that gold nanoparticles can act as a matrix on which Förster resonance energy transfer (FRET) is promoted between two BODIPY chromophores which are electronically distinct. This process of energy transfer across the multichromophoric nanocomposite facilitated radiative decay pathways, rendering fluorescence to the nanocomposite. Photoinduced hot electron transfer between BODIPY and gold also caused efficient photosensitized generation of singlet oxygen. They also reported the synthesis and photophysical properties of a water-soluble supramolecular nanocomposite that consisted of gold nanoparticles and a naphthalidenimine-boron complex which contained stimuli-responsive (diethyl) amino co-workers[93]. As the pH of the medium changed, the composite also exhibited luminescence switching behaviour in response. Ultrafast spectroscopy studies further indicate reversal in the direction and dynamics of hot electron transfer in this system relative to the previously reported BODIPY containing systems. Here, hot electrons migrated from gold to BODIPY resulting in an increase in luminescence owing to the very fast photo relaxation process. Furthermore, the plasmon-molecule coupling also allowed for efficient singlet oxygen generation. So, union of both pH-sensitive luminescence and singlet oxygen generation facilitated the photodynamic cancer cell death as well differentiation between normal and cancer cell lines.

1.4.1.3. Drawbacks of BODIPYs

While incorporation of heavy atoms and transition metal atoms are the two major strategies opted to generate and modulate the triplet states of BODIPYs, there are other lesser opted methods like incorporation of spin convertors or through excitonic couplings in the excited state. It is worth noting that despite interesting photophysics and facile functionalization, the one issue commonly faced by scientists working with BODIPYs is low reaction yield and precise reaction conditions. In order to address the associated challenges, another class of tetracoordinate boron compounds popularly known as boranils were further opted as the compound of interest. While BODIPYs do show good absorption in far visible and NIR region, even the simplest BODIPY skeleton absorbs in the green region beyond 500 nm. Induction of photosensitizing ability further pushes it towards the higher wavelength end of the electromagnetic spectrum. Hence, it is difficult to achieve BODIPYs as photosensitizers which are able to absorb near high energy UV light up to ~450 nm. In this regard, boranils present themselves as potent alternatives to BODIPY which can be structurally tuned according to the choice of starting aldehydes and amines. Based on the functionalization on the starting materials, it is quite feasible to obtain boranils that can absorb light from near UV to near-infrared region. Thus, they can be completely colorless to pale yellow relative to BODIPYs that always impart intense color to the material due to strong visible light absorption. Simple one-step or two-step synthesis and high reaction yields further make boranils synthetically more feasible than BODIPYs that demand precise reaction conditions and have low reaction yields.

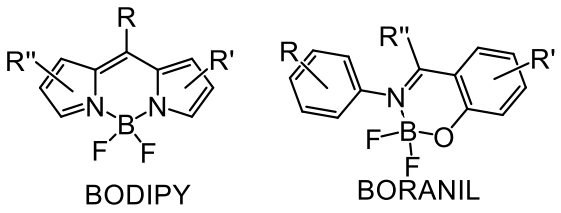

Figure 1.21. Structures of basic skeletons of BODIPY and boranil.

1.4.2. Boranils

Borate complexes based on aniline-imine scaffold or precisely salicylideneimine ligands called as boranils have emerged as interesting class of luminescent molecules wherein N,O- ligands are used for configurationally rigidifying the compound. Alongside easy synthesis even in multigram scale and very good reaction yields, they are easy in terms of handling and fine tuning the emission properties. Boranils are prepared with commercially

available substituted salicylaldehydes and anilines which subsequently complex with trivalent boron moiety. Scheme 1 demonstrates the general synthesis scheme for preparation of boranils.

There are studies reporting coordinatively saturated boron complexes using N^N^O^O-tetradentate ligands, O^N^O tridentate ligands, or N^O-bidentate ligands[94]. They either form five-membered rings with quinolines or six-membered rings with salicylaldehydes, acylpyrrole, oxazolylphenolates, or pyridine phenolates. Complexation of anils (aniline-imines) with trivalent boron (III) precursors leads to stable boranils. Their intense fluorescence originates from an intraligand charge transfer (ILCT) state with the achieved quantum yields as high as 90%.

Preparation of the anil involves a straightforward method wherein the reactants are refluxed in ethanol or dichloromethane with addition of trace amounts of acid. Usually the target imines precipitate pure out of the crude mixture through the reaction course within a few hours. Subsequent boron complexation with excess of $BF_3.Et_2O$ under basic conditions (DIPEA or NEt_3) yields boranils upon purification on silica chromatography. Disappearance of the downfield peak around δ 11-15 ppm in the ^1H NMR spectrum attributed to H-bonded phenolic proton indicates completion of boron complexation. Also, in the ^{11}B NMR, coupling of the imine proton to the ^{11}B center is observed, resulting into a broad quartet.

Though heavy atom incorporation is a commonly opted strategy for populating the triplet states via enhanced spin orbit coupling, boranils and other similar tetracoordinate boron chelates have been rarely explored to achieve triplet states. There are decent number of reports on the luminescence properties of these systems[94–96]luminescent, but their photosensitization abilities have been rarely reported and are almost unexplored.

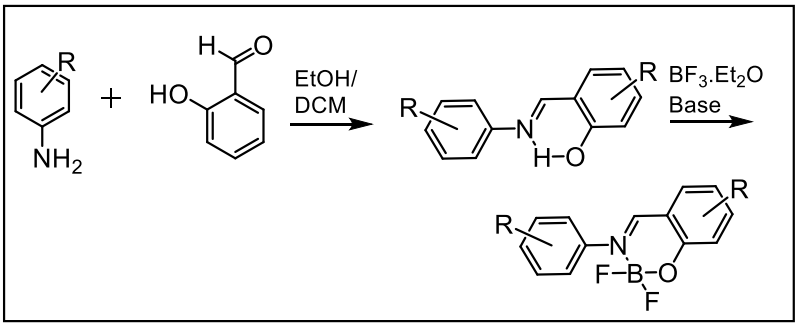

Scheme 1.1. General scheme for the preparation of boranils.

Typical synthesis of boranil complexes takes place in two steps from commercially available starting materials, i.e., substituted anilines and salicylaldehydes (Scheme 1).

Preparation of the anil derivatives is highly straightforward and can be easily achieved by refluxing reactants in a suitable solvent. During the course of the reaction the target imines typically precipitate pure out of the crude mixture within a few hours. Scientists working in the area have made efforts to fine-tune the emission color over the entire visible range of electromagnetic spectrum alongside exhibiting strong emission intensity both in solution as well as solid state. Most of the fluorescent derivatives reported so far have a dialkylamino moiety installed on the phenolic end of the chromohpores in order to further stabilize the corresponding boron complexes in solution. Na Zhao et al[97] designed AIE active boranils **31a-d** by incorporating phenyl rings as intramolecular rotors into the associated anil ligand. Distorted configuration and restriction of intramolecular rotation in the aggregated form was ascribed to the observed AIE activity. The complexes showed good biocompatibility and lipophilicity abilities and selectively stained lipid droplets in living cells in rapid and wash-free mode. In vivo studies were carried out with **31d** to stain yolk lipids in zebrafish. Aishan Ren and co-workers[98] designed complex **32** wherein presence of hydroxyl group enabled further installation of wide range of recognition groups. It showed significant fluorescence enhancement by ~36-folds, 27-folds and 19-folds for cysteine, glutathione and homocysteine detection. The response in fluorescence was attributed to thiol-induced cleavage of 2,4-dinitrobenzenesulfonyl (DNBS) group which was adopted as the recognition unit. DNBS group quenched the fluorescence to reduce background and modify the hydroxyl group to yield a turn-on fluorescent probe for biothiols. Fluorescence imaging of biothiols was successfully performed in living cells. Frath and co-workers[99] further reported π-extended dye **33** which showed strong solvatochromic fluorescence emission across visible to NIR region up to a maximum of 764 nm with high fluorescence quantum yields of up to 69%. Implanting of the dye in amphiphilic block polymer Cremophor ELS caused strong emission at 617 nm in PBS buffer. Furthermore, large two photon cross-section of 420 GM enabled the utility of the dye towards 2P-excitation fluorescence microscopy. Fluorescence lifetime imaging microscopy (FLIM) and real-time widefield imaging studies illustrated the cellular uptake and distribution of **33** in Hela cells. The local environment had a strong impact on the emission of the dye and the dye selectively internalized in acidic vesicles like endosomes or lysosomes. Frath[100] also reported a series of polyanils and subsequent polyboranils **34** via straightforward condensation between phenylenediamine derivatives and 4-(diethylamino)salicylaldehyde. Another series was obtained from condensation between 4,6-dihydroxyiso/ptere-phthalaldehyde and differently substituted anilines. The reported polyanils chelated to trivalent boron fragments such as BF_2 and BPh_2 to generate the corresponding polyboranils. Differently substituted

polyboranils in various solvent environments showed emission maxima ranging from visible to NIR with the fluorescence quantum yields spanning from 0.02 to 0.90. While most of the polyanils were nearly non-fluorescent in molecular state, they exhibited AIE behaviour upon addition of increasing water fraction in THF. It was observed that chelation with boron units intensified the fluorescence emission for the otherwise non-fluorescent polyanils.

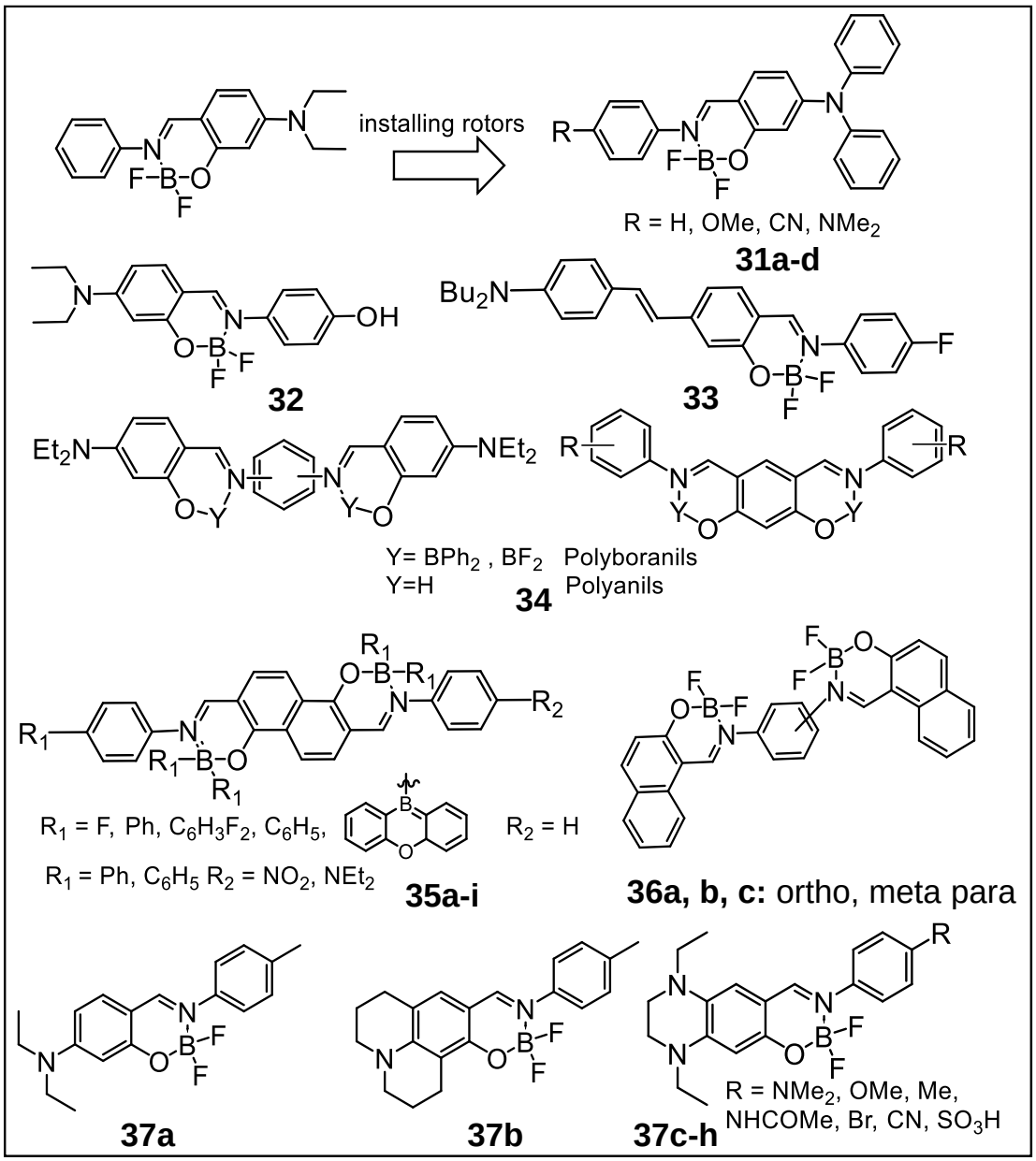

Figure 1.22. Structures of molecules **31-37.**

Mateusz Urban et al[101] designed bis-boranils **35a-i** with different substitutions at boron atom and extending the π-conjugation with electron-withdrawing (NO_2) or electron-donating (NEt_2) functional groups. The resulting complexes were attained from a ditopic tetradentate

1,5-dihydroxy-2,6-bis(N-phenyliminomethylene) naphthalene ligand via one pot condensation. Relative to simple boranils, dinuclear boranil complex with a central phenyl linker rigidified the skeleton which can be proven by high fluorescence quantum yield of 90%. Incorporation of central naphthalene backbone further led to bathochromic shifts in emission, up to 683 nm and tuned to strong PL quantum yield values up to 83%. The compounds exhibited red-shifted absorption and emission up to red region over the entire visible spectrum (λ_{max} = 495−590 nm, λ_{em} = 533−683 nm) with fluorescence quantum yields as high as 83%. Installation of NO_2 and NEt_2 at the extreme ends of the π-conjugated bis(boranil) skeleton led to push-pull feature with charge transfer characteristic. The synthesised bis-boranils showed improved thermal, hydrolytic and electrochemical stability along with good solubility and high fluorescence in organic solvents.

Ziegler and co-workers[102] designed π-extended salphen–BF_2 complexes **36a-c** with 2-hydroxynaphthaldimines including hydrazine and phenylene diamine derivatives with ortho, meta and para substitution patterns. p-Phenylene bridged compound **36c** shows the most red-shifted absorption and emission and the highest PL quantum yield of ~25%, followed by meta, **36b** and ortho, **36a** which showed only 6%. It is worth mentioning that similar compounds wherein the heteroatoms were not occupied by BF_2 coordination on one of the ends exhibit lowest fluorescence quantum yields of > 0.01. Simple boranil dyes with diethylamino moiety usually displayed UV-centered fluorescence emission with a weak quantum fluorescence yield. As an example, **37a** displayed low ϕ_f of 0.07 with an emission maximum of 456 nm[103]. This feature was ascribed to twisted intramolecular charge transfer (TICT), amongst other molecular motions occurring in the excited-state leading to fluorescence quenching. Introducing rigid electron donating groups such as julolidine or 1,2,3,4-tetrahydroquinoxaline on the phenolic side drastically improved the fluorescence quantum yield to 0.24 and 0.49 respectively for **37b** and **37e** along with shifting the emission maxima to 469 and 617 nm with appropriate substitution. Upon incorporation of rigid tetrahydroquinoxaline donor into D-A type complexes **37c-h,** the ICT effect was strongly enhanced to red-shift the emission maxima to a range of 609-656 nm and caused large Stokes shifts up to 178 nm. Filter paper strips coated with **37e** were tested against subsequent acid (TFA) and base (TEA) vapor exposure and it was observed that **37e** had the ability to act as reversible acid-base fluorometric sensor. Imaging experiments were performed in cells and zebrafish with dye **37h** which penetrated the cell-membrane and was used as staining agent.

While these are a few examples from recent past that throw some light on the interesting photophysics exhibited by boranils, there still exists enormous room for functionalization as their photosensitization abilities are yet to be explored.

1.5. Scope and Objectives of the Present Investigation

Tetracoordinate organoboron compounds have emerged as fascinating class of luminescent molecules and photosensitizers. Incorporation of tetracoordinate boron onto organic chelates red shifts the absorption and emission properties and stabilizes the skeleton. In above sections, we have summarized how appropriate functionalization can beautifully tune the associated photosensitization properties in these molecules. We have designed a few halogenated BODIPY derivatives and studied their photophysics. Systematic introduction of transition metal complex containing CO releasing core onto the BODIPY skeleton further improved the overall photodynamic abilities. Although BODIPYs are well established as photosensitizers, they still have oceans of caliber and hence invoke interest to better understand the underlying fundamentals and the associated structure property relationships. A major drawback with BODIPYs is low reactions yields and precise reaction conditions. This issue can be overcome by boranils as they can be easily synthesized in good reaction yields using simple, commercially available starting materials like amines and aldehydes. This methodology enables the synthesis of wide variety of molecules whose properties can be easily tuned across the entire range of electromagnetic spectrum with suitable derivatization accordingly on the aldehyde or amine. While the photosensitization properties of boranils still remained unexplored to date, we achieved high singlet oxygen quantum yields with applications in water decontamination and as antimicrobial coatings. It is pertinent to mention that colorless boranils can be obtained unlike BODIPYs which always possess intense color. We strongly believe that they can be a potent class of tetracoordinate boron containing photosensitizers with proper choice of substituents on the starting materials. This thesis dissertation is devoted to the design and synthesis of novel tetracoordinate boron-containing organic compounds as photosensitizers with the objective of tuning photosensitizing abilities. To summarise, we have presented an extensive overview of tetracoordinate organoboron compounds from literature with attractive photophysical properties in Chapter 1. Chapter 2 describes the synthesis procedures and associated characterizations of the designed boron difluoride complexes. Chapter 3 discusses the photosensitizing abilities of the synthesized compounds and our results underline the importance of appropriate functionalization on the BODIPY/boranil skeletons. Finally, Chapter 4 focuses on the potential applications of all the

synthesized molecules towards heterogeneous degradation of water contaminants, as antimicrobial coatings and as antibacterial photodynamic agents.

1.6. References

[1] Y. Lin, Y. Li, X. Zhan, *Chem. Soc. Rev.* **2012**, *41*, 4245–4272.

[2] J. Zhao, K. Xu, W. Yang, Z. Wang, F. Zhong, *Chem. Soc. Rev.* **2015**, *44*, 8904–8939.

[3] D. Sasikumar, A. T. John, J. Sunny, M. Hariharan, *Chem. Soc. Rev.* **2020**, *49*, 6122–6140.

[4] M. A. Filatov, S. Baluschev, K. Landfester, *Chem. Soc. Rev.* **2016**, *45*, 4668–4689.

[5] Q. Chen, Y. Liu, X. Guo, J. Peng, S. Garakyaraghi, C. M. Papa, F. N. Castellano, D. Zhao, Y. Ma, *J Phys Chem A* **2018**, 122, 33, 6673–6682.

[6] N. J. Turro, V. Ramamurthy, V. Ramamurthy, J. C. Scaiano, *Principles of Molecular Photochemistry: An Introduction*, University Science Books, **2009**.

[7] C. A. M. Salla, G. Farias, M. Rouzières, P. Dechambenoit, F. Durola, H. Bock, B. de Souza, I. H. Bechtold, *Angew. Chem. Int. Ed.* **2019**, *58*, 6982–6986.

[8] O. Bolton, K. Lee, H.-J. Kim, K. Y. Lin, J. Kim, *Nature Chem* **2011**, *3*, 205–210.

[9] T. Liu, G. Zhang, R. E. Evans, C. O. Trindle, Z. Altun, C. A. DeRosa, F. Wang, M. Zhuang, C. L. Fraser, *Chem. Eur. J.* **2018**, *24*, 1859–1869.

[10] K. Gollnick, A. Griesbeck, *Angew. Chem., Int. Ed.* **1983**, *22*, 726–727.

[11] S. P. McGlynn, J. Daigre, F. J. Smith, *J. Chem. Phys.* **1963**, *39*, 675–679.

[12] X.-F. Zhang, *J. Photochem. Photobiol., A Chem.* **2018**, *355*, 431–443.

[13] K. N. Solov'ev, E. A. Borisevich, *Phys.-Usp.* **2005**, *48*, 231.

[14] J. Tatchen, N. Gilka, C. M. Marian, *Phys. Chem. Chem. Phys.* **2007**, *9*, 5209–5221.

[15] J. M. Kaminski, A. Rodríguez-Serrano, F. Dinkelbach, H. Miranda-Salinas, A. P. Monkman, C. M. Marian, *Chem. Sci.* **2022**, *13*, 7057–7066.

[16] K. M. Felter, F. C. Grozema, *J. Phys. Chem. Lett.* **2019**, *10*, 7208–7214.

[17] L. Mencaroni, B. Carlotti, F. Elisei, A. Marrocchi, A. Spalletti, *Chem. Sci.* **2022**, *13*, 2071–2078.

[18] A. Escudero, C. Carrillo-Carrión, M. Carmen Castillejos, E. Romero-Ben, C. Rosales-Barrios, N. Khiar, *Mater. Chem. Front.* **2021**, *5*, 3788–3812.

[19] M. Tavakkoli Yaraki, B. Liu, Y. N. Tan, *Nano-Micro Lett.* **2022**, *14*, 123.

[20] S. S. Murali, J. K. Gallaher, C. Janiseck, E. J. Tay, I. Wagner, K. E. Thorn, A. Ilina, R. R. Tamming, J. Wang, C. Sester, J. J. Sutton, M. B. Price, K. C. Gordon, K. Chen, X. Zhan, J. M. Hodgkiss, P. A. Hume, *J. Am. Chem. Soc.* **2023**, *145*, 732–744.

[21] K. Nagarajan, A. R. Mallia, K. Muraleedharan, M. Hariharan, *Chem. Sci.* **2017**, *8*, 1776–1782.

[22] M. C. DeRosa, R. J. Crutchley, *Coord. Chem. Rev.* **2002**, *233–234*, 351–371.

[23] L. F. Agnez-Lima, J. T. A. Melo, A. E. Silva, A. H. S. Oliveira, A. R. S. Timoteo, K. M. Lima-Bessa, G. R. Martinez, M. H. G. Medeiros, P. Di Mascio, R. S. Galhardo, C. F. M. Menck, *Mutat. Res.-Rev. Mutat. Res.* **2012**, *751*, 15–28.

[24] J. R. Lakowicz, Ed. , in *Principles of Fluorescence Spectroscopy*, Springer US, Boston, MA, **2006**, pp. 841–859.

[25] P. R. Ogilby, *Chem. Soc. Rev.* **2010**, *39*, 3181–3209.

[26] M. Verrucchi, G. E. Giacomazzo, P. S. Sfragano, S. Laschi, L. Conti, M. Pagliai, C. Gellini, M. Ricci, E. Ravera, B. Valtancoli, C. Giorgi, I. Palchetti, *Langmuir* **2023**, *39*, 679–689.

[27] J. Al-Nu'airat, I. Oluwoye, N. Zeinali, M. Altarawneh, B. Z. Dlugogorski, *Chem. Rec.* **2021**, *21*, 315–342.

[28] T. Montagnon, D. Kalaitzakis, M. Triantafyllakis, M. Stratakis, G. Vassilikogiannakis, *Chem. Commun.* **2014**, *50*, 15480–15498.

[29] N. Charbonnet, E. Riguet, C. G. Bochet, *Synlett* **2011**, *2011*, 2231–2233.

[30] A. Fall, M. Sène, E. Tojo, G. Gómez, Y. Fall, *Synthesis* **2010**, *2010*, 3415–3417.

[31] A. Kouridaki, T. Montagnon, D. Kalaitzakis, G. Vassilikogiannakis, *Org. Biomol. Chem.* **2012**, *11*, 537–541.

[32] G. Vassilikogiannakis, I. Alexopoulou, M. Tofi, T. Montagnon, *Chem. Commun.* **2010**, *47*, 259–261.

[33] A. Kouridaki, M. Sofiadis, T. Montagnon, G. Vassilikogiannakis, *Eur. J. Org. Chem.* **2015**, *2015*, 7240–7243.

[34] A. Sagadevan, K. C. Hwang, M.-D. Su, *Nat Commun* **2017**, *8*, 1812.

[35] R. Gerdes, O. Bartels, G. Schneider, D. Wöhrle, G. Schulz-Ekloff, *Polym. Adv. Technol.* **2001**, *12*, 152–160.

[36] N. Panigrahy, A. Priyadarshini, M. M. Sahoo, A. K. Verma, A. Daverey, N. K. Sahoo, *Environ. Technol. Innov.* **2022**, *27*, 102423.

[37] N. Zeinali, I. Oluwoye, M. Altarawneh, B. Z. Dlugogorski, *Ecotoxicol. Environ. Saf.* **2019**, *184*, 109605.

[38] T. Kohn, K. L. Nelson, *Environ. Sci. Technol.* **2007**, *41*, 192–197.

[39] C. M. B. Neves, O. M. S. Filipe, N. Mota, S. A. O. Santos, A. J. D. Silvestre, E. B. H. Santos, M. G. P. M. S. Neves, M. M. Q. Simões, *J. Hazard. Mater.* **2019**, *370*, 13–23.

[40] R. Lyubimenko, D. Busko, B. S. Richards, A. I. Schäfer, A. Turshatov, *ACS Appl. Mater. Interfaces* **2019**, *11*, 31763–31776.

[41] Y. Ren, D. Guo, Z. Zhao, P. Chen, F. Li, J. Yao, H. Jiang, Y. Liu, *J. Chem. Eng."***2022**, *435*, 134832.

[42] I. Yoon, J. Z. Li, Y. K. Shim, *Clin Endosc* **2013**, *46*, 7–23.

[43] S. D'Alessandro, R. Priefer, *J. Drug Deliv. Sci. Technol.* **2020**, *60*, 101979.

[44] E. Bassan, A. Gualandi, P. Giorgio Cozzi, P. Ceroni, *Chem. Sci.* **2021**, *12*, 6607–6628.

[45] R. Prieto-Montero, A. Prieto-Castañeda, R. Sola-Llano, A. R. Agarrabeitia, D. García-Fresnadillo, I. López-Arbeloa, A. Villanueva, M. J. Ortiz, S. de la Moya, V. Martínez-Martínez, *Photochem. Photobiol.* **2020**, *96*, 458–477.

[46] D. Li, H. Zhang, Y. Wang, *Chem. Soc. Rev.* **2013**, *42*, 8416–8433.

[47] K. Tanaka, Y. Chujo, *NPG Asia Mater.* **2015**, *7*, e223.

[48] J. Bañuelos, *Chem. Rec.* **2016**, *16*, 335–348.

[49] A. Loudet, K. Burgess, *Chem. Rev.* **2007**, *107*, 4891–4932.

[50] A. Kamkaew, S. Hui Lim, H. Boon Lee, L. Voon Kiew, L. Yong Chung, K. Burgess, *Chem. Soc. Rev.* **2013**, *42*, 77–88.

[51] J. J. Chen, S. M. Conron, P. Erwin, M. Dimitriou, K. McAlahney, M. E. Thompson, *ACS Appl. Mater. Interfaces* **2015**, *7*, 662–669.

[52] A. C. Benniston, G. Copley, *Phys. Chem. Chem. Phys.* **2009**, *11*, 4124–4131.

[53] T. Yogo, Y. Urano, Y. Ishitsuka, F. Maniwa, T. Nagano, *J. Am. Chem. Soc.* **2005**, *127*, 12162–12163.

[54] J. H. Gibbs, L. T. Robins, Z. Zhou, P. Bobadova-Parvanova, M. Cottam, G. T. McCandless, F. R. Fronczek, M. G. H. Vicente, *Bioorg. Med. Chem.* **2013**, *21*, 5770–5781.

[55] A. Gorman, J. Killoran, C. O'Shea, T. Kenna, W. M. Gallagher, D. F. O'Shea, *J. Am. Chem. Soc.* **2004**, *126*, 10619–10631.

[56] N. Adarsh, R. R. Avirah, D. Ramaiah, *Org. Lett.* **2011**, *13*, 2146–2146.

[57] S. G. Awuah, J. Polreis, V. Biradar, Y. You, *Org. Lett.* **2011**, *13*, 3884–3887.

[58] W. Wu, H. Guo, W. Wu, S. Ji, J. Zhao, *J. Org. Chem.* **2011**, *76*, 7056–7064.

[59] X.-F. Zhang, X. Yang, *J. Phys. Chem. B* **2013**, *117*, 5533–5539.

[60] M. J. Ortiz, A. R. Agarrabeitia, G. Duran-Sampedro, J. Bañuelos Prieto, T. A. Lopez, W. A. Massad, H. A. Montejano, N. A. García, I. Lopez Arbeloa, *Tetrahedron* **2012**, *68*, 1153–1162.

[61] Y. Zhao, Z. Lu, X. Dai, X. Wei, Y. Yu, X. Chen, X. Zhang, C. Li, *Bioconjugate Chem.* **2018**, *29*, 3222–3230.

[62] D. Chen, J. Zhang, Y. Tang, X. Huang, J. Shao, W. Si, J. Ji, Q. Zhang, W. Huang, X. Dong, *J. Mater. Chem. B* **2018**, *6*, 4522–4530.

[63] W. Xiao, P. Wang, C. Ou, X. Huang, Y. Tang, M. Wu, W. Si, J. Shao, W. Huang, X. Dong, *Biomaterials* **2018**, *183*, 1–9.

[64] Z. Ruan, Y. Zhao, P. Yuan, L. Liu, Y. Wang, L. Yan, *J. Mater. Chem. B* **2018**, *6*, 753–762.

[65] Z. Ruan, P. Yuan, T. Li, Y. Tian, Q. Cheng, L. Yan, *Eur. J. Pharm. Biopharm.* **2019**, *135*, 25–35.

[66] H. He, P.-C. Lo, S.-L. Yeung, W.-P. Fong, D. K. P. Ng, *J. Med. Chem.* **2011**, *54*, 3097–3102.

[67] J. H. Gibbs, Z. Zhou, D. Kessel, F. R. Fronczek, S. Pakhomova, M. G. H. Vicente, *J. Photochem. Photobiol. B, Biol.* **2015**, *145*, 35–47.

[68] J. Zhu, J. Zou, Z. Zhang, J. Zhang, Y. Sun, X. Dong, Q. Zhang, *Mater. Chem. Front.* **2019**, *3*, 1523–1531.

[69] J. Zhu, J. Zou, J. Zhang, Y. Sun, X. Dong, Q. Zhang, *J. Mater. Chem. B* **2019**, *7*, 3303–3309.

[70] E. Dai, W. Pang, X.-F. Zhang, X. Yang, T. Jiang, P. Zhang, C. Yu, E. Hao, Y. Wei, X. Mu, L. Jiao, *Chem. Asian J.* **2015**, *10*, 1327–1334.

[71] Z. Ruan, W. Miao, P. Yuan, L. Le, L. Jiao, E. Hao, L. Yan, *Bioconjugate Chem.* **2018**, *29*, 3441–3451.

[72] E. Palao, R. Sola-Llano, A. Tabero, H. Manzano, A. R. Agarrabeitia, A. Villanueva, I. López-Arbeloa, V. Martínez-Martínez, M. J. Ortiz, *Chem. Eur. J.* **2017**, *23*, 10139–10147.

[73] J. Wang, Y. Lu, N. McGoldrick, C. Zhang, W. Yang, J. Zhao, S. M. Draper, *J. Mater. Chem. C* **2016**, *4*, 6131–6139.

[74] L. Tabrizi, H. Chiniforoshan, *RSC Adv.* **2017**, *7*, 34160–34169.

[75] H. Jia, B. Küçüköz, Y. Xing, P. Majumdar, C. Zhang, A. Karatay, G. Yaglioglu, A. Elmali, J. Zhao, M. Hayvali, *J. Mater. Chem. C* **2014**, *2*, 9720–9736.

[76] F. Zhong, A. Karatay, L. Zhao, J. Zhao, C. He, C. Zhang, H. G. Yaglioglu, A. Elmali, B. Küçüköz, M. Hayvali, *Inorg. Chem.* **2015**, *54*, 7803–7817.

[77] M. Üçüncü, E. Karakuş, E. Kurulgan Demirci, M. Sayar, S. Dartar, M. Emrullahoğlu, *Org. Lett.* **2017**, *19*, 2522–2525.

[78] V. Ramu, S. Gautam, A. Garai, P. Kondaiah, A. R. Chakravarty, *Inorg. Chem.* **2018**, *57*, 1717–1726.

[79] M. Galletta, S. Campagna, M. Quesada, G. Ulrich, R. Ziessel, *Chem. Commun.* **2005**, 4222–4224.

[80] F. Nastasi, F. Puntoriero, S. Campagna, S. Diring, R. Ziessel, *Phys. Chem. Chem. Phys.* **2008**, *10*, 3982–3986.

[81] W. Wu, J. Zhao, H. Guo, J. Sun, S. Ji, Z. Wang, *Chem. Eur. J.* **2012**, *18*, 1961–1968.

[82] H. Chen, T. Ming, L. Zhao, F. Wang, L.-D. Sun, J. Wang, C.-H. Yan, *Nano Today* **2010**, *5*, 494–505.

[83] K. Oishi, K. Kajikawa, *Opt. Commun.* **2011**, *284*, 3445–3448.

[84] L. Tong, H. Wei, S. Zhang, H. Xu, *Sensors* **2014**, *14*, 7959–7973.

[85] J. L. Brooks, C. L. Warkentin, D. Saha, E. L. Keller, R. R. Frontiera, *Nanophotonics* **2018**, *7*, 1697–1724.

[86] Y. Zhang, K. Aslan, M. J. R. Previte, C. D. Geddes, *Proc. Natl. Acad. Sci. U.S.A* **2008**, *105*, 1798–1802.

[87] X. Huang, X.-J. Tian, W. Yang, B. Ehrenberg, J.-Y. Chen, *Phys. Chem. Chem. Phys.* **2013**, *15*, 15727–15733.

[88] H. Zhang, H. Li, H. Fan, J. Yan, D. Meng, S. Hou, Y. Ji, X. Wu, *Nano Res.* **2018**, *11*, 1456–1469.

[89] B. Hu, X. Cao, K. Nahan, J. Caruso, H. Tang, P. Zhang, *J. Mater. Chem. B* **2014**, *2*, 7073–7081.

[90] N. Macia, R. Bresoli-Obach, S. Nonell, B. Heyne, *J. Am. Chem. Soc.* **2019**, *141*, 684–692.

[91] A. Rahman, P. P. Praveen Kumar, P. Yadav, T. Goswami, A. Shanavas, H. N. Ghosh, P. P. Neelakandan, *ACS Appl. Nano Mater.* **2022**, *5*, 6532–6542.

[92] P. P. P. Kumar, A. Rahman, T. Goswami, H. N. Ghosh, P. P. Neelakandan, *ChemPlusChem* **2021**, *86*, 87–94.

[93] A. Rahman, T. Goswami, N. Tyagi, H. N. Ghosh, P. P. Neelakandan, *J. Photochem. Photobiol., A Chem.* **2022**, *432*, 114067.

[94] D. Frath, J. Massue, G. Ulrich, R. Ziessel, *Angew. Chem., Int. Ed.* **2014**, *53*, 2290–2310.

[95] D. Frath, S. Azizi, G. Ulrich, P. Retailleau, R. Ziessel, *Org. Lett.* **2011**, *13*, 3414–3417.

[96] J. Massue, D. Jacquemin, G. Ulrich, *Organics* **2021**, *2*, 365–375.

[97] N. Zhao, C. Ma, W. Yang, W. Yin, J. Wei, N. Li, *Chem. Commun.* **2019**, *55*, 8494–8497.

[98] A. Ren, D. Zhu, Y. Luo, *J. Mol. Struct.* **2020**, *1209*, 127914.

[99] D. Frath, P. Didier, Y. Mély, J. Massue, G. Ulrich, *ChemPhotoChem* **2017**, *1*, 109–112.

[100] D. Frath, K. Benelhadj, M. Munch, J. Massue, G. Ulrich, *J. Org. Chem.* **2016**, *81*, 9658–9668.

[101] M. Urban, K. Durka, P. Jankowski, J. Serwatowski, S. Luliński, *J. Org. Chem.* **2017**, *82*, 8234–8241.

[102] L. A. Crandall, M. B. Dawadi, T. Burrell, A. Odoom, C. J. Ziegler, *Photochem Photobiol Sci* **2017**, *16*, 627–632.

[103] X. Ren, F. Zhang, H. Luo, L. Liao, X. Song, W. Chen, *Chem. Commun.* **2020**, *56*, 2159–2162.

Chapter 2

Synthesis and characterization of tetracoordinate boron-difluoride compounds

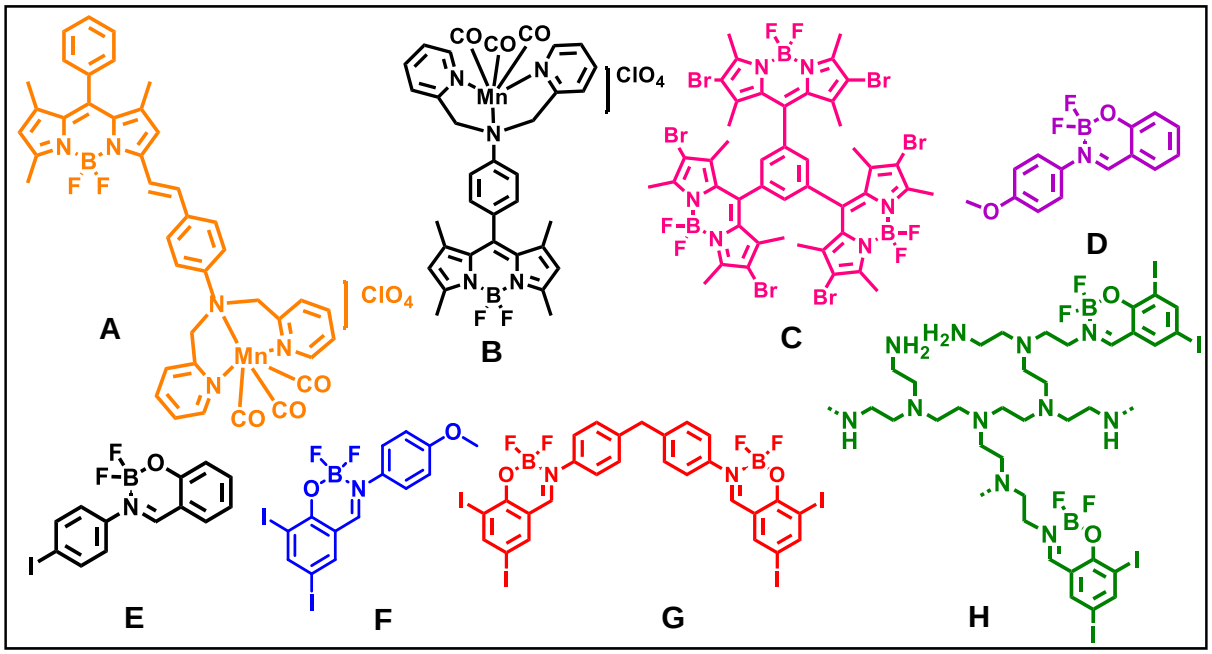

2.1. Introduction

Development of novel photosensitizers is intriguing to researchers as they are extensively employed for a range of applications from photodynamic therapy to organic synthesis to wastewater treatment[1–3]. In the past few decades, development of BODIPYs as potent photosensitizers has attracted widespread interest because of their exciting properties and the potential for real-life applications[4,5]. They are a prominent class of dyes which have gained immense attention in various fields such as bioimaging, organic light emitting diodes, lasers, dye-sensitized solar cells, nonlinear optics, sensing, photodynamic therapy and many more. In an attempt to synthesize acylated pyrrole from dimethyl pyrrole and acetic anhydride using $BF_3.OEt_2$ as a Lewis acid, Treibs and Kreuzer accidently discovered BODIPY in 1968. The BODIPY skeleton contains two pyrrole heterocycle units linked by a methine bridge and a boron atom in between. Scheme 2.1 represents the general synthesis of BODIPY by the condensation of pyrrole derivatives with acyl chlorides followed by complexation with boron difluoride (Scheme 2.1). BODIPYs are known to exhibit large absorption coefficients,

excellent photostability, sharp absorption and emission profiles, high fluorescent quantum yields and relatively long excited-state lifetimes. Their photophysical properties can be tuned through simple functionalization on the BODIPY core at the α-, β-, meso- and B(III) positions by incorporation of desired substituents with diverse electron densities. Incorporation of heavy atoms and transition metal complexes on to BODIPYs is a commonly opted strategy to improve the photosensitization efficiency of organic photosensitizers and achieve high triplet state quantum yields[6].

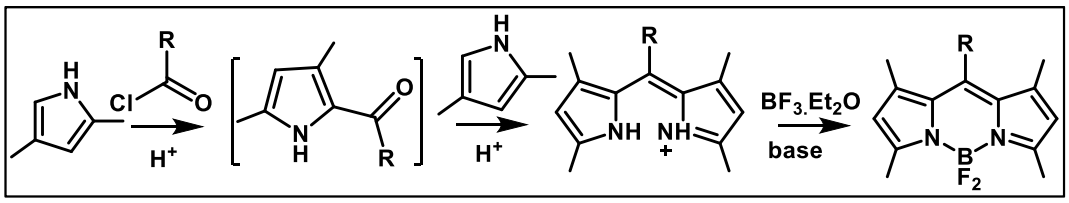

Scheme 2.1. General synthesis of BODIPY by the condensation of pyrrole with acyl chloride.

Light activated CO Releasing Molecules popularly known as photoCORMs have emerged in last decades as a smart strategy to deliver CO in cellular systems in a controlled manner[7,8]. Choice of a suitable chromophore is necessary to the design of potential photoCORMs and BODIPYs can be potent candidates for the choice of ligand in this regard. The proven ability of BODIPYs to act as efficient photosensitizers can lead to both CO release and generation of reactive oxygen species upon conjugation with suitable CO releasing core leading to utility in photodynamic therapy and antibacterial applications. While photoCORMs containing iron, ruthenium, rhenium, zinc and manganese as metal centers[7,9–17] have been reported, manganese and iron have gained particular attention due to their biocompatibility. Hence, systematic tethering of CO releasing manganese complex onto BODIPY can have huge impact on the absorption profiles and the CO release efficiencies.

Similar to transition metal incorporation, another strategy to achieve populated triplet states is heavy atom functionalization[3]. And although heavy atom incorporation is a commonly employed strategy, functionalization of peculiar shaped BODIPY cores is still intriguing to scientists as a minimal change in the electronic structure of BODIPYs can lead to drastically different and exciting photophysical properties.

Despite the interesting photophysics and facile derivatization, BODIPYs mostly suffer from low reaction yields and precise reaction conditions. As a result, researchers are increasingly interested in developing new class of photosensitizers that address these challenges. Another class of tetracoordinate boron compounds popularly known as boranils[18]

wherein the boron is coordinated to an organic ligand are intriguing in this regard. The overlap of the empty *p*-orbital of boron with the organic moieties in such compounds leads to the delocalization of the electron cloud and planarization of the π-systems thereby resulting in interesting photophysical properties (Figure 2.1). B(III) coordination also imparts charge transfer character owing to its electron deficient nature and results in red shifted absorption and emission as compared to the corresponding chelating units.

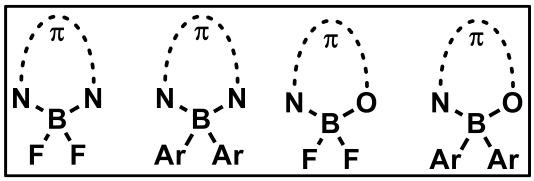

Figure 2.1. Illustration of tetracoordinate boron compounds. The dotted lines represent a π-conjugated system.

Several tri- and tetra-coordinated boron compounds have been synthesized by the complexation of boron with organic ligands containing hetero atoms but four-coordinate boron compounds based on an imine scaffold are reported to have higher stability as compared to tricoordinate boron compounds due to coordination saturation[19,20]. Boron-containing compounds can be categorized based on the types of elements present in the ring formed after complexation with B(III). Boron difluoride or diphenyl tetracoordinate boron complexes with N-B-O, N-B-N and O-B-O mode of chelation has been extensively studied out of which N-B-O has garnered significant interest. Boron complexes of Schiff bases are attractive because of their synthetic simplicity and excellent photophysical properties. The properties of the boron-containing organic compounds can be easily tuned by appropriately choosing the starting materials like amines and aldehydes which react readily to form the corresponding chelating units. Boranils can be synthesized in high yields for industrial-scale applications in simple one or two step process. As shown in Scheme 2.2, the first step involves the reaction between derivatives of salicylaldehyde and amine so as to yield the anil and the second step leads to the formation of boranil via complexation between the anil and $BF_3.Et_2O$ or $B(C_6H_5)_3$. Their facile and large-scale synthesis in high reaction yields, and the feasibility to choose simple aldehydes and amines from large libraries makes them an interesting candidate. Although the luminescent properties of boranils are well documented, photosensitization properties of such molecules have rarely been explored. The objectives for designing heavy atom functionalized boranils as photosensitizers are to (i) accelerate and upscale multi-step syntheses, (ii) achieve high singlet

oxygen quantum yields and (iii) obtain tunable absorption and emission over the entire range of electromagnetic spectrum.

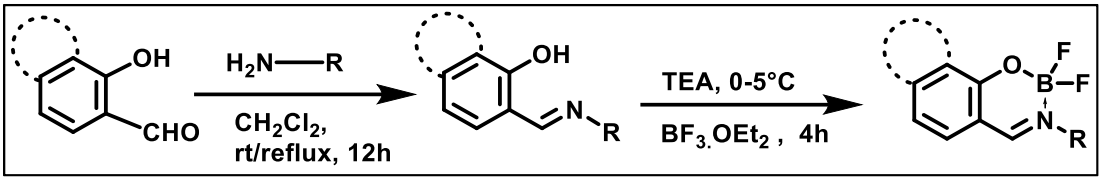

Scheme 2.2. General reaction scheme for the preparation of boranils.

We have synthesized various boron difluoride complexes ranging from heavy metal and transition metal complex incorporated BODIPYs (**A-C**) to N,O-chelated salicylideneimine boron difluoride complexes popularly known as boranils (**D-G**) to diiodosalicylideneimine-boron difluoride functionalized polyethyleneimine (**H**).

2.2. Results and Discussion

The reaction of **I** (aniline) with **J** (2-(chloromethyl) pyridine hydrochloride) gave **K**, which further upon formylation yielded 4-[bis(pyridin-2-ylmethyl)amino]benzaldehyde (**L**). Formation of **L** was confirmed by ATR-FTIR analysis which indicated the presence of -C=O peak at 1650 cm^{-1} and ^1H NMR spectroscopy which showed the presence of aldehydic proton at δ 9.73 ppm. Similarly, benzoyl chloride, **M** upon condensation with 2,4-dimethylpyrrole, **N** followed by complexation with boron trifluoride etherate gave the BODIPY **O** which exhibited presence of two pyrrolic protons at δ 5.98 ppm in the ^1H NMR spectrum. Ligand **P** was prepared by the Knoevenagel condensation reaction between BODIPY **O** and the aldehyde **L** in the presence of glacial acetic acid and piperidine in toluene. ^1H NMR spectrum of ligand **P** indicated existence of pyridyl protons observed as a singlet at δ 4.8 ppm. Complex **A** was synthesized by reaction between $Mn(CO)_5Br$ with ligand **P** followed by the addition of $NaClO_4$ in a 1:1 mixture of dichloromethane and methanol. Coordination of ligand **P** to Mn(I) and the formation of low-spin (d6) complex was confirmed by ATR-FTIR and ^1H NMR analysis. Splitting of the singlet at δ 4.89 ppm corresponding to pyridyl protons in **P** into two doublets further confirmed the coordination with Mn(I) in the final complex **A** (Figure 2.2). Scheme 2.3 shows all the steps involved in the synthesis of BODIPY complex **A.**

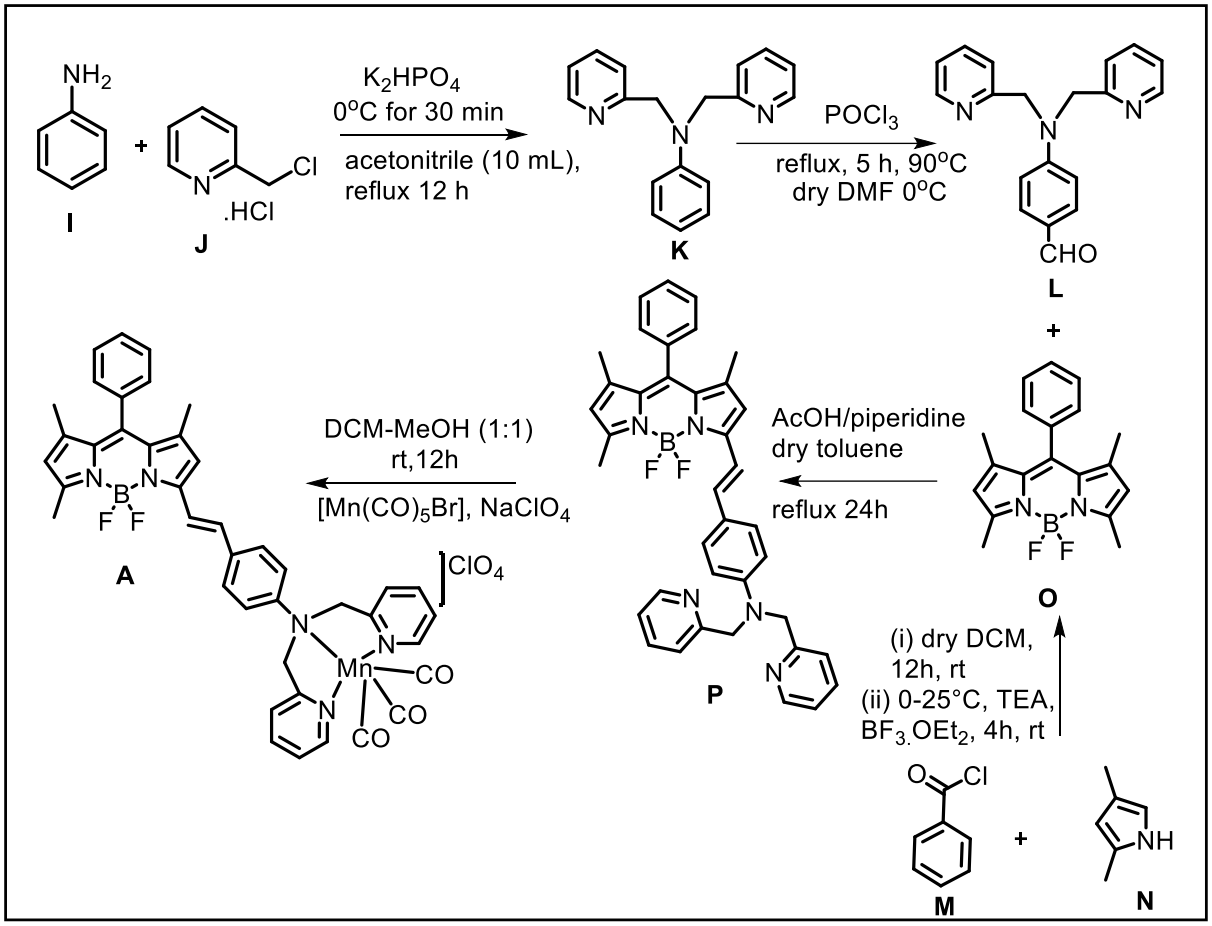

Scheme 2.3. Synthesis of BODIPY complex **A**.

The reaction of aldehyde, **L** with 2,4-dimethylpyrrole, **N** followed by complexation with boron trifluoride etherate yielded BODIPY ligand **Q**. The ^{1}H NMR spectrum of **Q** showed characteristic peak of pyridyl protons at δ 4.87 ppm. Complex **B** was synthesized by reaction between $Mn(CO)_5Br$ with ligand **Q** followed the addition of $NaClO_4$ in a 1:1 mixture of dichloromethane and methanol. Coordination of ligand **Q** to Mn(I) and the formation of low-spin (d6) complex was confirmed by ATR-FTIR and ^{1}H NMR analysis. Splitting of the singlet at δ 4.87 ppm corresponding to pyridyl protons in **Q** into two doublets further confirmed the coordination with Mn(I) in the final complex **B** (Figure 2.3). Scheme 2.4 shows all the steps involved in the synthesis of BODIPY complex **B.**

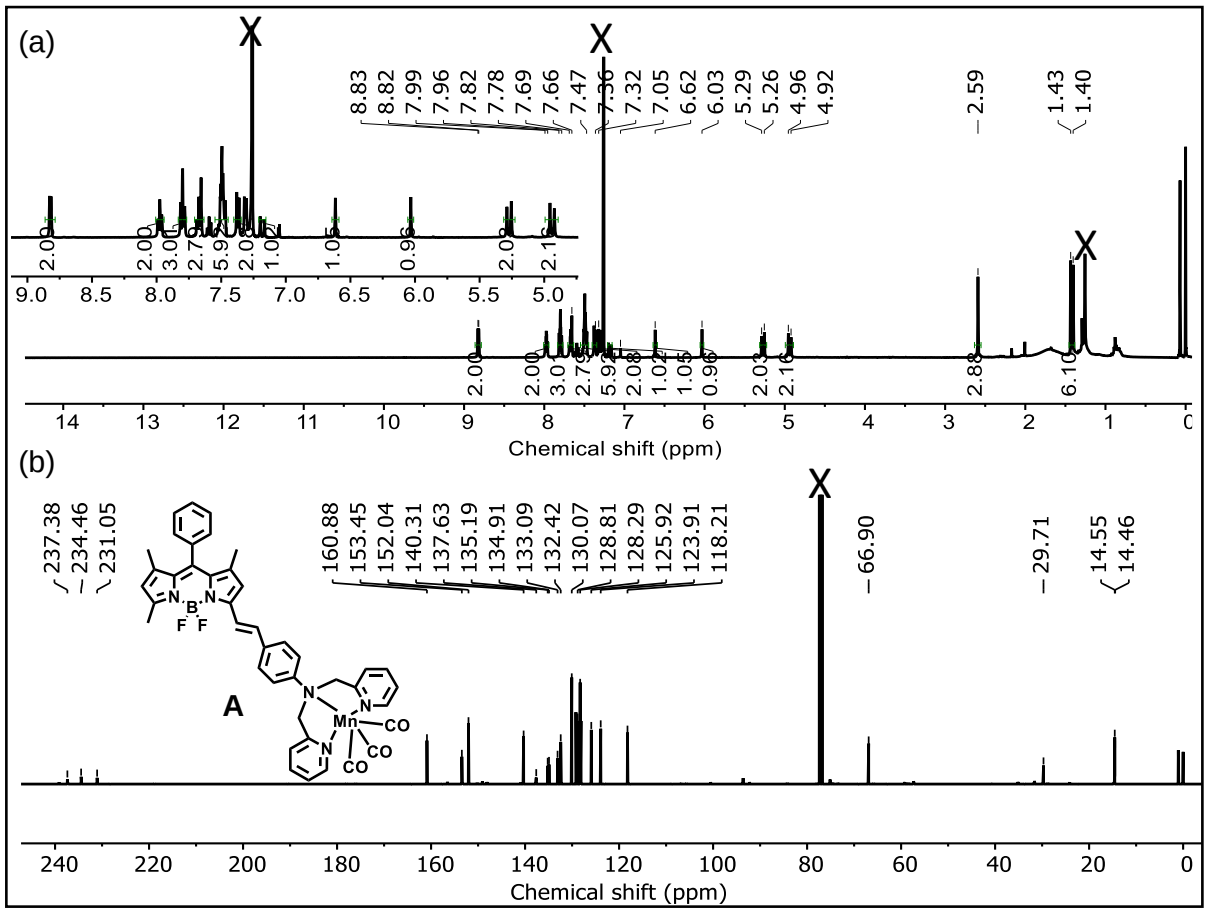

Figure 2.2. (a) ^{1}H and (b) ^{13}C NMR spectra of **A** in $CDCl_3$ at 298 K. Selected regions of the spectra are enlarged as insets in (a).

Furthermore, complexes **A** and **B** also exhibited characteristic carbonyl peaks beyond δ 200 ppm in ^{13}C NMR spectrum further confirming the formation of corresponding carbonyl complexes. Attenuated Total Reflectance Fourier Transform Infrared (ATR-FTIR) spectra also displayed two strong ν(CO) stretching bands at 1937 and 2036 cm^{-1} along with ClO_4^- stretching at ~1093 cm^{-1} which clearly indicated the presence of facially disposed carbonyls at octahedral manganese(I) centres. The identity of the complexes was further confirmed by high resolution mass spectra (HRMS) and single crystal XRD analysis.

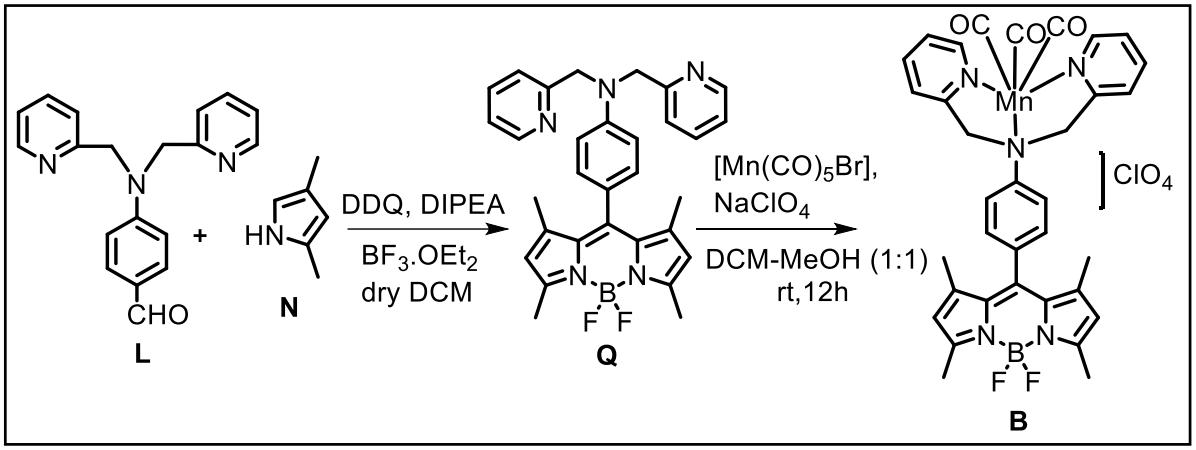

Scheme 2.4. Synthesis of BODIPY complex **B**.

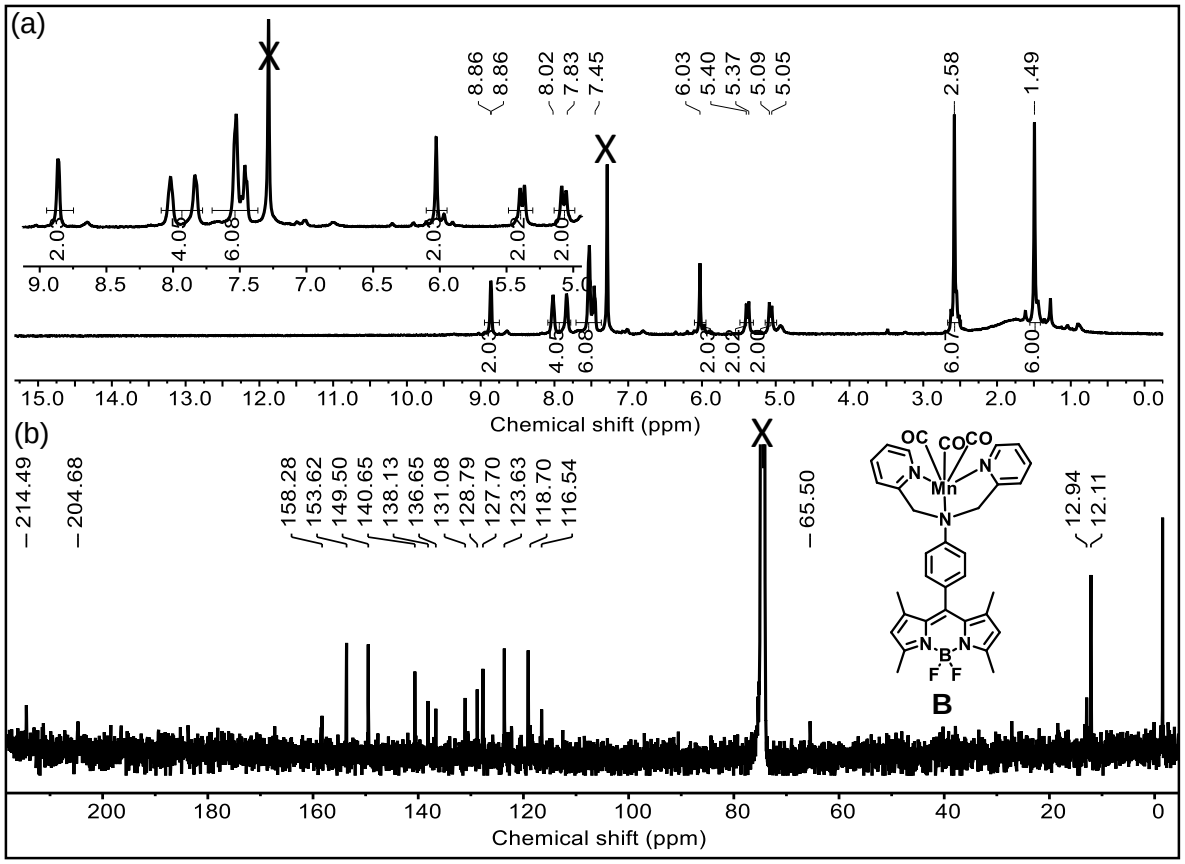

Figure 2.3. (a) ^{1}H and (b) ^{13}C NMR spectra of **B** in $CDCl_3$ at 298 K. Selected regions of the spectra are enlarged as insets in (a).

A control complex **Z** (Scheme 2.5) which has the same structural features as complexes **A** and **B** but is devoid of BODIPY was further synthesized to investigate the effect of BODIPY on the overall structural and photophysical aspects of the compounds **A** and **B**. Complex **Z** was

characterized via ^{1}H, ^{13}C NMR and ATR-FTIR spectroscopy which clearly indicates facially disposed carbonyls (Figure 2.4).

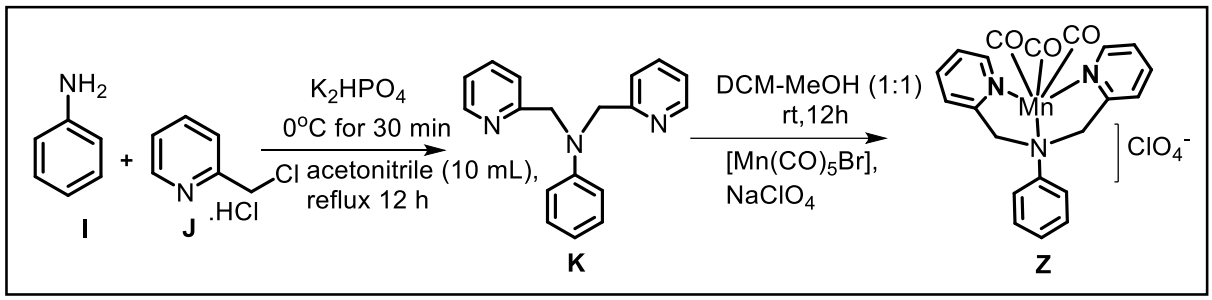

Scheme 2.5. Synthesis of BODIPY complex **Z**.

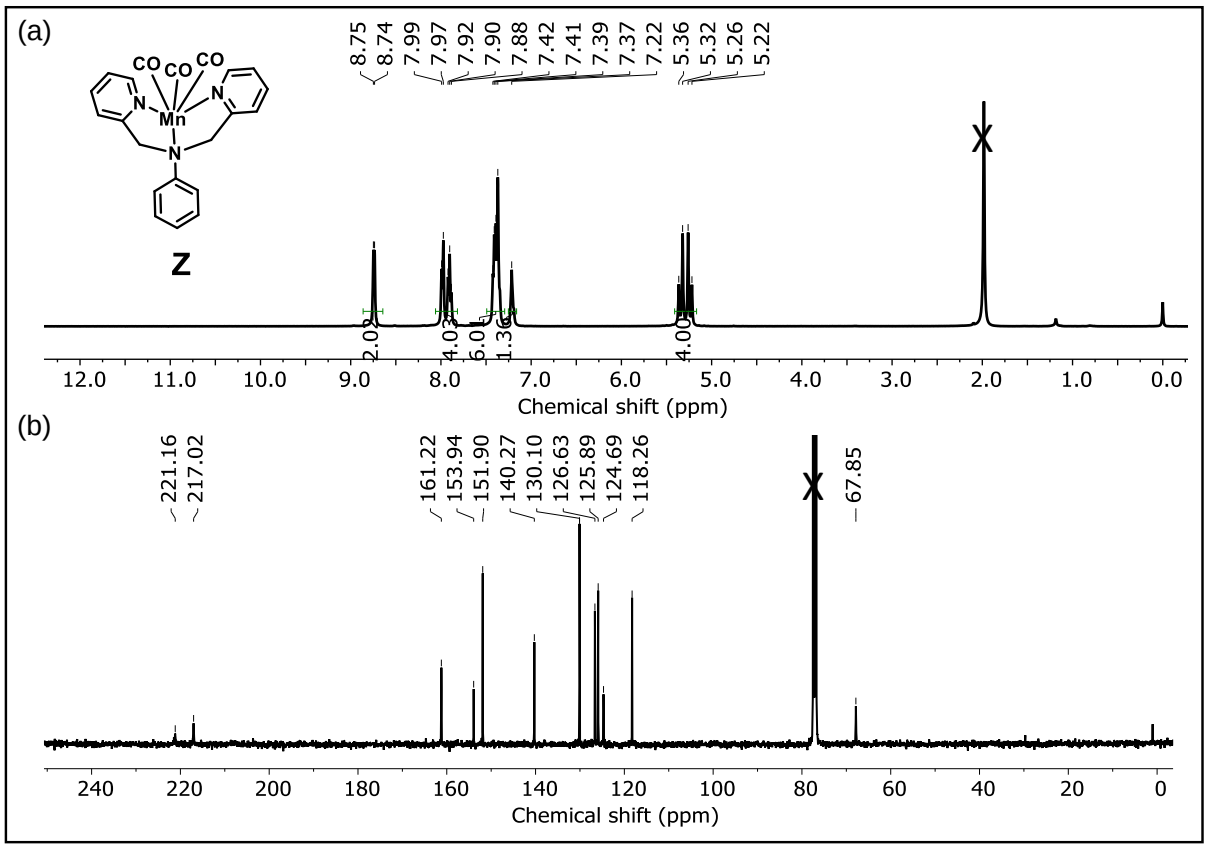

Figure 2.4. (a) ^{1}H and (b) ^{13}C NMR spectra of control compound **Z** in $CDCl_3$ at 298 K.

The synthesis of the BODIPY molecule **S** was achieved by the reaction between 1,3,5-benzene tricarbonyl chloride, **R** and 2,4-dimethylpyrrole, **N** followed by complexation with $BF_3.Et_2O$. Subsequent bromination was carried out at room temperature with dropwise addition of N-bromosuccinimide in a mixture of 1:1 anhydrous dichloromethane and N,N-dimethylformamide which yielded BODIPY **C** with a yield of ~80% (Scheme 2.6). Successful

functionalization was confirmed by ^{1}H NMR spectroscopy wherein the peaks at δ 5.98 ppm corresponding to pyrrolic hydrogens disappeared due to bromination at the respective positions (Figure 2.5).

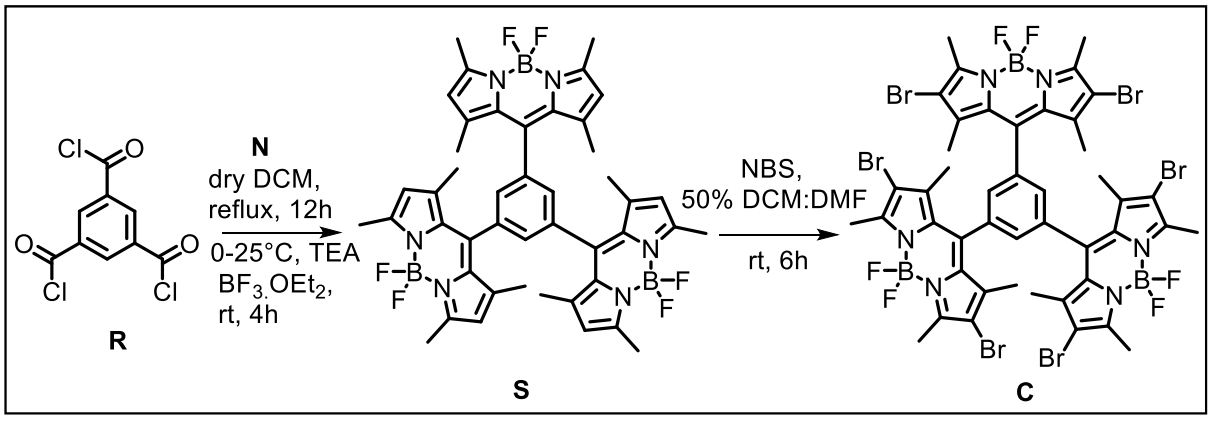

Scheme 2.6. Synthesis of BODIPY **C**.

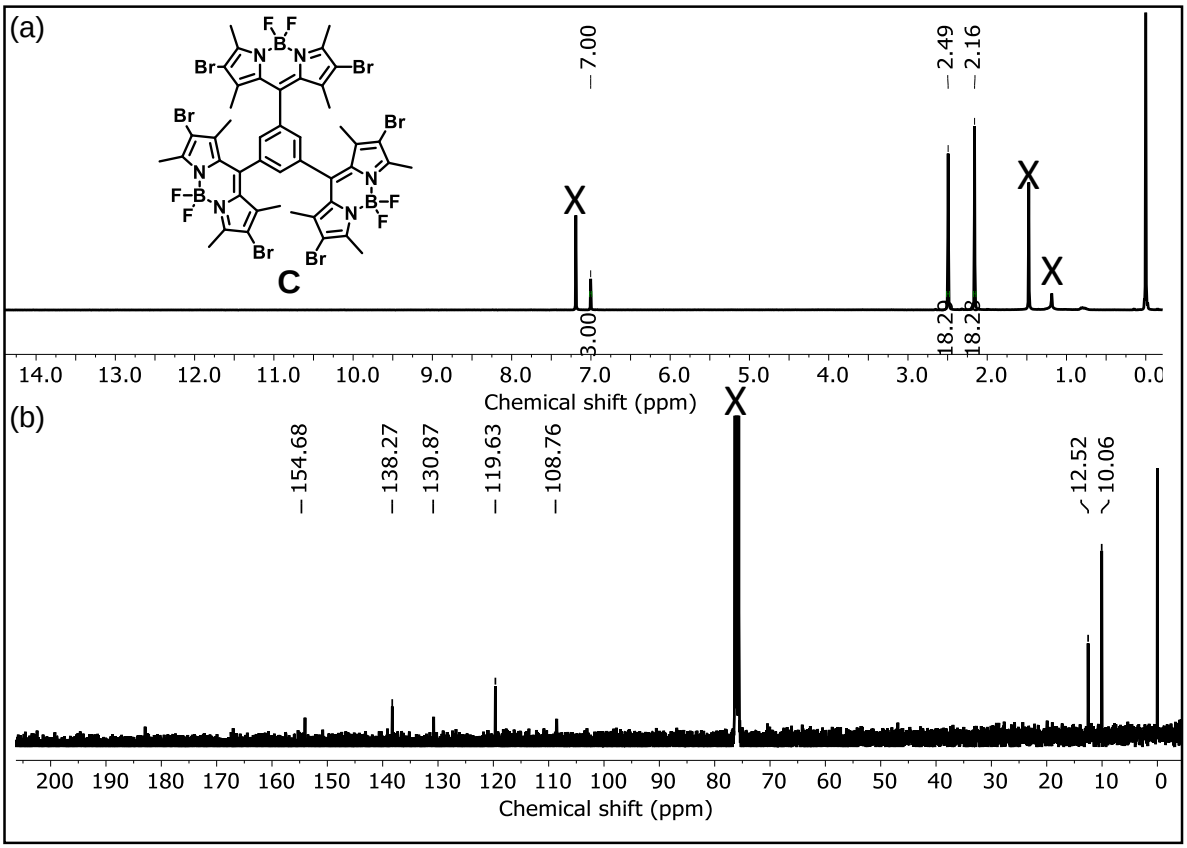

Figure 2.5. (a) ^{1}H and (b) ^{13}C NMR spectra of **C** in $CDCl_3$ at 298 K.

Compound **D** was synthesized by the reaction of salicylaldehyde, **T** with p-anisidine, **V** in anhydrous dichloromethane followed by boron complexation as shown in Scheme 2.7.

The reaction was performed in the presence of catalytic amounts of formic acid and the Schiff base was further isolated via rotary evaporation before subjecting to immediate complexation with boron trifluoride etherate. Reaction between salicylaldehyde, **T** and 4-iodoaniline, **W** also led to the mono-iodinated boron complex **E** in a similar manner.

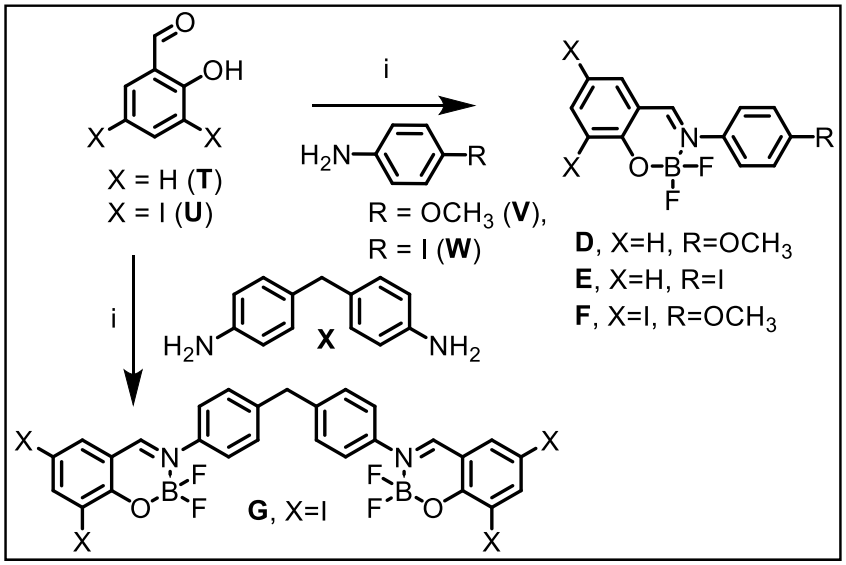

Scheme 2.7. Synthesis of boranils **D**-**G**.

In order to systematically increase the iodine substitution, the aldehydic core was changed to 3,5-diiodosalicylaldehyde, **U** which reacted with p-anisidine, **V** to yield diiodinated salicylideneimine boron difluoride complex **F** upon complexation with boron trifluoride diethyl etherate. Furthermore, reaction of 3,5-diiodosalicylaldehyde, **U** with 4,4'-diaminodiphenylmethane, **X** in anhydrous dichloromethane followed by boron complexation yielded complex **G** which was systematically substituted with four iodine atoms. All compounds were obtained in good yields and were yellow colored solids. All the heavy atom substituted boranils exhibited characteristic imine hydrogen peaks in the ^{1}H NMR spectrum around δ 9 ppm. A primary indication of complexation is the broadening of the signal of the singlet attributed to the imine proton in the ^{1}H NMR spectrum of the compounds **D**-**G**. Figures 2.6-2.9 depict the ^{1}H and ^{13}C NMR spectra for the respective compounds **D**-**G** indicating their successful synthesis. The identity of the compounds was further characterized by HRMS.

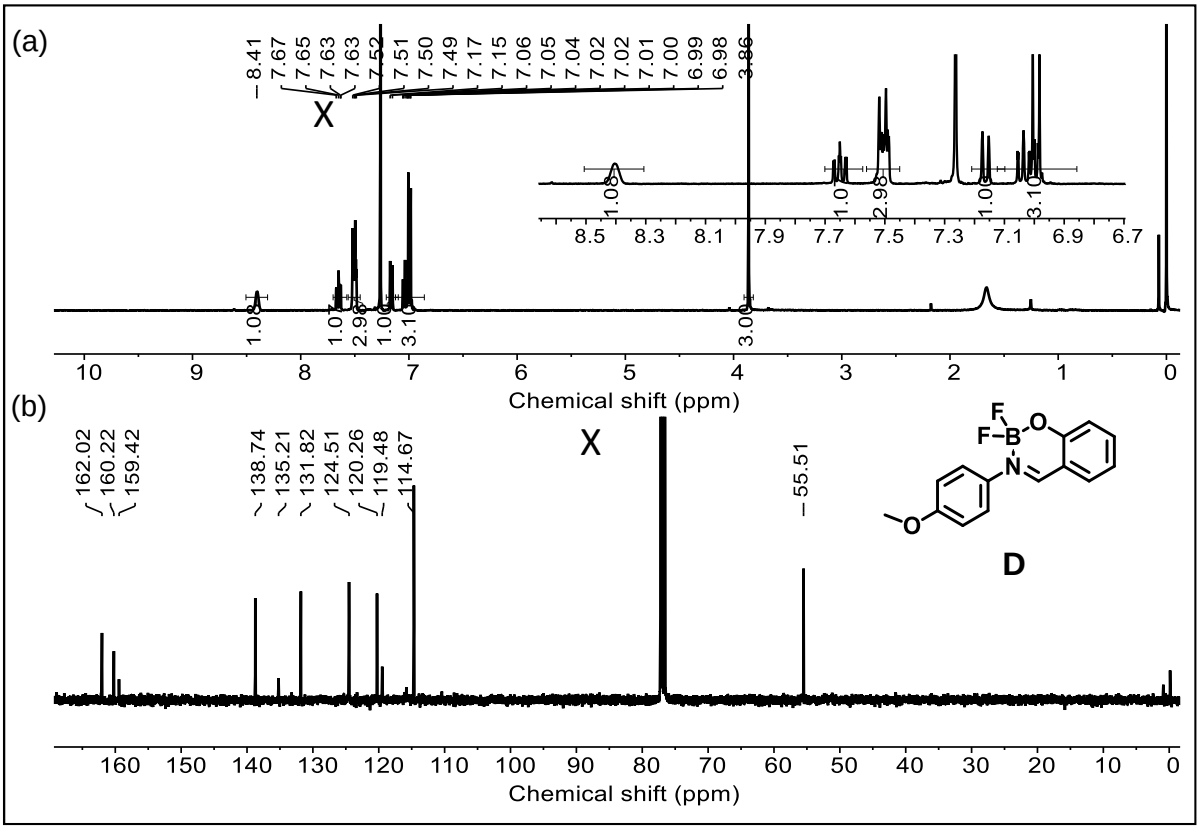

Figure 2.6. (a) ^{1}H and (b) ^{13}C NMR spectra of **D** in $CDCl_3$ at 298 K. Selected regions of the spectra are enlarged as insets in (a).

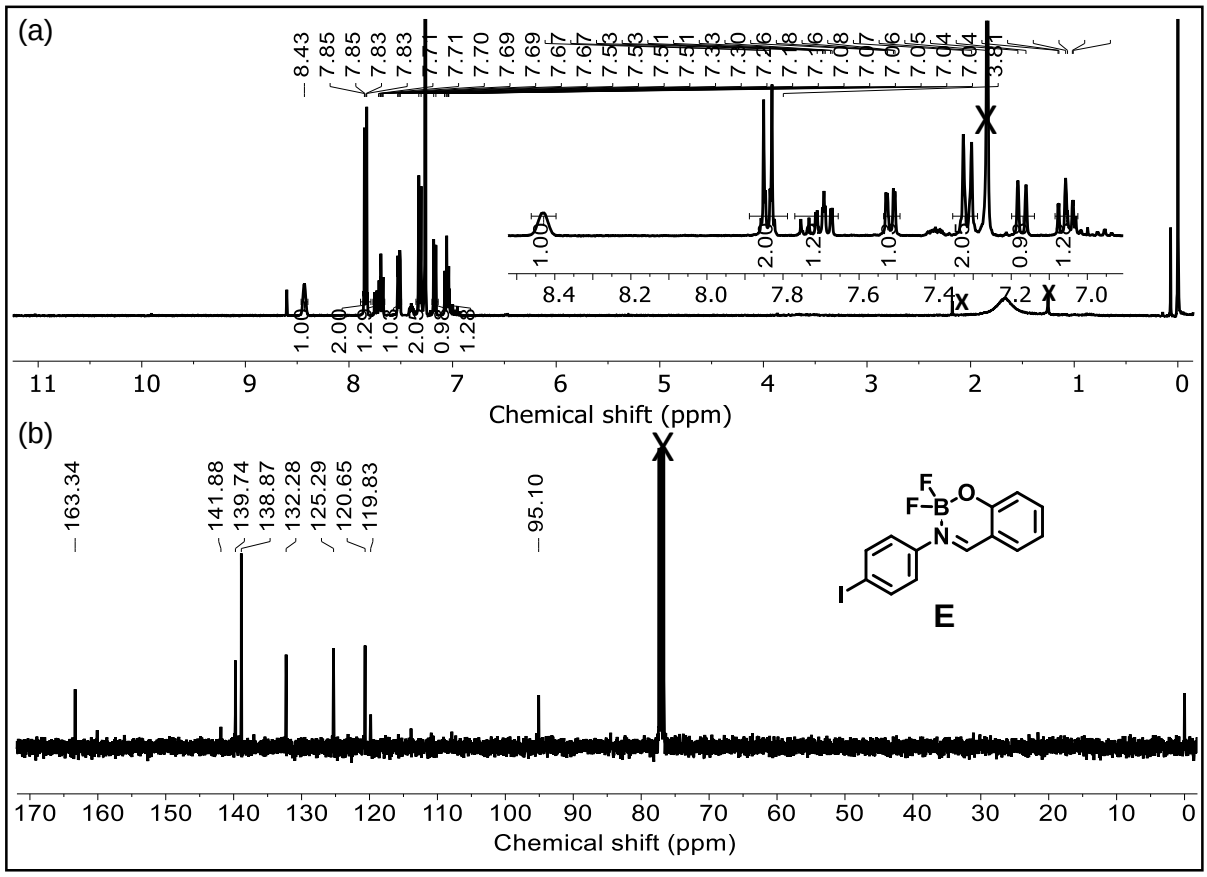

Figure 2.7. (a) ^{1}H and (b) ^{13}C NMR spectra of **E** in $CDCl_3$ at 298 K. Selected regions of the spectra are enlarged as insets in (a).

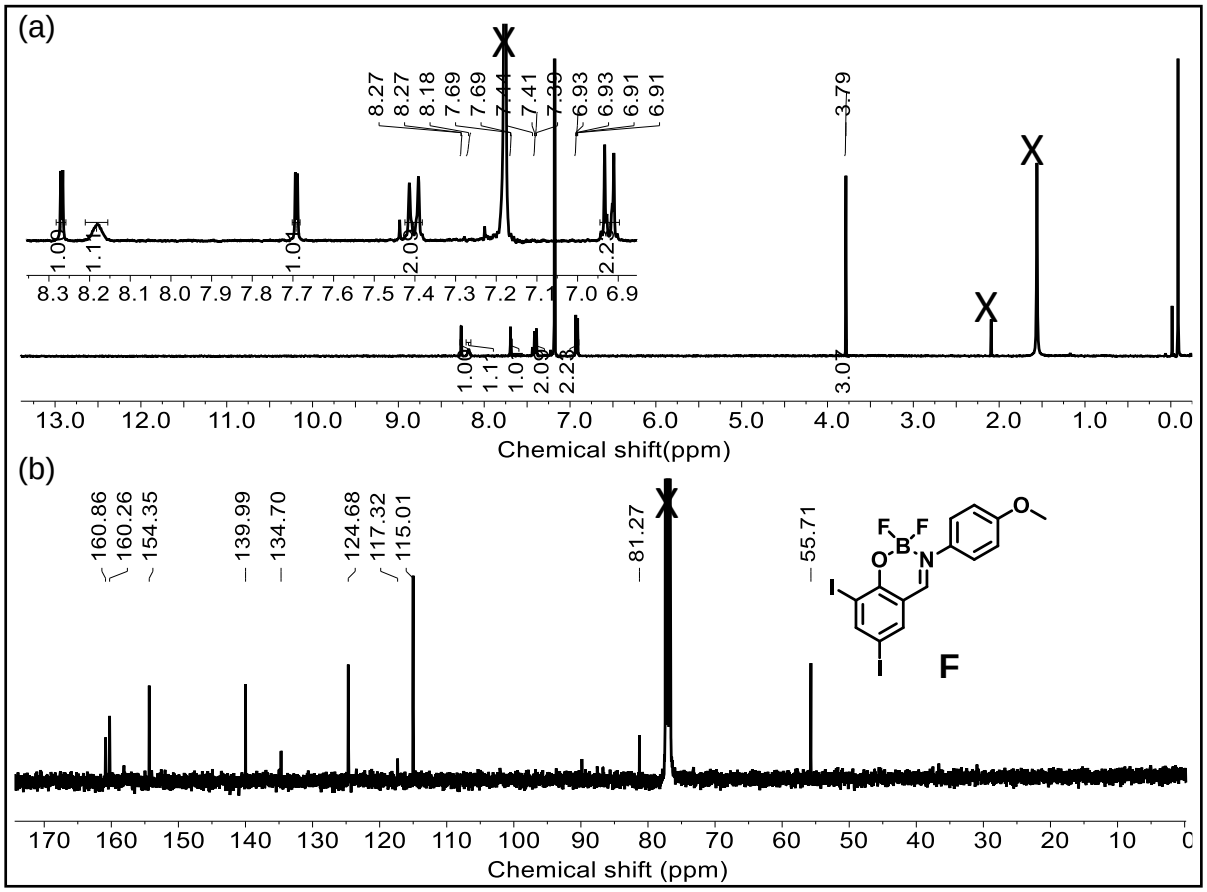

Figure 2.8. (a) ^{1}H and (b) ^{13}C NMR spectra of **F** in $CDCl_3$ at 298 K. Selected regions of the spectra are enlarged as insets in (a).

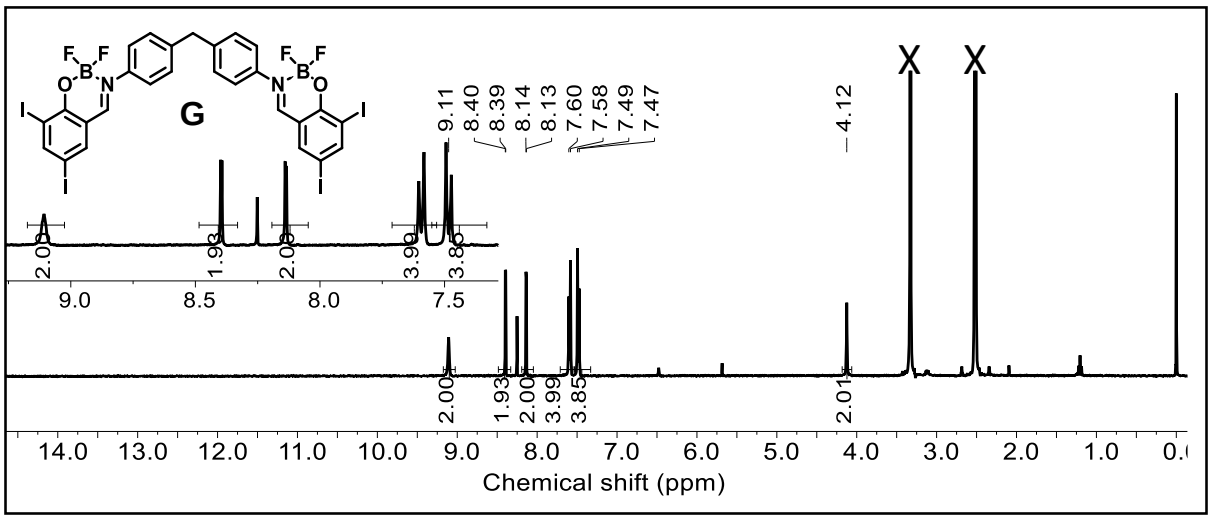

Figure 2.9. (a) ^{1}H and (b) ^{13}C NMR spectra of **G** in $CDCl_3$ at 298 K. Selected regions of the spectra are enlarged as insets in (a).

Boranil functionalized polymer **H** was obtained by a one pot condensation reaction between 3,5-diiodosalicylaldehyde and the primary amine groups of polyethyleneimine, **Y**

which yielded a gel-like precipitate from the reaction mixture upon complexation with boron trifluoride etherate (Scheme 2.8). The crude product was reprecipitated using diethyl ether and redissolved in water for further dialysis. The dried product was obtained by lyophilization and it was then characterized by ^{1}H and ^{19}F NMR (Figure 2.10), XPS and ATR-FTIR spectroscopy. The ^{1}H NMR spectrum of **H** contained a broad multiplet in the aromatic region from δ 7.9-8.2 ppm. These peaks have been attributed to the aromatic and imine protons which could have merged together owing to the complex environment offered by the branched polyethyleneimine, **Y** scaffold. As the aromatic region of **Y** is devoid of any peaks, the presence of broad peaks in the ^{1}H NMR spectrum of polymer **H** clearly verifies the effective conjugation of diiodosalicylideneimine boron difluoride moieties to the backbone of **Y**. Further evidence for the successful modification with boron difluoride was obtained from ^{19}F NMR spectral data. Organic compounds containing the BF_2 group typically show a quartet in the ^{19}F NMR spectrum because the signals of the fluorine atoms are split by the adjacent boron atom (^{11}B). However, in the case of **H,** three broad multiplet signals at δ −127.3 to −127.5, −142.2 to −142.9 and −149.8 to −150.06 ppm were observed in the ^{19}F NMR spectrum. The observation of three signals suggests the presence of non-equivalent BF_2 groups that are attached on different side-arms of the backbone of **Y**. Although all primary amine nitrogens in **Y** are present in the periphery of the polymer, only a fraction of them are functionalised and thus the functionalized moieties would have non-equivalent chemical environments. Moreover, in branched **Y**, the primary amino groups are connected to methylene units attached to both secondary and tertiary amines thereby resulting in non-equivalent chemical environments. Hence it is inferred that the different diiodosalicylideneimine-boron difluoride units have different chemical environments resulting in the observation of multiple signals in the ^{19}F NMR spectrum.

ATR-FTIR spectrum of **Y** exhibited the characteristic absorption peaks of the amine groups around 3400 and 1651 cm^{-1} whereas the stretching and bending vibrations of the N–H and $–NH_2$ groups were observed at 3281 and 1576 cm^{-1}, respectively (Figure. 2.11). The decrease in the intensity of the amine vibration band around 3400 cm^{-1} post modification indicates the functionalization of **Y**. It is assumed that the imine stretching (-C=N-) around 1620-1670 cm^{-1} merged with the stretching of the amine groups in **Y** and was not observed. It is also necessary to mention that as a consequence of low degree of functionalization of the **Y** backbone, the appearance of signature stretching indicative of the modification is not very prominent.

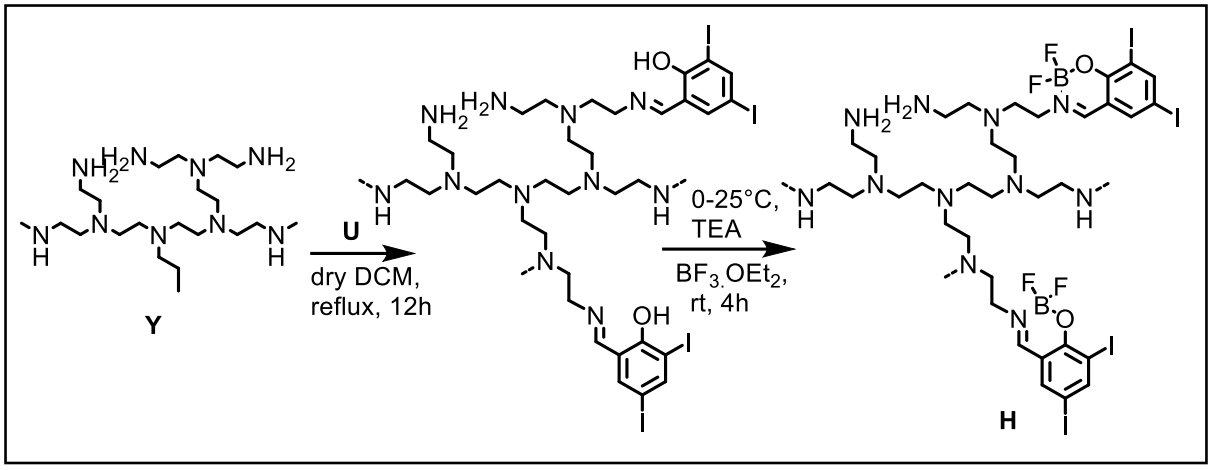

Scheme 2.8. Synthesis of boron difluoride functionalized polyethyleneimine polymer **H**.

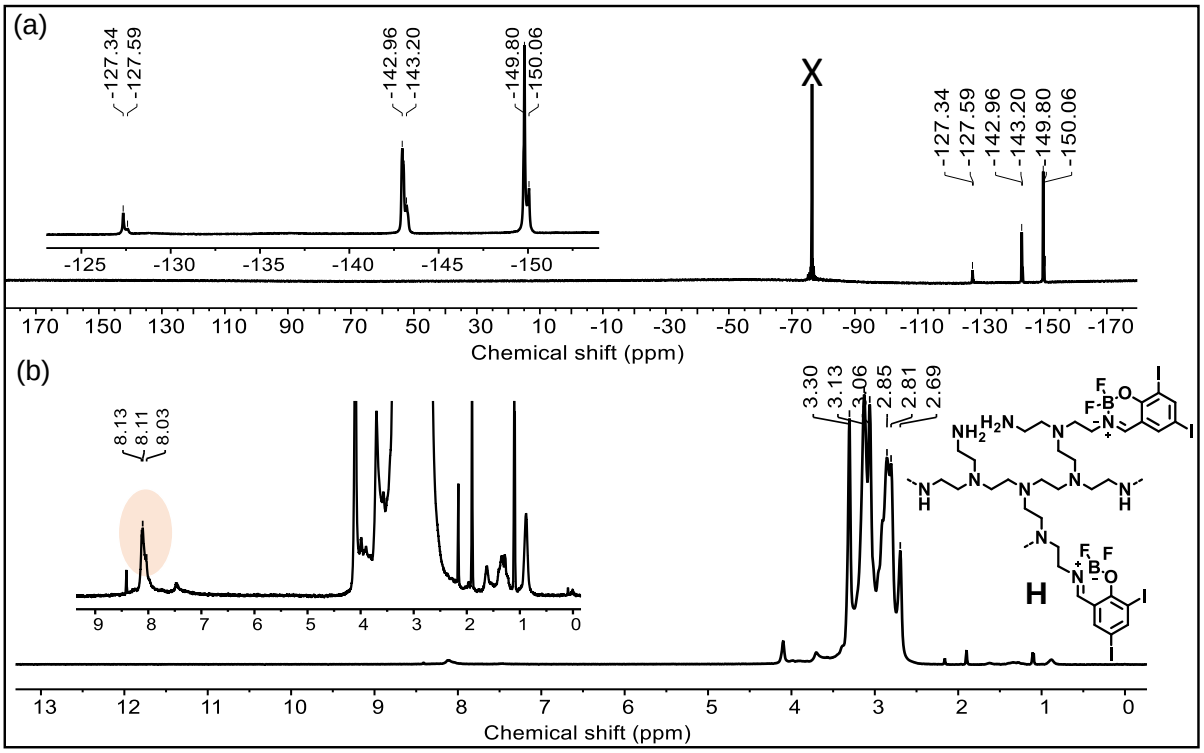

Figure 2.10. (a) ^{19}F and (b) ^{1}H NMR spectra of **H** in $CDCl_3$ at 298 K. Selected regions of the spectra are enlarged as insets in (a). Shaded region in the ^{1}H NMR spectra highlights presence of peaks in the aromatic region.

To determine the content of diiodosalicylideneimine-boron difluoride in the functionalised polymer and to further characterize polymer **H**, X-ray photoelectron spectroscopy (XPS) analysis was carried out which gave a mean value of 2.44 ± 0.4, 2.37 ± 0.4 and 0.80 ±0.5% for boron, fluorine and iodine, respectively, as key elements other than the major elements carbon and nitrogen (Figure. 2.12). Due to the volatile nature of halogens

particularly iodine, their percent elemental composition could have been affected due to prolonged X-ray exposure. Furthermore, it is pertinent to mention that the parent PEI was devoid of boron, fluorine or iodine. This observation conclusively supports the functionalization of PEI with diiodosalicylideneimine-boron difluoride complex.

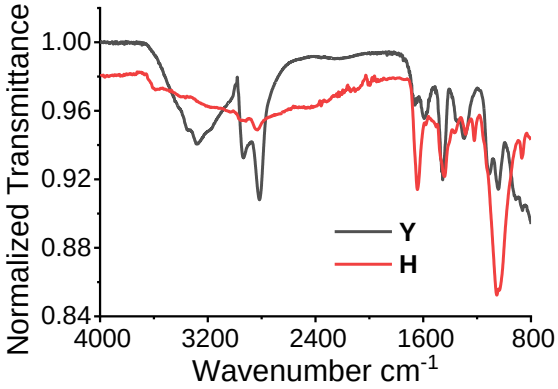

Figure 2.11. ATR-FTIR spectrum of polymers **Y** and **H**.

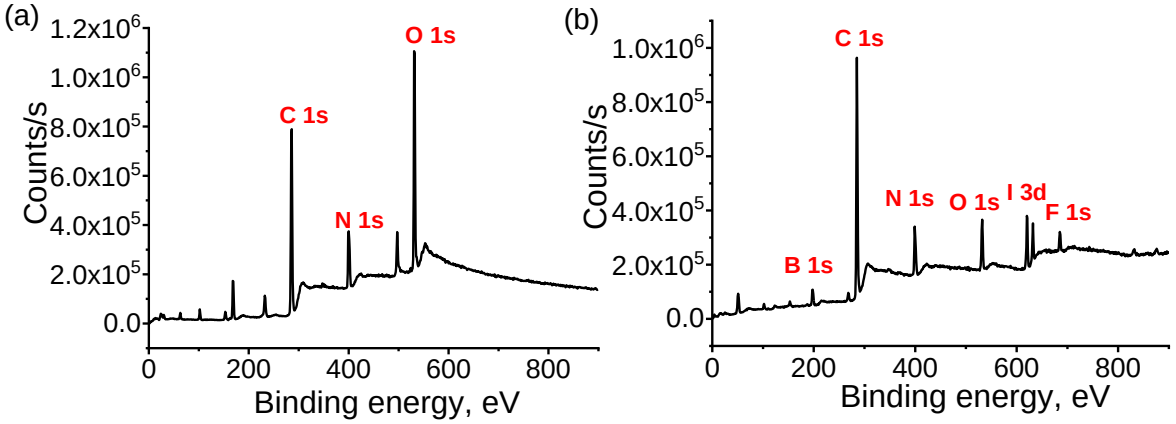

Figure 2.12. XPS survey scan spectra for (a) polyethyleneimine, **Y** (b) Polymer **H** demonstrating presence of all key elements.

2.3. Single crystal XRD.

The molecular structures of **A** and **B** were further authenticated by single crystal X-ray diffraction (Tables 2.1-2.4) for which crystals were obtai.ned by the slow evaporation of **A** or **B** from a mixture of DCM and methanol (1:1). In the case of **A**, the BODIPY unit was not coplanar with the phenyl linker and the dihedral angle between two moieties was ~22.8°. Furthermore, boron atom showed a distorted tetrahedral geometry, and the Mn(I) coordinated complexes exhibited a distorted octahedral geometry wherein the BODIPY moiety and the three CO ligands were observed in a facial configuration. In both complexes **A** and **B**, the Mn-

carbonyl bond lengths were observed to be shorter than the Mn-N bonds which may be attributed to the strong π-back-bonding interactions between the metal-carbonyl moieties. The presence of the ligand with the σ-donating amine (N3) and pyridyl nitrogens (N1,N2) positioned *trans* to the CO enhances the CO photolability. In the case of **B**, the amine nitrogen does not lie on the same plane as the linker and was observed to be 0.443 Å above the phenyl ring presumably due to coordination strain.

Table 2.1. Crystallographic data and refinement parameters for **A**.

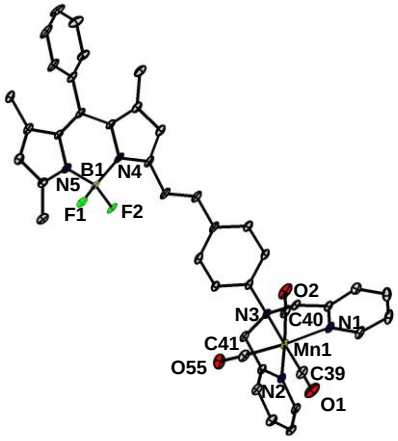

CCDC	2129779
Empirical formula	$C_{41}H_{34}BF_2MnN_5O_3.\ ClO_4$
Formula weight	847.93
Temperature/K	293(2)
Crystal system	Monoclinic
Space group	P 21/n
a/Å	12.3199(4)
b/Å	25.2308(6)
c/Å	13.3345(4)
α/°	90
β/°	110.775(3)
γ/°	90
Volume/$Å^3$	3875.4(2)
Z	4
$\rho_{calc}g/cm^3$	1.453
μ/mm^{-1}	0.477

F(000)	1744
Crystal size/mm^3	0.25 x 0.15 x 0.15
Radiation	MoKα (λ = 0.71073)
2θ range for data collection/°	3.3530-26.3130
Index ranges	-15≤ h ≤ 15, -25≤ k ≤ 32, -16≤ l ≤ 16
Reflections collected	35477
Data/restraints/parameters	8229/0/526
Goodness-of-fit on F^2	1.075
Final R indexes [I>=2σ (I)]	R_1 = 0.0692, wR_2 = 0.1930
Final R indexes [all data]	R_1 = 0.1004, wR_2 = 0.2141

Table 2.2. Selected bond lengths (Å) and bond angles (˚) for **A** derived experimentally from single crystal XRD data.

Bond length $(Å)_{Exp}$		Bond angle $(^o)_{Exp}$	
Mn1-N2	2.053(3)	N2 Mn1 N3	78.63(11)
Mn1-N1	2.048(3)	N1 Mn1 N3	81.49(11)
Mn1-N3	2.133(3)	N1 Mn1 N2	90.86(12)
Mn1 C40	1.804(4)	C40 Mn1 N3	95.97(15)
Mn1 C39	1.800(4)	C40 Mn1 N2	174.54(15)
Mn1 C41	1.809(4)	C40 Mn1 N1	89.10(16)
O2-C40	1.149(5)	C40 Mn1 C41	87.41(19)
O55-C41	1.137(5)	C39 Mn1 N3	174.03(15)
O1-C39	1.156(5)	C39 Mn1 N2	96.14(16)
N1-C1	1.347(5)	C39 Mn1 N1	95.81(16)
N1-C5	1.345(5)	C39 Mn1 C40	89.30(18)
N2-C11	1.349(4)	C39 Mn1 C41	86.70(19)
N2-C7	1.357(5)	C41 Mn1 N2	92.37(16)
N3-C13	1.462(4)	C41 Mn1 N1	175.68(16)
N3-C6	1.501(4)	N4 B1 N5	108.2(3)
N4-C24	1.405(4)	F1 B1 F2	107.4(3)
N4-C21	1.352(4)	C5 N1 Mn1	115.9(2)
N5 C32	1.410(4)	N1 C5 C6	115.8(3)

N4 B1	1.531(5)	F1 B1 F2	107.4(3)
N3 C12	1.503(4)	C6 N3 Mn1	108.2(2)
N5 B1	1.541(5)		

Table 2.3. Crystallographic data and refinement parameters for **B**.

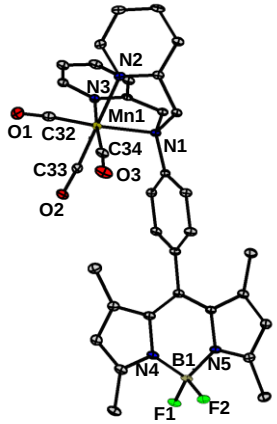

CCDC	2129780
Empirical formula	$C_{34}H_{30}BF_2MnN_5O_3.ClO_4$
Formula weight	759.83
Temperature/K	293(2)
Crystal system	Monoclinic
Space group	P 21/n
a/Å	10.1745(2)
b/Å	24.2359(5)
c/Å	13.7165(3)
α/°	90
β/°	97.060(2)
γ/°	90
Volume/$Å^3$	3356.67(13)
Z	4
$\rho_{calc}g/cm^3$	1.504
μ/mm^{-1}	0.541
F(000)	1560
Crystal size/mm^3	0.25 × 0.15 × 0.10
Radiation	MoKα (λ = 0.71073)

2Θ range for data collection/°	3.109-27.367
Index ranges	-12≤ h ≤ 13, -29≤ k ≤ 30, -17≤ l ≤ 13
Reflections collected	13569
Data/restraints/parameters	7036/0/464
Goodness-of-fit on F^2	1.085
Final R indexes [I>=2σ (I)]	R_1 = 0.0490, wR_2 = 0.1158
Final R indexes [all data]	R_1 = 0.0812, wR_2 = 0.1294

Table 2.4. Selected bond lengths (Å) and bond angles (˚) for **B** derived experimentally from single crystal XRD data.

	Bond length $(Å)_{Exp}$		Bond angle $(Å)_{Exp}$
Mn1-N2	2.044(2)	N2 Mn1 N1	81.34(8)
Mn1-N1	2.156(2)	N3 Mn1 N1	79.26(8)
Mn1-N3	2.042(2)	C34 Mn1 N2	90.31(10)
Mn1-C34	1.805(3)	C34 Mn1 N1	98.84(11)
Mn1-C33	1.814(3)	C34 Mn1 N3	174.86(11)
Mn1-C32	1.795(3)	C34 Mn1 C33	87.87(12)
O3-C34	1.145(3)	C33 Mn1 N2	174.74(12)
O2-C33	1.143(3)	C33 Mn1 N1	94.06(11)
O1-C32	1.157(3)	C33 Mn1 N3	97.01(11)
N1-C13	1.468(3)	C32 Mn1 N2	97.82(11)
N1-C11	1.507(3)	C32 Mn1 N1	175.50(11)
N2-C10	1.346(3)	C32 Mn1 N3	96.28(11)
N2-C6	1.348(3)	C32 Mn1 C34	85.57(13)
N3-C5	1.349(3)	C32 Mn1 C33	86.97(13)
N3-C1	1.339(3)	C13 N1 Mn1	110.74(15)
F2-B1	1.388(3)	F2 B1 F1	109.6(2)
F1-B1	1.388(3)	C13 N1 C11	111.45(19)
N5-B1	1.540(4)	C5 N3 Mn1	115.17(17)
N4-B1	1.547(4)	C1 N3 Mn1	125.61(19)

2.4. Conclusion

In summary, a series of boron difluoride complexes ranging from BODIPYs to boranils were designed and synthesized. Two transition metal conjugated BODIPYs **A** and **B** were designed wherein the meso-phenyl or β-pyrrolic positions of BODIPY core was successfully functionalised with Mn(I)-carbonyl complexes. Furthermore, a tripodal BODIPY derivative **C** was designed wherein three BODIPY units are connected to a benzene ring and was functionalized with six bromine atoms. Boranils **D-H** were then designed as an alternate strategy to overcome the issues commonly faced with BODIPYs. The synthesis was based on salicylideneimine as a core wherein the starting aldehyde and amine was appropriately chosen according to the number of iodines desired on the final boranil complexes. The number of heavy atoms were varied with the objective of investigating their effect on the photophysical properties. All the compounds were fully characterized through ^{1}H, ^{13}C and high-resolution mass spectrometry. The structures of **A** and **B** were further elucidated by single crystal XRD analysis.

2.5. Experimental section

2.5.1. General Techniques

All experiments were carried out at room temperature (25±1 °C) unless otherwise mentioned. NMR spectra were measured on a 500 MHz Bruker Avance Neo or 400 MHz Bruker Avance Neo spectrometer.^{1}H NMR spectra were internally referenced to residual solvent signal at δ 7.26 ppm for $CDCl_3$. CF_3COOH (trifluoro acetic acid) was used as the internal standard for ^{19}F NMR spectra in D_2O and the reference peak position for ^{19}F was taken as δ -76.55 ppm. High resolution mass spectra (HRMS) was measured using Waters Q-TOF Micromass (ESI-MS) Spectrometer or XEVO G2-XS QTOF spectrometer. Crystals were observed with an optical microscope (Olympus BX53F).

2.5.2. Crystallography

Crystals were mounted on Hampton cryoloops. All geometric and intensity data for the crystals were collected using a Super-Nova (Mo) X-ray diffractometer equipped with a microfocus sealed X-ray tube Mo-Kα (λ = 0.71073 Å) X-ray source, and HyPix3000 detector with increasing ω (width of 0.3 per frame) at a scan speed of either 5 or 10 s/frame. The CrysAlisPro software was used for data acquisition, and data extraction. Using Olex, the structure was solved with the SIR2004 structure solution program using Direct Methods and

refined with the ShelXL refinement package using Least Squares minimization. Detailed crystallographic data and structural refinement parameters are summarized in Tables 2.1-2.4 and data can be obtained free of charge from the Cambridge Crystallographic Data Centre.

2.5.3. Materials

Boron trifluoride diethyl etherate, 1,3,5-benzenetricarbonyl trichloride, formic acid, bromopentacarbonyl manganese(I), N-bromosuccinimide, 3,5-diiodosalicylaldehyde, salicylaldehyde, 4,4'-diaminodiphenylmethane and branched polyethyleneimine (PEI, M_W = 25000 g/mol) were purchased from Sigma-Aldrich and used as received. Aniline, picolyl chloride, potassium oxychloride, triethylamine, 2,4-dimethylpyrrole, trifluoroacetic acid, 2,3-dichloro-5,6-dicyano-1,4-benzoquinone (DDQ), ethyl-N,N-diisopropylamine, 2-ethynylpyridine, 1,5-dihydroxynapthalene and piperidine were purchased from TCI Chemicals. Silica gel (60-120 mesh), methanol, dichloromethane, hexane, acetone, ethyl acetate, dichloromethane and potassium hydrogen phosphate were purchased locally. Solvents were distilled and dried before use. N-bromosuccinimide was recrystallised in deionised water and dried properly before use.

2.6. Syntheses

2.6.1. Synthesis of K

To a solution of aniline (**I**) (0.903 mL, 10 mmol) and potassium hydrogen phosphate (5.22 g, 30 mmol) in acetonitrile (10 mL), 2-(chloromethyl)pyridine hydrochloride (**J**) (4.57 g, 27.8 mmol) was added portion wise at 0 ℃ for 30 minutes. The mixture was stirred vigorously and then refluxed at 80 ℃ for 12 hours. The reaction mixture was quenched with water and extracted with dichloromethane. After evaporation of the solvent, the desired product was obtained as beige solid after column chromatography on silica with ethyl acetate:hexane 1:1, v/v. Yield 0.679 g, 65%. ^{1}H NMR (400 MHz, $CDCl_3$), δ (ppm): 4.83 (s, 4H), 6.72-6.71 (m, 3H), 7.17-7.15 (m, 4H), 7.28-7.30 (d, 2H, J = 8 Hz), 7.63- 7.61 (t, 2H, J = 8 Hz), 8.59-8.60 (d, 2H, J = 4 Hz).

2.6.2. Synthesis of L

Phosphorus oxychloride (0.163 mL, 1.75 mmol) was mixed with N,N-dimethylformamide (0.550 mL) under N_2 atmosphere and the reaction mixture was stirred for 30 minutes at 0 ℃. Compound **K** (0.1 g, 0.36 mmol) was added in portion and refluxed for 12

hours at 90°C. Reaction mixture was quenched by adding ice and further maintained at pH 7 by adding sodium acetate. The reaction mixture was washed with water and extracted with chloroform. The desired product upon drying was purified by column chromatography on silica by using hexane:acetone, 5:3 v/v and obtained as yellow oil. Yield, 0.073 g, 67%. ^{1}H NMR (400 MHz, $CDCl_3$), δ (ppm): 4.92 (s, 4H), 6.79-6.77 (d, 2H, J = 8Hz), 7.24-7.21 (m, 4H), 7.65-7.69 (m, 4H), 8.62-8.61 (d, 2H, J = 4 Hz), 9.73 (s, 1H).

2.6.3. Synthesis of O

Benzoyl chloride (**M**) (0.413 mL, 3.55 mmol) was dissolved in dry dichloromethane (150 mL) and purged with N_2 for 1 hour at room temperature. 2,4-Dimethylpyrrole (**N**) (0.725 mL, 7.1 mmol) was then added to the reaction mixture under dark conditions and the resulting solution was stirred for 12 hours at room temperature. After cooling the reaction mixture to 0 °C, triethylamine (10 mL) was added and stirred for 30 minutes followed by the addition of boron trifluoride diethyl etherate (7 mL). The reaction mixture was further stirred for 2 hours at room temperature. The reaction mixture was then washed with water, organic layer was collected and dried with sodium sulphate. Organic layer was evaporated and the desired product was obtained via column chromatography on silica by using dichloromethane:hexane 1:9, v/v. Yield, 0.280 g, 25%. ^{1}H NMR (400 MHz, $CDCl_3$), δ (ppm): 7.50-7.46 (m, 3H), 7.27-7.29 (m, 2H), 5.98 (s, 2 H), 2.56 (s, 3H), 1.37 (s, 3H).

2.6.4. Synthesis of P[21]

In a 100 mL round-bottomed flask were added 40 mL of anhydrous toluene, BODIPY **O** (0.37 mmol, 0.12 g), compound **L** (0.37 mmol, 0.11 g), acetic acid (0.2 mL), and piperidine (0.2 mL). The reaction mixture was refluxed for 12 hours and the progress of the reaction was monitored by TLC (ethyl acetate: methanol = 97: 3). After consumption of the starting material, water (100 mL) was added to the reaction mixture and the resulting solution was extracted with chloroform. The organic layer was dried on anhydrous Na_2SO_4 and evaporated. Column chromatographic separation over 60-120 mesh silica gel using a 97:3 mixture of ethyl acetate and methanol yielded desired the product **P** as a dark blue solid. Yield, 0.053 g, 30%. ^{1}H NMR (400 MHz, $CDCl_3$), δ (ppm): 8.62-8.61 (d, J = 4 Hz, 2H), 7.68-7.65 (t, J = 8Hz, 4Hz, 2H), 7.47-7.41 (m, 6H), 7.30-7.28 (m, 2H), 7.22-7.20 (t, J = 4Hz, 2H), 7.16-7.13 (d, 12 Hz, 1 H), 6.71-6.79 (d, J = 32 Hz, 2 H), 6.55 (s, 1H), 5.96 (s, 1H), 4.89 (s, 4 H), 2.56 (s, 3 H), 1.40-1.37 (d, J = 12 Hz, 6 H). ^{13}C NMR (100 MHz, $CDCl_3$), δ (ppm): 158.16, 154.23, 153.32, 149.59, 149.49,

148.89, 139.31, 137.20, 137.14, 136.77, 135.27, 132.88, 131.46, 129.25,129.00, 128.79, 128.35, 126.01, 122.34, 120.97, 117.57, 115.31, 112.71, 112.69, 95.26, 57.18,14.70, 14.18.

2.6.5. Synthesis of Q[21]

Compound **L** (0.26 g, 0.86 mmol) was dissolved in dry dichloromethane (100 mL) and purged with N_2 for 1 hour at room temperature. 2,4-Dimethylpyrrole (**N)** (0.174 mL, 1.72 mmol) was added dropwise to the above reaction mixture under dark along with 2-3 drops of trifluoroacetic acid. Resulting solution was stirred at room temperature for 12 hours. After addition of 2,3-dichloro-5,6-dicyano-1,4-benzoquinone (DDQ) (0.390 g, 1.72 mmol), stirring was continued for another 30 minutes. 2 mL of N,N-diisopropylethylamine and 5 mL of $BF_3.OEt_2$ were successively added and after 2 hours, the reaction mixture was washed with water (3 x 300 mL) and dried over anhydrous Na_2SO_4. The solvent was evaporated and the residue was purified by column chromatography on 60-120 mesh silica with 9.7:0.3 v/v dichloromethane: methanol to give an orange solid. Yield, 0.157 g, 35 %. ^{1}H NMR (400 MHz, $CDCl_3$), δ (ppm): 8.60-8.59 (d, J = 4 Hz, 2H), 7.65-7.62 (t, J = Hz, 2H), 7.23-7.18 (m, 4H), 7.00-6.98 (d, J = 8 Hz, 2H), 6.80-6.78 (d, J = 8 Hz, 2H), 5.95 (s, 2H), 4.87 (s, 4H), 2.53 (s, 6H), 1.44 (s, 6H). ^{13}C NMR (100 MHz, $CDCl_3$), δ (ppm): 153.51, 150.13, 145.04, 144.02, 138.34, 132.04, 127.30, 124.18, 118.59, 117.51, 116.17, 108.46, 52.70, 9.81.

2.6.6. Synthesis of complex A

A solution of compound **P** (0.010 g, 0.017 mmol) and $Mn(CO)_5Br$ (0.05 g, 0.017 mol) in 10 mL of dichloromethane and methanol (1:1) was stirred for 12 hours at room temperature under dark conditions. After 12 hours, the colour of the reaction mixture was observed to have turned pink from blue. Excess of sodium perchlorate (0.005 g) was then added to the reaction mixture in 2.5 mL of methanol and further stirred for 1 hour. The reaction mixture was filtered and concentrated to 5 mL followed by dropwise addition of diethyl ether to obtain pinkish-blue precipitate, which was filtered, washed with water and dried in vacuum. The product was further purified by column chromatography on alumina with ethyl acetate to give purple coloured solid. Yield, 0.011 g, 80%. ^{1}H NMR (400 MHz, $CDCl_3$), δ (ppm): 8.83-8.82 (d, J = 4 Hz, 2H), 7.99-7.96 (t, J= 8Hz, 2H), 7.76-7.66 (d, J= 4 Hz, 2H), 7.50-7.49 (m, 6H), 7.38-7.36 (d, J = 8 Hz, 2H), 7.32-730 (m, 2H), 7.20-7.16 (d, J= Hz, 1H), 6.62 (s, 1H), 6.03 (s, 1H), 5.29-5.25 (d, J = 16 Hz, 2H), 4.96-4.92 (d, J= 16 Hz, 2H), 2.59 (s, 3 H), 1.43-1.40 (d, J = 12 Hz, 6 H). ^{13}C NMR (100 MHz, $CDCl_3$), δ (ppm): 237.38, 234.46, 231.05, 160.88, 153.45, 152.04, 140.31, 137.63, 135.19, 134.91, 133.09, 132.42, 130.07, 128.81, 128.29, 125.92, 123.91,

118.21, 66.90, 29.71, 14.55, 14.46. HRMS: m/z calculated $C_{41}H_{34}BF_2MnN_5O_3$ $[M]^+$: 748.2103, found: 748.2100.

2.6.7. Synthesis of complex B

A solution of **Q** (0.02 g, 0.038 mmol) and $Mn(CO)_5Br$ (0.010 g, 0.038 mmol) in 10 mL of dichloromethane and methanol (1:1) was stirred for 12 hours at room temperature under dark conditions. Excess of sodium perchlorate (0.001 g) was then added to the reaction mixture in 5 mL of MeOH and further stirred for 2 hours. Reaction mixture was filtered and concentrated to 5 mL followed by dropwise addition of diethyl ether to give a yellow precipitate, which was filtered and washed with water. The product was further purified by column chromatography on alumina with 1:1 v/v dichloromethane:methanol to give an orange solid. Yield, 0.02 g, 65%. ^{1}H NMR (400 MHz, $CDCl_3$), δ (ppm): 8.84-8.83 (d, J = 4 Hz, 2H), 8.00 (d, 2H), 7.81-7.80 (d, J = 4Hz, 2H), 7.4-7.50 (m, 6H), 6.00 (s, 2H), 5.38-5.34 (d, J= 16 Hz, 2H) 5.06-5.03 (d, J= 12 Hz, 2H), 2.55 (s, 3H), 1.47 (s, 3H). ^{13}C NMR (100 MHz, $CDCl_3$), δ (ppm): 214.75, 205.17, 158.20.66, 153.62, 150.13, 149.22, 140.64, 137.81, 131.34, 128.83, 127.64, 122.22, 118.70, 116.60, 65.52, 13.01, 12.10. HRMS: m/z calculated $C_{34}H_{30}BF_2MnN_5O_3$ $[M]^+$: 660.1790, found: 660.1793.

2.6.8. Synthesis of S[22]

1,3,5-Benzenetricarbonyl trichloride (**R**) (2.55 mmol, 660 mg) was dissolved in anhydrous dichloromethane (70 mL), degassed and stirred for 30 minutes. 2,4-Dimethylpyrrole (**N**) (15 mmol, 1.42 g) was added to the solution and refluxed for 12 hours under an atmosphere of nitrogen. The reaction mixture was then brought to 0 °C, triethylamine (7 mL) was added and stirred for another 5 minutes. To this ice cooled solution, $BF_3.OEt_2$ (7.5 mL) was added and reaction mixture was stirred for another 4 hours at room temperature. The reaction mixture was washed with brine solution (3 × 50 mL) and the organic layer was collected and dried over anhydrous sodium sulphate. Evaporation of the solvent yielded the crude product as a dark brown residue which was purified via column chromatography using a mixture of DCM and hexane (10:90) as eluents. Yield, 30 mg, 21%. ^{1}H NMR ($CDCl_3$, 400 MHz) δ (ppm) 2.18 (s, 18H), 2.45 (s, 18H), 5.98 (s, 6H), 6.96 (s, 3H). HRMS: m/z calculated for $C_{45}H_{46}B_3F_6N_6$ [M+H]: 817.3967, found: 817.3960.

2.6.9. Synthesis of C

To a well-stirred solution of **S** (0.049 mmol, 25 mg) in 1:1 mixture of dry DCM-DMF mixture (20 mL), N-Bromosuccinimide (0.32 mmol, 73 mg) in DCM was added dropwise under nitrogen and the reaction was stirred for 4 hours at 25 °C. The reaction mixture was then washed with water (3 × 50 mL), and the organic layer was collected and dried over anhydrous sodium sulphate. Evaporation of the solvent yielded the crude product as a red residue which was purified by column chromatography using a mixture of DCM and hexane as eluents. Yield, 22 mg, 80%. ^{1}H NMR ($CDCl_3$, 400 MHz) δ (ppm) 2.16 (s, 18H), 2.49 (s, 18H), 7.00 (s, 3H). ^{13}C NMR ($CDCl_3$, 100 MHz) δ (ppm) 10.06, 12.02, 108.76, 119.63, 130.87, 138.27, 154.68. HRMS: m/z calculated for $C_{45}H_{40}B_3F_6N_6Br_6$ [M+H+ACN] 1325.8520, found:1325.8530.

2.6.10. Synthesis of D

Salicylaldehyde (**T)** (135 µL, 1.20 mmol) and p-anisidine (**V**) (250 mg, 1.14 mmol) were dissolved in 10 mL dry dichloromethane along with 0.1 mL formic acid and the reaction mixture was stirred under reflux for 15 hours. Upon cooling down to 0°C, the Schiff base precipitated and the solvent was evaporated using rotary evaporator. Residue obtained was dissolved in DCM and cooled down to 0 °C using an ice bath. 1.1 mL triethylamine was then added and the reaction mixture was stirred for 30 minutes followed by the addition of 1.9 mL $BF_3{\cdot}OEt_2$. After stirring the reaction mixture for 6 hours at room temperature, the solvents were evaporated off in a rotary evaporator and the crude product was purified by column chromatography on silica gel using a 1:1 mixture of DCM-hexane as the eluent to give **D** as a pale-yellow powder. Yield, 220 mg, 80%. ^{1}H NMR (400 MHz, $CDCl_3$): δ (ppm) 3.86 (s, 3H), 6.97-7.06 (m, 3H), 7.15-7.17 (d, 1H, J= 8 Hz), 7.49-7.52 (m, 3H), 7.63-7.67 (m, 1H), 8.41 (s, 1H). ^{13}C NMR (100 MHz, $CDCl_3$): δ (ppm) 55.5, 114.7, 116.0, 119.5, 120.3, 124.5, 131.8, 135.2, 138.7, 159.4, 160.2, 162.0. HRMS: m/z calculated for $C_{14}H_{13}BF_2NO_2$ $[M+H]^+$: 276.1007, found: 276.1017.

2.6.11. Synthesis of E

Salicylaldehyde (**T)** (239 µL, 2.23 mmol) and 4-iodoaniline (**W)** (250 mg, 1.14 mmol) were dissolved in 10 mL dry dichloromethane along with 0.1 mL formic acid and the reaction mixture was stirred under reflux for 15 hours. Solvent was evaporated using rotary evaporator. The residue obtained was dissolved in DCM and cooled down to 0 °C using an ice bath. 1.1 mL of triethylamine was then added and the reaction mixture was stirred for 30 minutes

followed by the addition of 1.9 mL $BF_3 \cdot OEt_2$. After stirring the reaction mixture for 25 hours at room temperature, the solvents were evaporated off in a rotary evaporator and the crude product was purified by column chromatography on silica gel using a mixture of 1:1 DCM-hexane as the eluent to yield **E** as a pale-yellow powder. Yield, 296 mg, 80%. ^{1}H NMR (400 MHz, $CDCl_3$): δ (ppm) 7.49-7.47 (3H, m), 7.29-7.26 (2H, m), 5.98 (2H, s), 2.56 (6H, s), 1.37 (6H, s). ^{13}C NMR (100 MHz, 298 K, $CDCl_3$): δ (ppm) 94.9, 113.9, 119.7, 120.5, 125.1, 132.1, 138.7, 140.0, 141.8, 159.9, 163.2. HRMS: m/z calculated for $C_{13}H_{10}BF_2INO$ $[M+H]^+$: 371.9868, found: 371.9883.

2.6.12. Synthesis of F

3,5-Diiodosalicylaldehyde (**U)** (350 mg, 0.935 mmol) and *p*-anisidine (**V)** (115 mg, 0.935 mmol) were dissolved in 15 mL dry dichloromethane along with 0.1 mL formic acid and the reaction mixture was stirred under reflux for 18 hours. Solvent was evaporated using rotary evaporator and the orange powder was dissolved in 25 mL dry DCM and cooled down to 0 °C using an ice bath. 1.2 mL of triethylamine was then added and the reaction mixture was stirred for 30 minutes at room temperature followed by the addition of 3 mL $BF_3 \cdot OEt_2$. The reaction mixture was then stirred at room temperature for four hours and was washed with 15 mL water twice. The organic layers were collected and dried over sodium sulphate. The solvent was evaporated off using a rotary evaporator, and the product was purified twice by column chromatography on silica gel (60-120 mesh) initially using a 1:1 mixture of hexane and ethyl acetate and further with 3:1 mixture of hexane and ethyl acetate to yield **F** as yellow powder. Yield, 148 mg, 30%. ^{1}H NMR (400 MHz, $CDCl_3$): δ (ppm) 3.79 (s, 3H), 6.91-6.93 (d, 2H, J= 8Hz), 7.39-7.41 (d, 2H, J= 8Hz), 7.69 (d, 1H, J=2Hz), 8.18 (s, 1H), 8.27 (d, 1H. J=2Hz). ^{13}C NMR (100 MHz, $CDCl_3$): δ (ppm) 55.5, 81.1, 89.7, 114.8, 117.2, 124.5, 134.5, 139.8, 154.3, 158.3, 160.3, 160.9. HRMS: m/z calculated for $C_{14}H_{11}BF_2I_2NO_2$ $[M+H]^+$: 527.8940, found: 527.8947.

2.6.13. Synthesis of G

3,5-Diiodosalicylaldehyde (**U**) (400 mg, 1.07 mmol) and 4,4'-diaminodiphenylmethane (**X)** (106 mg, 0.535 mmol) were dissolved in 20 mL dry dichloromethane along with 0.1 mL formic acid and the reaction mixture was stirred under reflux for 18 hours. The precipitated orange residue was filtered and collected, dried and dissolved in 30 mL dry DCM. The reaction mixture was ultrasonicated for 5 minutes and cooled down to 0 °C using an ice bath. 0.6 mL

of triethylamine was then added and the reaction mixture was stirred for 30 minutes followed by the addition of 2 mL $BF_3{\cdot}OEt_2$ and stirred for 17 hours at room temperature. The precipitated product was filtered and the residue was washed with 15 mL of diethylether thrice to obtain **G** as a pale-yellow powder. Yield, 483 mg, 90%. ^{1}H NMR (400 MHz, $CDCl_3$: DMSO-d_6 (9:1)): δ (ppm) 4.12 (s, 2H), 7.47-7.49 (d, 4H, J= 8Hz), 7.58-7.60 (d, 4H, J=8Hz), 8.13-8.14 (d, 2H, J=4Hz), 8.38-8.40 (d, 2H, J=8Hz), 9.11 (s, 2H). The compound was too insoluble to record a ^{13}C NMR spectrum. HRMS: m/z calculated for $C_{27}H_{16}B_2F_4I_4N_2O_2Na$ $[M+Na]^+$: 1028.7410, found: 1028.7440.

2.6.14. Synthesis of H

PEI (**Y)** (1.0 g, 0.04 mmol) was dissolved in 50 mL anhydrous dichloromethane followed by the addition of 3,5-diiodosalicylaldehyde (**U)** (606 mg, 1.62 mmol) at room temperature. The resulting solution was stirred and refluxed at 40 ^{o}C for 18 hours, until complete disappearance of 3,5-diiodosalicylaldehyde was observed via TLC. The reaction mixture was further cooled down to 0 °C by using an ice bath. Triethylamine (4.2 mL) was then added and the reaction mixture was stirred for 30 minutes at room temperature followed by the addition of $BF_3{\cdot}OEt_2$ (3 mL). The reaction mixture was stirred until the attainment of room temperature for 6 hours. The product obtained had a gel like texture that had precipitated from the reaction mixture with time. After decanting dichloromethane, crude product was reprecipitated using diethyl ether and redissolved in water. After dialysing (12 kD) in deionized water for 3 days, the product was dried by lyophilisation. ^{1}H NMR (400 MHz, D_2O): δ (ppm) 2.69-3.30 (m), 8.03-8.13 (m). ^{19}F NMR (400 MHz, D_2O, CF_3COOH as reference, δ = −75.0 ppm): δ (ppm) -150.06 to -149.80 (m), -143.20 to -142.96 (m), -127.59 to -127.34 (m).

2.6.15. Synthesis of Z

A solution of **K** (0.08 g, 0.29 mmol) and $Mn(CO)_5Br$ (0.079 g, 0.29 mmol) in 10 mL of dichloromethane was stirred for 12 hours at room temperature under dark conditions. Excess of sodium perchlorate (0.001 g) was then added to the reaction mixture and further stirred for 2 hours. Reaction mixture was filtered and concentrated to 5 mL followed by layering with diethyl ether. The solution was then left overnight in dark and bright crystals were obtained next morning which were filtered and dried to give complex **Z**. Yield, 0.096 g, 80%. ^{1}H NMR (400 MHz, $CDCl_3$), δ (ppm): 8.74-8.75 (m, 2H), 7.99-7.88 (m, 4H), 7.42-7.37 (m, 6H), 7.22 (m, 1H), 5.36-5.22 (m, 4H). ^{13}C NMR (100 MHz, $CDCl_3$), δ (ppm): 221.16, 217.02, 161.22, 153.94, 151.90, 140.27, 130.10, 126.63, 125.89, 124.69, 118.26, 67.85.

2.7. References

[1] M. C. DeRosa, R. J. Crutchley, *Coord. Chem. Rev.* **2002**, *233–234*, 351–371.

[2] P. R. Ogilby, *Chem. Soc. Rev.* **2010**, *39*, 3181–3209.

[3] S. Callaghan, M. O. Senge, *Photochem. Photobiol. Sci.* **2018**, *17*, 1490–1514.

[4] A. Kamkaew, S. Hui Lim, H. Boon Lee, L. Voon Kiew, L. Yong Chung, K. Burgess, *Chem. Soc. Rev.* **2013**, *42*, 77–88.

[5] E. Bassan, A. Gualandi, P. Giorgio Cozzi, P. Ceroni, *Chem. Sci.* **2021**, *12*, 6607–6628.

[6] J. Wang, Q. Gong, L. Wang, E. Hao, L. Jiao, *J. Porphyrins Phthalocyanines* **2020**, *24*, 603–635.

[7] E. Kottelat, Z. Fabio, *Inorganics* **2017**, *5*, 24.

[8] U. Schatzschneider, *Inorganica Chimica Acta* **2011**, *374*, 19–23.

[9] X. Jiang, Z. Xiao, W. Zhong, X. Liu, *Coord. Chem. Rev.* **2021**, *429*, 213634.

[10] L. Long, X. Jiang, X. Wang, Z. Xiao, X. Liu, *Dalton Trans.* **2013**, *42*, 15663–15669.

[11] Z. Xiao, R. Jiang, J. Jin, X. Yang, B. Xu, X. Liu, Y. He, Y. He, *Dalton Trans.* **2019**, *48*, 468–477.

[12] S. J. Carrington, I. Chakraborty, J. M. L. Bernard, P. K. Mascharak, *Inorg. Chem.* **2016**, *55*, 7852–7858.

[13] I. Chakraborty, S. J. Carrington, P. K. Mascharak, *Acc. Chem. Res.* **2014**, *47*, 2603–2611.

[14] A. Acosta, J. Antipán, M. Fernández, G. Prado, C. Sandoval-Altamirano, G. Günther, I. Gutiérrez-Urrutia, I. Poblete-Castro, A. Vega, N. Pizarro, *RSC Adv.* **2021**, *11*, 31959–31966.

[15] R. N. Pickens, B. J. Neyhouse, D. T. Reed, S. T. Ashton, J. K. White, *Inorg. Chem.* **2018**, *57*, 11616–11625.

[16] J. Jimenez, I. Chakraborty, S. J. Carrington, P. K. Mascharak, *Dalton Trans.* **2016**, *45*, 13204–13213.

[17] S. J. Carrington, I. Chakraborty, P. K. Mascharak, *Chem. Commun.* **2013**, *49*, 11254–11256.

[18] J. Massue, D. Jacquemin, G. Ulrich, *Organics* **2021**, *2*, 365–375.

[19] A. C. Murali, P. Nayak, K. Venkatasubbaiah, *Dalton Trans.* **2022**, *51*, 5751–5771.

[20] D. Frath, J. Massue, G. Ulrich, R. Ziessel, *Angew. Chem., Int. Ed.* **2014**, *53*, 2290–2310.

[21] O. A. Bozdemir, R. Guliyev, O. Buyukcakir, S. Selcuk, S. Kolemen, G. Gulseren, T. Nalbantoglu, H. Boyaci, E. U. Akkaya, *J. Am. Chem. Soc.* **2010**, *132*, 8029–8036.

[22] A. Loudet, K. Burgess, *Chem. Rev.* **2007**, *107*, 4891–4932.

Chapter 3

Photophysical properties of tetracoordinate boron difluoride compounds

3.1. Introduction

BODIPY dyes are unique fluorophores that exhibit interesting photophysical properties like high molar absorptivity, tunable absorption and emission energies, and high fluorescence quantum yields[1,2]. They show fascinating changes in photophysical aspects upon derivatization at various positions on the main core. Since transition metal complexes render flexibility to tune their physical and chemical attributes by variation in the metal core, oxidation state, and ligand environment, employing BODIPY as the ligands can further push the absorption of the metal complex towards the biologically relevant region of the spectrum. Owing to the therapeutic applications of CO delivery[3–5] and the proven ability of BODIPYs to act as efficient photosensitizers[6–8], simultaneous CO release and generation of reactive oxygen species can lead to utility in photodynamic therapy and antibacterial applications. The intrinsic fluorescence properties of BODIPYs can further allow them to be tracked in cells, making these systems valuable.

On a similar note, understanding the mechanistic aspects of molecular self-assembly and controlled dye aggregation of BODIPYs can push their utility to the fields of bioimaging, disease diagnosis and treatments. Though supramolecular dye aggregates consisting of closely packed chromophores have garnered attention across wide range of applications[9,10], mechanistic insights into the fundamental aspects of aggregation is vital with respect to understanding the main driving forces carrying out the aggregation pathway complexities. Appropriate substitution on the dye can largely govern the aggregation behavior and also control the extent of non-radiative decays. In this regard, incorporation of heavy atoms has been a heavily practiced methodology to induce spin orbit coupling, thereby causing non-radiative decay pathways and generating triplet excited states[7,8]. Both bromines and iodines have been successfully exploited for the said purpose and have been interchangeably used to functionalize chromophores in order to achieve significant photosensitization properties for a wide range of applications. Although molecular aggregate science has now become a new generation smart approach contributing immensely towards technological advancements, an elucidated vision of the differences in the structure property relationship of aggregates upon

heavy atom incorporation remains unexplored. In a recent work published by our group[16], we reported a peculiar shaped BODIPY molecule **I6** containing six iodo-substituents (Figure 3.1). It was observed that while the luminescence of **I6** was highly quenched in solution owing to the heavy atom effect exhibited by iodine atoms, the nanoaggregates of the same molecule exhibited significantly enhanced emission intensity. On a similar note, the nanoaggregates were highly efficient in generating singlet oxygen as compared to **I6** in solution and the quantum yield of singlet oxygen generation was found to be 0.82 contrary to 0.21 in solution with **I6**. So, molecule **C** was studied with the objective of elucidating the differences between iodine and bromine substitution on a peculiar BODIPY skeleton and investigate the impact on the associated photophysics.

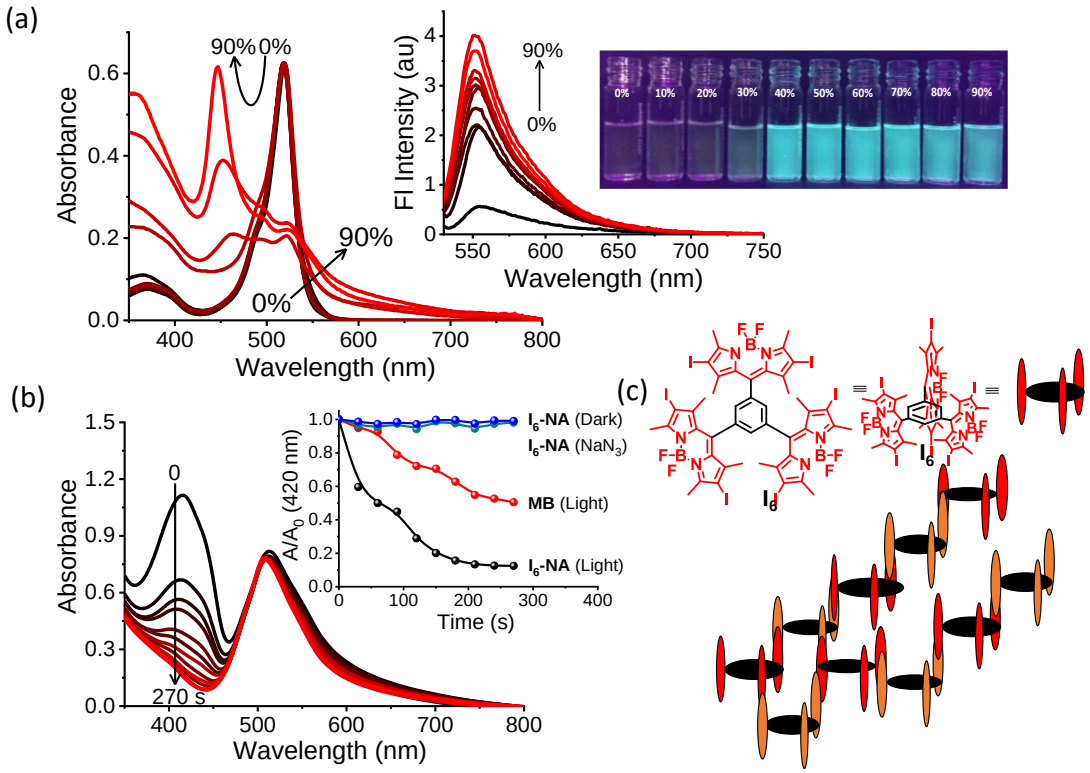

Figure 3.1 (a) Absorption, emission (inset) spectra, λ_{ex} = 520 nm and visual fluorescence change, λ_{ex} = 365 nm of **I6** (4.5 mM) in different acetonitrile–water mixtures (b) Changes in the UV-Vis absorption spectrum of a mixture of 1,3-diphenylisobenzo-furan (DPBF, 90 mM) and **I6-NA** as a function of irradiation time in 20% ethanol–water Inset shows the relative decrease in the absorption of DPBF at 420 nm in the presence of **I6-NA** or methylene blue (MB) under different experimental conditions (c) Schematic representation of aggregation in **I6**.[16]

Similar to BODIPYs, boranils are intriguing as overlap of the empty *p*-orbital of boron with π- conjugated organic core leads to the delocalization of the electron cloud and planarization of the π-systems thereby resulting in interesting photophysical properties[17,18]. Boron coordination also results in red shifted absorption and emission as compared to the corresponding chelating units. Functionalization with appropriate groups allows tuning of the physical properties of small organic compounds and the attachment of heavy atoms such as iodine or bromine can significantly enhance their photosensitization efficiency. While the luminescence properties of the tetracoordinate boron-containing organic compounds have been extensively studied, their photosensitization properties have garnered limited attention. Hence, we were motivated to study the photosensitizing abilities of the synthesized salicylideneimine boron difluorides. Similarly, we were intrigued to investigate the effect of incorporation of multiple boranil units onto the backbone of a polymer on the overall photophysical properties. It is worth mentioning that while small molecules are interesting for various applications, appropriately functionalized polymers are highly desirable as they have high mechanical stability, good processability for thin film formation and higher versatility for practical applications than small molecules. In this chapter, we will discuss the photophysical aspects of all the synt0hesized molecules in four parts, with each part dedicated to a certain set of molecules (Figure 3.2).

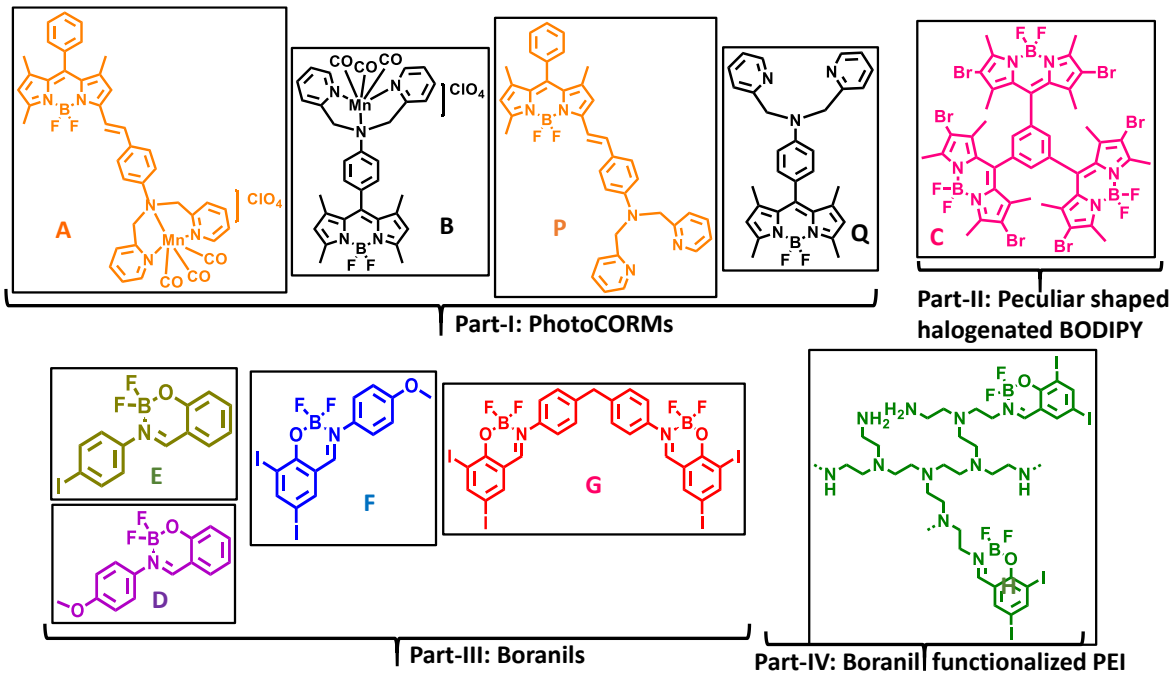

Figure 3.2. Illustration of the structures of molecules **A-H,** divided into different parts.

3.2. Part I. PhotoCORMs A and B

3.2.1. Absorption and emission properties

The photophysical properties of complexes **A** and **B** are presented in Table 3.1. The electronic absorption spectrum of the complex **A** displayed a maximum at 558 nm (ε = 1.45 x 10^5 $M^{-1}cm^{-1}$) along with a shoulder at 521 nm whereas its emission maximum was observed at 570 nm along with a shoulder at 615 nm (Figure 3.1). Meanwhile, the complex **B** displayed absorption and emission maxima at 499 nm (ε = 1.09 x 10^5 $M^{-1}cm^{-1}$) and 510 nm, respectively, exhibiting a blue shift upon coordination to Mn(I) center. It is noteworthy that upon binding with the Mn(I) center, the emission spectra of **Q** showed an enhancement in fluorescence intensity which can be attributed to the restricted photoinduced electron transfer (PET) from the dipicolylamine moiety to the BODIPY core (Figure 3.2). Complexes **A** and **B** were highly soluble in common organic solvents and were stable under dark conditions (Figures 3.3 and 3.4).

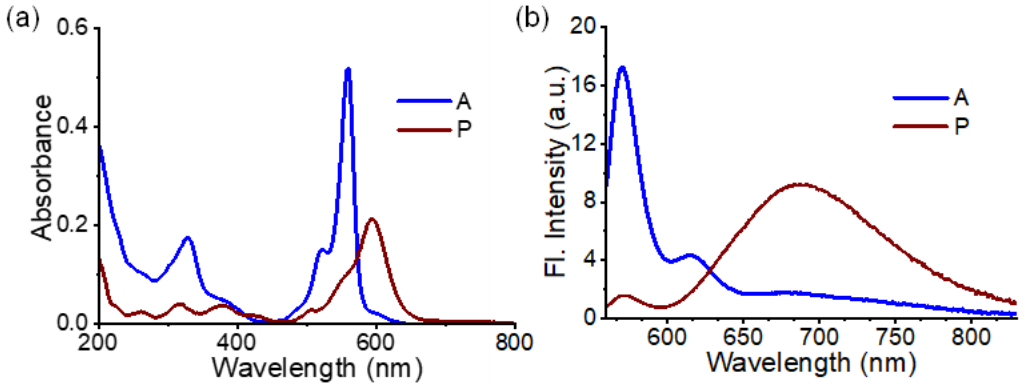

Figure 3.3. (a) UV-vis absorption and (b) emission spectra of **A** (3.6 µM) and the corresponding ligand **P** (3.6 µM) in acetonitrile. λ_{ex} = 560 nm.

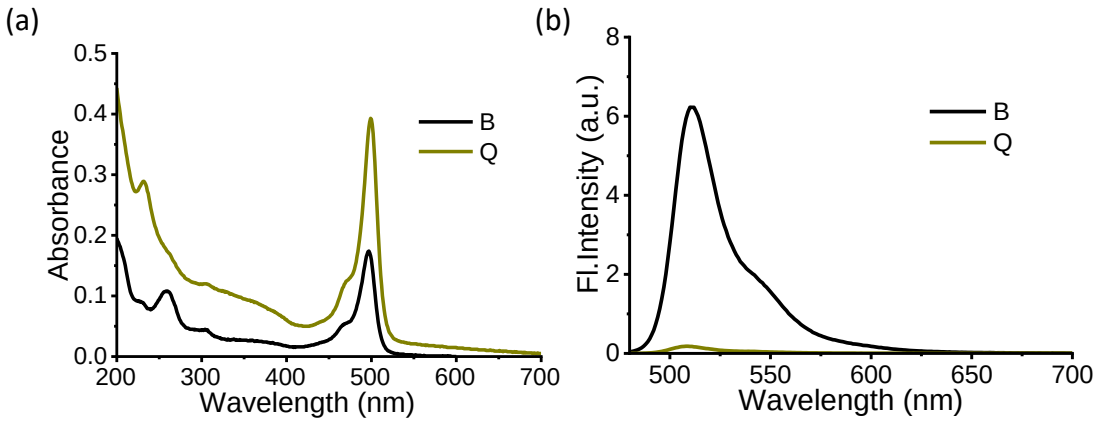

Figure 3.4. (a) UV-vis absorption and (b) emission spectra of **B** (3.6 µM) and the corresponding ligand **Q** (3.6 µM) in acetonitrile. λ_{ex} = 470 nm.

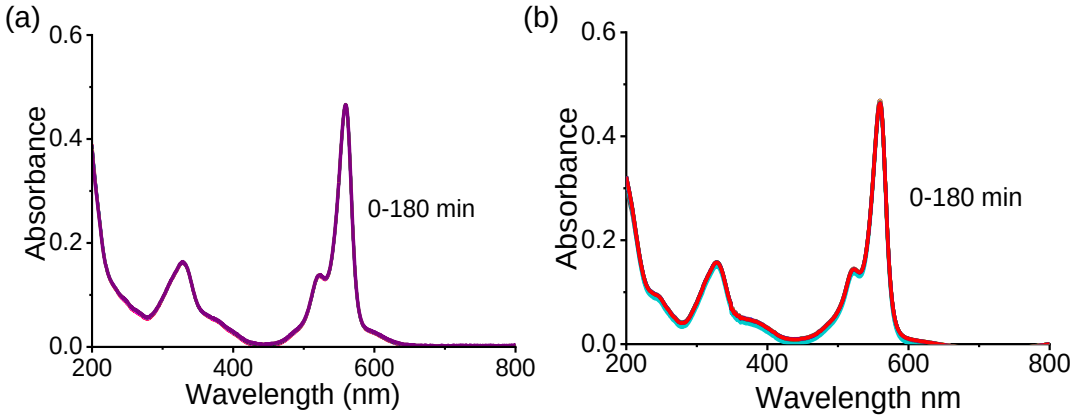

Figure 3.5. UV-vis absorption spectra of **A** in (a) nitrogen bubbled acetonitrile and (b) normal air saturated acetonitrile recorded under dark conditions for every 10-minute interval up to 180 minutes.

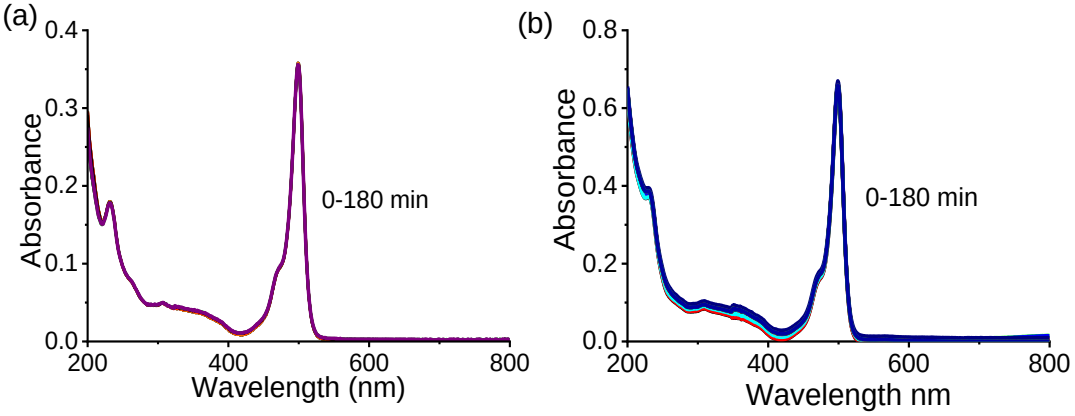

Figure 3.6. UV-vis absorption spectra of **B** in (a) nitrogen bubbled acetonitrile and (b) normal air saturated acetonitrile for every 20-minute interval up to 180 minutes under dark conditions.

3.2.2. Photoinduced CO release

In order to observe the photoinduced release of CO, changes in the electronic absorption spectrum of **A** upon exposure to 550 nm light were recorded as a function of irradiation time (Figure 3.5a and 3.5b). We observed the emergence of a new peak at 593 nm along with a concomitant decrease in the intensity of the peak at 558 nm besides an isosbestic point at 572 nm post irradiation. The isosbestic point at 572 nm clearly indicates one step formation of a new species after CO release. It was also observed that the intensity of the emission at 570 nm showed a drastic decrease and was accompanied by an increase in the emission at 700 nm. The kinetic analysis of the CO release upon photolysis of a solution of **A** in acetonitrile at 560 nm gave a first order CO releasing rate constant of (k_{CO}) 0.01389 s^{-1} and a half-life of 49.9 s (Figure 3.6). Since complex **B** did not exhibit any prominent changes in the long wavelength region after CO release owing to the meso functionalization of the BODIPY core, we could not analyze the CO release kinetics at longer wavelength and corresponding rate constant values (Figure 3.7). Notably, meso functionalization did not significantly impact the absorption properties in the long wavelength region as the meso carbon is a nodal point[19] and hence there is minimal electronic interaction between BODIPY and Mn-CO core. Hence, the reduced π-conjugation between the BODIPY and picolyl counterpart due to the orthogonal orientation of BODIPY might account for the minimal change observed in the absorption and emission maxima of **B** after release of CO.

Light-induced release of CO from **A** and **B** was further confirmed by the Myoglobin assay (Figures 3.8 and 3.9). Therein, the released CO reacts with deoxymyoglobin (dMb), obtained by the reduction of myoglobin with sodium dithionate, to yield carboxymyoglobin (Mb-CO). After irradiation of **A** for 10 minutes, the UV-Vis absorption peak of dMb at 557 nm was observed to decrease whereas the characteristic peaks of Mb-CO adduct at 540 and 577 nm emerged. Furthermore, the absorption peak of dMb at 434 nm shifted to 424 nm thereby confirming the conversion of dMb to Mb-CO.

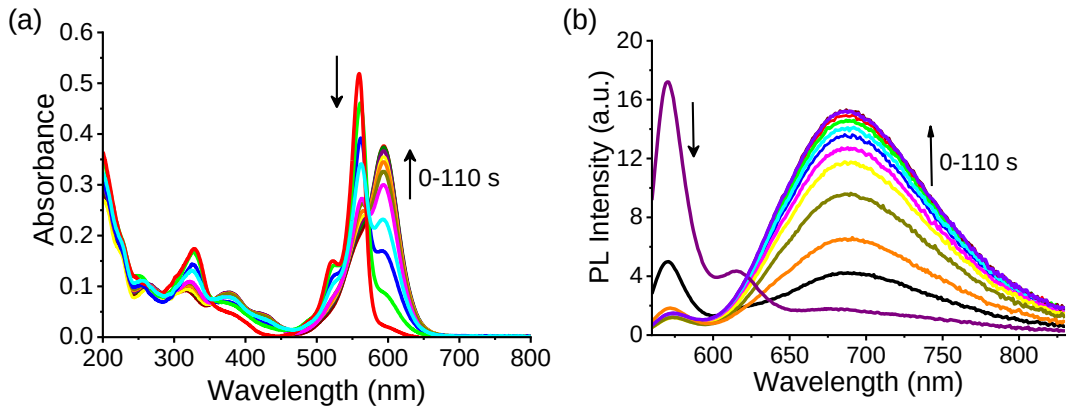

Figure 3.7. Changes in the (a) UV-vis absorption and (b) emission spectra of **A** (3.6 μM) in acetonitrile upon exposure to 550 nm light from a 350 W Xenon lamp.

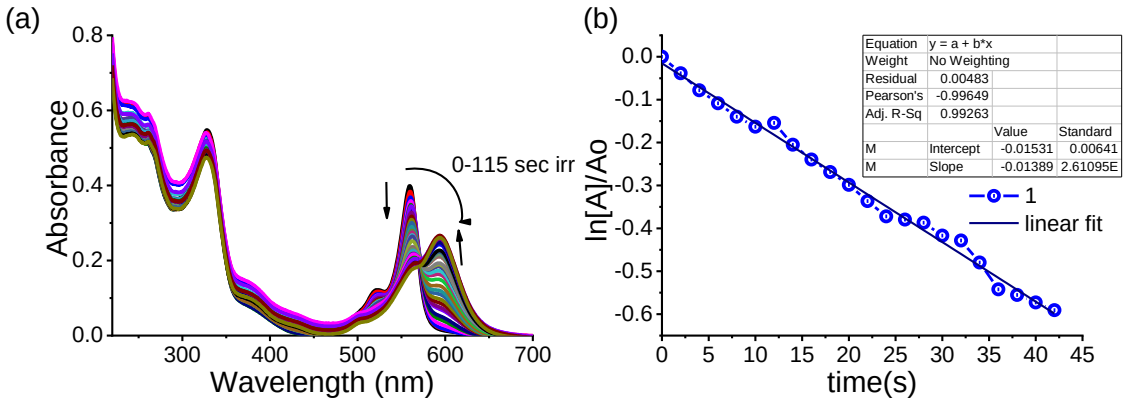

Figure 3.8. (a) Changes in the UV-vis absorption spectrum of **A** (2.9 μM) in acetonitrile upon exposure to visible light (550 nm bandpass filter) at intervals of 2 seconds. (b) Change in absorbance as monitored by the decrease in the absorbance at 560 nm following exposure to UV light vs time intervals of 2 seconds. Linear fitting is represented by a solid line (apparent rate constant k_{CO} = 0.01389 s^{-1}).

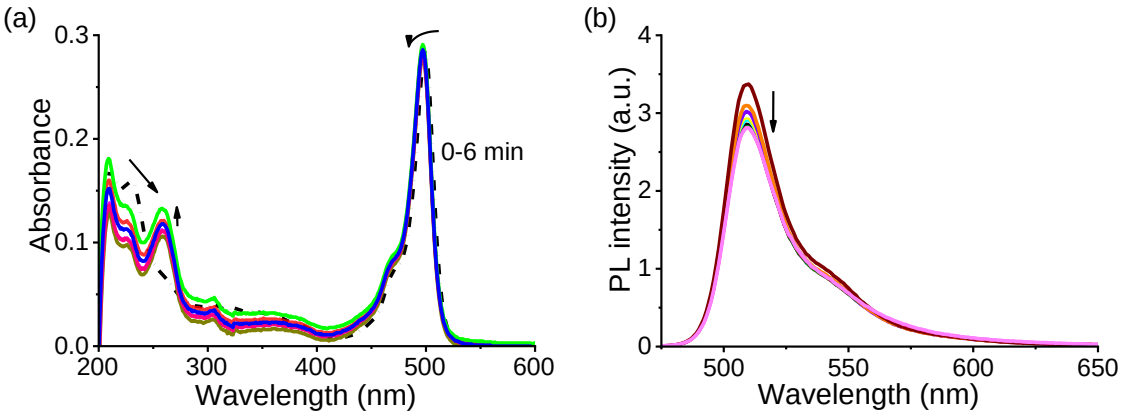

Figure 3.9. Changes in the (a) UV-vis absorption and (b) emission spectra (λ_{ex} = 480 nm) of **B** (2.7 µM) in acetonitrile upon exposure to visible light for 6 minutes (λ_{irr} > 475 nm).

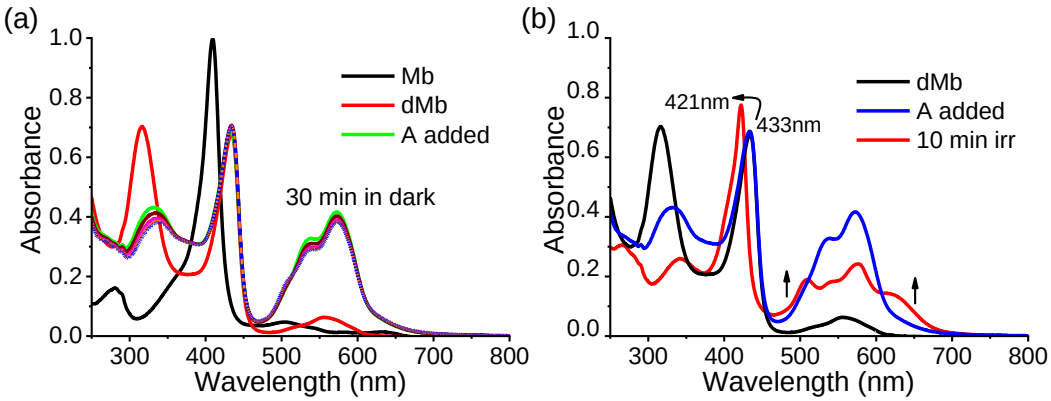

Figure 3.10. (a) Electronic absorption spectral traces of **A** (3.6 µM) in the presence of sodium dithionite (24 mg.mL^{-1}) and myoglobin (2 mg.mL^{-1}, 66 µL) recorded under dark conditions for 30 minutes. (b) Time-dependent absorption spectra of myoglobin showing the conversion of deoxy-Mb (dMb, 0.1 mM) to MbCO with CO units released from **A** as determined by myoglobin assay in 10% ACN phosphate buffer (0.1 M, pH 7.4 at 37 °C).

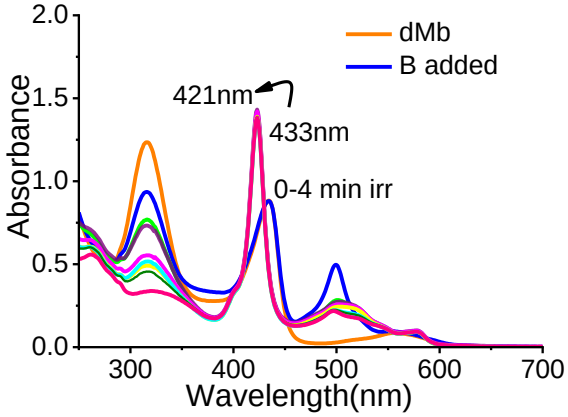

Figure 3.11. Conversion of reduced Mb to Mb-CO in a mixture of **B** (3.6 μM) and reduced Mb (0.1 mM) in 10% ACN phosphate buffer (pH 7.4) upon exposure to light for 4 minutes (λ_{irr} > 475 nm, xenon arc lamp 350 W).

ATR-FTIR spectroscopy further confirmed the photo-release of CO from **A** and **B** in acetonitrile as the % transmittance of the CO stretching bands at 1937 and 2034 cm^{-1} decreased after light exposure (Figure 3.10). Photo-release of CO was further quantified using gas chromatography using a thermal conductivity detector (GC-TCD), and it was observed that while the amount of CO released from **A** in acetonitrile (1 mg/mL) was 75 ppm in the dark, it drastically increased to 2345 ppm upon light exposure for 10 minutes which indicates the release of 2.4 units of CO per molecule (Figure 3.11). Similarly, in the case of **B** (2 mg/mL) in acetonitrile which showed 12 ppm of CO in dark and 5150 ppm in light, the estimated release was 2.6 units of CO per molecule (Figure 3.12). Considering the handling error during injection and the plausible oxidation of the CO to CO_2 by the atmospheric oxygen, it is assumed that all the three molecules of CO are released per molecule of **A** or **B**. Furthermore, the quantum yield for CO release are calculated via ferrioxalate actinometry and found to be 0.42 and 0.025 respectively for **A** and **B** at 475 nm.

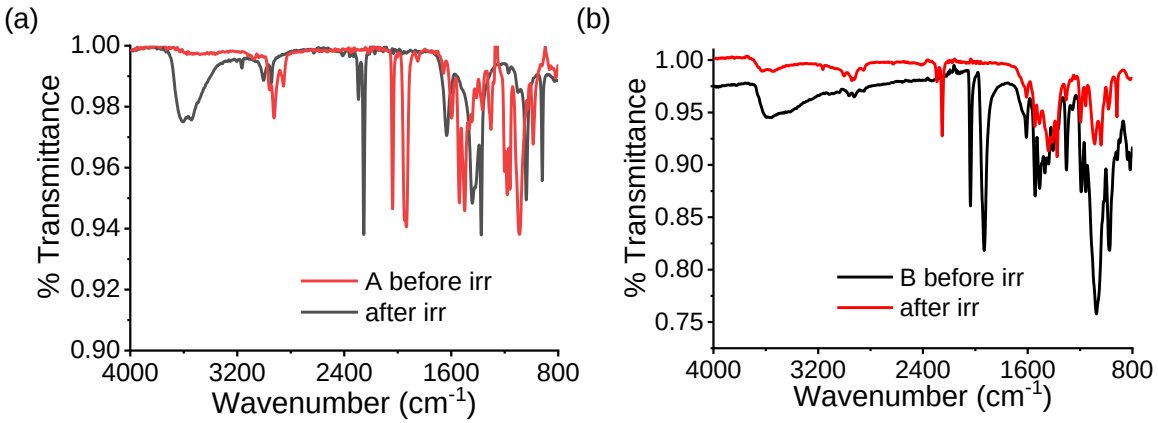

Figure 3.12. ATR-FTIR spectra of complexes (a) **A** and (b) **B** in acetonitrile before (red line) and after irradiation (black line). The spectra show the loss of CO vibration bands (between 1900–2100 cm^{-1}) after the irradiation at 550 nm and 475 nm, respectively, using a 350 W Xenon arc lamp.

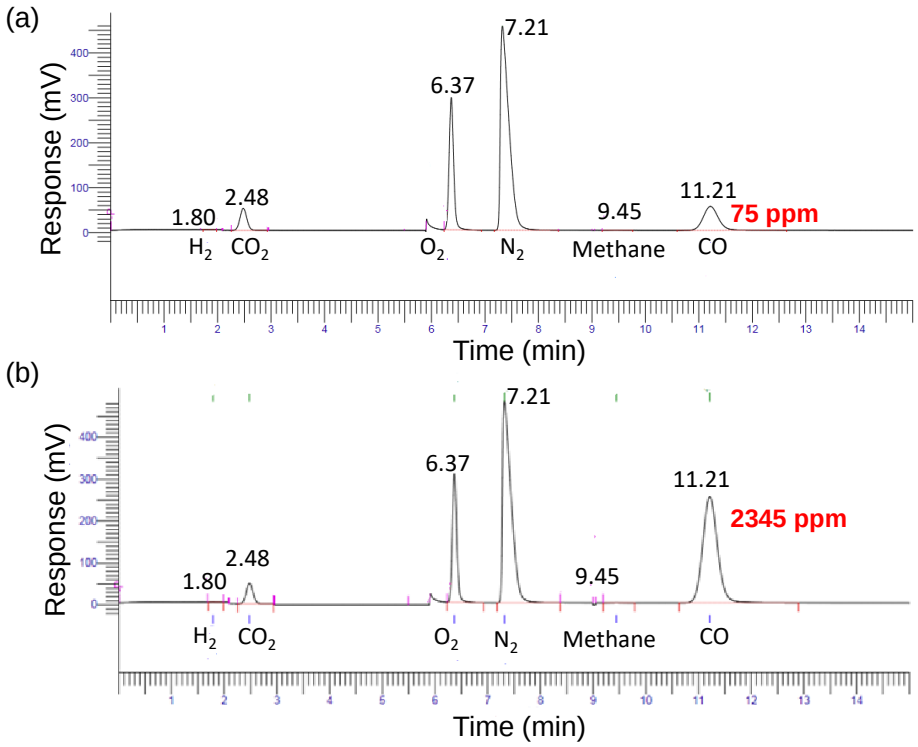

Figure 3.13. GC-TCD data showing release of CO in a 2 mL GC vial containing a solution of complex **A** (1.33 mM) in acetonitrile under (a) dark conditions and (b) upon irradiation with visible light for 30 minutes.

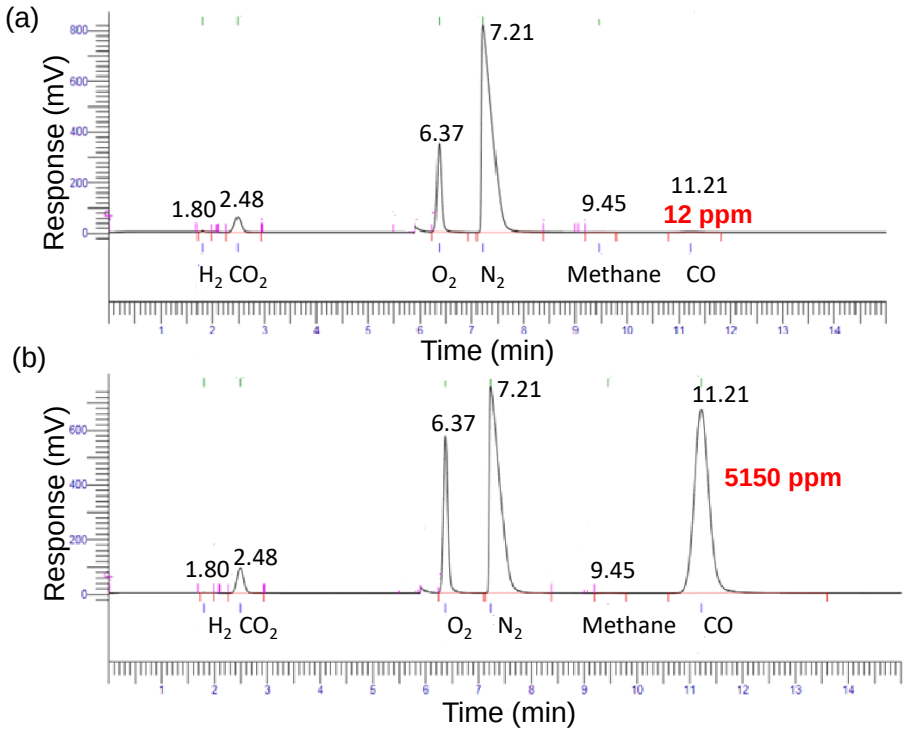

Figure 3.14. GC-TCD data showing release of CO in a 2 mL GC vial containing a solution of complex **B** (3.03 mM) in acetonitrile under (a) dark conditions and (b) upon irradiation with visible light for 30 minutes.

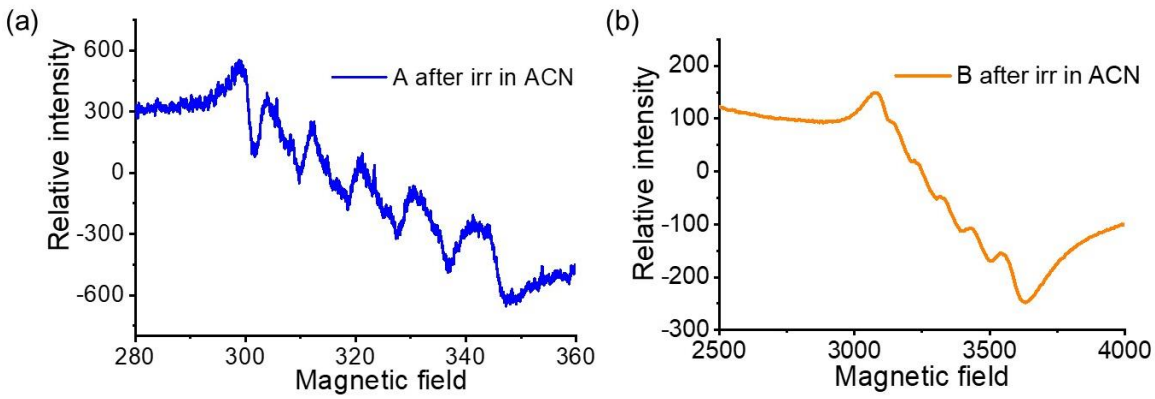

Figure 3.15. X-band ESR spectra of frozen solutions of complex **A** (a) and **B** (b) dissolved in acetonitrile at 77 K upon light exposure.

To understand the chemistry behind the photoinduced CO release, we employed various spectroscopy techniques. It is expected that the release of CO from **A** will result in a change in the oxidation state of manganese from +1 (low spin) to +2 (high spin). The X-band Electron Spin Resonance (ESR) spectra of the photolyzed solutions of the complexes **A** and **B** in acetonitrile displayed six lines (Figure 3.13) thereby indicating formation of paramagnetic

Mn(II) species from the diamagnetic Mn(I) state. The absorption and emission spectra of the photolyzed solution of **A** in acetonitrile resembled that of the ligand **P** and the HRMS of the photolyzed solution also showed a peak at m/z 609.3448 corresponding to the presence of free ligand **P**. ^{1}H NMR spectrum of the extensively irradiated solution of **A** further indicated the presence of free ligand in the solution (Figure 3.14). These observations implied that the photolysis of **A** likely afforded a free ligand and a Mn(II) species. Complex **B**, on the other hand, upon CO release yielded the ligand **Q** that remained bound to the Mn centre. This inference relies on the observation that the ^{1}H NMR spectrum of the photolyzed solution of **B** in $CDCl_3$ exhibited considerable broadening of the peaks throughout the aliphatic and aromatic regions indicating the presence of paramagnetic Mn(II) species (Figure 3.14b).

In order to understand the effect of using near UV and green light separately on the CO release dynamics with complex **A**, we also exposed the sample to near UV light (365 nm) and systematically recorded the absorption spectra. It was observed that there was a slow increase in the absorption corresponding to the ligand at 600 nm during the first minute of irradiation after which no further increase in the absorption was observed until 3 minutes (Figure 3.15a). Co-existence of complex **A** and the ligand **P** was observed indicating that the complete release of CO could not be facilitated with near UV-light. So, as compared to green light exposure of **A** at 550 nm (Figure 3.15b), near UV light irradiation led to a much slower and incomplete CO release process. To support our claim, we also recorded the ATR-FTIR spectrum of **A** after prolonged exposure to 365 nm light and it was observed that the peaks corresponding to CO were diminished but not completely vanished (Figure 3.16). Furthermore, when we exposed the solution to green light, the CO peaks immediately vanished within a few seconds. Hence, it is conclusively proven that direct irradiation of the BODIPY chromophore with visible/green light plays a crucial role towards achieving good CO release efficiency.

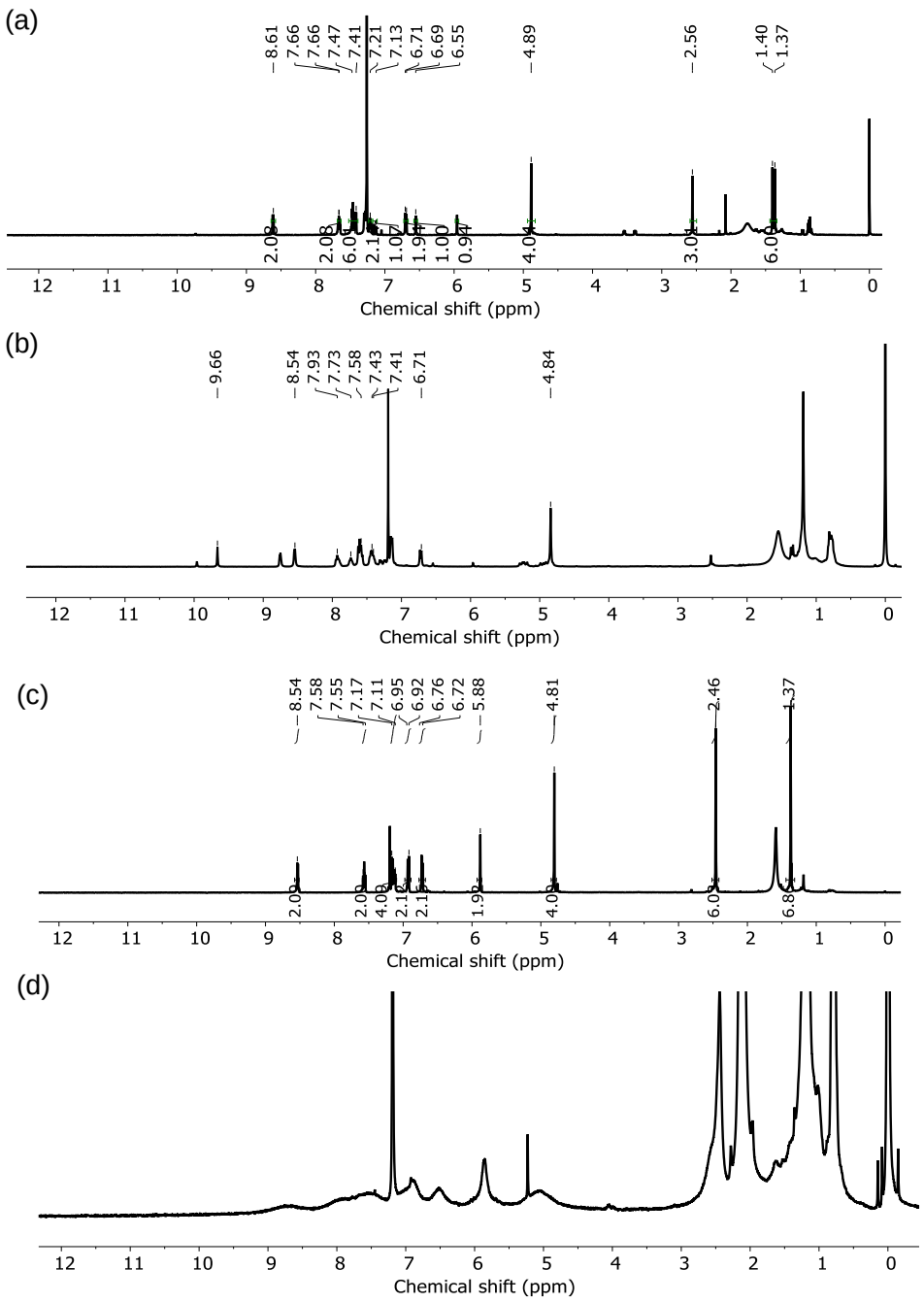

Figure 3.16. ^{1}H NMR spectrum of solution of (a) **P,** (b) photolyzed solution of **A,** (c) **Q** and (b) photolyzed solution of **B** in $CDCl_3$ recorded at 298K.

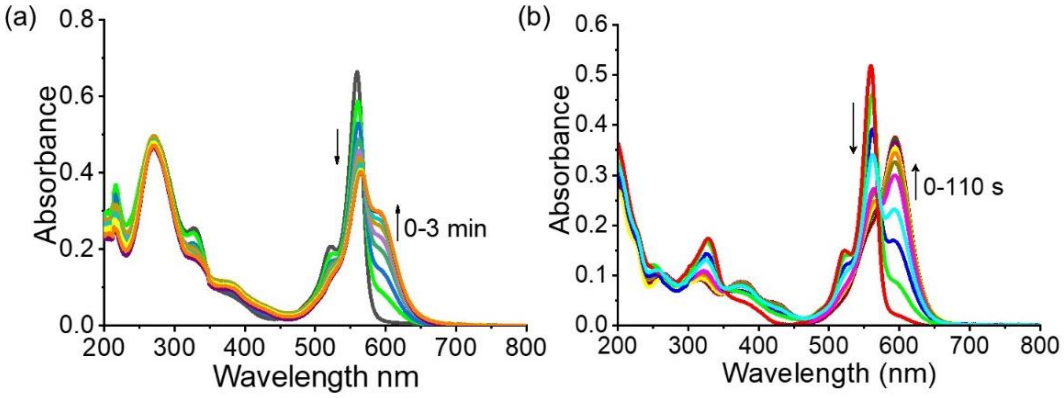

Figure 3.17. Changes in the UV-vis absorption spectra of complex **A** (3.9 µM) under (a) near UV light (365 nm) for 3 minutes and (b) green light (550nm) exposure for 2 minutes.

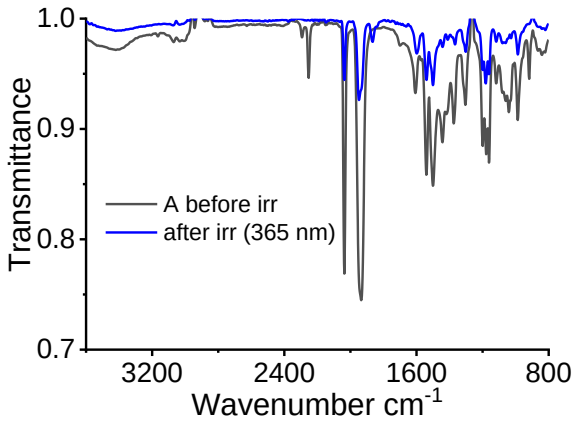

Figure 3.18. ATR-FTIR spectra of complex **A** in acetonitrile before (black line) and after prolonged irradiation (blue line) for 10 minutes under near UV light (365 nm). The spectra show the incomplete loss of CO vibration bands (between 1900–2100 cm^{-1}) after the irradiation.

To further validate our inference that incorporation of BODIPY helps to achieve efficient CO release and singlet oxygen generation, we synthesized a control complex **Z** which has the same structural features as complexes **A** and **B** but is devoid of BODIPY. Photophysical analysis showed that the complex **Z** did not show any absorption beyond 430 nm and exhibited a half-life of 1.7 min for the photorelease of CO upon irradiation with light of wavelength higher than 345 nm. On the other hand, after attaching BODIPY onto the metal carbonyl complex, i.e. the complex **A**, an extended absorption upto 600 nm was observed and the CO release half-life was reduced to 6.8 seconds under similar conditions (Figure 3.17). Hence it is inferred that employing BODIPY plays a substantial role towards more efficient and faster CO release apart from achieving attractive photophysical properties.

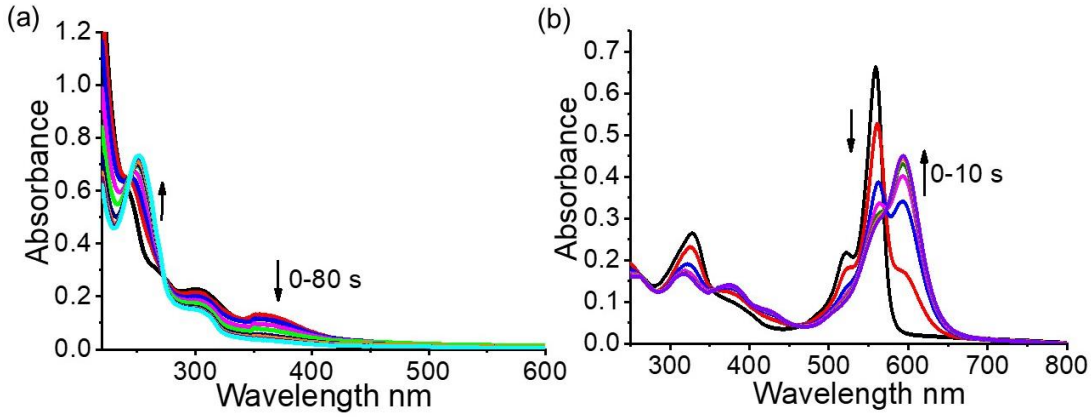

Figure 3.19. (a) Changes in the UV-vis absorption spectra of (a) complex **Z** (0.21μM) and (b) **A** (3.2 μM) upon exposure to white light (>345 nm; Xenon lamp 350W).

3.2.3. Photosensitized generation of singlet oxygen

As BODIPYs are known to photosensitize the generation of singlet oxygen, we investigated singlet oxygen generation with **A** and **B** and the corresponding ligands **P** and **Q** (Figure 3.18-3.20). 1,3-Diphenylisobenzofuran (DPBF), a singlet oxygen trap, was used to monitor the formation of singlet oxygen. We observed that the absorption of DPBF at 410 nm decreased in the copresence of **A** and light thereby indicating the presence of singlet oxygen. The plot of the rate of change in absorbance of **A**, **B** and the corresponding ligands at 410 nm against time showed fastest decrease with **A** and the slowest with the ligands (inset of Figure 3.18). This observation further substantiates the role of metal center towards efficient singlet oxygen generation possibly through the formation of triplet excited states. As observed in the case of complex **A** (Figure 3.18), while the ligand generation post CO release is observed at 590 nm, a simultaneous decrease in the absorption of DPBF at 420 nm is observed indicating that both the processes of CO release and singlet oxygen generation occur simultaneously. To ascertain the generation of singlet oxygen, we conducted control experiments in the absence of light and oxygen. It was observed that the decrease in the absorbance of DPBF in the presence of complexes **A** and **B** was either significantly low or negligible under inert and dark conditions (Figures 3.21 and 3.22). These results further support our inference of the generation of singlet oxygen by **A** and **B**. Estimation of singlet oxygen quantum yields against DPBF was carried out in acetonitrile using methylene blue as reference and they were calculated to be 0.14 and 0.08 respectively, for compounds **A** and **B**. Though it is worth mentioning that as CO release is a much faster process than singlet oxygen generation and the complexes **A** and **B** are no more in their original state post CO release, these numbers cannot be completely relied on and are not representative of exact singlet oxygen quantum yield throughout the process. Control

compound **Z** was also investigated for its singlet oxygen generation ability, and 1,5-dihydroxynaphathalene (DHN) was used as the singlet oxygen trap. The absence of peak around 420 nm corresponding to juglone formation under nitrogen and normal air saturated (oxygenated) conditions indicates that complex **Z** does not yield singlet oxygen. The changes in the spectra corresponding to DHN absorbance around 293 nm can be attributed to simultaneous CO release occurring during the course of experiment (Figure 3.23).

Furthermore, to investigate if any amount of H_2O_2 formation owing to the presence of Mn has occurred with complexes **A** and **B** upon light exposure, an experiment was carried out wherein fenton's test was adopted as the strategy to check for the presence of H_2O_2. It is known that Fenton's test leads to the oxidation of Fe(II) to Fe(III) with H_2O_2 which acts as the oxidising agent to yield highly reactive hydroxyl and superoxide radicals which are further monitored spectrophotometrically. The experiment was conducted with $FeCl_2$ as precursor in the presence of irradiated solutions of the complexes **A** and **B** under dark. No change in the absorption of the mixture monitored at 560 nm was observed upon incubation for a period of 35 minutes in the presence of the irradiated forms of complexes **A** and **B** in methanol thereby ruling out the possibility of H_2O_2 formation (Figure 3.24). Similarly, 2,2-diphenyl-1-picrylhydrazyl (DPPH) radical quenching experiment was carried out to investigate the presence of free radicals and examine the anti-oxidant nature of the complexes. Methanolic solution of complex **A** was irradiated using 550 nm light, followed by immediate addition of DPPH in dark. No change in the absorption spectrum during dark incubation for 30 minutes monitored at 517 nm shows the absence of free radicals and anti-oxidant activity of complexes **A** and **B** (Figure 3.25).

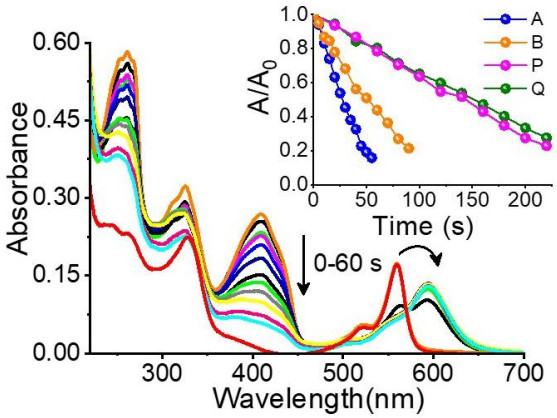

Figure 3.20. Changes in the UV-vis absorption spectrum of a mixture of **A** (1.1 μM) and 1,3-diphenylisobenzofuran (DPBF, 10 μM) in acetonitrile upon light exposure. Inset shows the rate

of decrease in the absorbance of DPBF (10 μM) at 410 nm in presence of **A** (1.1 μM), **B** (1.43 μM), **P** (1.2 μM) and **Q** (2.5 μM) in acetonitrile recorded as a function of irradiation time.

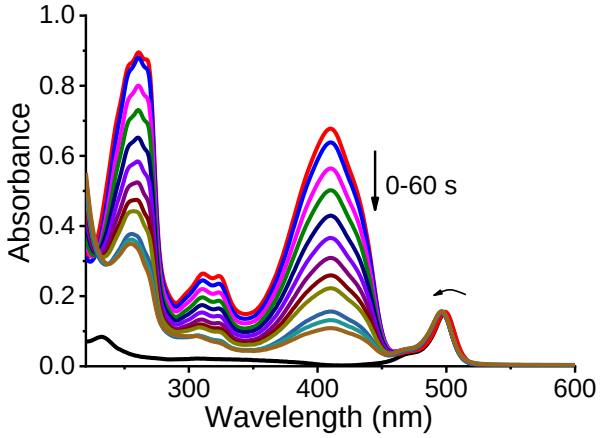

Figure 3.21. Changes in the UV-Vis absorption spectrum of a mixture of **B** (1.43 μM) and DPBF (25 μM) in acetonitrile upon light exposure.

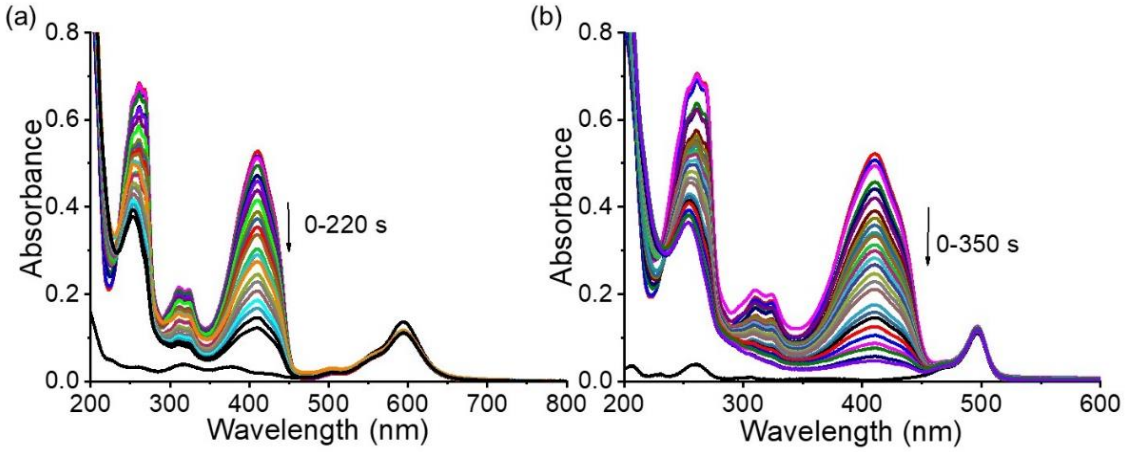

Figure 3.22. Changes in the UV-Vis absorption spectrum of DPBF (18.5 μM) in the presence of (a) **P** (1.2 μM**)** and (b) **Q** (2.5 μM) in acetonitrile upon light exposure.

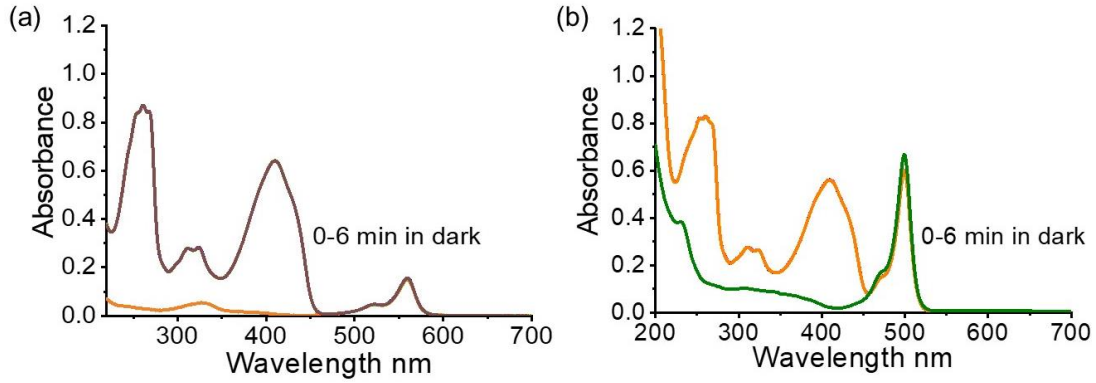

Figure 3.23. Changes in the UV-Vis absorption spectrum of DPBF (25 μM) in the presence of (a) **A** (1.18 μM) and (b) **B** (3.28 μM) in acetonitrile under dark conditions for a period of 6 minutes.

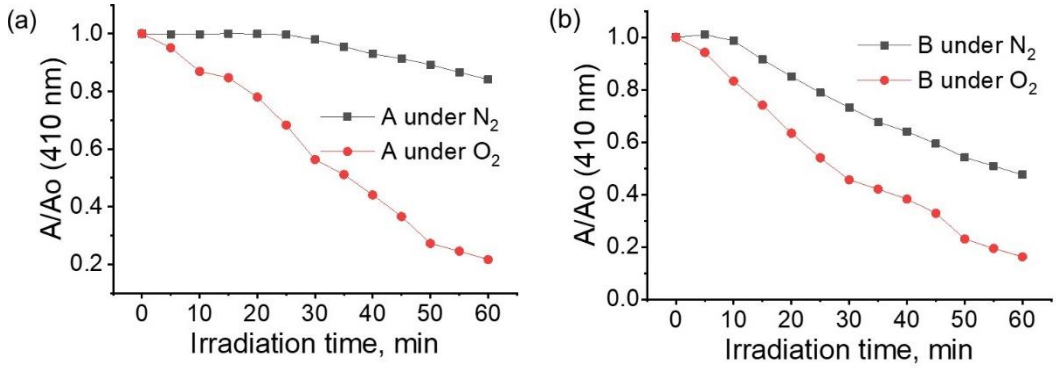

Figure 3.24. Decrease in the absorbance of DPBF (25 μM) at 410 nm with respect to irradiation time in the presence of (a) **A** (1.18 μM) and (b) **B** (3.28 μM) in acetonitrile, under inert (nitrogen bubbled) conditions and normal air saturated (oxygenated) conditions.

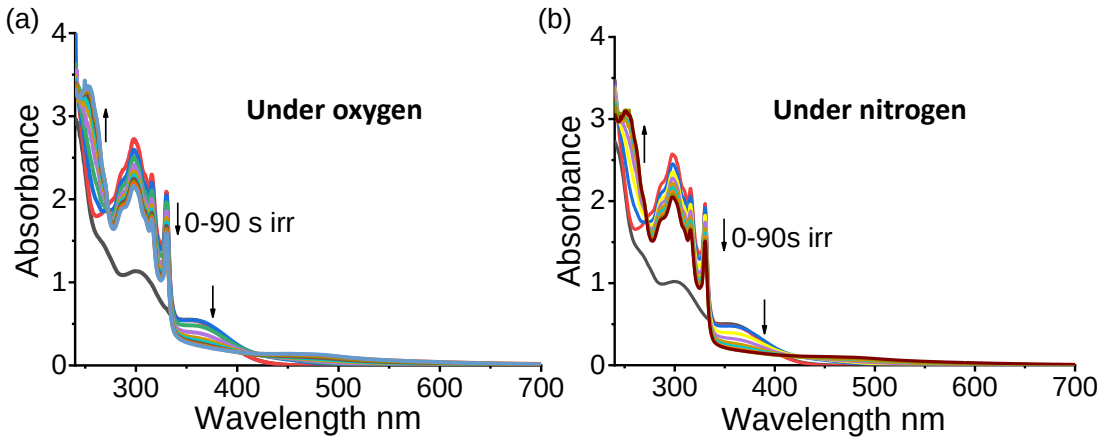

Figure 3.25. (a) Changes in the UV-vis absorption spectra of DHN (0.28 mM) in acetonitrile with complex **Z** (0.36μM) (a) under normal air saturated (oxygenated) and (b) nitrogen bubbled conditions upon exposure to white light (>345 nm; xenon lamp 350W).

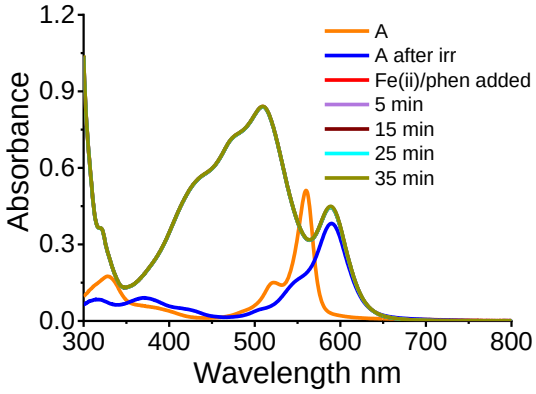

Figure 3.26. Changes in the UV-Vis absorption spectrum of a mixture of photolyzed solution of **A (**3.25 µM), 30 µL of 1mmol $FeCl_2$ and 45 µL of 1mmol 1,10-phenanthroline in methanol under dark. 350W Xenon lamp with 550 nm bandpass filter was used for irradiation of **A** for 5 minutes.

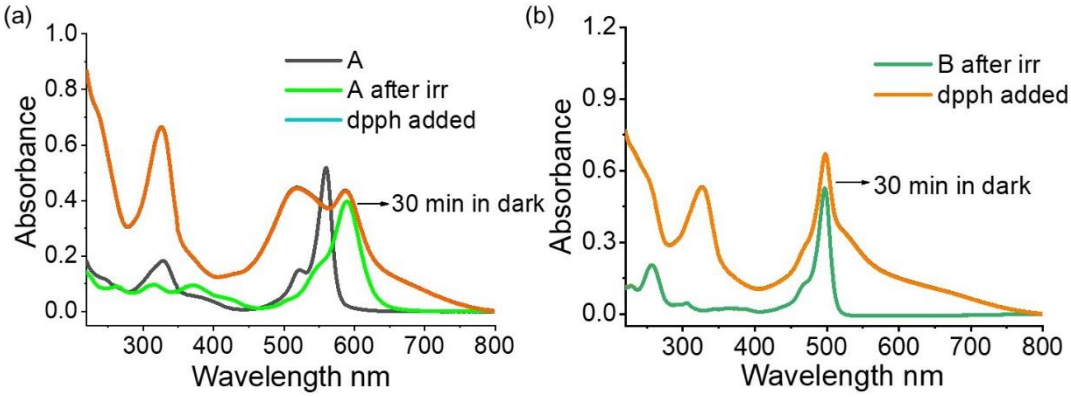

Figure 3.27. Changes in the UV-Vis absorption spectrum of a mixture of DPPH and photolyzed form of (a) **A** (3.2 µM) and (b) **B** (2.9 µM) in methanol under dark. 350W Xenon lamp with 550 nm bandpass filter was used for irradiation of **A** and (>475 nm) for **B** for a duration of 5 minutes.

It is worth discussing that the Mn centre is expected to be detached from the metal complex **A** post release of all COs and more than half of the contribution to the overall singlet oxygen quantum yield comes from the detached ligand itself. However, the photosensitization efficiency of the pristine ligand **P** is quite lower. Thus, to explain these contradictory observations, it is proposed that the enhanced singlet oxygen generation exhibited by the detached ligand **P** might have aroused from the presence of a paramagnetic Mn(II) species in the close proximity of the free ligand. To support our assumption, we calculated the fluorescence quantum yields for the ligand **P** and compared it to the photolyzed solution of

complex **A** which had afforded the free ligand **P** and an Mn(II) species. The fluorescence quantum yield for the pristine ligand **P** was calculated to be 0.4 while the photolyzed solution of **A** afforded a quantum yield of 0.25. The 1.6 times decrease in the quantum yield suggests a strong interaction between the paramagnetic Mn(II) species and the ligand **P**. This observation can be correlated to the fact that paramagnetic species tend to quench the fluorescence usually via photoinduced electron transfer (PET) between the singlet excited state of a fluorophore and the paramagnetic metal center.

3.2.4. TD-DFT calculations

To elucidate the photophysical mechanism of simultaneous CO release and singlet oxygen generation, time-dependent density functional theory (TD-DFT) calculations were performed with **A** and **B** in acetonitrile (Figure 3.26). At the outset, the highest occupied molecular orbital (HOMO) and lowest unoccupied molecular orbital (LUMO) distributions and the ΔE_{ST} values of all the compounds were investigated (Tables 3.1 to 3.4). Figures 3.27 and 3.28 represent the nature of HOMOs and LUMOs for **A** and **B**, respectively. In the case of **A**, HOMO is mainly located on the BODIPY ligand along with the phenyl linker whereas the HOMO–1 and HOMO–4 are on the π orbital of the BODIPY ligand with the aminophenyl linker and the (Mn−CO) dπ orbitals (Figure 3.27). On the other hand, the LUMO is on the π* orbital of the BODIPY. From the TD-DFT calculations, it is inferred that the lowest absorption band of **A** mainly resulted from a transition from the HOMO (π_{BODIPY}) to LUMO (π_{BODIPY}*) (94%, f: 1.86) at 482 nm (2.57 eV) and corresponds to the first singlet excited state ($S_0 \rightarrow S_1$) thereby representing the intraligand charge transfer (ILCT) character of the transition. The electron densities for the HOMO and LUMO being localized on the BODIPY core indicated a significant role for the BODIPY moiety on the photophysical properties of the complexes. Additionally, a MLCT band was calculated at 367 nm (3.379 eV) in **A** which originated from the HOMO−4 (Mn(dπ)-π_{CO}*) to the LUMO (π^*_{BODIPY}) level (89.4%, f: 0.094).

It is anticipated that the BODIPY moiety is the chromophore that absorbs the green/visible light and gets excited to its singlet excited state. The CO release from Mn complex involves an electronic interaction between the two components and is possibly triggered via a photoinduced electron transfer from the manganese center to the BODIPY core. Upon excitation, as an electron from the HOMO-based Mn gets transferred to the π cloud of BODIPY, the reduced electron density on the manganese centre reduces the strength of π-back bonding between manganese and CO resulting in the photo-dissociation of CO. Upon the

release of all CO ligands, the oxidized Mn centre in **A** is expected to dissociate from the ligand leading to regeneration of the corresponding BODIPY ligand.

To understand the underlying mechanism behind the achieved photosensitization with **A** and **B**, ΔE_{S1-T1} values were calculated from the TD-DFT calculations. The energies of the first triplet excited states were calculated to be 1.417 and 1.679 eV for **A** and **B**, respectively. The higher energy levels of the triplet excited states as compared to the energy required for the singlet oxygen generation (0.98 eV) indicated that these molecules could be potent triplet energy donors leading to production of singlet oxygen via energy transfer. In ac cordance with the experimentally depicted trends with singlet oxygen generation, we observed a lower value of ΔE_{S1-T1} = 1.158 eV for **A** in contrary to 1.449 eV obtained for **B**. The reduced ΔE_{S1-T1} could have helped to improve the photosensitization ability of **A** as compared to **B** and substantiates the importance of functionalization at α/β-positions than the *meso*-position of BODIPY. In order to rationalize the photosensitization taking place in **A** and **B**, their relative energy levels for both singlet and triplet states and their spin-orbit coupling constant (SOC values) were calculated. It was observed that **A** and **B** exhibited SOC values of 0.087 cm^{-1} and 0.01 cm^{-1} which are considered sufficient enough to induce ISC.

Table 3.1. Photophysical parameters for complexes **A** and **B** in acetonitrile. Fluorescence quantum yield was measured using fluorescein and cresyl violet as the reference in 0.1 M NaOH and methanol, respectively, for **A** and **B**.

Compound	λ_{abs}/nm	$\varepsilon \times 10^{5}/M^{-1}\ cm^{-1}$	λ_{em}/nm	Φ_f
Complex **A**	558	1.45	570	0.29
Complex **B**	499	1.09	510	0.023

Table 3.2. First eight excited singlet states of **A** calculated at the TD-B3LYP/Def2TVZP level of theory in acetonitrile. Only transitions with a weight above 10% are included.

State	λ (nm)	f_{osc} value	Transition	Weight
S1	481.6	1.865159497	192a -> 193a	0.941228
S2	400.1	0.000799543	188a -> 195a 188a ->196a 188a -> 197a	0.118149 0.126751 0.255263
S3	389.4	0.011879057	187a -> 196a	0.103809

			187a -> 197a	0.202406
			191a -> 197a	0.135161
S4	380.0	0.001675092	190a -> 197a	0.126368
			191a -> 193a	0.123570
S5	377.5	0.003183231	192a -> 194a	0.580367
S6	369.1	0.014679749	191a -> 193a 192a -> 194a	0.163450
			192a -> 195a	0.300676
			192a -> 196a	0.238508
				0.168571
S7	367.0	0.094564213	189a -> 193a	0.894683
S8	360.6	0.024109555	191a -> 200a	0.154430
			190a -> 200a	0.190722

Table 3.3. First ten excited singlet states of **B** calculated at the TD-B3LYP/Def2TVZP level of theory in acetonitrile. Only transitions with a weight above 10% are included.

State	λ (nm)	fosc value	Transition	Weight
S1	396.4	0.002542543	165a -> 173a	0.250775
			167a -> 173a	0.237757
S2	393.5	0.834474677	169a -> 170a	0.860219
S3	385.3	0.012923778	163a -> 173a	0.171335
			165a -> 173a	0.111859
			168a -> 173a	0.242484
S4	375.0	0.002446629	165a -> 173a	0.173912
			168a -> 172a	0.110627
			168a -> 173a	0.336209
S5	359.1	0.018518942	167a -> 170a	0.290418
			168a -> 170a	0.242330
S6	358.9	0.020331151	167a -> 170a	0.169293
			168a -> 176a	0.178067
S7	348.4	0.196076168	166a -> 170a	0.832916
S8	343.2	0.001892253	169a -> 171a	0.946363
S9	342.5	0.000103443	167a -> 170a	0.286236

			168a -> 170a	0.648754
S10	334.4	0.000144782	169a -> 172a	0.933791

Table 3.4. First three excited triplet states of **A** calculated at the TD-B3LYP/Def2TVZP level of theory in acetonitrile. Only transitions with a weight above 10% are included.

State	λ (nm)	Transition	Weight
T1	874.7	192a -> 193a	0.969482
T2	501.6	187a -> 197a	0.101335
		191a -> 196a	0.121470
		191a -> 197a	0.238765
T3	489.3	188a -> 195a	0.111574
		188a -> 196a	0.144803
		188a -> 197a	0.318065

Table 3.5. First three excited triplet states of **B** calculated at the TD-B3LYP/Def2TVZP level of theory in acetonitrile. Only transitions with a weight above 10% are included.

State	λ (nm)	Transition	Weight
T1	738.4	169a -> 170a	0.988451
T2	498.3	168a -> 172a	0.118109
		168a -> 173a	0.552862
T3	484.4	165a -> 173a	0.303239

Table 3.6. Calculated electronic transition energies for **A** and **B** using TD-DFT calculations.

	A	**B**
S1	2.575 eV	3.128 eV
S2	3.099 eV	3.151 eV
S3	3.184 eV	3.218 eV
T1	1.417 eV	1.679 eV
T2	2.472 eV	2.488 eV
T3	2.534 eV	2.560 eV

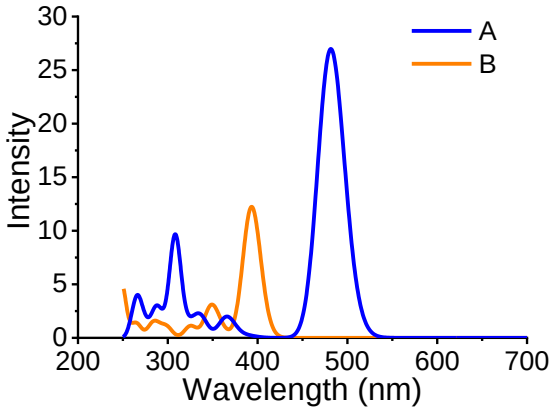

Figure 3.28. Simulated UV-Vis spectra of **A** and **B** in acetonitrile obtained using TD-DFT calculations.

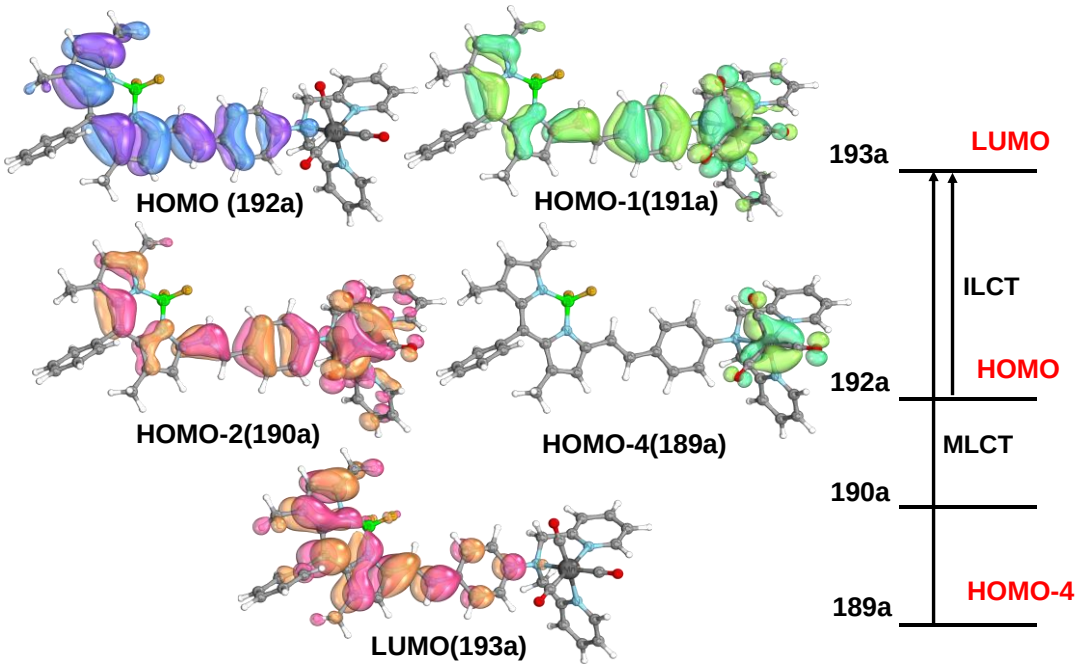

Figure. 3.29. The optimized geometry and pictorial representation of the frontier molecular orbitals of **A** in the ground state calculated using TD-DFT calculations in acetonitrile.

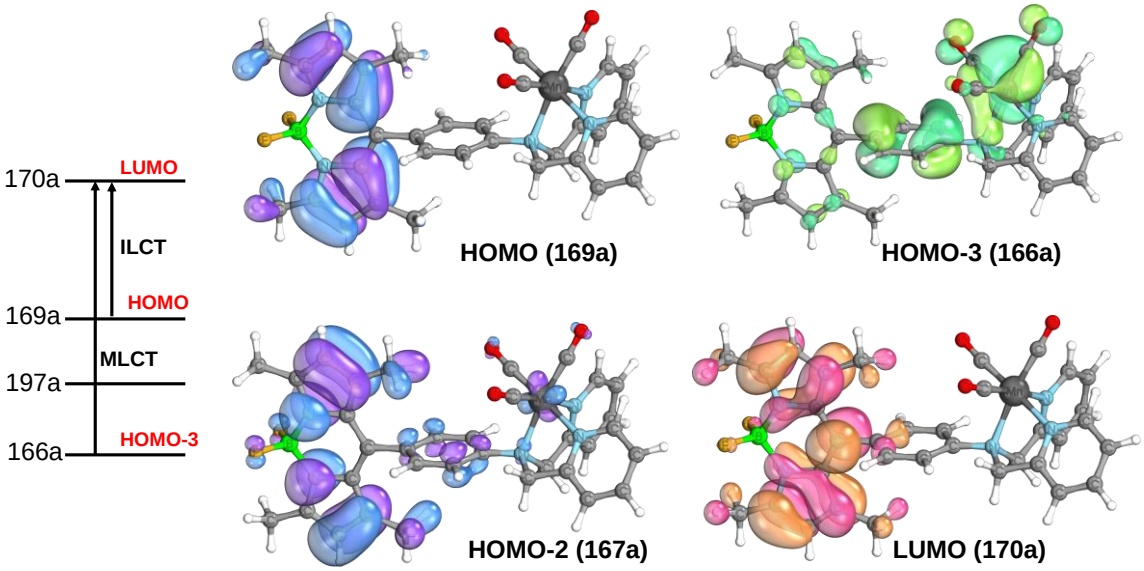

Figure 3.30. Pictorial representation of HOMOs and LUMO of **B** using TD-DFT calculations.

3.3. Part II. Peculiar shaped halogenated BODIPY C

3.3.1. Absorption and emission properties

The photophysical properties of the hexabrominated BODIPY **C** were then studied under a variety of conditions. Figure 3.31 shows the absorption and emission spectra of **C**, while its comparison with **S** and I_6 is stated in Table 3.7. The absorption maximum of **C** was observed at 526 nm in acetonitrile while that of the **I_6** and **S** are at 520 nm and 501 nm, respectively indicating that the BODIPY chromophores are not conjugated and there could be some amount of twisting between the BODIPY units. The red shifted absorption maxima of the brominated and iodinated BODIPYs relative to the parent BODIPY relies on the fact that halogen atoms have the potential to act as electron acceptors which facilitates their conjugation with the BODIPY core. The corresponding fluorescence maxima were observed at 510, 538 and 550 nm, respectively for **S**, **C** and **I_6** in acetonitrile.

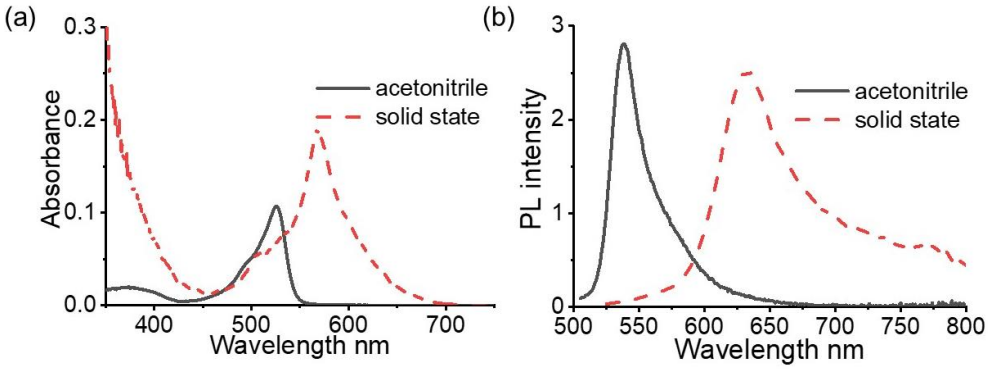

Figure 3.31. (a) UV-vis absorption and (b) fluorescence spectra of **C** (2.4 μM) in acetonitrile and in the solid state.

The hexabrominated BODIPY **C** was moderately fluorescent and the fluorescence quantum yield was found to be 0.26 in acetonitrile. On the other hand, $\mathbf{I_6}$ and **S** showed significantly low fluorescence quantum yields of 0.03 and 0.0005, respectively, in acetonitrile. The solid-state absorption spectrum of **C** exhibited a significant bathochromic shift with a peak at 568 nm and the emission maximum appeared at 632 nm indicating extensive aggregation in the solid state. The parent BODIPY **S** was observed to be non-emissive in the solid state. It is noteworthy that $\mathbf{I_6}$ exhibited an emission band at 604 nm which is hypsochromically shifted by 28 nm relative to **C**. This further indicates substantial π-conjugation in the solid state of **C**.

To obtain insights into the photophysical properties of **C**, we studied the effect of temperature on its absorption and emission behaviour. When a solution of **C** in acetonitrile was heated from 5 to 70 °C, it was observed that while the absorption spectrum remained unaffected, the emission intensity suffered a regular decrease in intensity (Figure 3.32). This decrease in emission intensity could be attributed to an increase in the free rotation of BODIPY units which further leads to non-radiative decay pathways of relaxation upon increasing the temperature.

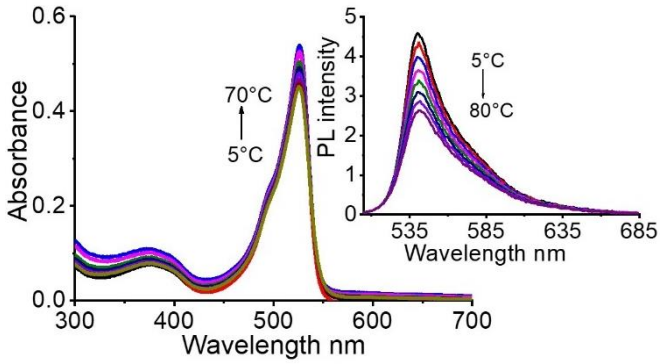

Figure 3.32. Changes in the UV-vis absorption and emission (inset) spectra of **C** (5.2 μM) as a function of varying temperature in acetonitrile. Excitation wavelength is 495 nm.

3.3.2. Aggregation studies

Next, we studied the aggregation of **C** in acetonitrile-water mixtures. **C**, which showed an absorption peak at 526 nm in acetonitrile, exhibited significantly broadened and blue-shifted absorption upon increasing water content. In 80% water-acetonitrile mixture, the long-wavelength absorption band was observed to undergo a blueshift and a new absorption band appeared at 455 nm (Figure 3.33). Moreover, the fluorescence intensity of **C** was observed to systematically decrease with the addition of water and we found almost complete quenching of the fluorescence in 90% water-acetonitrile mixture. These changes could be visually observed by a change in the fluorescence colour from bright yellowish green in acetonitrile to colourless in 90% water-acetonitrile mixture. On the basis of these observations, it is assumed that **C** exhibits aggregation-caused quenching (ACQ) which is a common phenomenon exhibited by organic dyes.

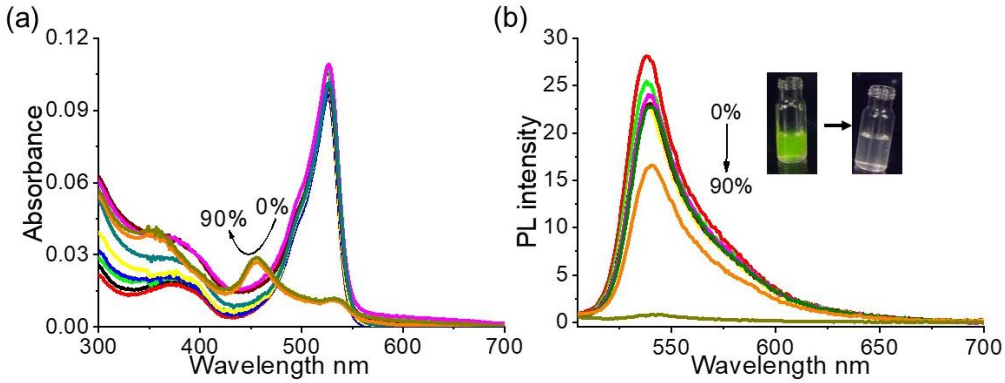

Figure 3.33. (a) UV-vis absorption and (b) emission spectra of **C** (2.6 µM) in acetonitrile-water mixtures. Excitation wavelength is 495 nm. Inset of (b) shows the visual fluorescence change of **C** in acetonitrile to aggregated state upon excitation with a UV lamp.

3.3.3. Photosensitized generation of singlet oxygen

As incorporation of heavy atoms leads to triplet state population which in turn generates singlet oxygen upon light irradiation, the $^1O_2$ generation capability of **C** was measured. The photosensitized reaction of $^1O_2$ with 1,5-dihydroxynaphthalene (DHN) yielding Juglone can be monitored by UV-Vis spectroscopy and this serves as a convenient technique to examine the formation of singlet oxygen. Hence the absorption spectra of a mixture of DHN and **C** in acetonitrile were recorded at regular intervals after light irradiation. As shown in Figure 3.34a, we observed a regular decrease in the absorbance of DHN at 293 nm along with the concomitant formation of a broad peak in the longer wavelength region around 420 nm upon

continued irradiation. These spectral changes indicate the conversion of DHN to Juglone, which suggested the formation of $^1O_2$. The singlet oxygen quantum yield of **C** was estimated using methylene blue as the reference and was found to be 0.59. The calculated $^1O_2$ quantum yield of **C** is significantly higher than that of **I$_6$** in acetonitrile which was observed to be 0.21. Furthermore, the singlet oxygen generation capability of the aggregates of **C** was investigated in 90% water-acetonitrile mixture. When an aerated mixture of DHN and the aggregates of **C** was irradiated, it was surprising to observe that there was minimal formation of Juglone thereby suggesting negligible generation of $^1O_2$ (Figure 3.34b).

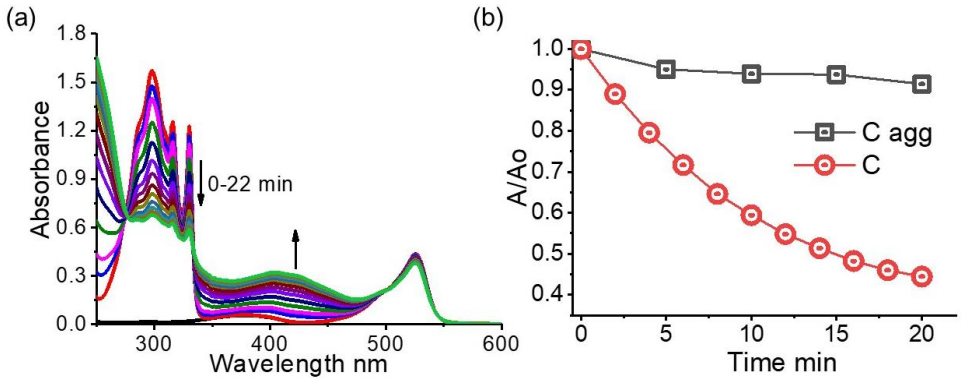

Figure 3.34. (a) Changes in the UV-Vis absorption spectrum of a mixture of 1,5-dihydroxynaphthalene (DHN, 0.24 mM) and **C** (5.0 µM) in acetonitrile. (b) Relative rate of decrease of the absorbance of DHN (0.47 mM) at 393 nm in presence of **C** in acetonitrile and **C** aggregates in 9:1 water: acetonitrile as a function of irradiation time.

Figure 3.35 shows an overview of the photophysical properties of **C**, **I$_6$** and their aggregates. The photophysics shown by **S**, I$_6$ and **C** differ drastically from one another despite having similar structures and the key behind these interesting observations is the presence of heavy atoms which are deemed to be quite similar in nature. While heavy atoms are capable of facilitating intersystem crossing and increase the $^1O_2$ quantum yield, they also have significant enough sizes to effectively control the twisting of BODIPY cores. It is hypothesized that owing to the smaller size of bromine than iodine, **C** is able to adopt a nearly planar conformation in the course of the aggregation process. This inference is based on the observation that the UV-Vis absorption spectra of **C** showed a blue shift as the percentage of water exceeded 80% which is indicative of the extensive π-π interactions between the BODIPY moieties. Such typical H-aggregation is usually observed in highly planar organic molecules. This hypothesis has been pictorially demonstrated in Figure 3.36.

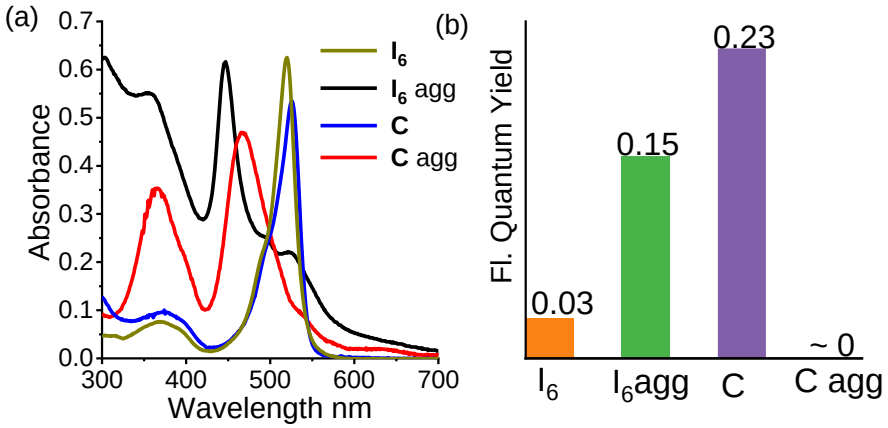

Figure 3.35. (a) UV-Vis absorption spectra and (b) fluorescence quantum yields of **C** and **I6** in acetonitrile and their aggregates in 9:1 water: acetonitrile.

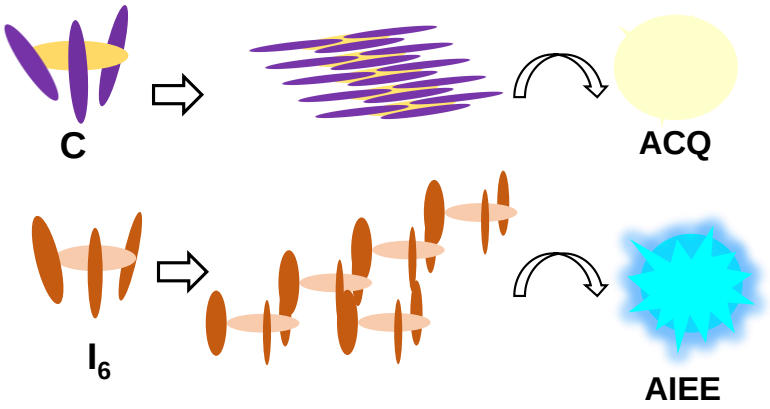

Figure 3.36. Schematic representation of aggregation of **C** and **I6**.

A chromophore upon light absorption majorly relaxes via fluorescence emission, heat or photochemical reactions. It is presumed that as fluorescence and photochemical reactions are suppressed upon aggregation in the case of **C**, an exclusive conversion from light to heat is highly probable. This might potentially point towards developing highly efficient BODIPY based photothermal nanomaterials. Also, as these BODIPY chromophores are structurally peculiar, it is difficult to precisely comment on the type of aggregates they typically form. The electron cloud of the starting BODIPY dye **S** has a substantial role to play towards forming the indicative *J*-aggregates as reported elsewhere as the repulsions between the electron clouds of **S** owing to the presence of aromatic units would have pushed the BODIPY units to slip stack in an offset manner. On the other hand, bromine substitution could have possibly overcome the steric effect as it is less bulky than iodine. Furthermore, owing to the presence of halogen bonds

and other intramolecular interactions, the **C** aggregates were able to attain the spectral features of typical *H*-aggregates.

3.3.4. TD-DFT Calculations

Time-dependent density-functional theory (TD-DFT) calculations were performed to substantiate our model (Figure 3.37 and Tables 3.8 to 3.12). It was observed that the optimized geometry and the orbitals associated for **C** and **I$_6$** are quite similar. In both the compounds, the LUMOs are delocalized over two of the BODIPY cores with a small contribution from the third. Moreover, the HOMOs of **C** and **I$_6$** delocalize over the BODIPY core and the associated halogens. Next, we calculated the spin orbit coupling (SOC) matrix elements in order to rationalize the intersystem crossing in **C** and **I$_6$**. The vertical excitation energies for low singlet and triplet states at the optimized S_1 geometries and the SOCs between the involved singlet and triplet excited states are listed in Figure 3.37. Intersystem crossing is majorly governed by small singlet-triplet energy gaps and significant SOC. Based on the calculations, we propose S_1-T_2 (SOC value of 1.549 cm^{-1}) and S_1-T_1 (3.314 cm^{-1}) to be the main deactivation channels for **C** and **I$_6$**, respectively. The almost similar energy gaps (ΔE_{ST}) between S_1-T_1 and S_1-T_2 for **C** (S_1-T_1 = 0.799 eV, S_1-T_2 = 0.794 eV) and **I$_6$** (0.789 eV, S_1-T_2 = 0.78 eV) pushes the SOCs to be the deciding factor for the triplet deactivation channel.

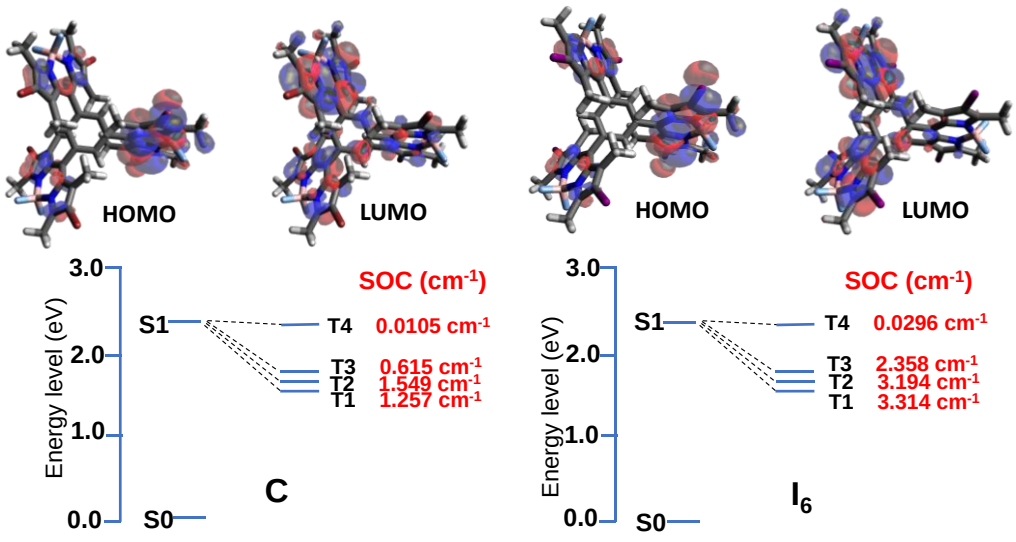

Figure 3.37. Orbital representation of HOMOs and LUMOs associated with **C** and **I$_6$** and the calculation of spin orbit coupling between the involved excited states.

Table 3.7. Photophysical properties of various BODIPY molecules.

	λ_{abs} (nm)			λ_{em} (nm)			ϕ_f		ϕ_Δ	
	a	b	c	a	b	c	a	b	a	b
O	501	550	-	510	505	-	0.64	NA	0.008	NA
S	501	502	-	510	550	-	0.0005	0.013	Photobleaching	Photobleaching
C	526	468	568	538	NA	632	0.23	~0	0.59	Very low
I_6	520	506	542	550	566	604	0.03	0.15	0.21	0.82

a In solution. b As aggregates in aqueous medium. c solid state.

Table 3.8. Main optimized geometrical parameters of **C** and **I_6** at B3LYP/def2-TZVP level. For **C**.

	C-X bond length (A ^{o}) where X = Br/I			Angle between various BODIPY units			Angle between central phenyl ring and BODIPY(^{o})	
	C	**I_6**		**C**	**I_6**		**C**	**I_6**
C1-X1	2.08796	1.88834	BDP1-BDP2	60.27	60.29	Ph-BDP1	82.75	82.94
C2-X2	2.08863	1.88844	BDP2-BDP3	59.80	60.34	Ph-BDP2	83.08	82.40
C3-X3	2.08827	1.88840	BDP1-BDP3	60.21	60.42	Ph-BDP3	82.27	81.75
C4-X4	2.08821	1.88855						
C5-X5	2.08832	1.88856						
C6-X6	2.08910	1.88813						

Table 3.9. First eight excited singlet states of **C** calculated at the TD-B3LYP/Def2TVZP level of theory in acetonitrile. Only transitions with a weight above 15% are included.

State	λ (nm)	fosc value	Transition	Weight
S1	516.9	0.001507425	314a -> 315a	0.652015
S2	514.3	0.008439558	312a -> 315a	0.391886

			313a -> 315a	0.247839
			313a -> 316a	0.223805
S3	513.0	0.009845392	312a -> 316a	0.516130
			313a -> 316a	0.261702
S4	493.8	0.020690493	314a -> 316a	0.281959
			314a -> 317a	0.456175
S5	492.1	0.018558117	313a -> 317a	0.502319
			312a -> 315a	0.231752
S6	490.8	0.044808630	312a -> 317a	0.485453
			313a -> 315a	0.263965
S7	439.0	0.212536712	313a -> 317a	0.362499
			312a -> 315a	0.230738
S8	438.0	0.217794685	314a -> 317a	0.368116
			312a -> 316a	0.161745

Table 3.10. First three excited triplet states of **C** calculated at the TD-B3LYP/Def2TVZP level of theory in acetonitrile. Only transitions with a weight above 15% are included.

State	λ (nm)	Transition	Weight
T1	874.7	313a -> 315a	0.397115
		312a -> 315a	0.218436
T2	501.6	314a -> 316a	0.474817
		314a -> 317a	0.189615
T3	489.3	312a -> 316a	0.264479
		313a -> 316a	0.239871
		312a -> 316a	0.264479

Table 3.11. First eight excited singlet states of **I_6** calculated at the TD-B3LYP/Def2TVZP level of theory in acetonitrile. Only transitions with a weight above 15% are included.

State	λ (nm)	fosc value	Transition	Weight
S1	481.6	0.003580304	368a -> 369a	0.795621
S2	400.1	0.006112414	366a -> 369a	0.395149
			367a -> 370a	0.390335

S3	389.4	0.009072631	366a -> 370a 367a -> 370a 367a -> 369a	0.467691 0.212445 0.169041
S4	380.0	0.022963081	368a -> 370a 368a -> 371a 366a -> 370a	0.337032 0.410952 0.180787
S5	377.5	0.021126197	367a -> 371a 366a -> 369a	0.478135 0.285203
S6	369.1	0.061452921	366a -> 371a 367a -> 369a	0.463952 0.279801
S7	367.0	0.178551693	366a -> 369a 367a -> 371a	0.201815 0.402649
S8	360.6	0.169389438	368a-> 371a	0.392266

Table 3.12. First three excited triplet states of **I_6** calculated at the TD-B3LYP/Def2TVZP level of theory in acetonitrile. Only transitions with a weight above 15% are included.

State	λ (nm)	Transition	Weight
T1	774.9	367a -> 369a 366a -> 369a	0.390369 0.197499
T2	770.6	366a -> 369a 367a -> 370a	0.197769 0.202007
T3	769.0	368a -> 370a 368a -> 371a 366a -> 370a	0.402870 0.271909 0.189201

3.4. Part III: Salicylideneimine boron difluoride-based compounds D-G

3.4.1. Experimental and theoretical insights

Structures optimized with density functional theory (DFT) calculations reveal that the salicylaldehyde moiety is not coplanar with aniline moiety in **D**-**G** and a dihedral angle of ~40º is observed between these units (Figures 3.38 and Tables 3.13-3.14). For all the molecules, N–B and O–B bond length was ~1.62 Å and 1.47 Å, respectively thereby indicating that boron

forms a much stronger covalent bond with oxygen as compared to nitrogen. Figure 3.39 shows the experimental absorption and emission spectra of **D**-**G** in acetonitrile and Table 3.15 summarizes their photophysical properties. We observed the lowest energy absorption peak for **D**-**G** at 368, 360, 390 and 387 nm, respectively, whereas the TD-DFT calculations showed the corresponding transitions at 397, 358, 405 and 408 nm, respectively (Figure 3.39 and Table 3.16). The absorption maxima for **F** and **G** were observed to be bathochromically shifted and suggests that the iodo-functionalization of the salicylaldehyde moiety, as compared to the aniline moiety, has a greater influence on the electronic properties of the boranils. We also observed a similar bathochromic shift in the computed UV-Vis spectra for **F** and **G** in acetonitrile (Figure 3.39).

The orbitals associated with lowest energy transitions are HOMO→LUMO for **D**-**F**, whereas the dominant contribution arises from the HOMO→LUMO+1 transition for **G** (Figures 3.38c and 3.40). The orbital contributions of major peaks for **G** are tabulated in Table 3.17. As shown in Figure 3.41, it is evident that the energy gap between LUMO and LUMO+1 for **G** is smaller as compared to **D**-**F**. Owing to this small energy gap along with the orbital symmetries, HOMO→LUMO+1 transition becomes dominant in the case of **G**.

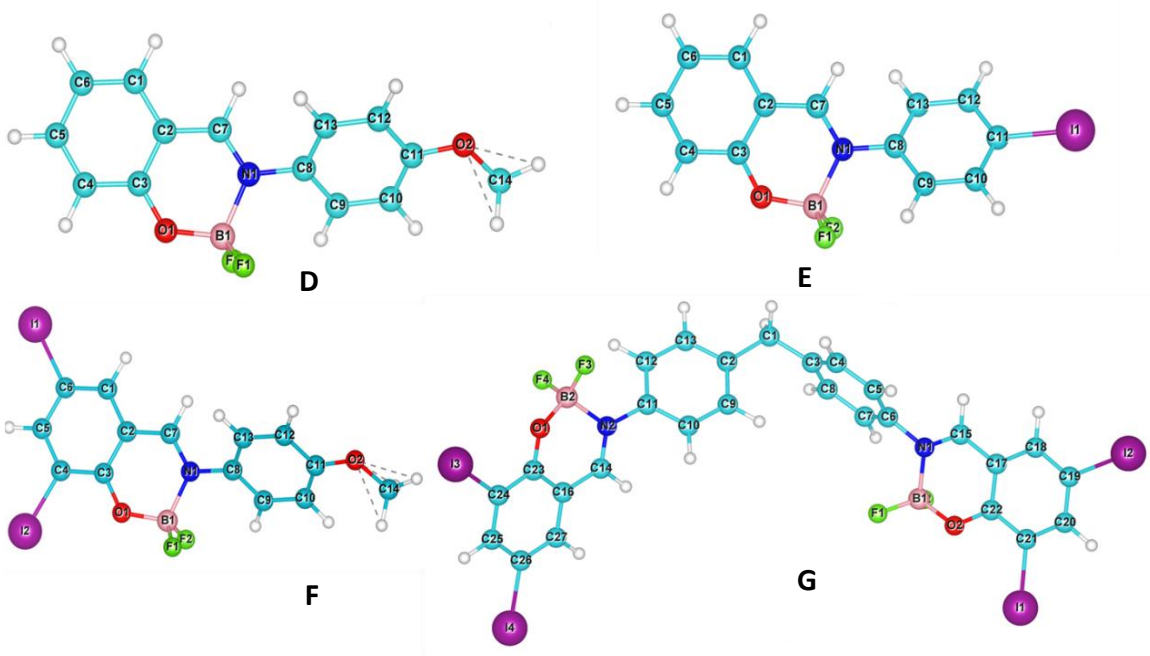

Figure 3.38. Optimized geometries of molecule **D-G** at B3LYP/def2-TZVP level of theory.

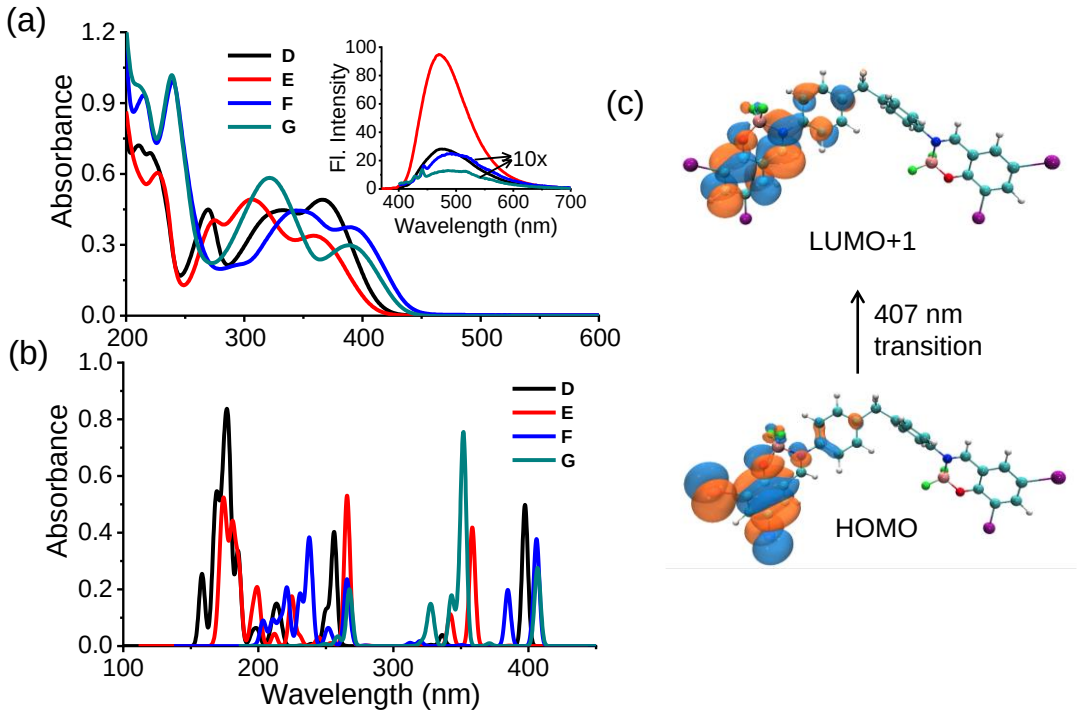

Figure 3.39. (a) Experimental UV-Vis absorption and (inset) emission spectra of **D** (30 μM), **E** (30 μM), **F** (91 μM) and **G** (50 μM) in acetonitrile. Excitation wavelength, 366, 359, 392 and 390 nm for **D-G**, respectively. (b) UV-Vis electronic spectra of **D-G** in acetonitrile obtained from the time-dependent density functional theory (TD-DFT) calculations. (c) The optimized structure and the molecular orbitals associated with the electronic transitions at the lowest energy peak for **G** at 407 nm.

The emission maximum of **D-G** was experimentally observed at 473, 471, 490 and 495 nm, respectively and the fluorescence quantum yield was determined to be 0.0172, 0.0061, 0.0027 and 0.0009 for **D-G**, respectively. The observation of red-shifted emission maxima and negligible fluorescence for **F** and **G** (having the iodo-substitutions on the salicylaldehyde moiety) as compared to **D** and **E** (having the iodo-substitutions on the aniline moiety) substantiates the effect of functionalization of salicylaldehyde moiety on the electronic properties.

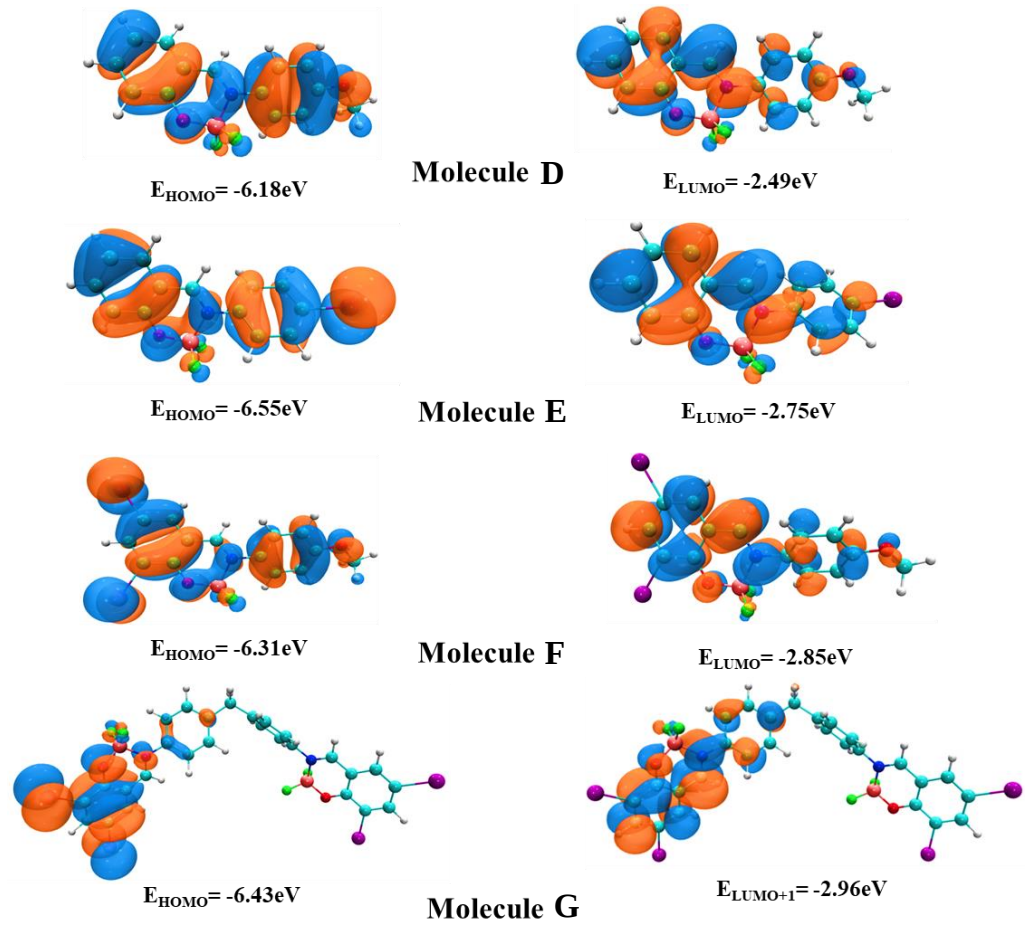

Figure 3.40. Molecular orbitals associated with primary excitation of molecule **D-G** along with the energies in eV.

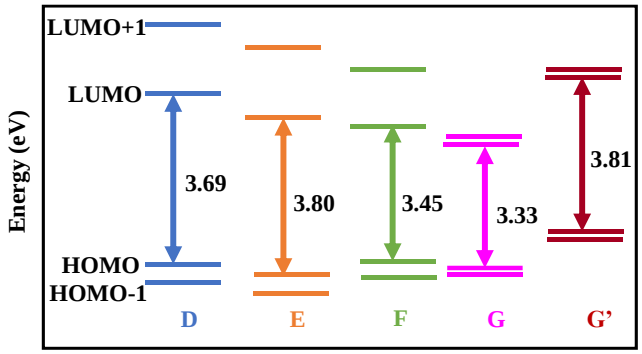

Figure 3.41. The frontier orbital energies for all the considered molecules along with HOMO–LUMO energy gap in eV.

To understand the effect of boron on the structure and electronic properties of these compounds, we computed the structure of the imine **G'** which is devoid of the BF_2 moiety (Figure 3.42). A comparison of the computed electronic spectra of **G'** and **G** shows that the peak at ~400 nm is absent in **G'**. Thus, it is inferred that boron not only contributes in increasing

the planarity of the chromophoric subunit of **G**, but also contributes in reducing the HOMO–LUMO/LUMO+1 energy gaps. As displayed in the orbital diagram (Figures 3.43 and 3.44), the orbital energies are deeply affected on incorporating boron and a significant stabilization of the frontier orbitals were observed. LUMO and LUMO+1 were stabilized by 0.86 and 0.89, eV respectively. However, this stabilization was lower for HOMO and HOMO+1 wherein the calculated values are 0.38 eV and 0.40 eV, respectively. It was also observed that the HOMO–LUMO gap (ΔE) was lowered by 0.48 eV giving rise to an additional peak at 407nm.

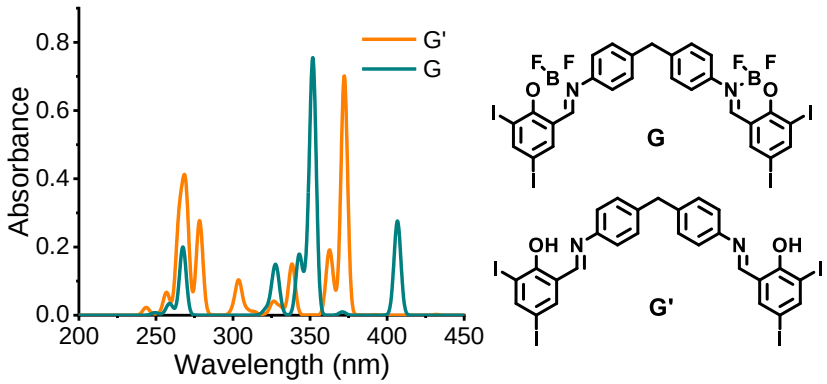

Figure 3.42. Chemical structure and the UV-Vis electronic spectra of **G'** and **G** obtained from the TD-DFT calculations.

We were also interested in studying the role of iodine on the electronic spectra of **G**. This was elucidated from the contribution of iodine towards the HOMO/LUMO+1 of **G**. For the lowest energy peak associated with the HOMO→LUMO+1 transition, the contribution of iodine in HOMO is significant whereas its contribution is negligible in LUMO+1. This indicates that HOMO→LUMO+1 excitation can effectively move the electronic distribution from iodine to other parts of the molecule. All the other orbitals contributing significantly to the electronic transitions are shown in Figure 3.43 and it is evident that iodine is playing a significant role in all the transitions. The contribution of iodine in the electronic spectra has a great significance because being a heavy element, the spin-orbit coupling and vibronic effects on the electronic spectra are expected to broaden the observed peaks. These effects are not included in the conventional TD-DFT spectra.

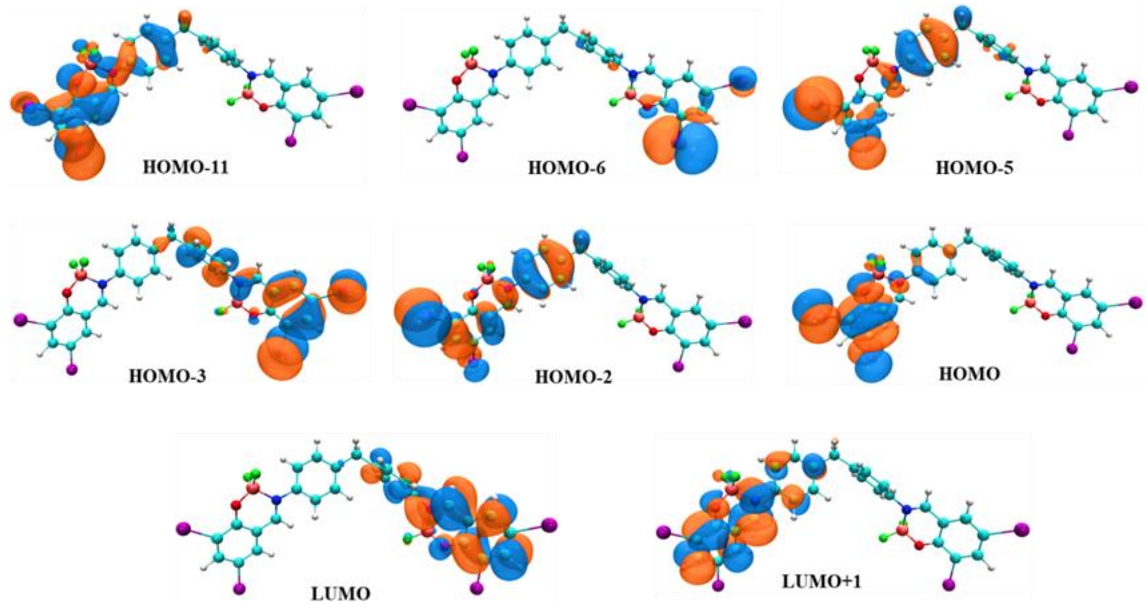

Figure 3.43. The molecular orbitals associated with the dominant electronic transitions for molecule **G**. The surfaces are generated with an isovalue 0.02 a.u.

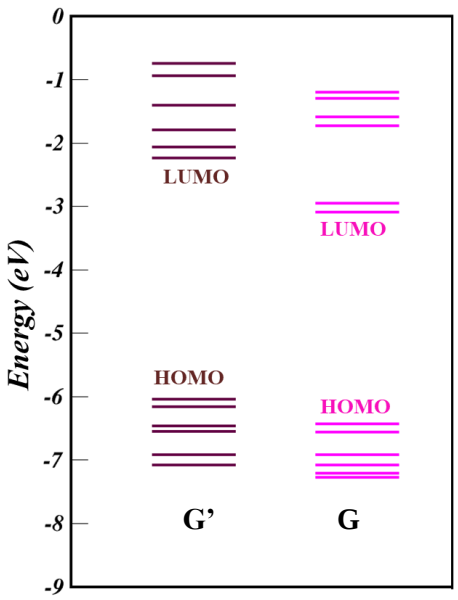

Figure 3.44. Comparison of the frontier orbital energies of **G** and **G′** (without BF_2).

After establishing the structure and electronic properties of the boranils, we set out to examine their photostability by monitoring the changes in the absorption spectrum of **D-G** upon light irradiation. As shown in Figure 3.45, we observed significant photobleaching for **D-F** under our experimental conditions whereas negligible changes were observed in the absorption spectrum of **G** upon irradiation thereby indicating its photostability. It is reported that boranils are prone to deboronation[20]. On a similar note, the observed changes in the

absorption spectra could be attributed to the elimination of the BF_2 moiety resulting in the formation of the corresponding imines.

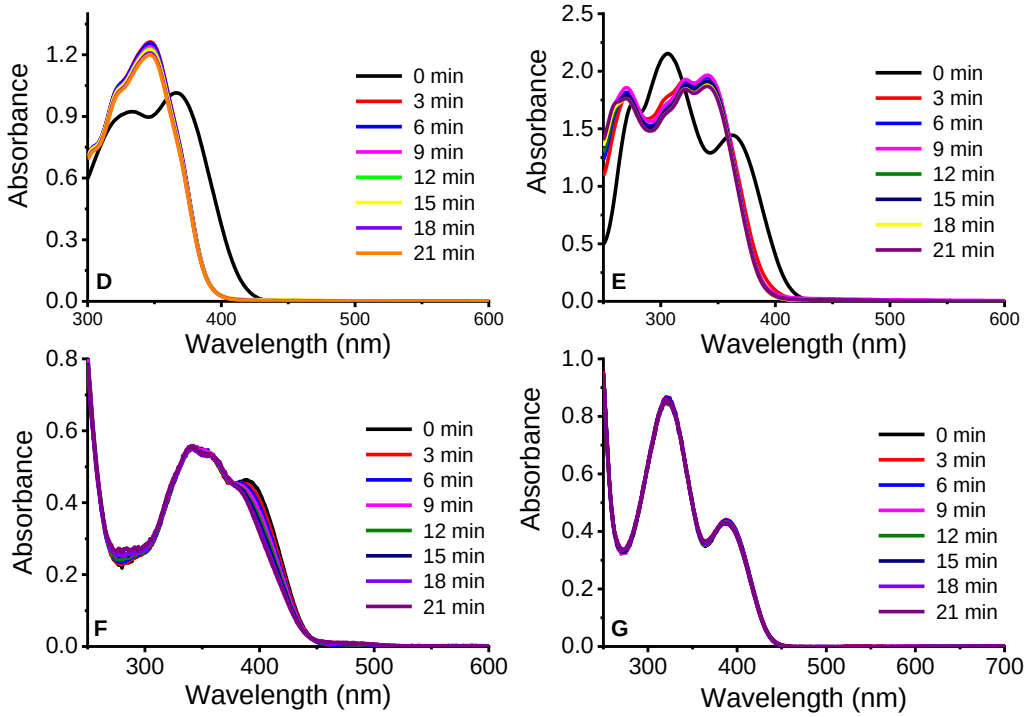

Figure 3.45. Changes in the UV-vis absorption spectrum of **D** (0.063 mM), **E** (0.129 mM), **F** (0.112 mM) and **G** (0.073 mM) in acetonitrile upon irradiation.

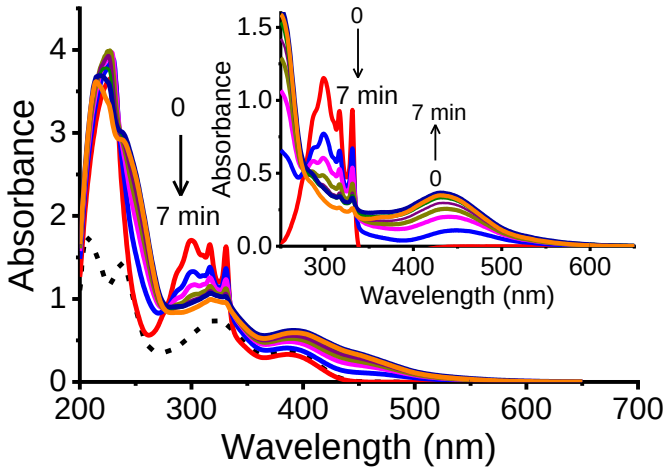

Figure 3.46. The changes in the UV-Vis absorption spectrum of a mixture of 1,5-dihydroxynaphthalene (DHN, 0.18 mM) and **G** (36 μM) in 9:1 acetonitrile: ethanol as a function of irradiation time. Black dotted line shows the absorption spectrum of **G**. Inset shows the corrected absorption spectra wherein the absorption of **G** was subtracted from that of a mixture of DHN and **G** for clarity.

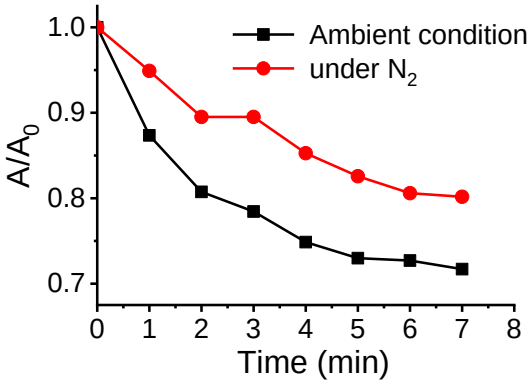

Figure 3.47. The decrease in the absorbance of DHN (0.037 mM) at 300 nm in the presence of **G** (0.043 mM) in 9:1 acetonitrile:ethanol as a function of irradiation time under ambient conditions and an atmosphere of nitrogen.

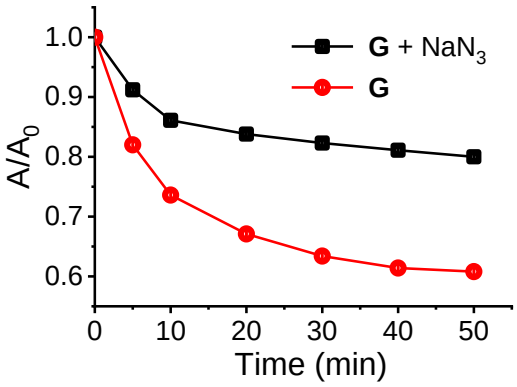

Figure 3.48. The decrease in the absorbance of DHN (2.247 mM) at 300 nm in the presence of **G** (0.039 mM) in 9:1 acetonitrile:ethanol as a function of irradiation time in the absence and presence of sodium azide (1 mM) with a 400 nm cut-off filter.

3.4.2. Photosensitized generation of singlet oxygen

As the molecule **G** was found to be photostable, we were interested in evaluating its photosensitization properties. 1,5-Dihydroxynaphthalene (DHN) was selected as a substrate for singlet oxygen because of its compatibility with both the organic and aqueous media. Moreover, the photosensitized reaction of DHN with $^1O_2$ yielding Juglone can be conveniently monitored by UV-Vis spectroscopy. To study the photosensitization properties of **G**, a solution containing a mixture of DHN and **G** in acetonitrile-ethanol was irradiated, and the absorption spectra were recorded at regular intervals. As shown in Figure 3.46, we observed a regular decrease in the absorbance of DHN at 298 nm along with the concomitant formation of a broad peak in the longer wavelength region upon continued irradiation. These spectral changes

indicate the conversion of DHN to Juglone which in turn suggests the formation of $^1O_2$ thereby implying the photosensitization effect of **G**.

To ascertain the role of singlet oxygen in the photooxidation process, we carried out control experiments in the presence of sodium azide and in the absence of oxygen. It was observed that the decrease in the absorbance of DHN was significantly low under these conditions (Figures 3.47 and 3.48) and supported our inference of the generation of $^1O_2$ by **G**. The singlet oxygen quantum yield of **G** was calculated by using methylene blue as a reference and was found to be 0.94. The efficient generation of singlet oxygen by **G** is attributed to the heavy-atom effect which favours the formation of triplet states through spin-orbit coupling.

Table 3.13. Main optimized geometrical parameters of **D-F** at B3LYP/def2-TZVP level.

Bond length (Å)	**D**	**E**	**F**
B(O1-C3)	1.314	1.313	1.307
B(O1-B1)	1.471	1.470	1.475
B(B1-N1)	1.622	1.626	1.623
B(B1-F1)	1.374	1.372	1.372
B(B1,F2)	1.385	1.381	1.382
B(N1,C7)	1.300	1.301	1.297
B(N1,C8)	1.429	1.430	1.431
Bond angle (º)	**D**	**E**	**F**
A(F1,B1,F2)	112.85	112.79	113.58
A(C3,O1,B1)	125.81	125.83	126.15
A(O1,B1,N1)	109.14	108.78	108.63
A(B1,N1,C8)	120.07	120.16	119.96
A(C7,N1,C8)	119.50	119.38	119.63
D(C7,N1,C8,C9)	-142.42	135.41	-140.12

Table 3.14. Main optimized geometrical parameters of **G** at B3LYP/def2-TZVP level.

Bond length (Å)		Bond length (Å)	
B(C1,C2)	1.524	B(C1,C3)	1.507
B(N1,C6)	1.431	B(N2,C11)	1.427
B(N1,C15)	1.298	B(N2,C14)	1.297
B(N1,B1)	1.628	B(N2,B2)	1.624

B(B1,F1)	1.370	B(B2,F3)	1.365
B(B1,F2)	1.381	B(B2,F4)	1.383
B(B1,O2)	1.473	B(B2,O1)	1.471
B(O2,C22)	1.307	B(O1,C23)	1.311
B(I1,C21)	2.101	B(I3,C24)	2.101
B(I2,C19)	2.110	B(I4,C26)	2.108
Bond angle (º)		Bond angle (º)	
A(C2,C1,C3)	115.54		
A(C6,N1,C15)	120.364	A(C11,N2,C14)	120.833
A(C6,N1,B1)	118.73	A(C11,N2,B2)	120.09
A(N1,B1,O2)	107.79	A(N2,B2,O1)	107.37
A(F1,B1,F2)	112.82	A(F3,B2,F4)	113.17

Table 3.15. Experimental absorption and emission properties of **D**-**G**.

Compound	λ_{abs} (nm)	ε ($M^{-1}cm^{-1}$)	λ_{em} (nm)	ϕ_F ($\times 10^{-2}$)
D	269, 330, 368	16700, 15200, 16000	473	1.7
E	225, 272, 306, 360	25000, 18900, 17250, 11100	471	0.61
F	239, 348, 390	10600, 4800, 4100	490	0.27
G	239, 321, 387	20300, 11700, 6000	495	0.09

Table 3.16. Calculated λ_{max} values for **D-G** in gas phase and acetonitrile with the associated shift.

Molecule	λ_{max} (nm)		Shift (nm)	Experimental value (nm)
	Gas	Acetonitrile		
D	367	397	30	368
E	359	358	1	360
F	404	405	1	390
G	407	408	1	387

Table 3.17. UV-Vis electronic spectra: excitation wavelengths, oscillator strengths (*f*) & dominant electronic transitions of **G** in acetonitrile.

S. No.	λ (nm)	*f*	Main Transitions
1	407.0	0.204	H → L+1(75.6%)
2	351.8	0.728	H-3 → L (30.2%) H-2 → L+1(54.4%)
3	342.9	0.175	H-3 → L (42.2%) H-2 → L+1(20%)
4	326.7	0.086	H-6 → L (51.2%) H-5 → L (22.0%)
5	267.6	0.114	H-11 → L+1(78.8%)

3.5. Part-IV: Boranil functionalized Polyethyleneimine H

3.5.1. Photophysical properties

The absorption spectrum of **H** was recorded in deionised water (Figure 3.49) and the appearance of long wavelength peaks from 400 to 500 nm clearly indicates the presence of aromatic units in the polymer backbone which may be attributed to n→π* and π→π* transitions occurring in the diiodosalicylideneimine-boron scaffold. **H** was observed to be non-fluorescent indicating heavy atom effect of iodine atoms that populates the triplet excited states through spin-orbit coupling thus exhibiting photosensitization properties.

In order to evaluate the photosensitization properties of **H** in solution, its stability was monitored in water via UV-Vis absorption spectroscopy over a period of few days. As shown in Figure 3.50, we observed change in the absorption spectrum of **H** after around 3 days. The observed instability could be ascribed to deboronation in the polymer in the presence of light. The loss of the long wavelength band in the UV-Vis spectra further validates the possibility of deboronation. Since, the polymer **H** was unstable in solution, we did not proceed to investigate its photosensitization abilities.

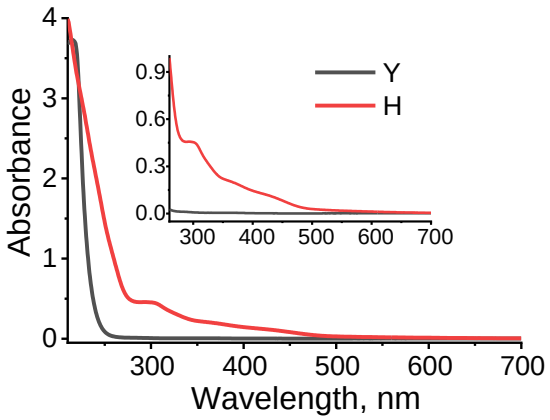

Figure 3.49. UV-vis absorption spectra of polyethyleneimine, **Y** and polymer, **H**. Inset shows zoomed region between 300-700 nm wherein only **H** shows prominent absorption.

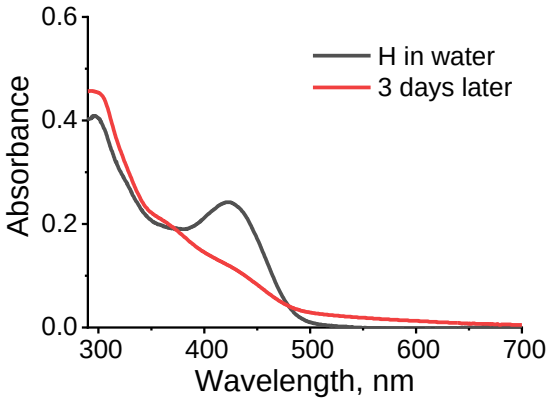

Figure 3.50. Change in the UV-Vis absorption spectrum of polymer, **H** in water under ambient conditions upon ageing.

3.6. Conclusion

In conclusion, we have discussed the photophysical properties of the synthesized compounds with respect to their absorption, emission and singlet oxygen generation abilities and our results underline the importance of appropriate functionalisation on the BODIPY/boranil skeletons. The ease of synthetic functionalization at meso and pyrrolic positions of the BODIPY resulted in diverse structural and photophysical features. We demonstrate that facile CO release and singlet oxygen generation could be simultaneously achieved from the single component photoCORMs **A** and **B** upon red light irradiation. High CO quantum yield (ϕ_{CO}) of 0.42 was obtained with complex **A.** Incorporation of BODIPY onto the Mn-CO releasing core was able to push the photorelease of CO towards biologically relevant absorption window (up to 600 nm) making it suitable for biological applications.

While compound **C** and its iodo-substituted counterpart **I_6** have structural and electronic similarities, the properties of their aggregates were completely different. While **I_6** aggregates were observed to show aggregation induced emission enhancement, **C** aggregates showed complete quenching of fluorescence. On the other hand, **C** aggregates exhibited drastic decrease in the photosensitization ability contrary to the **I_6** aggregates which showed significant enhancement in triplet state population. It is quite surprising to observe such vast differences in the behaviour patterns with bromine and iodine substitution on the same chromophoric core. These fundamental insights might help to understand the effect of halogenation on excited state behaviours and molecular packings in the heavily pursued aggregated state of BODIPY dyes.

While molecules **D-F** were unstable in solution, compound **G** showed good photostability and exceptionally high singlet oxygen quantum yield of 94% owing to the presence of heavy atoms. On the other hand, boranil functionalized polymer **H** absorbed in the visible region of electromagnetic spectrum but was found to be unstable in solution.

3.7. Experimental Section

3.7.1. Materials and Methods

All experiments were carried out at room temperature (25 ± 1 °C) unless otherwise mentioned. Absorption spectra were recorded on a Shimadzu UV-Vis spectrophotometer in 3 mL quartz cuvettes having a path length of 1 cm. Fluorescence spectra were recorded on Fluorolog 3−221 fluorimeter equipped with 450 W Xenon lamp or an Edinburgh FS5 spectrofluorometer. Photosensitization experiments were carried out using a 350 W Xenon arc lamp (Oriel instruments) with a 345 or 475 nm cut-off filter and 550 nm bandpass filter (Newport Corporation). For headspace GC-TCD analysis, ThermoScientific TRACE 1300 GC series systems with TCD (Thermal Conductivity Detector) detector and M sieve column were used. 100 ppm of gas standard mixed with helium was adopted for gas quantification. All solvents were distilled and dried before use.

1,5-Dihydroxynaphthalene was purchased from TCI Chemicals and used as received. Quinine sulphate and rhodamine 6G was purchased from Sigma-Aldrich and used as received. Solvents were distilled before use. Distilled water was used for all experiments.

3.7.2. Calculation of fluorescence quantum yield

Fluorescence quantum yield were calculated using formula:

$$\phi_F(sample) = \phi_F(ref) \times \frac{I(sample) \times OD(ref) \times n^2(sample)}{I(ref) \times OD(sample) \times n^2(ref)}$$

where I is the integrated intensity, OD is optical density at the excitation wavelength, n is the refractive index of the solvent, ref stands for reference standard i.e. quinine sulphate in 0.1 M H_2SO_4 (ϕ_f = 0.577) and rhodamine 6G in ethanol (ϕ_f = 0.95).

3.7.3. Investigation of singlet oxygen generation

A solution of the desired compound in acetonitrile was taken in a 3 mL cuvette and an absorption spectrum was recorded. To this solution, an aliquot of DHN or DPBF was added and absorption spectrum was recorded. The sample was then irradiated using a 350 W Xenon arc lamp with a 345 nm/475 nm cut-off filter or 550 nm bandpass filter and the progress of the reaction was monitored by recording UV-Vis spectra at regular intervals.

3.7.4. Determination singlet oxygen quantum yield

Singlet oxygen quantum yield was calculated with reference to methylene blue (MB) in ethanol which is reported to have a quantum yield of 0.52. Singlet oxygen quantum yield was calculated according to the equation:

$$\phi_\Delta(sample) = \phi_\Delta(ref) \times \frac{m\ (sample)}{m(ref)} \times \frac{F(ref)}{F(sample)}$$

where m is the slope of difference in change in absorbance of DHN (at 297 nm) or DPBF (at 410 nm) with the irradiation time, and F is the absorption correction factor, which is given by $F = 1 - 10^{-OD}$.

3.7.5. Calculation of half-life ($t_{1/2}$) and Rate Constant (k)

The rate constant of CO release from **A** was calculated by fitting data to the first order kinetic equation $\ln[A]/[A_o] = -kt$ where [A] and $[A_o]$ are the absorbance at time t and t = 0 respectively and k is the rate constant. The natural logarithm of the absorption value of **A** at 560 nm was plotted against time. Then the linear curve was plotted and the value of slope was calculated which gives the rate constant. Half- life ($t_{1/2}$) was calculated using the equation $t_{1/2} = \ln 2/k$ wherein k is the rate constant. Half-life for complex **Z** was also calculated by plotting the natural logarithm of the absorption value 303 nm against time in a similar manner.

3.7.6. Myoglobin assay

Myoglobin assay was carried out in 10% acetonitrile-phosphate buffer (0.1 M, pH 7.4) wherein horse heart myoglobin (2mg.mL^{-1}, 66 µL) was dissolved and the resulting solution was bubbled with nitrogen for at least 20 minutes. This was followed by reduction via addition of freshly prepared solution of sodium dithionate, $Na_2S_2O_4$ (24mg.mL^{-1}). Now, to the resulting deoxymyoglobin (dMb), aliquots of **A** (3.6 µM) and **B** (3.6 µM) in acetonitrile were added and the conversion of dMb to carboxymyoglobin (MbCO) was monitored upon exposure to 550 nm light in case of **A** and visible light (> 475nm) with **B**. Formation of MbCO was characterized by the shift in λ_{max} from 434 nm to 424 nm along with the appearance of new bands at 530 and 580 nm.

3.7.7. GC-TCD analysis for CO quantification

Photochemical release of CO from complexes **A** and **B** was confirmed by headspace analysis using GC-TCD technique. 1 mL solution of complex **A** (1.33 mM) and **B** (3.03 mM) in acetonitrile was placed in a 2 mL screw capped vial with a septum. The solution containing **A** was irradiated with 550 nm light (Xenon lamp, 350 W) and solution containing **B** was exposed to visible light (> 475 nm) for 30 minutes. 1 mL aliquot of the headspace was injected into the GC inlet. Identification of carbon monoxide was carried out on the basis of retention time already calibrated using standard gas mixtures.

3.7.8. Quantification of CO released from A and B in acetonitrile with GC-TCD

Amount of CO released was quantified using GC-TCD in units of parts per million (ppm). Molarity of **A** (mol. wt. 748 g/mol) in a stock solution of 1 mg/mL in acetonitrile is 0.00133 M, moles of CO released per litre is 0.003135, number of CO released per unit of = (moles of CO per litre) / (moles of **A** per litre) which is calculated as 2.4. Similarly, molarity of **B** (mol. wt. 660 g/mol) in a stock solution of 1 mg/0.5 mL in acetonitrile is 0.00303 M, moles of CO released per litre is 0.007803, number of CO released per unit of **B** = (moles of CO per litre) / (moles of **B** per litre) which is calculated as 2.6.

3.7.9. Calculation of CO release quantum yield with A and B via ferrioxalate actinometry

CO release quantum yields for **A** and **B** were calculated via ferrioxalate actinometry using 350W xenon lamp light source (475 nm cut off filter). Photon flux of the light and the

resulting quantum yield for photorelease of CO was calculated according to the already reported procedures.

3.7.10. DPPH free radical scavenging activity[21]

DPPH is a stable nitrogen based free radical which turns yellow in solution from dark purple upon reduction by either electron transfer or hydrogen transfer. In the radical form, DPPH has an absorbance at 517 nm which begins to disappear as soon as it accepts an electron or hydrogen radical. Methanolic solution of complex **A** (3.2 μM) was taken in a closed container and subjected to photolysis under visible light (550 nm) irradiation. To that solution, 20 μL DPPH (0.08 mM) in methanol was added and the resulting solution was shaken thoroughly and allowed to stand at room temperature for 30 minutes during which absorption spectra were recorded at an interval of 5 minutes under dark.

3.7.11. Hydroxyl radical scavenging activity via indirect detection of presence of H_2O_2[22]

Fenton's reaction was used a standard method to yield hydroxyl radicals which are generated in presence of H_2O_2 and Fe(II). Reaction mixture containing 30 μL of 1 mmol of $FeCl_2$ and 45 μL of 1 mmol of 1,10-phenanthroline along with photolyzed solution of complex **A** (3.5 μM) was incubated in methanol for 5 minutes under dark. Absorbance of the resulting solution was then spectrophotometrically recorded at 560 nm.

3.7.12. Computational Methodologies

TD-DFT calculations for compounds A and B. DFT calculations were done at B3LYP level using triple zeta basis set with new polarization functions for compounds **A** and **B**. Frequency calculations were also performed and ground state was ensured by the absence of negative frequency. Calculations were performed in acetonitrile using Control of conductor-like Polarizable Continuum Model (CPCM). Spin orbit coupling between singlet and triplet state was calculated using DOSOC. All calculations were performed using ORCA 5.0 an ab-initio, DFT and semi empirical SCF-MO package which is available as free for the scientific community. Iboview software has been used for pictorial illustration of HOMO and LUMO frontier molecular orbitals. Triplet energy transfer between the photosensitizer and oxygen molecules leads to generation of singlet oxygen, $^1O_2$ which is promoted by inter system crossing (ISC) to the triplet state of the photosensitizer. Efficient generation of triplet state is necessary for the photosensitization mechanism which is estimated by ISC rate constant, k_{ISC}

$\propto$ [<S|H_{SO}|T>/ΔE_{ST}]^2 where <S|H_{SO}|T> is the spin-orbit coupling (SOC) constant between singlet and triplet states and ΔE_{ST} is the energy difference between singlet (S) and triplet (T) states[23].

$$SOC = \sqrt[2]{(\sum_{i=x,y,z} |\Psi S1|HSO|\Psi T1|)^{2\,i}}$$

SOC electronic components for coupling between S1-T1 for **A** in acetonitrile: X (0.00, 0.06) Y (0.00, 0.02) Z (-0.00, 0.06) SOC electronic components for coupling between S_1-T_1 for **B** in acetonitrile: X (0, -0.0) Y (0, -0.0) Z (-0, 0.01).

TD-DFT calculations for compound C. DFT calculations were done at B3LYP level using triple zeta basis set with new polarization functions for compound **C**. Frequency calculations were also performed and ground state was ensured by the absence of negative frequency. Calculations were performed in acetonitrile using Control of conductor-like Polarizable Continuum Model (CPCM). Spin orbit coupling between singlet and triplet state was calculated using DOSOC. All calculations were performed using ORCA 5.0 an ab-initio, DFT and semi empirical SCF-MO package which is available as free for the scientific community. Efficient generation of triplet state is necessary for the photosensitization mechanism which is estimated by ISC rate constant, $k_{ISC} \propto$ [<S|H_{SO}|T>/ΔE_{ST}]^2 where <S|H_{SO}|T> is the spin-orbit coupling (SOC) constant between singlet and triplet states and ΔE_{ST} is the energy difference between singlet (S) and triplet (T) states.

TD-DFT Calculations for compounds D-F. The molecular geometries for **D-F** were optimized applying density functional theory (DFT) based first principle calculations adopting B3LYP hybrid functional for exchange-correlation (XC) approximations. The atom centered polarized triple-zeta basis sets, def2-TZVP, were used for all the atoms. The calculations were accelerated by employing the Resolution of Identity (RI) approximation using auxiliary basis sets. To achieve higher integral accuracy, we used larger grid5 for numerical integration. 'Chain of Spheres Exchange' (COSX) is used for calculating the exchange terms effectively. All the calculations were performed using ORCA 4.0.1 quantum chemical code. The electronic spectra (UV-Vis) were calculated applying time dependent DFT (TD-DFT). A total of 100 consecutive excited states were accounted in order to ensure that the observed spectral range. All the TD-DFT calculations were performed at B3LYP/def2-TZVP level of theory. Since all the experimental data in this study were obtained in acetonitrile, the implicit solvent effects were also incorporated in the calculations by using Conductor like Polarizable Continuum

Model (C-PCM) as implemented in ORCA. A dielectric constant of 36.6 was utilized to mimic the acetonitrile solvent environment. The electronic spectra calculations were performed in gas phase as well as in solvent for molecules **D**-**G** in which only singlet-singlet excitations were accounted.

3.8. References

[1] J. Bañuelos, *Chem. Rec.* **2016**, *16*, 335–348.

[2] A. C. Benniston, G. Copley, *Phys. Chem. Chem. Phys.* **2009**, *11*, 4124–4131.

[3] A. Ismailova, D. Kuter, D. S. Bohle, I. S. Butler, *Bioorg. Chem. Appl.* **2018**, *2018*, e8547364.

[4] K. Ling, F. Men, W.-C. Wang, Y.-Q. Zhou, H.-W. Zhang, D.-W. Ye, *J. Med. Chem.* **2018**, *61*, 2611–2635.

[5] H. Yan, J. Du, S. Zhu, G. Nie, H. Zhang, Z. Gu, Y. Zhao, *Small* **2019**, *15*, 1904382.

[6] S. G. Awuah, Y. You, *RSC Adv.* **2012**, *2*, 11169–11183.

[7] J. Wang, Q. Gong, L. Wang, E. Hao, L. Jiao, *J. Porphyrins Phthalocyanines* **2020**, *24*, 603–635.

[8] E. Bassan, A. Gualandi, P. Giorgio Cozzi, P. Ceroni, *Chem. Sci.* **2021**, *12*, 6607–6628.

[9] F. Würthner, T. E. Kaiser, C. R. Saha-Möller, *Angew. Chem., Int. Ed.* **2011**, *50*, 3376–3410.

[10] S. Li, X. Yan, J. Zhang, X. Guo, Y. Zhang, M. Su, C. Yang, H. Zhang, C. Li, *Adv. Funct. Mater.* **2021**, *31*, 2105189.

[11] D. O. Frimannsson, M. Grossi, J. Murtagh, F. Paradisi, D. F. O'Shea, *J. Med. Chem.* **2010**, *53*, 7337–7343.

[12] X.-F. Zhang, X. Yang, *J. Phys. Chem. B* **2013**, *117*, 5533–5539.

[13] L. Wang, K. Zhu, Q. Chen, M. He, *Dyes Pigm.* **2015**, *112*, 274–279.

[14] F. Ponte, G. Mazzone, N. Russo, E. Sicilia, *J Mol Model* **2018**, *24*, 183.

[15] Z. Ruan, Y. Zhao, P. Yuan, L. Liu, Y. Wang, L. Yan, *J. Mater. Chem. B* **2018**, *6*, 753–762.

[16] P. P. P. Kumar, P. Yadav, A. Shanavas, P. P. Neelakandan, *Mater. Chem. Front.* **2020**, *4*, 965–972.

[17] J. Massue, D. Jacquemin, G. Ulrich, *Organics* **2021**, *2*, 365–375.

[18] A. Haque, R. A. Al-Balushi, P. R. Raithby, M. S. Khan, *Molecules* **2020**, *25*, 2645.

[19] O. A. Bozdemir, R. Guliyev, O. Buyukcakir, S. Selcuk, S. Kolemen, G. Gulseren, T. Nalbantoglu, H. Boyaci, E. U. Akkaya, *J. Am. Chem. Soc.* **2010**, *132*, 8029–8036.

[20] G. Wesela-Bauman, M. Urban, S. Luliński, J. Serwatowski, K. Woźniak, *Org. Biomol. Chem.* **2015**, *13*, 3268–3279.

[21] N. Tyagi, A. Chakraborty, U. P. Singh, P. Roy, K. Ghosh, *Org. Biomol. Chem.* **2015**, *13*, 11445–11458.

[22] Y. Wenli, Z. Yaping, S. Bo, *Food Chem.* **2004**, *86*, 525–529.

[23] V.-N. Nguyen, Y. Yim, S. Kim, B. Ryu, K. M. K. Swamy, G. Kim, N. Kwon, C.-Y. Kim, S. Park, J. Yoon, *Angew. Chem. Int. Ed.* **2020**, *59*, 8957–8962.

[24] F. Neese, F. Wennmohs, A. Hansen, U. Becker, *Chem. Phys.* **2009**, *356*, 98–109.

Chapter 4

Applications

4. Introduction.

Stimuli-responsive materials in response to triggers like light, temperature, pH or electric fields offer great potential for therapeutic applications[1–4]. They have the ability to allow for targeted and controlled drug delivery and hence assist in development of smart drug delivery systems, tissue engineering scaffolds, and diagnostic devices that respond to specific stimuli. In pursuit of light responsive materials, compounds that release controlled CO and singlet oxygen upon light exposure are highly desirable for phototherapeutic applications. Transition metal complexes are interesting in this regard as they offer good flexibility and diversity in terms of their chemical composition and CO release efficiencies[5–7]. Although a few reports mention simultaneous CO release and singlet oxygen generation with metal based photoCORMs[8], the byproducts that are left over after CO release are a cause of concern in those systems and new strategies are needed to sequester the byproducts without compromising on the CO release. Non-woven fabrics are attractive for such applications as they are easy to process and handle. Moreover, the non-woven fabrics offer a great promise to address the problems caused by the probable toxic metal byproducts left behind upon photolysis as they would be kept trapped within the scaffold after CO release. Although there are a few reports of non-woven fabrics incorporating manganese complexes for CO release applications[9–11], many of them require high energy blue light or consist of multiple components. The lability of the inorganic complexes further restricts the usage of these materials to a few days. To circumvent these drawbacks, herein we present a simple strategy to achieve simultaneous release of CO and singlet oxygen using a single component photoCORM incorporated into a non-woven fabric that can be activated using visible light.

While photosensitizers are extensively employed as photodynamic therapy agents, they also find good utility in wastewater treatment, synthetic organic chemistry, as antimicrobial photodynamic agents and in pesticide degradation[12–17]. As four-coordinate boron compounds based on an imine scaffold are known to have high stability and good photophysical properties, they can be used to promote photooxidation reactions in a heterogeneous manner upon incorporation into a polymer matrix. Since molecule **G** exhibited high photostability and singlet oxygen quantum yield, we were keen to incorporate it into poly(methylmethacrylate) (PMMA)

matrix in order to develop a reusable heterogeneous medium for the degradation of a variety of organic water pollutants.

Another application with photosensitizing agents is their ability to kill bacteria. Recent times have depicted how bacterial and fungal infections can take toll over the entire world in a short span[18,19]. Transmission of infections through contaminated surfaces is a matter of grave concern and contributes significantly to the spread of infections. Self-cleaning surfaces that can be catalytically triggered by using external stimuli like light to generate bactericidal agents present themselves as a smart medium in the pursuit of light-regulated antibacterial activity[6,20–22]. Photoactive antimicrobial coatings are controllable, minimally invasive, effective and function using light as a stimulus. Hence, photodynamic coatings hold great promise as antibacterial coatings and are superior to the conventional sterilization procedures for medical devices and storage containers. Although small organic molecules can also be embedded inside a polymer film for various photooxidation processes, but the lack of processability of these small molecules usually hinders their applicability for practical functional coatings. In this regard, polymer-based coatings are always advantageous for the preparation of films and coatings as they offer versatility for surface modification as well as good processability for thin film formation[23]. Layer-by-layer (LbL) assembly based immersive coating technique provides an easy approach that can be applied to coat any surface with complex geometries[24–26]. This process involves dipping the substrate alternately in oppositely charged polyelectrolytes solution and the formation of multilayer film is primarily driven by electrostatic interactions. Because of tunability and processability, LbL multilayer coatings have found applications in protective coatings, drug delivery, gas barrier, surface wettability, sensing, and antifouling[25,27–32]. Hence, it intrigued us to adopt LbL assembly for coating our salicylideneimine boron difluoride functionalized polymer **H** on desired surfaces.

Overall, our results indicate that the incorporation of boron-containing compounds into polymers allows preparation of materials that could be activated using light. The non-woven fabrics with **A** and **B** was observed to quantitatively release CO and generate singlet oxygen thereby exemplifying the multi-functional nature of these materials. In vitro studies suggest that while no significant cell death was observed in the dark, a remarkable killing of c6 cancer cells and *E. coli* bacteria was observed with the fabrics when exposed to white light. Furthermore, by incorporating the molecule **G** into a poly(methylmethacrylate) (PMMA) matrix, we were able to develop a reusable heterogeneous medium for the degradation of a variety of organic water pollutants. Boron-functionalized polyethyleneimine, **H** was used to prepare photoactive polymer coatings via LbL assembly and that the resultant coating

displayed excellent stability and remarkable anti-microbial activity towards gram positive and gram-negative bacteria. The uniqueness of the system is that the incorporation of boron complex resulted in lower-visible light absorption which not only allowed usage of visible light for bactericidal studies, but also resulted in a practically transparent coating which makes it ideal for several applications. Moreover, LbL assembly could potentially be used to prepare coatings on any surface which greatly improves the practical utility of our system.

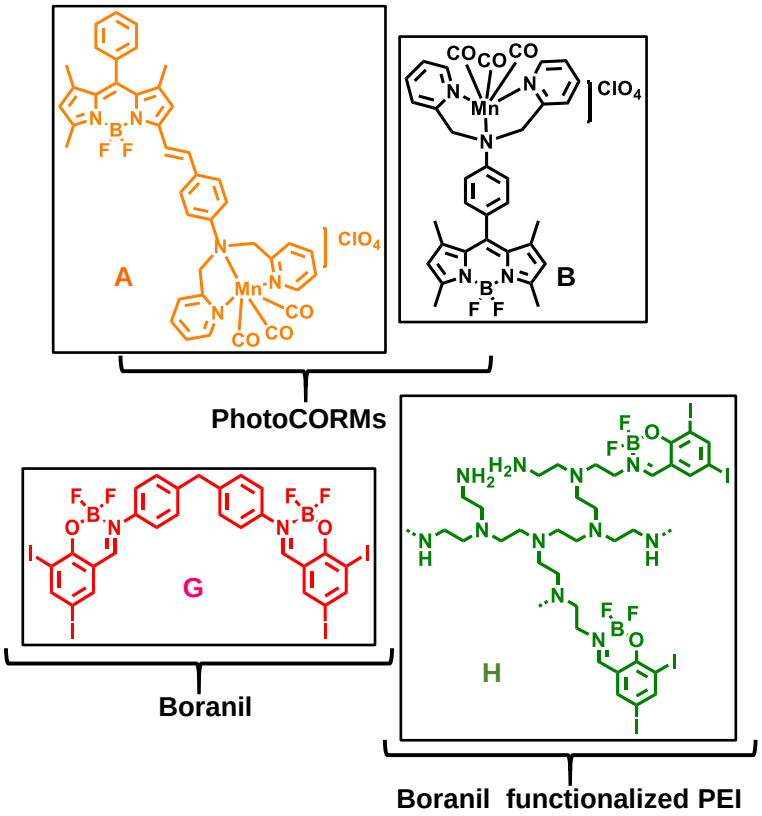

Figure 4. Illustration of the structures of molecules **A-H,** divided into different parts.

4.1. CO release with nonwoven fabrics of A and B.

For practical applications, it is desired that the photorelease of CO is achieved in the solid state. To test this, we checked the release of CO from the single crystals of **B** wherein we observed the emergence of numerous bubbles upon irradiation from the crystals placed in silicone oil (Figure 4.1). A similar observation was made with the crystals of **A**, but due to the dark color of the crystals of **A**, emergence of bubbles on its surface was not as clearly visible as in the case of **B**. Further, we were interested to embed the complexes **A** and **B** in a flexible matrix which would be easy to handle as compared to crystals. This was achieved by non-

covalently embedding **A** and **B** into poly(methyl methacrylate) (PMMA) polymer matrix via electrospinning to yield the corresponding non-woven fabrics.

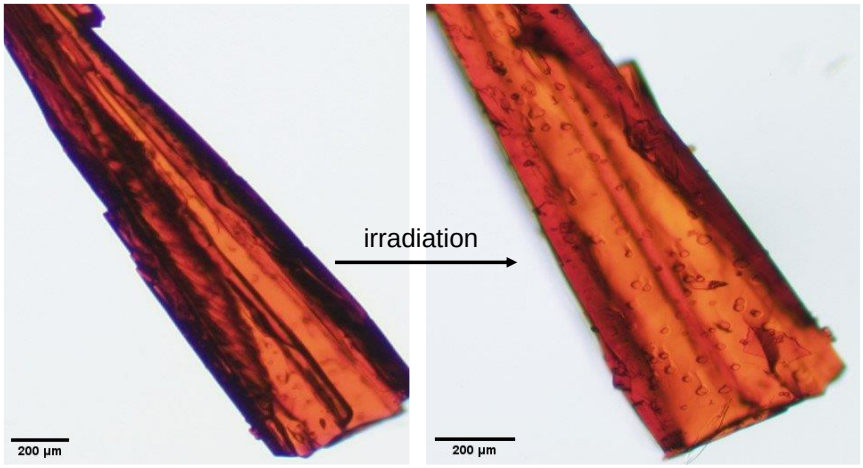

Figure 4.1. Optical microscope images showing the emergence of bubbles on the surface of the crystal of **B** dipped in silicone oil after irradiation for 30 minutes with a 350 W Xenon lamp. (Scale bar: 200µm)

The prepared non-woven fabric with **A**, namely $\mathbf{A_F}$, showed purple color and was easy to handle, detach and cut. Fabric prepared with **B**, namely $\mathbf{B_F}$, on the other hand, displayed yellow color. FESEM images confirmed the formation of robust fiber mats with an approximate diameter of 1.7 µm (Figures 4.2 and 4.3). The absorption spectra of the non-woven fabrics matched with that of the complexes in solution albeit minor peak-broadening. Similarly, the emission spectra of the fabrics exhibited broad peaks (Figure 4.4).

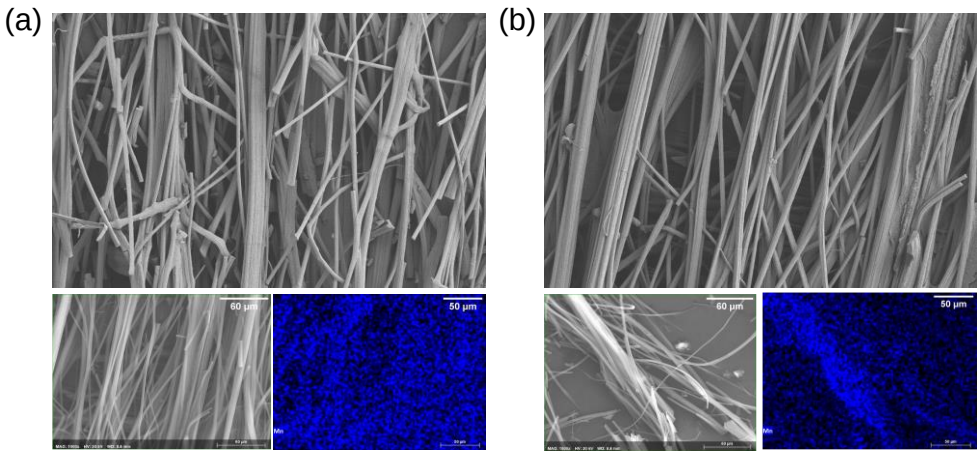

Figure 4.2. FESEM images and EDX mapping representing the presence of manganese in the electrospun non-woven fabrics of **A** and PMMA (a) before and (b) after extensive irradiation under a 350 W Xenon arc lamp.

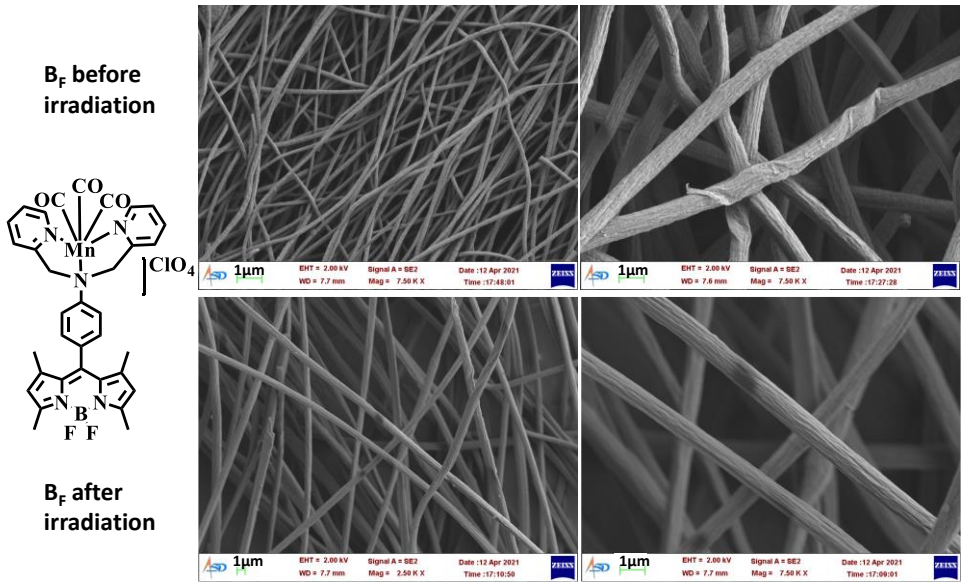

Figure 4.3. (a) FESEM images of the non-woven fabric prepared with **B** and PMMA polymer namely $\mathbf{B_F}$ before (top) and after irradiation (bottom) for 30 minutes.

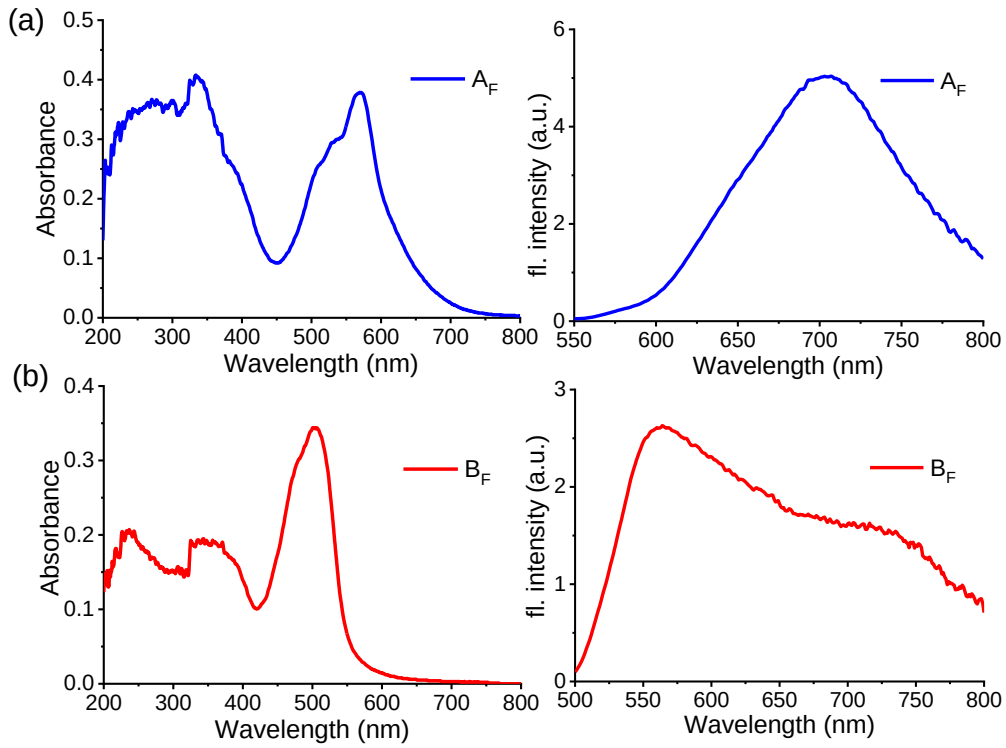

Figure 4.4. Solid state absorption and emission spectra of the fabrics (a) $\mathbf{A_F}$ and (b) $\mathbf{B_F}$. λ_{ex} for $\mathbf{A_F}$ and $\mathbf{B_F}$ are 540 and 490 nm, respectively.

The electrospun fibres of **A** and **B** were also monitored via confocal fluorescence microscope (Figure 4.5) and a strong fluorescence was observed throughout the non-woven scaffold in green and red detector channels. The fibres exhibited green and red emission signals even without labelling with any external fluorescent dyes. It is noteworthy that the photoCORMs **A** and **B** were distributed along the entire lengths of the fibres without aggregation. This validated the stability of the photoCORMs throughout the electrospinning process and ruled out the release of CO during electrospinning thereby signifying the stability of these complexes. The non-woven fabrics were then dissolved in DCM and analyzed by UV-Vis spectroscopy and the resulting spectra before and after light exposure were found to be consistent with the results observed in solution (Figure 4.6). These experiments helped to rule out any strong irreversible interactions of **A** or **B** with the polymer PMMA.

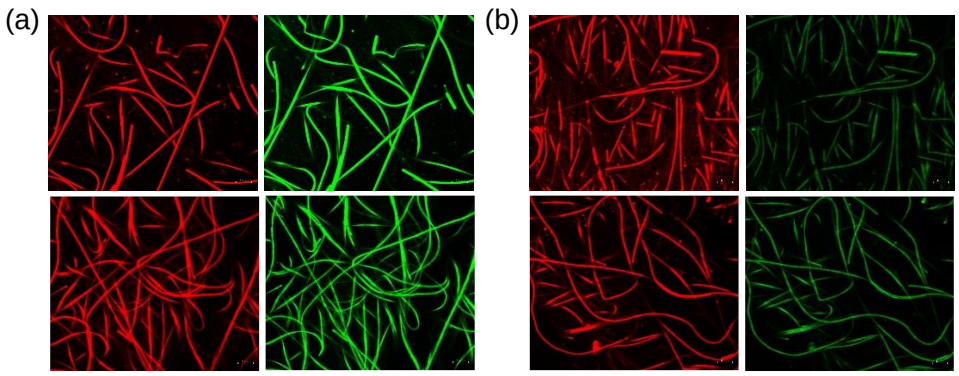

Figure 4.5. Confocal microscopy images of fluorescent fibres $\mathbf{A_F}$ (a) and $\mathbf{B_F}$ (b) with 488 nm and 561 nm laser in the red and green region.

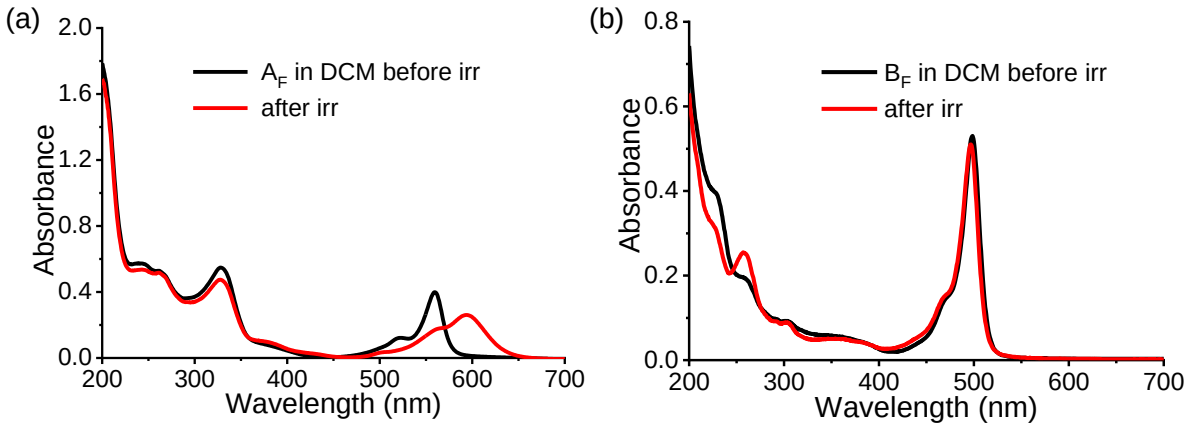

Figure 4.6. Changes in the UV-Vis absorption spectra of (a) $\mathbf{A_F}$ and (b) $\mathbf{B_F}$ dissolved in DCM before and after irradiation with visible light using a 350 W Xenon arc lamp.

The fabrics were then investigated for their CO releasing properties. A small piece of the non-woven fabrics $\mathbf{A_F}$ and $\mathbf{B_F}$ was added to a cuvette containing solution of dMb in PBS buffer at pH 7.4 under dark and the resulting solution was irradiated for 60 seconds. We observed that the soret band of Mb shifted from 432 to 423 nm along with the appearance of new bands at 535 and 575 nm (Figure 4.7). The spectral changes are in accordance with the photoactivated release of CO from $\mathbf{A_F}$ and $\mathbf{B_F}$. Gas Chromatography analysis using a Pulsed Discharge Detector (GC-PDD) further confirmed the CO release from direct irradiation of the fabrics and the amount of CO released was estimated to be 375 and 343 ppm/mg for $\mathbf{A_F}$ and $\mathbf{B_F}$, respectively (Figures. 4.8 and 4.9). It is worth noting that the fabric in contrast to the solution hardly released any CO under dark conditions which shows that CO release from the fabrics can be controlled and activated using light.

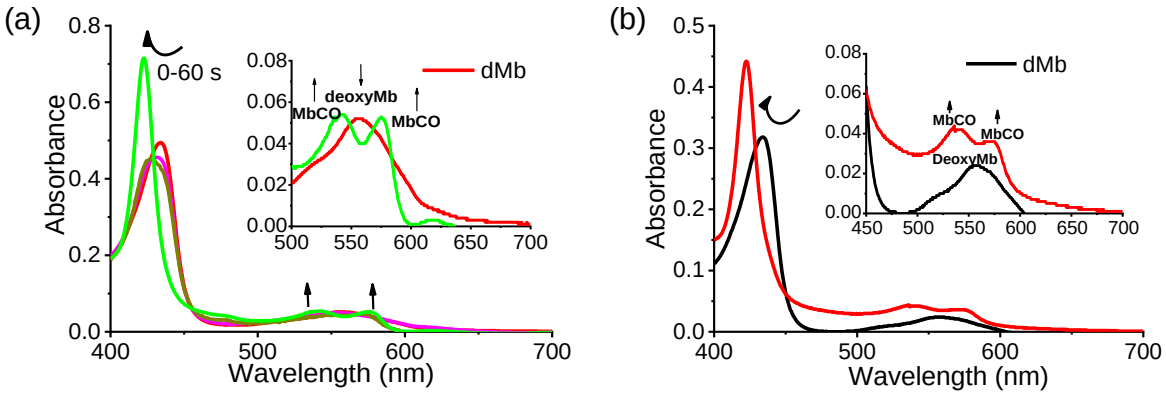

Figure 4.7. (a) Investigation of CO release from $\mathbf{A_F}$ (0.5 x 3 cm^2) and $\mathbf{B_F}$ (0.5 x 3 cm^2) in a heterogeneous myoglobin assay. During irradiation, CO is released and reacts with horse heart myoglobin (Mb) (2 $mg.mL^{-1}$) reduced with sodium dithionate (24 $mg.mL^{-1}$) to form carboxy-myoglobin (Mb-CO). Inset shows the emergence of new peaks at 535 and 575 nm after irradiation for 60 seconds.

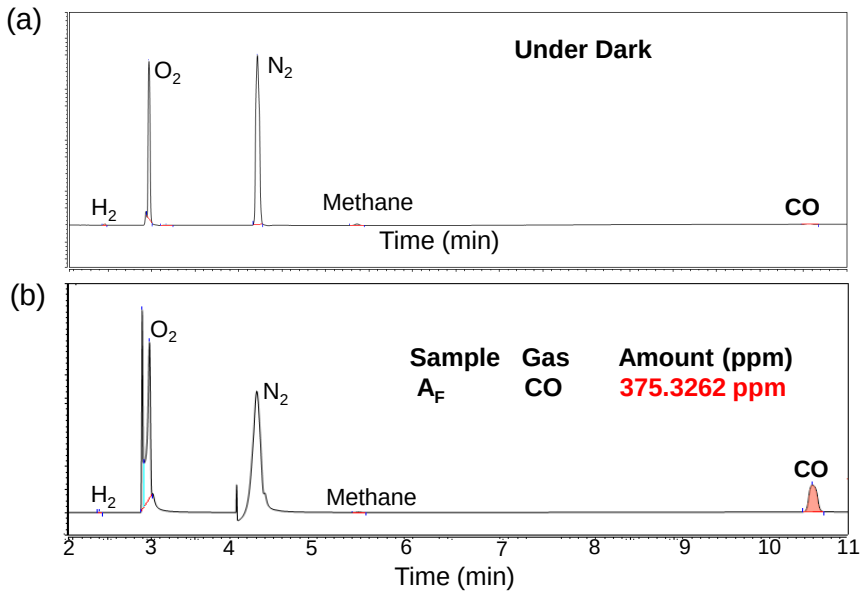

Figure 4.8. GC-PCD data showing release of CO in a 2 mL GC vial containing 1 mg of the fabric $\mathbf{A_F}$ under (a) dark conditions and (b) upon irradiation with visible light.

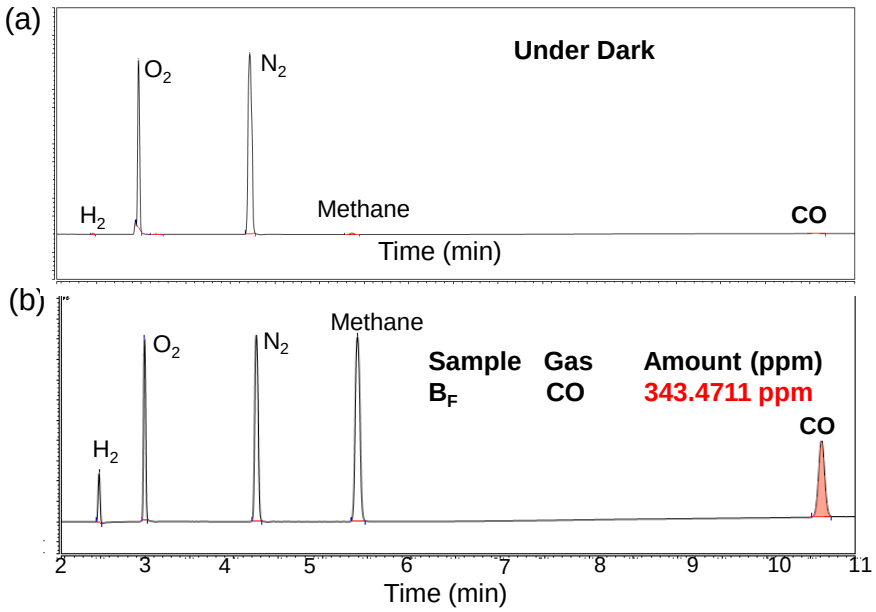

Figure 4.9. GC-PDD data showing release of CO in a 2 mL GC vial containing 1 mg of the fabric **B_F** under (a) dark conditions and (b) upon irradiation with visible light.

In order to observe the photorelease of CO from **A_F** and **B_F** as a function of irradiation time, GC-PDD technique was employed. We were interested to observe controlled release of CO and ensure that no background release occurs in dark. It was observed that while systematic release of CO had occurred upon light exposure, no release had occurred in complete dark conditions (Figure 4.10). Hence it can be concluded that controlled release of CO could be achieved from the fabrics using light.

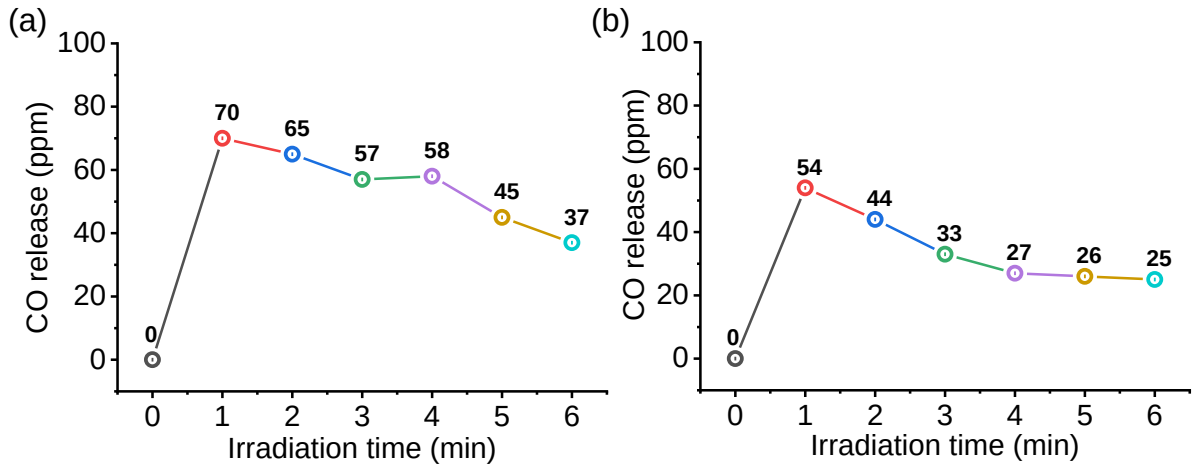

Figure 4.10. Investigation of controlled release of CO from (a) **A_F** (1 mg) and (b) **B_F** (1 mg) under light exposure ("On") and complete dark ("Off") conditions. Low intensity 15 W

incandescent lamp was used as source of irradiation and the sample was placed at a distance of 5 cm.

Furthermore, the ATR-FTIR spectra showed a reduction in the peak intensity corresponding to the CO stretching at 1937 and 2036 cm^{-1} upon CO release from both the fabrics (Figure 4.11). Hence these observations establish the immense potential of the non-woven fabrics towards heterogenous release of CO.

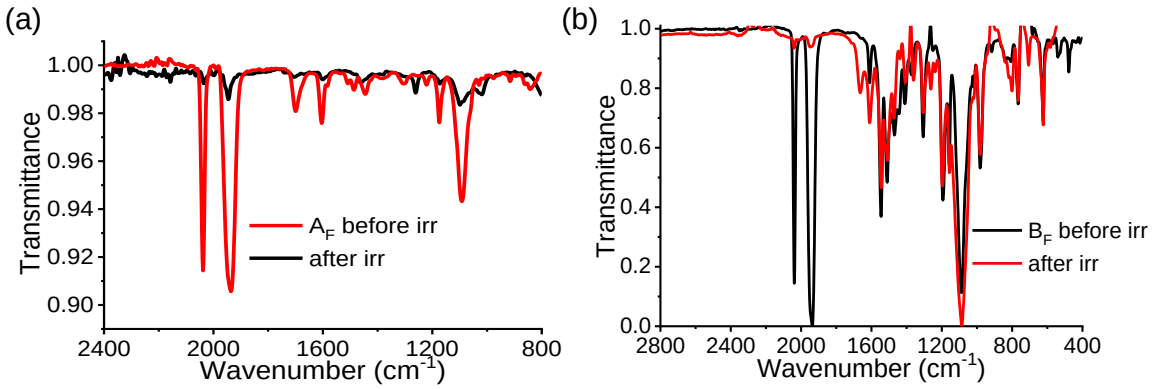

Figure 4.11. ATR-IR spectra of (a) $\mathbf{A_F}$ and (b) $\mathbf{B_F}$ before and after irradiation. The spectra show the loss of CO vibration bands between 1900–2100 cm^{-1} after the irradiation.

The X-band ESR spectra of the extensively irradiated fabrics $\mathbf{A_F}$ and $\mathbf{B_F}$ displayed six lines indicating the formation of paramagnetic Mn(II) species (Figure 4.12). The presence of manganese in the fabrics $\mathbf{A_F}$ and $\mathbf{B_F}$ before and after prolonged irradiation was then confirmed by EDX mapping thereby suggesting that Mn(II), produced after CO release, was retained in the non-woven fabrics (Figures 4.2 and 4.13). To further support this inference, the total manganese content in the fabric was determined with Inductively Coupled Plasma Mass Spectroscopy (ICPMS) which showed a retention of 96 and 99% of the initially introduced **A** and **B** in $\mathbf{A_F}$ and $\mathbf{B_F}$, respectively post irradiation.

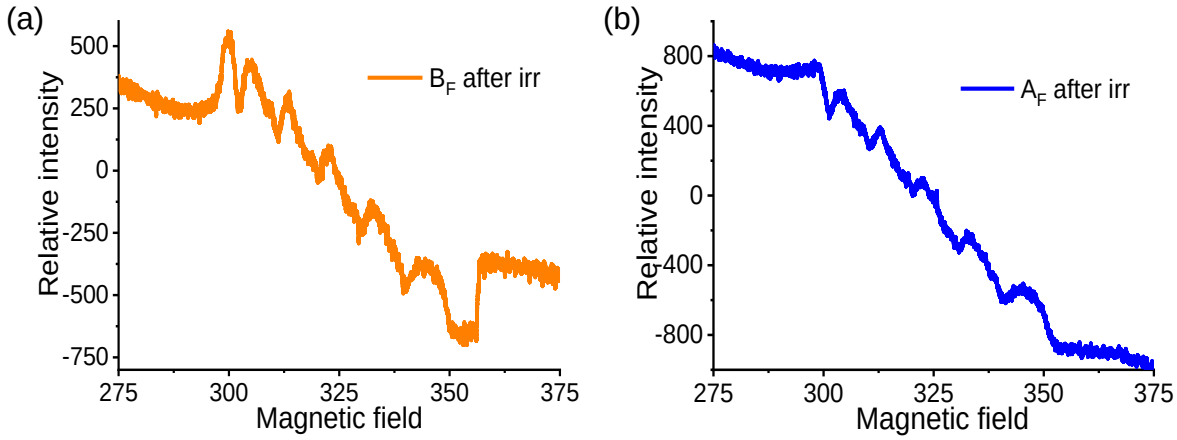

Figure 4.12. X-band ESR spectra of the fabrics (a) $\mathbf{A_F}$ and (b) $\mathbf{B_F}$ at 77 K after light exposure for 15 minutes.

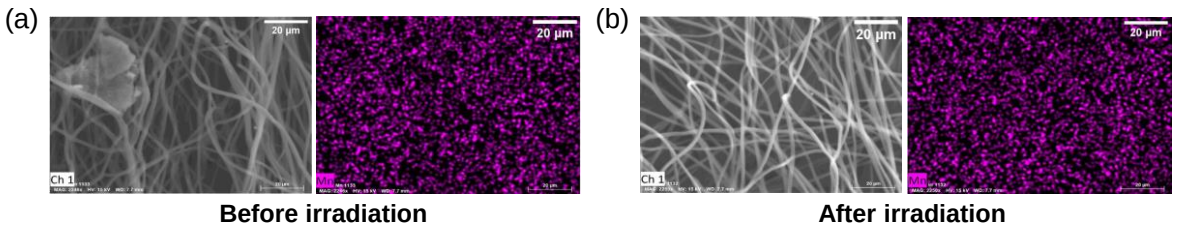

Figure 4.13. Energy dispersive X-ray (EDX) elemental mapping representing presence of manganese in the electrospun non-woven fabric $\mathbf{B_F}$ before and after extensive irradiation.

Besides the simple strategy, the non-woven fabrics are superior from the stability point of view as well. To date, the reported CO releasing non-woven fabrics usually suffer from stability issues either during the electrospinning process or they undergo degradation in a span of few days assumably due to the lability of inorganic metal complexes involved. Even refrigeration also restricted the usage to around two weeks. Our fabrics were not only stable throughout the electrospinning process, but they can indefinitely be stored under ambient conditions in a closed box. Figure 4.14 shows that the absorption spectra of the fabrics remained consistent even after twelve months of preparation. This observation also substantiates the role of covalent modification with BODIPY towards the stabilization of CO releasing core. The complexes **A** and **B** as well as their respective non-woven fabrics were then monitored for their stability under physiological conditions (Figure 4.15). It was observed after incubating the complexes **A** and **B** in PBS buffer, although a decrease in the absorption was observed after 6 hours of incubation which can be associated with aggregation of the complexes in PBS buffer (pH 7.4), the absorption maxima still remained unchanged indicating that the

complexes had not yet released CO even after 6 hours. Similarly the fabrics $\mathbf{A_F}$ and $\mathbf{B_F}$ were dipped in PBS buffer in dark conditions for 24 hours and their absorption spectra were recorded post drying in vacuum dessicator. Figure 4.15 clearly indicates that they fabrics did not lose the integrity and were found to be quite stable.

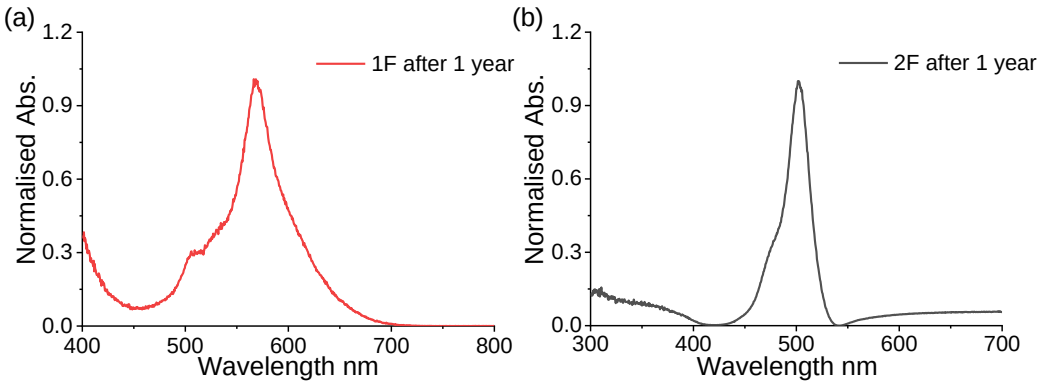

Figure 4.14. Solid state absorption spectra for (a) $\mathbf{A_F}$ and (b) $\mathbf{B_F}$ after one year.

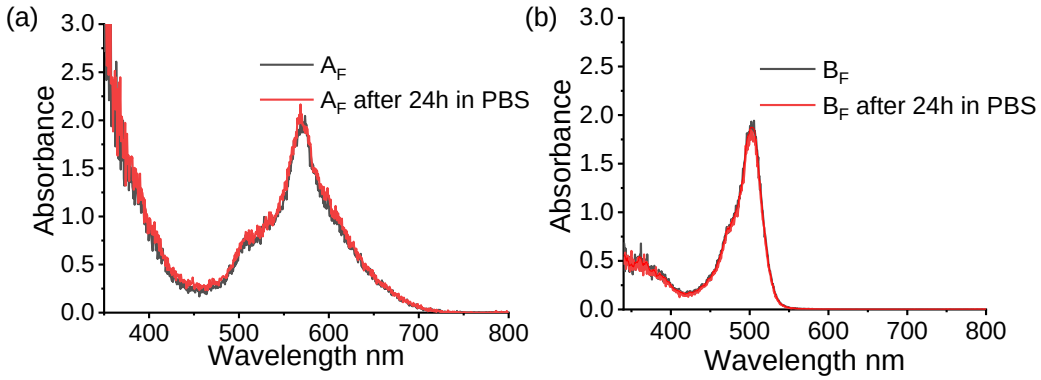

Figure 4.15. Absorption spectra of fabrics (a) $\mathbf{A_F}$ and (b) $\mathbf{B_F}$ post incubation in PBS buffer (pH 7.4) for 24 hours.

4.2. Photosensitization properties of the nonwoven fabrics.

Our next focus was on investigating the photosensitization properties of the non-woven fabrics. 1,5-Dihydroxynaphthalene (DHN) was chosen as a substrate for singlet oxygen generation due to its compatibility with aqueous media. Moreover, the photosensitized reaction of DHN with $^1O_2$, yielding Juglone can be conveniently monitored by UV-Vis spectroscopy. Hence a solution containing a mixture of DHN and $\mathbf{A_F}$ in water was irradiated, and the absorption spectra were recorded at regular intervals upon light irradiation. As shown in Figure 4.16, we observed a regular decrease in the absorbance of DHN at 298 nm along with the concomitant formation of a broad peak in the longer wavelength region around 420 nm upon

continued irradiation. These spectral changes indicate the conversion of DHN to Juglone, which in turn suggested the formation of $^1O_2$ thereby confirming that the non-woven fabric can act as a photosensitizer.

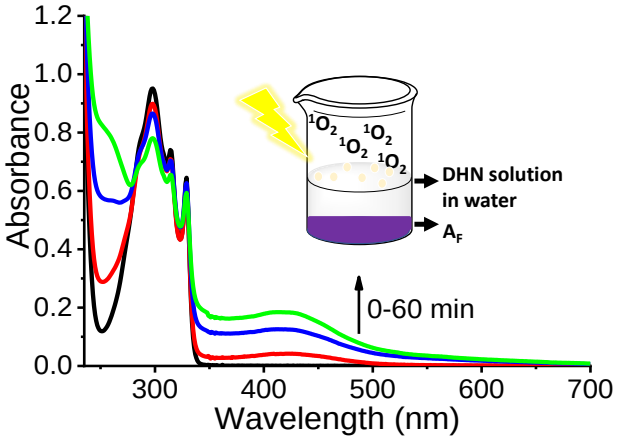

Figure 4.16. The changes in the UV-Vis absorption spectrum of a mixture of 1,5-dihydroxynaphthalene (DHN, 0.14 mM) and $\mathbf{A_F}$ (3 x 3 cm^2) in water as a function of irradiation time. Inset shows the setup adopted for investigation of singlet oxygen.

4.3. In vitro biological studies with non-woven fabrics.

To evaluate if the non-woven fabrics could be used for biological applications, concentration dependent toxicity of $\mathbf{A_F}$ and $\mathbf{B_F}$ from 1 to 4 mg was tested against l929 cell lines. In vitro experiments revealed that the CO releasing fabrics were non-cytotoxic to l929 cell lines for an incubation time of 24 hours and displayed negligible dark toxicity making them promising candidates for photodynamic therapy and wound healing applications (Figure 4.17). The cytotoxicity of the fabrics was further evaluated against c6 cancer cells via MTT assay wherein the fabrics were incubated for 24 hours in the dark and also put under low intensity incandescent light for a period of 60 minutes. Figure 4.18a indicates that while no significant cell death was observed in the dark, a remarkable killing of more than 90% cells was observed with $\mathbf{A_F}$ against c6 cell lines when exposed to white light. It is worth mentioning that 50% of cell death was observed after an irradiation for 15 minutes with $\mathbf{A_F}$. On the other hand, $\mathbf{B_F}$ caused some dark toxicity and around 65% cells were viable in the dark against c6 cancer cell lines while around 87% of cell death was observed in the presence of light.

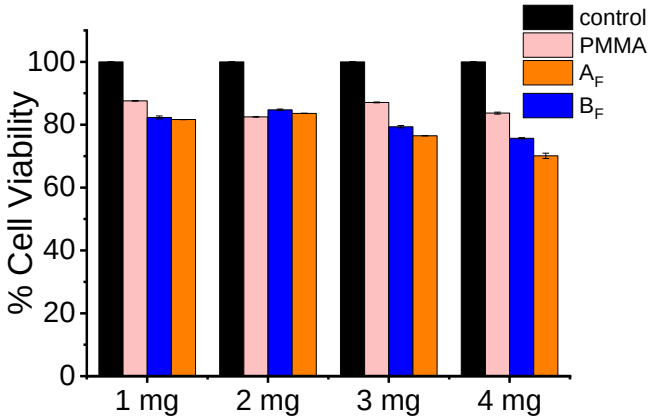

Figure 4.17. Biocompatibility of the fabrics **A_F**, **B_F** and PMMA towards l929 cell lines.

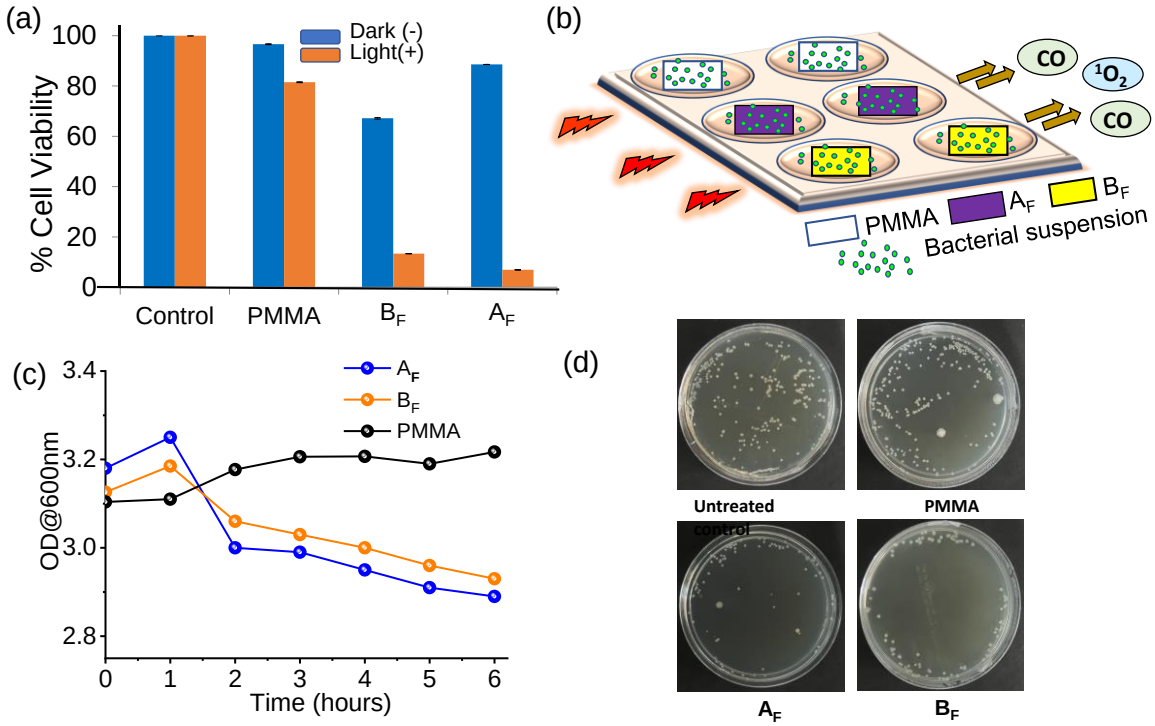

Figure 4.18. (a) Cell viability of c6 cancer cells upon treatment with **A_F** (1 mg, 21 µM), **B_F** (1 mg, 30 µM) and PMMA (1 mg) fabrics under dark and in presence of white light for 60 minutes under a low intensity incandescent lamp with power density of 286.5 W/m^2. (b) A schematic representing the set up adopted for the activity investigation. (c) Changes in the absorbance recorded at 600 nm for the investigation of the antibacterial activity against *E. coli* with **A_F**, **B_F** and PMMA (control) fabrics. (d) Digital photographs of the dishes containing colony forming units of *E. coli* bacteria pretreated with **A_F**, **B_F** under light conditions along with an untreated control.

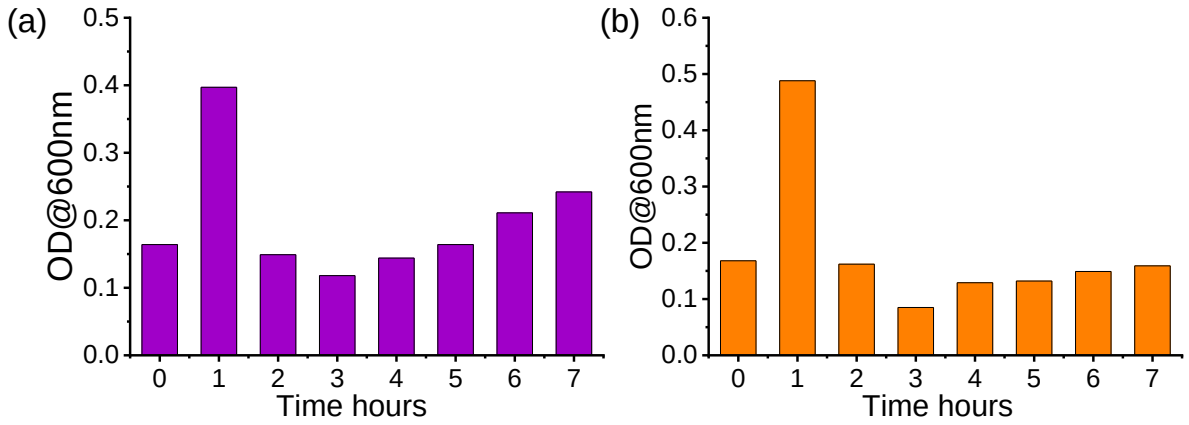

Figure 4.19. Change in OD at 600 nm for an equivalent amount of bacterial suspension (control) without any fabrics in (a) presence and (b) absence of white light (15 W).

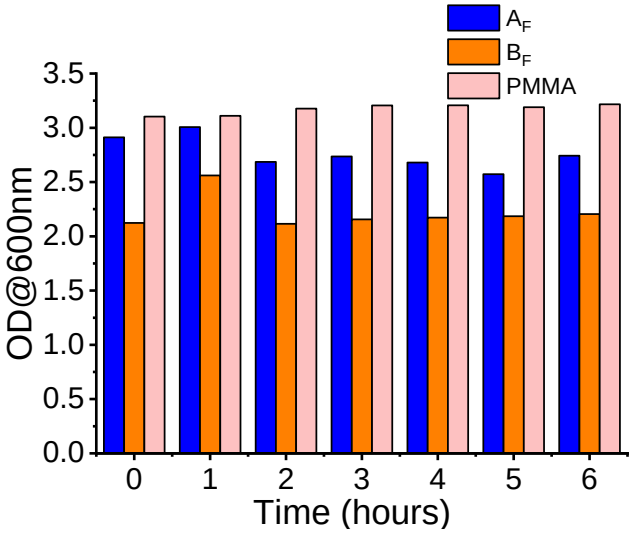

Figure 4.20. Changes in the absorbance recorded at 600 nm for the investigation of the antibacterial activity against *E. coli* with **A**$_{\mathbf{F}}$, **B**$_{\mathbf{F}}$ and PMMA (control) fabrics under dark.

Additionally, for the fabrics to be put forth for wound healing applications, preliminary antibacterial studies were performed using *E. coli* as the bacterial strain and a low intensity 15 W incandescent lamp as the irradiation source. Figure 4.18b shows the setup representing the antibacterial activity against *E. coli* with the fabrics **A**$_{\mathbf{F}}$, **B**$_{\mathbf{F}}$ and PMMA (control). While the control fabric containing PMMA alone did not show any antibacterial properties in the presence of light, while **A**$_{\mathbf{F}}$ and **B**$_{\mathbf{F}}$ showed significant reduction in bacterial growth upon irradiation for 6 hours (Figure 4.18). As depicted in Figure 4.18d, the untreated control plates demonstrated significant number of colonies after 6 hours contrary to **A**$_{\mathbf{F}}$ and **B**$_{\mathbf{F}}$ treated plates wherein a huge reduction in colony forming units were observed under light conditions against *E. coli*.

Furthermore, Figure 4.19 shows that the control containing an equal amount of bacterial suspension as the fabrics exhibited increase in the bacterial growth with and without light. Fabrics under complete dark conditions also did not cause any toxicity and bacterial cell death (Figure 4.20). These observations validate the role of the nonwoven fabrics towards the observed decrease in optical density upon irradiation. While preliminary biological studies indicated the potency of these fabrics towards phototherapeutic applications, detailed in vitro and in vivo studies are in process for improved illustration.

4.4. Film with G as heterogeneous medium for pollutant degradation.

Photochemical oxidation is emerging as a viable approach for the degradation of toxic water and/or air pollutants. Organic photosensitizers capable of inducing electron and/or energy transfer processes are particularly interesting in this regard. Several organic dyes and transition metal complexes have been employed as photocatalysts for water decontamination. As the newly synthesized boranil **G** exhibited good singlet oxygen generation capabilities, we were interested in exploring the possibility of employing this molecule as a photocatalyst for the degradation of organic water contaminants. However, as **G** was not soluble in water, its utility was limited in the aqueous medium. To overcome this, we prepared films of compound **G** using poly(methylmethacrylate) (PMMA) as a matrix. The PMMA films incorporating **G** thus could be expected to serve as a heterogeneous medium for the photosensitized degradation of water contaminants. Moreover, being heterogeneous, the PMMA films would be reusable thereby making it attractive for real-world applications.

Figure 4.21 shows the absorption spectrum of **G** incorporated into a PMMA film wherein broad absorption peaks were observed in the region between 350-420 nm. To check the utility of the PMMA films of **G** as a photocatalyst, we selected the molecules shown in Chart 4.1 as substrates which belong to different classes of water contaminants.

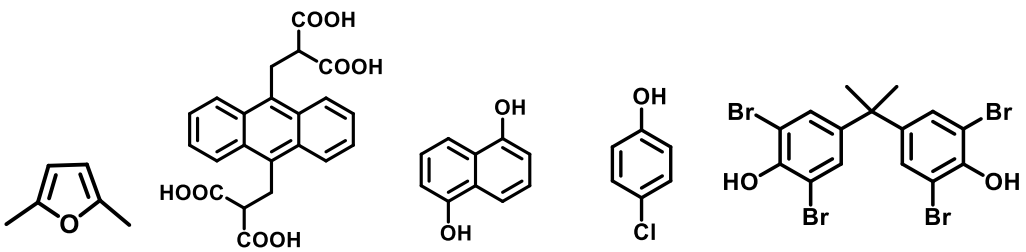

Chart 4.1. Chemical structures of water pollutant molecules studied as substrates for singlet oxygen.

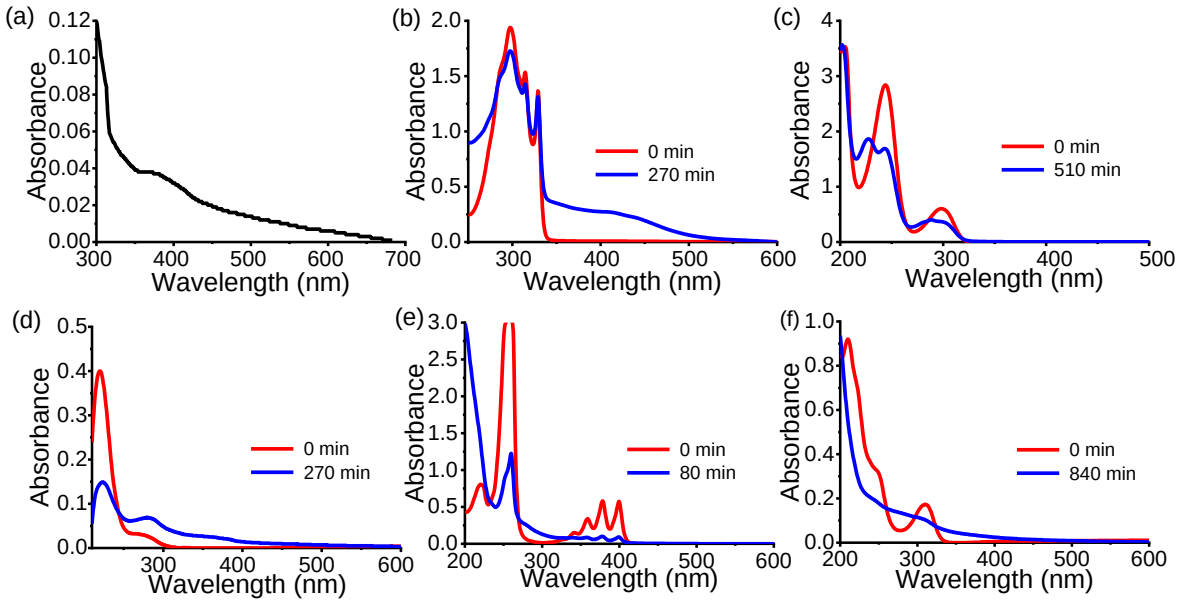

Figure 4.21. (a) The absorption spectrum of the PMMA film incorporating **G**. The changes in the UV-Vis absorption spectrum of (b) 1,5-dihydroxynaphthalene (0.3 mM), (c) 4-chlorophenol (0.34 mM), (d) 2,5-dimethylfuran (6.2 mM), (e) 9,10-anthracenediyl-bis(methylene) dimalonic acid (0.11 mM) and (f) 3,3',5,5'-tetrabromobisphenol A (0.11 mM) in water before and after irradiation wherein the PMMA films was used as a heterogeneous medium for photosensitization.

PMMA films of **G** were prepared by drop-casting chloroform solutions of a mixture of PMMA and **G** in a glass beaker and allowing the solvent to evaporate under ambient conditions. Aqueous solutions of the water contaminants were then taken in the beaker containing the PMMA films of **G** and were exposed to light. Figures 4.21b-f show the UV-Vis absorption spectrum of various substrates in aqueous medium before and after irradiation. We observed a decrease in the absorbance of DHN at 298 nm along with the formation of a new broad peak in the longer wavelength region after exposure to light. These observations are in tune with the results obtained in solution and indicates that **G** embedded in the PMMA films is indeed functioning as a photocatalyst for the photosensitized oxidation of DHN.

The reusability of the PMMA films incorporating **G** for the photooxidation process was studied and our results indicate that these films were stable and could be reused for at least three cycles under ambient conditions (Figure 4.22). Moreover, the same PMMA film was employed for studying the photodegradation of other substrates shown in Chart 1. The photosensitized degradation of 4-chlorophenol (CP), 2,5-dimethylfuran (DMF), 9,10-anthracenediyl-bis(methylene) dimalonic acid (ADMA) and 3,3',5,5'-tetrabromobisphenol A

(TBB) were studied by following the same protocol used for the photooxidation of DHN. Upon irradiation of the aqueous solutions in the presence of PMMA films of **G**, we observed a decrease in the absorbance of these substrates thereby indicating the degradation of these molecules. These experiments substantiate the utility of the PMMA films of **G** as a heterogeneous medium capable of degrading a variety of water contaminants through photosensitized generation of singlet oxygen.

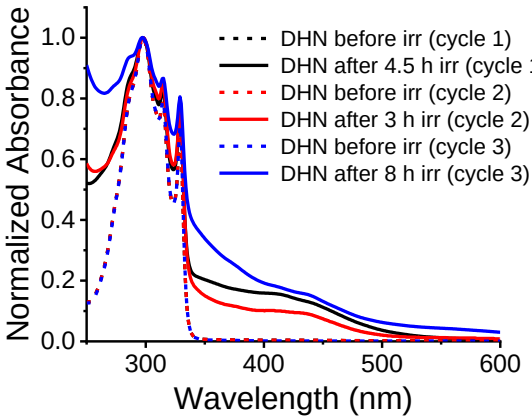

Figure 4.22. Normalized absorption spectrum of DHN before and after irradiation for three cycles wherein **G** embedded on PMMA films was used as a heterogeneous medium for photosensitization.

4.5. Photoactive multilayer coatings with polymer H.

To prevent photobleaching in solution phase, polymer **H** was applied as surface coating via LbL assembly technique that was expected to impart the stability of the functional polymer on solid surface. The polyelectrolyte multilayer film was constructed by alternate deposition of polymer **H** at pH 6 and polyacrylic acid (PAA) at pH 4 as shown in Scheme 4.1.

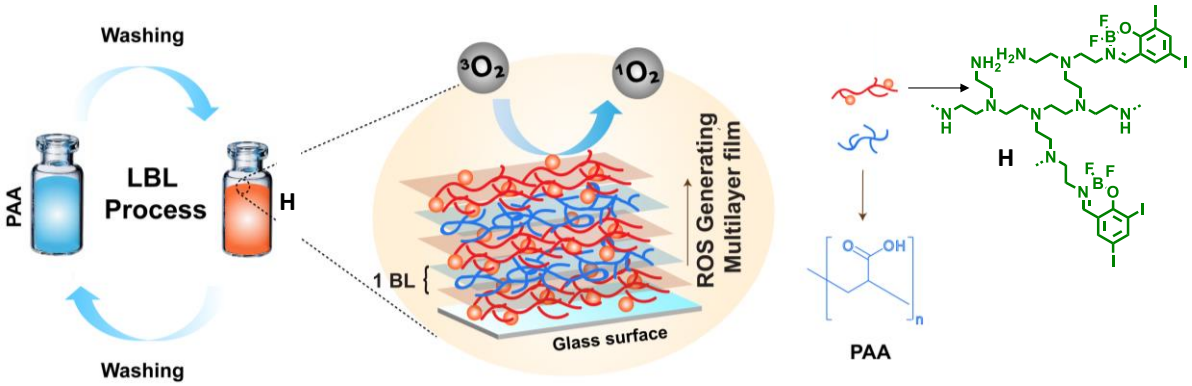

Scheme 4.1. Schematic of fabrication of multilayer film via LbL process inside glass vial.

To understand the growth pattern of **H**/PAA multilayer films, different number of **H**/PAA bilayers (BLs: consisting of one positive layer and one negative layer) were initially grown on a silicon wafer and the film thickness was measured using atomic force microscopy (AFM) as shown in Figure 4.23. It has been observed that the film exhibited a linear growth till 5BLs with a thickness of 45 ± 0.5 nm. However, 10 BLs film exhibited a nonlinear increase in thickness of 112 ± 1.8 nm. This type of behaviour is very common for films consisting of weak polyelectrolytes and constructed in high pH and low pH conditions. The pH-tunable charge density and the diffusivity of the weak polyelectrolytes causes accelerated multilayer growth. The **H**/PAA nanofilm was also grown on a quartz substrate to monitor the film growth using UV-Vis absorption spectroscopy and the absorbance at 430 nm which is a characteristic of the aromatic units in the polymer backbone, attributed to n→π* and π→π* transitions occurring in the diiodosalicylideneimine-boron complex, increased linearly with increase in number of BLs (Figure 4.23). Further, the roughness of the films measured by AFM showed Rq values of 7.1 and 11.9 nm for 5BLs and 10BLs, respectively, (Figure 4.23c) indicating increased roughness at higher number of BLs.

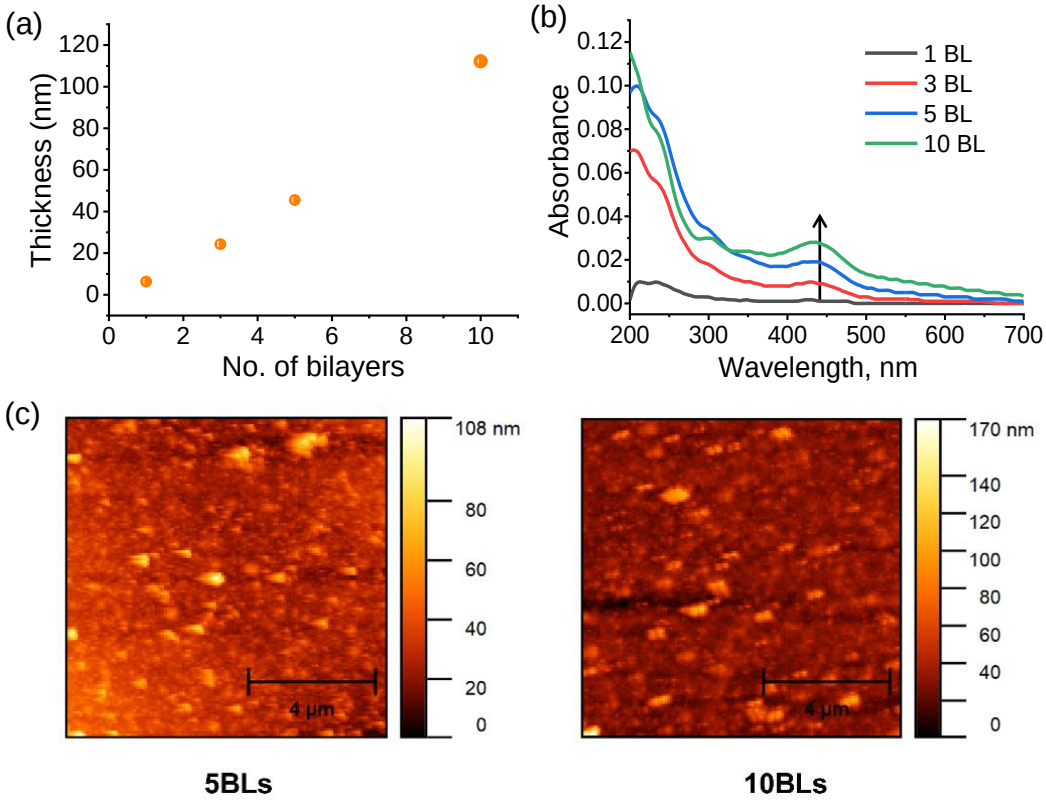

Figure 4.23. (a) Thickness of **H**/PAA multilayer films as a function of number of BLs. (b) Absorption spectra of varying bilayers of **H**/PAA multilayer films grown on quartz slides. (c) AFM images corresponding to 5BLs and 10BLs representing the roughness of the film.

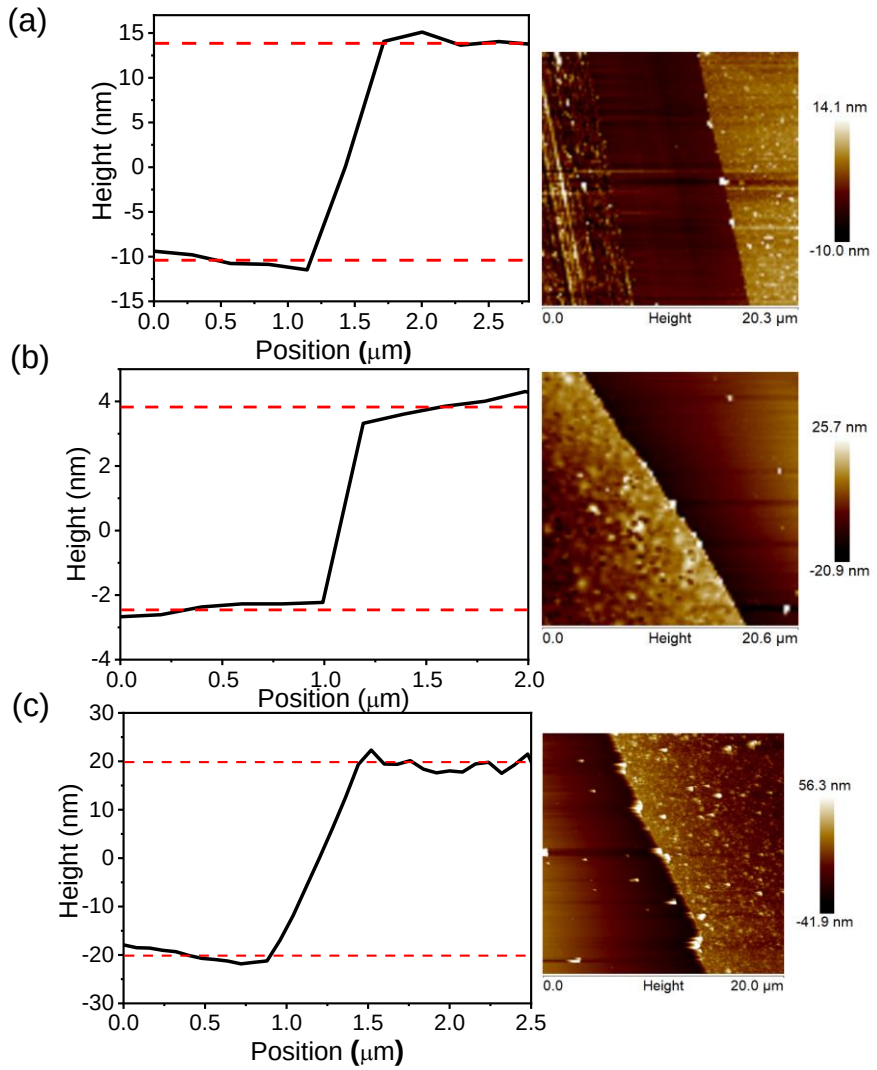

Figure 4.24. The thickness measurement of (a) 1BL, (b) 3BLs and (c) 5BLs **H**/PAA by AFM.

4.6. Stability of $(H/PAA)_{10}$ Coated Nanofilms.

It was crucial to assess the stability of any functional coating before applying it for further practical applications. The chemical stability of the film was assessed by dipping the films first at different pH solutions for 24 hours and then measuring the thickness after drying the films. The stability was tested for 10BLs **H**/PAA films and it was observed that the films are stable in the pH range of 4-10 as the thickness of the film remained unaltered in this range (Figure 4.25). However, a complete detachment of the film from the surface was observed at pH 2 and a partial degradation of the coating was observed in highly basic conditions at pH 12. Thermal stability is a significant criterion for outdoor applications since most organic coatings deteriorate under hot weather conditions. In the thermal stability study, the **H**/PAA coated films were placed in an oven for 2 hours at fixed temperature. The study was done with a 10BLs coated sample with thickness of 114 ± 3.7 nm at 60°C and it showed that the coating was fairly

stable up to 300 °C (Figure 4.26). The thickness of the film was reduced to 67.31 ± 5.61nm above 300°C as the films started to delaminate from surface above this temperature. Further, the stability of the film was tested by immersing **H**/PAA coated films in different solvents (ethanol, acetone and ethyl acetate) for 1 hour wherein no change in thickness was observed as shown in Figure 4.26b. Thus, the film was found to be highly robust even under harsh conditions of pH, temperature and solvent exposure. The photostability of the film was tested by exposing the 10BLs film under UV and visible light for 3-4 days. No change in thickness was observed indicating photostability of these electrostatically assembled multilayer films.

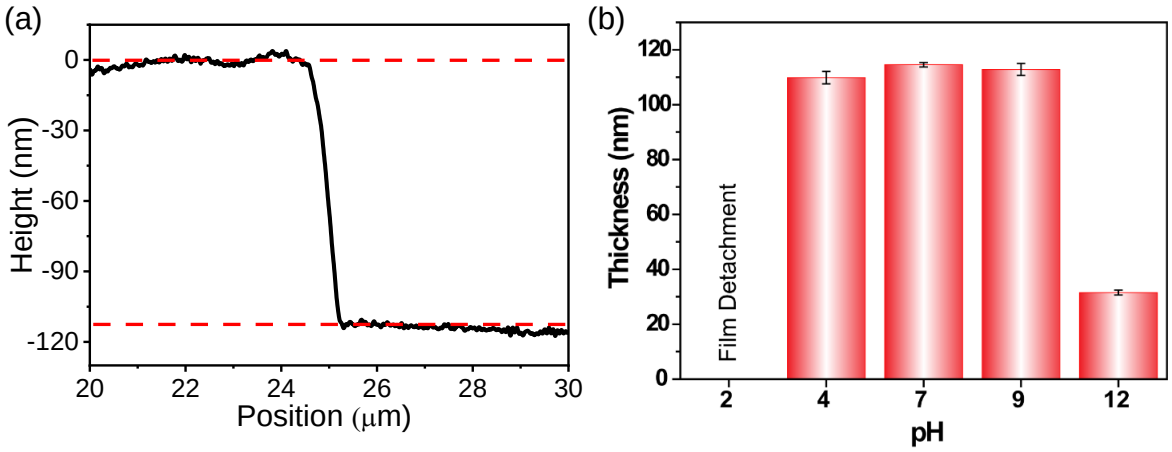

Figure 4.25. (a) The thickness measurement of 10BLs **H**/PAA by surface profilometry as measured after exposing the sample to UV and visible light for 3-4 days. (b) Stability of the 10BLs **H**/PAA film at different pH.

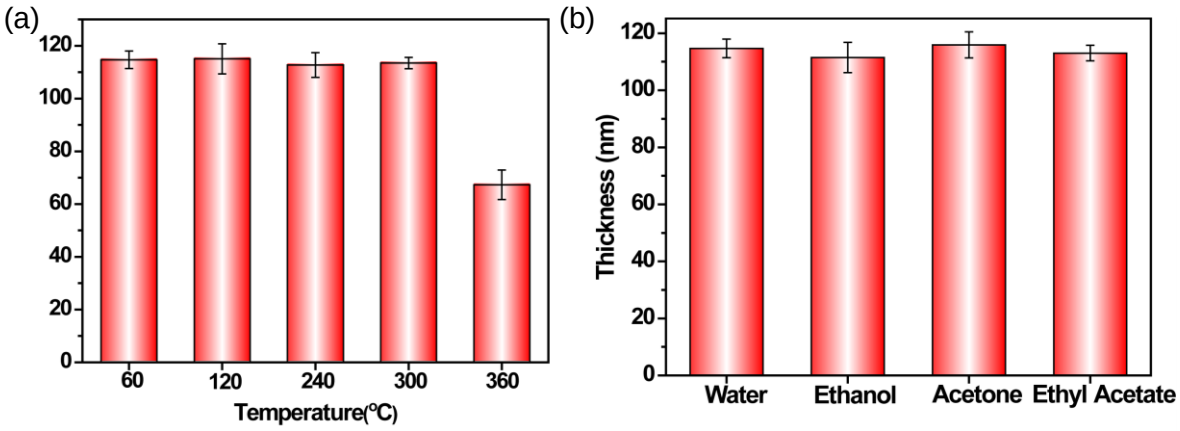

Figure 4.26. (a) Stability of the 10BLs **H**/PAA film at different temperatures and (b) in different organic solvents.

4.7. ROS Production inside H/PAA Coated Glass Vials.

ROS generation ability of the multilayer films was tested using glass vials that were coated with **H**/PAA BLs from inside as shown in Scheme 4.1. The ability of nanofilms in singlet oxygen generation was evaluated by the photooxidation of DHN, where DHN acts as an efficient $^1O_2$ scavenger to produce Juglone. Initially, an aqueous solution of DHN (0.012 mM) was taken inside a 5BLs coated glass vial in which the top layer corresponds to polymer **H.** Next, the vial was irradiated with visible light using Xe lamp and the absorption spectra of the solution were recorded at an interval of 20 minutes. The sequential decrease in absorbance of DHN at 298 nm was observed along with the formation of a new peak at 420 nm (Figure 4.27) and the color of the solution changed from colorless to yellow inside the vial (as shown in inset of Figure 4.27). These spectral changes indicate the conversion of DHN to Juglone, which in turn suggests the formation of $^1O_2$ along with substantiating the role played by LbL assembly towards maintaining the stability and activity of **H** upon photoactivation. Further, it was observed that the decrease in the absorbance of DHN at 298 nm as a function of irradiation time was relatively low in case of 5BLs as compared to that of 10BLs **H**/PAA coated vial (as shown in Figure 4.27b) at all intervals of time. Thus, 10BLs coated vial exhibited higher capability in $^1O_2$ generation owing to higher number of **H** moieties incorporated with increasing number of BLs. The reliability of the experiments was further tested by a control experiment with 10BLs PEI/PAA coated vial with no incorporation of the diiodosalicylideneimine-boron complex in the polymer multilayer film. The absorption spectra showed negligible changes at 298 and 420 nm indicating the vital role of the boron-complex incorporated in the multilayer film.

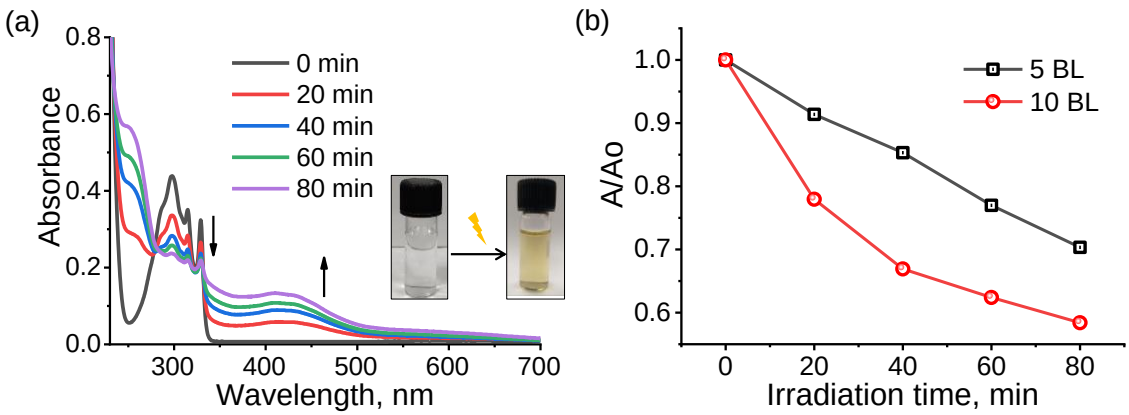

Figure 4.27. (a)The changes in the UV-Vis absorption spectrum of an aqueous solution of 1,5-dihydroxynaphthalene (DHN, 0.012 mM) as a function of irradiation time for 10BLs coated **H**/PAA vial. Inset shows the corresponding color change in the 10BLs coated vial. (b) Relative decrease in the UV-Vis absorbance of DHN at 298 nm obtained with 5 and 10BLs as a function of irradiation time.

To further elucidate the ROS induced bactericidal activity, **H**/PAA coated glass vials were tested. As reported by Acker et al. ROS augment the antibiotic induced cell death in bacteria due to the formation of free radicals that triggers damage in DNA, lipids and proteins leading to cell death. ROS-induced lethal effects occur via a series of oxidative reactions. It was found that **H** (10BLs) under dark conditions has the potential to instigate ROS in both *E. coli and S. aureus* cells. This is probably due to the inherent nature of PEI for imparting intracellular oxidative stress when present on surface. However, under light irradiation the intracellular ROS generated was significantly more (4.5-fold) with *E. coli.* as shown in Figure 4.28a. Similarly, the amount of ROS generated in *S. aureus* cells elevated up to ~5.5-fold under photo irradiation (Figure 4.28). These results strongly support the ability of polymer **H** to generate in vitro ROS on exposure to visible light which further prompted us to investigate the ROS production on exposure to direct sunlight.

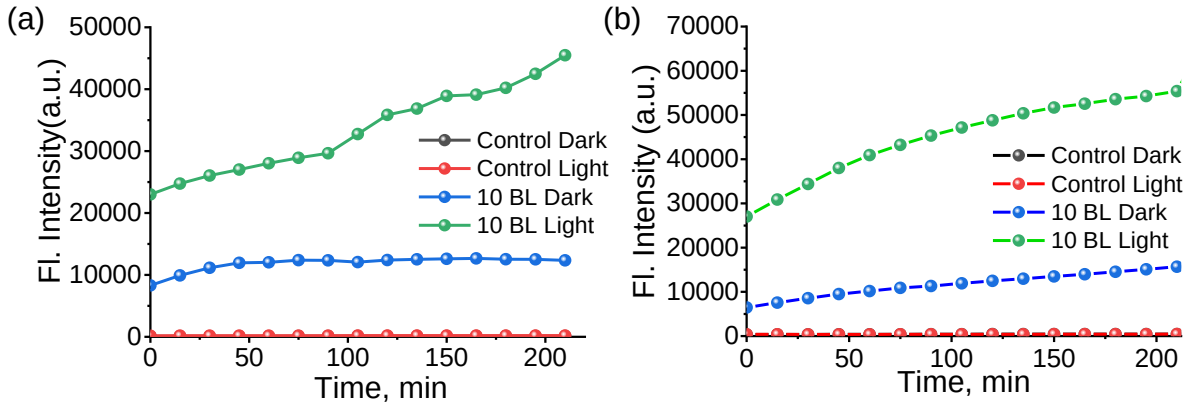

Figure 4.28. In vitro ROS measurements in (a) *E. coli* and (b) *S. aureus* treated with 10BLs **H**/PAA film.

4.8. Sunlight-Activated ROS Production of H/PAA Coated Glass Vials.

After the remarkable performance of nanofilm coated glass vials under the irradiation of Xenon lamp, these were tested for their efficacy in direct sunlight for more convenient usage. The experiment was carried out with 0.021 mmol solution of DHN inside a 10BLs **H**/PAA coated vial under direct sunlight, and the UV-Vis spectra was recorded at intervals of 30 minutes. A regular decrease in the absorbance of DHN at 298 nm along with the concomitant formation of a broad peak in the longer wavelength region around 420 nm, which is the characteristic peak of Juglone, was observed upon keeping the coated vial in direct sunlight for a duration of 150 minutes (Figure 4.29). This experiment revealed the indispensable role of coated glass vials in generating singlet oxygen. This led to further testing the antibacterial behavior of the nanofilms.

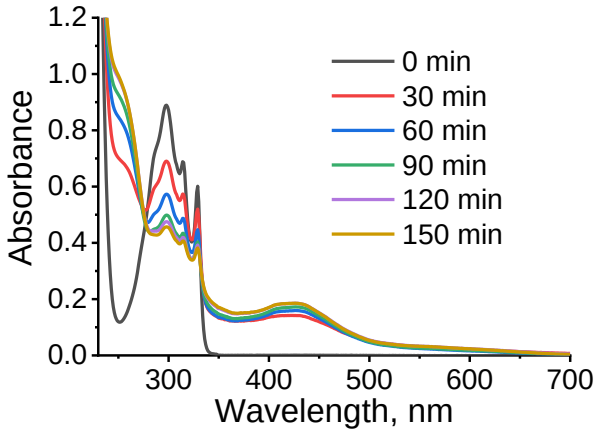

Figure 4.29. The changes in the UV-Vis absorption spectrum of an aqueous solution of 1,5-dihydroxynaphthalene (DHN, 0.021 mM) in 10BLs coated **H**/PAA vial upon exposure to sunlight.

4.9. Antibacterial Activity of Nanofilms.

As *E. coli* and *S. aureus* have been identified as serious etiological agents for food borne and hospital acquired infection causing severe morbidity, the antibacterial efficiency of the photoactive LbL coating was tested against these bacteria. As the number of bilayers increased from 3BLs to 5BLs, the cell viability reduced from ~53% to ~30% and further dropped to ~3% for 10BLs for in *E. coli* in light conditions. After exposure to white light, ~99% of *E. coli* and *S. aureus* cells were killed in the **H**/PAA coated vials labelled as treated vials as compared to control vials (10 BLs PEI/PAA coated vials in which the final layer corresponds to PEI) as shown in Figure 4.30b-c. The treated vials in dark conditions demonstrated marginal to negligible cell death in *E. coli* and *S. aureus* respectively at similar experimental conditions. It is known that both gram positive and negative bacteria express molecular pathways to adapt with oxidative stress. However intracellular ROS generated in both the bacteria under dark condition could impart cell death predominantly in *E. coli* compared to *S. aureus*[33,34]. The number of cells remained mostly constant in untreated vials (both dark and light conditions). Subsequently, MIC method was used to validate the previous results. MIC is defined as the lowest concentration of a material that can effectively inhibit the growth of a microorganism. As depicted in Figure 4.30d, the control plates did not demonstrate any significant decrease in the number of colonies in both dark and light conditions. However, there was ~50 and ~99% reduction in CFU (Colony Forming Unit) in the treated plate in dark and light conditions against *E. coli* cells. Interestingly, the *S. aureus* growth further declined to ~70 and ~99.9% under dark and light conditions with respect to the control plates. The above results corroborate the white light induced inactivation of Gram-negative *E. coli* and Gram-positive *S. aureus* in visible light conditions. Among all the other groups **H** dispensed significant antibacterial activity against both the bacterial species via singlet oxygen generation under visible light irradiation that could significantly cause oxidative stress leading to cell death.

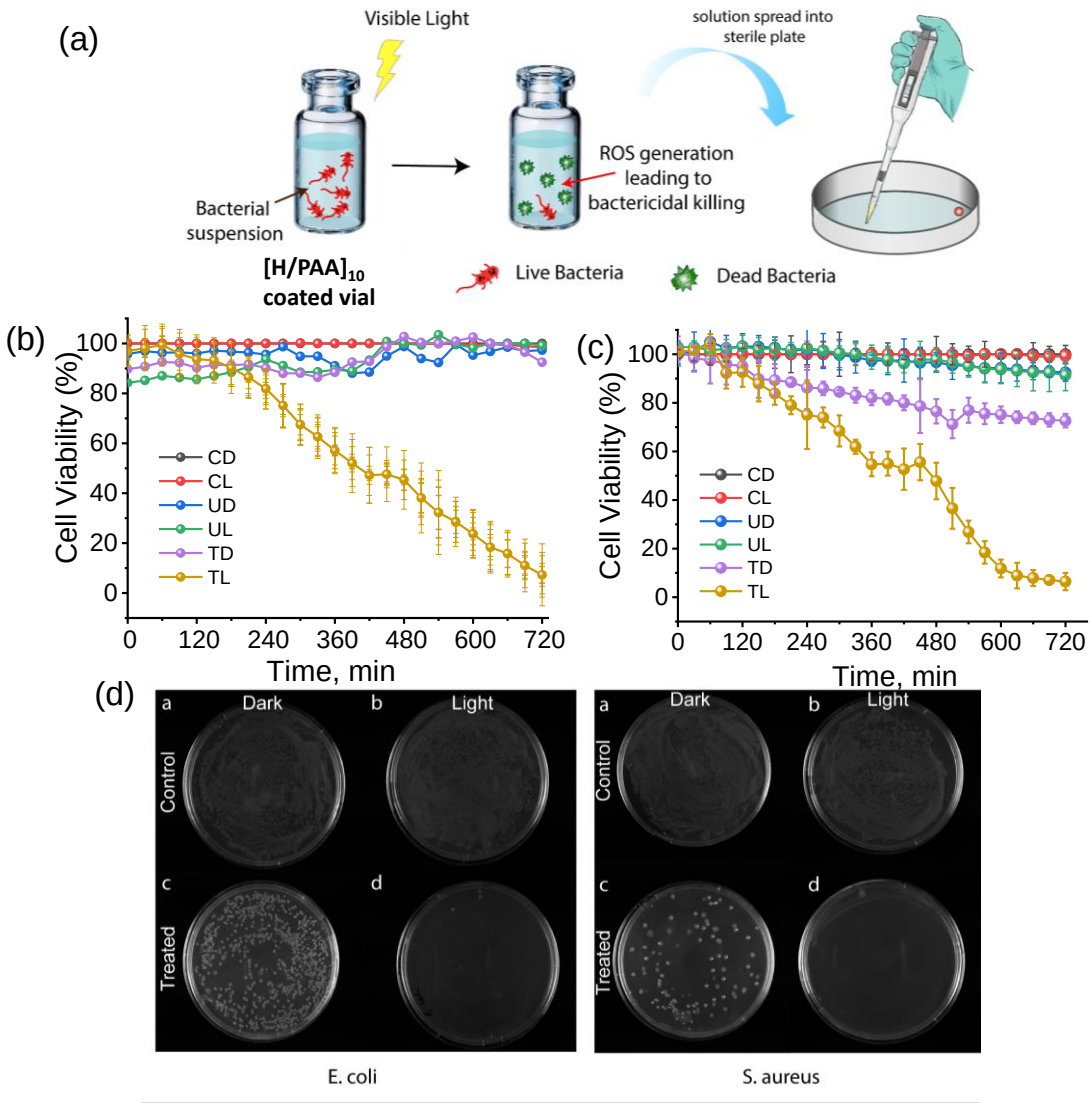

Figure 4.30. (a) Schematic of the procedure for testing antibacterial activity of **H**/PAA coated vials. Percentage survival ratio of (b) *E. coli* and (c) *S. aureus* under different treatment conditions. (d) Digital photographs of colony forming units of *E. coli* and *S. aureus* treated with 10BLs of **H**/PAA under dark and light conditions. The uncoated and coated vials have been represented as untreated and treated vials, respectively. Control refers to 10BLs PEI/PAA coated vials. (CD: Control Dark, CL: Control Light, UD: Untreated Dark, UL: Untreated Light, TD: Treated Dark, TL: Treated Light).

4.10. Conclusion.

We observed that incorporation of boron containing compounds into polymers allows for the preparation of light-activatable materials that are easy to process and handle. The resulting materials demonstrated high stability and good activity upon light exposure.

As the release of CO could be easily observed on the crystal surface through optical microscope, we were keen to pursue non-woven fabrics as they are better in terms of processability and handling. While the fabrics efficiently released CO and singlet oxygen, Mn metal remained trapped in the non-woven fabrics post CO release as validated by EDX elemental mapping and ICP-MS data indicating negligible release of any toxic by-products into the external environment. Furthermore, the non-woven fabrics exhibited negligible toxicity to l929 cell lines and caused significant c6 cancer cell death under low intensity light exposure. Preliminary antibacterial effects were also observed against *E. coli* with $\mathbf{A_F}$ and $\mathbf{B_F}$. These findings open a new door to making potential devices for wound-healing bandages via synergistic delivery of CO and singlet oxygen using non-woven fabrics. The efficiency of ROS generation can be further enhanced through heavy atom functionalization of the BODIPY core thus leading to improved utility of these complexes. There is further scope of tuning the metal center by incorporating heavier transition metals like rhenium into the CO releasing core. Non-woven scaffolds have demonstrated exciting progress in recent past for the local delivery of therapeutics on to the central nervous system or for topical application on skin as dressings. Controlled activity and stimuli responsive nature of our non-woven fabrics further add value to these systems. We believe that upon appropriate structural modifications, these category of molecules could have immense potential to establish themselves as heterogeneous dual-mode sensitizers for successful translation into clinical use.

PMMA films incorporating the molecule **G** functioned as a heterogeneous medium for the photodegradation of organic water pollutants. A variety of molecules such as 1,5-dihydroxynaphthalene, 4-chlorophenol, 2,5-dimethylfuran, 9,10-anthracenediyl-bis(methylene)dimalonic acid and 3,3’,5,5’-tetrabromobisphenol A were studied and were found to undergo photodegradation in the presence of PMMA films incorporating **G**. The film was found to be reusable for at least up to three cycles. As polymers have better processability than small molecules, our synthesized diiodosalicylideneimine boron difluoride functionalized polyethyleneimine polymer, **H** was used for surface coating of glass vials via LbL assembly technique and shown to generate ROS on exposure to visible light. The polymer coated glass vials displayed excellent antibacterial activity against both Gram-positive and Gram-negative bacteria, demonstrating that they function as self-cleaning vials. The addition of boron complex

resulted in lower-visible light absorption, allowing for not only the use of visible light for bactericidal research, but also a nearly transparent nanocoating, making it suitable for a variety of applications. Moreover, the coated glass vials were also functional in presence of direct sunlight for more convenient on-demand cleaning of large storage containers and medical devices. The fact that the LbL assembly may potentially be used to produce coatings on any surface significantly increases the practical usefulness of our method.

4.11. Experimental Section.

4.11.1. Materials and Methods.

All experiments were carried out at room temperature (25 ± 1 °C) unless otherwise mentioned. Boron trifluoride diethyletherate, 4-chlorophenol, 2,5-dimethylfuran, 9,10-anthracenediyl-bis(methylene) dimalonic acid, branched polyethyleneimine (PEI, MW = 25000 g/mol) and polyacrylic acid (PAA, MW ~10,000, 35wt% in water) were purchased from Sigma-Aldrich and used as received. 1,5-Dihydroxynaphthalene (DHN), poly(methylmethacrylate) (PMMA) (average molecular weight 120000) and 3,3',5,5'-tetrabromobisphenol A were purchased from TCI Chemicals and used as received. Quartz slides and Si-wafers were purchased from Techinstro. Distilled water was used for all experiments. The bacteria used in the studies were Methicillin-resistant Staphylococcus aureus (*S. aureus*) and Escherichia coli (*E. coli*). Absorption spectra were recorded on a UV-2600 Shimadzu UV-Vis spectrophotometer in 3 mL quartz cuvettes having a path length of 1 cm. Field effect scanning electron microscopy (FESEM) analysis was carried out in a JEOL JSM-IT 300 Scanning Electron Microscope. ICP-MS analysis of samples was obtained by ICP-MS, Agilent Technology 7700. Zeiss LSM 900 confocal microscope was used for confocal images. UV-Vis diffuse reflectance measurements were carried out in the range of 200-800 nm using Shimadzu UV-2600 spectrophotometer and $BaSO_4$ was used as reference. Crystals were observed with an optical microscope (Olympus BX53F). Optical densities and fluorescence intensity in the cells were measured by Biotek synergy microplate reader. Photosensitization and CO release experiments were carried out using a 350 W Xenon arc lamp (Oriel instruments) with a 475 nm cut-off filter (Newport Corporation) and 550 nm bandpass filter (Newport Corporation). For headspace GC-PDD analysis, ThermoScientific on TRACE 1300 GC series systems with PDD (Pulsed Discharge Detector) and Mseive column were used. 100 ppm of gas standard mixed with helium was adopted for gas quantification. The thickness of the multilayer film was measured by atomic force microscopy (Bruker Multimode 8 system) as well as by surface profilometry (Bruker DekTak XT profilometer). The LbL dipping process

for growing films on quartz and Si-wafer was done by automated multivessel dip coating unit (Apex instruments). Glass vials, silicon wafers and quartz were used as a substrate to fabricate the multilayer films. Silicon wafers were used as a substrate for measuring the thickness of the multilayer film. Quartz slides were used for recording absorption spectra of different bilayers. All substrates for multilayer coating studies were cleaned with piranha solution for 1 hour and washed with deionized water before deposition. Solvents were distilled and dried before use.

4.11.2. Electrospinning.

Electrospinning with solutions of **A** and **B** with the polymer matrix, poly(methylmethacrylate) (PMMA) was performed in N,N-dimethylformamide (DMF). 27 mg of **A** was added to 4 mL solution of PMMA (5 wt %) in DMF. Electrospinning was performed with an 11 kV voltage gradient, 0.8 mL/h flow rate and 12 cm distance of the tip from collector. The process was continued for around 5 hours onto the drum rotating at 1250 RPM. Similarly, 32 mg of **B** was added to 4 mL solution of PMMA (5 wt %) in DMF. Electrospinning was performed with an 8.8 kV voltage gradient, 0.7 mL/h flow rate and 12 cm distance of the tip from collector. The process was performed for 5 hours onto the drum rotating at 1000 RPM.

4.11.3. GC-PDD analysis for CO quantification from A_F and B_F fibres.

Precisely weighed 1 mg each of $\mathbf{A_F}$ and $\mathbf{B_F}$ was taken in 2 mL vials sealed with gas tight septa for GC-PDD analysis. 1 mL aliquot of the headspace was injected into the GC inlet before and after consequent irradiation of the fibres in the solid state for 30 minutes under a Xenon lamp. Presence of carbon monoxide was identified based on retention time which is already calibrated using standard gas mixtures.

4.11.4. CO release from A_F and B_F fibres as a function of irradiation time.

Photochemical release of CO from 1 mg each of $\mathbf{A_F}$ and $\mathbf{B_F}$ as a function of irradiation time was studied by headspace analysis using GC-PDD technique. The corresponding fibres were placed in GC vials and 1 mL aliquot of the headspace was regularly injected into the GC inlet under irradiated and dark conditions. The vial after light exposure was left in dark for equilibration for 9 minutes followed by injection of 1 mL of the head space into the GC inlet. After the irradiated sample was injected, the vial was opened in dark and any amount of residual CO left behind was released. The vial was then closed and kept in dark for another 15 minutes before carrying out the next set of headspace analysis to observe if any CO was released under dark. The same on-off cycle was subsequently repeated for 6 cycles. Carbon monoxide was

identified based on the retention time as calibrated using standard gas mixture. The experiment was performed in a set of doublet.

4.11.5. Heterogenous myoglobin assay.

Heterogenous myoglobin assay was carried out with the fabrics $\mathbf{A_F}$ and $\mathbf{B_F}$ of dimensions 0.5 cm x 3 cm placed in a 3 mL quartz cuvette. Upon the formation of deoxymyoglobin (dMb) via reduction of myoglobin (2 $mg.mL^{-1}$, 66 µL) with sodium thionate (24 $mg.mL^{-1}$), the non-woven fabrics adhered to the aluminium foil were placed in the cuvette and the neck was sealed with Teflon stopper. The absorbance was recorded before light exposure and then the emergence of MbCO was monitored upon irradiation with visible light using Xenon lamp (550 nm bandpass filter for $\mathbf{A_F}$ and 475 nm cut-off filter for $\mathbf{B_F}$**)**. The shifts in the λ_{max} from 434 to 424 nm along with the appearance of new bands at 530 and 580 nm confirmed the release of CO from the fabrics.

4.11.6. Singlet oxygen generation with A_F.

Heterogeneous release of singlet oxygen was monitored from the non-woven fabric $\mathbf{A_F}$ using 1,5-dihydoxynaphthalene (DHN) in water due to its compatibility with aqueous medium. A piece of fabric $\mathbf{A_F}$ with approximate dimensions of 3 x 3 cm^2 was placed in a 50 mL beaker and the prepared stock solution of DHN (0.14 mM) in water was added to it. The absorption spectrum of the solution was recorded and the set up was subjected to irradiation under 350 W Xenon arc lamp with a 345 nm cut-off filter. Progress of the conversion of DHN to juglone was subsequently monitored by recording the UV-Vis spectra at regular intervals.

4.11.7. Analysis of the total manganese content of A_F and B_F fabric before and after irradiation.

The overall manganese content within $\mathbf{A_F}$ and $\mathbf{B_F}$ was determined after sample destruction in 69% ultrapure nitric acid and subsequent dilution with MilliQ water. The quantity of manganese in the aqueous solutions was determined by Inductively Coupled Plasma Mass Spectrometry (ICP-MS). Calibration was performed with NIST traceable certified reference standard of manganese procured from Merck.

4.11.8. Biocompatibility/Cell viability studies.

The toxicity of $\mathbf{A_F}$ and $\mathbf{B_F}$ was tested against l929 cells using MTT assay for various amounts of fibres ranging from 1 mg to 4 mg. Cells were seeded in 6 well plate at a density of

$1x10^5$ cells per well for 24 hours at 37 ℃ under 5% CO_2. 1-4 mg each of the fabrics $\mathbf{A_F}$ and $\mathbf{B_F}$ with PMMA as control were carefully placed on the cells covering similar surface areas without any spreading of the fabrics throughout the wells. The fabrics were then used to treat the l929 cell lines for 24 hours in duplicates. After incubation, the cells were washed with pre-warmed PBS and incubated with fresh medium containing MTT dye. After 4 hours, the fabrics were removed from the well plates and the formed formazan crystals were dissolved in DMSO and absorbance of suspension was measured at 595 nm on plate reader.

4.11.9. Cytotoxicity studies.

Cytotoxicity of the $\mathbf{A_F}$ and $\mathbf{B_F}$ in the presence and absence of white light was measured using MTT assay against c6 glioblastoma cell lines. Cells were seeded in the 6 well plates in duplicates at a density of $1x10^5$ cells per well for 24 hours at 37 ℃ under 5% CO_2. The cells were treated with 1 mg each of the fabrics along with PMMA as control which were cautiously placed in the wells covering almost similar surface areas without much spreading of the fabrics throughout the wells. Afterwards, the fabrics were incubated for 12 hours followed by irradiation for 1 hour under low intensity incandescent lamp (15 W). Post irradiation, the fabrics were further incubated for 6 hours. After incubation, the cells were washed with pre-warmed PBS and incubated with fresh medium containing MTT dye. After 4 hours, media was removed along with the fabrics and DMSO was added to each well to dissolve the formazan crystals. The absorbance of suspension was measured at 595 nm on plate reader. Cell viability was calculated with following formula:

$$\text{cell viability } (\%) = OD\ (sample) - OD(Blank) \Big/ OD(control) - OD(Blank)$$

4.11.10. Antibacterial activity against *E. coli* with A_F and B_F.

All the microbial cultures were purchased from Microbial Type Culture Collection and Gene Bank, Chandigarh, India. Antibacterial activity was performed with Gram negative bacteria strain *E. coli*. Cultures were grown in Luria-Bertani broth (LB) incubated at 37°C in an orbital shaker operated at 250 rpm and the optical density (OD) was monitored at 600 nm with UV scanning spectrophotometer (plate reader). Culture was grown to an OD of ~0.2 which corresponds a bacterial concentration of 1-3 x 10^8 CFU/mL. 20 µL of the bacteria culture was added to 200 µL of PBS buffer to prepare the bacterial suspension. 1 mg each of the fabrics $\mathbf{A_F}$, $\mathbf{B_F}$ and **PMMA** (control) was fitted into the well bottoms of the 96 well plate to which 100 µL of the bacterial suspension was added and uniformly deposited on the top of each sample.

The plates were then irradiated (at 10 cm distance) with a low intensity incandescent lamp (15 W) at room temperature and the corresponding ODs at 600 nm were recorded at an interval of 1 hour. To avoid contamination, the aluminium foil was sterilized with ultraviolet light before depositing nonwoven fibre for 15 minutes. Also, the electrospinning setup was thoroughly sterilized with ethanol before the spinning process to avoid any contamination.

All the media and PBS used in this experiment were sterilized in an autoclave at 121 °C for 15 minutes. Initially, the culture was activated in Luria-Bertani broth (HiMedia) and cultured for 12 hours in an incubator shaker at 37 °C. Similarly, 100 μL of diluted bacterial suspension were added into wells incorporating the fabrics. Treated and control wells were exposed to a low intensity incandescent lamp (15 W) at room temperature for 20 minutes under uniform shaking conditions. 40 μL of reaction mixture was diluted by a factor of 10^{-5} and added on the LB agar (HiMedia) plate and uniformly distributed by an L-shaped spreader followed by incubation at 37 °C for 6 hours. The pictures of the of the dishes containing colony forming units of *E. coli* bacteria pretreated with $\mathbf{A_F}$, $\mathbf{B_F}$ and **PMMA** under light conditions along with an untreated control were taken.

4.11.11. General procedure for the preparation of film with G.

To 15 mL of a solution of poly(methylmethacrylate) (PMMA, 12.6 mg/mL in chloroform) in a beaker, 7.5 mg of **G** was added, and the mixture was stirred for 2 hours at 45 °C in a water-bath. The solution was allowed to cool down to room temperature and upon evaporation of the solvent under ambient conditions, a uniform film was obtained. To study the photosensitization properties, an aqueous solution of the substrate (Chart 4.1), was taken in the beaker containing the film and the solution was irradiated under a xenon lamp.

4.11.12. Investigation of singlet oxygen generation with G-embedded PMMA film.

A solution of compound **G** in a mixture of acetonitrile and ethanol (9:1) was taken in a 3 mL cuvette and an absorption spectrum was recorded. To this solution, an aliquot of DHN was added and absorption spectrum was recorded. The sample was then irradiated using a 400 W Xenon arc lamp (54 mW/cm^2) with a 345 nm cut-off filter and the progress of the reaction was monitored by recording UV-Vis spectra at regular intervals. A control experiment was carried out wherein DHN alone was irradiated in the absence of photosensitizers under identical experimental conditions. Another experiment was also carried out wherein DHN was irradiated under identical experimental conditions in the presence of a reference standard (methylene blue).

4.11.13. Preparation of polyelectrolyte multilayer coatings with H.

H/PAA multilayer films were constructed on different substrates (Si wafer, quartz) using the LbL technique. A given substrate was first dipped into the positively charged PEI solution (1.0 wt %, @ pH 10, primer) for 5 minutes, followed by washing with deionized water (twice) for 1 minute. The substrate was then dipped into the negatively charged PAA solution (0.2 wt % @ pH 4) for another 5 minutes, followed by washing steps. Next, the substrate was dipped into aqueous solution of **H** (1mg/mL @ pH 6) for 5 minutes, followed by washing steps. This resulted in the formation of a single bilayer (BL) after the primer layer. The remaining number of BLs were constructed using one minute dipping time in each solution. The adsorption and washing steps were repeated accordingly to form 1, 3, 5 and 10BLs. Glass vials were coated by the same procedure by injecting the positively and negatively charged solutions alternatively into the vial followed by washing steps.

4.11.14. Investigation of Singlet Oxygen Generation with H/PAA Coatings.

To investigate the utility of the coated glass vessels towards the photooxidation of DHN, an aliquot of DHN in deionised water (0.012 mM) was added to the polymer coated vessel and the absorption spectrum was recorded. The sample was then irradiated by using a 350 W Xenon arc lamp (44 $mWcm^{-2}$) with a 345 nm cut-off filter and the progress of the reaction was monitored by recording UV-Vis spectra at regular intervals.

4.11.15. *In Vitro* Detection of Reactive Oxygen Species (ROS) with H/PAA coatings.

In vitro reactive oxygen species generation was evaluated by 2,7-dichlorofluorescein diacetate (DCFDA, Sigma Aldrich) under visible light irradiation. DCFDA is a ROS sensitive fluorescent dye that diffuses into cells and reacts with reactive oxygen radicals. The quantity of ROS produced is directly proportional to the green fluorescence emitted by the dye (excitation wavelength of 488 nm and emission wavelength of 535 nm). 10^6 CFU/mL bacteria were added in control, 5 and 10BLs treated vials followed by exposure to white light for 20 minutes. The same set of control experiments were performed in dark conditions. Post irradiation, the bacterial cells were incubated with DCF-DA (2 µg/mL) and the fluorescence intensity was measured at regular intervals of 30 minutes.

4.11.16. Antibacterial Activity with H/PAA bilayers.

The antibacterial activity of **H** was studied by plotting the time-kill curve against *E. coli* (ATCC 25922) and *S. aureus* (ATCC 23235). All the microbial cultures were purchased

from Microbial Type Culture Collection and Gene Bank, Chandigarh, India. The numbers of bacteria were expressed as colonies forming unit (CFU) per mL. All the media and PBS used in this experiment were sterilized in an autoclave at 121 °C for 15 minutes. Initially, the culture was activated in Luria-Bertani broth (HiMedia) and cultured for 12 hours in an incubator shaker at 37 °C. The bacterial colonies were then diluted to 10^6 CFU/mL using sterile PBS. 100 μL of diluted bacterial suspension were added into **H** coated glass vials. Treated, untreated and control vials were exposed to visible light irradiation (12 V, 36 W lamp) at 37 °C (room temperature) for 20 minutes under uniform shaking conditions. The same set of experiments were repeated in dark conditions. Post irradiation, the bacterial optical density was recorded at 600 nm at a periodic interval of 30 minutes for 12 hours. All the experiments were carried out in triplicates. Next, the antimicrobial activity of these **H** polymer were assessed by the Minimum Inhibitory Concentration method (MIC) against both *E. coli* and *S. aureus* cells. 40 μL of reaction mixture was added on the LB agar (HiMedia) plate and uniformly distributed by an L-shaped spreader followed by incubation at 37 °C for 24 hours.

4.12. References.

[1] C. de las H. Alarcón, S. Pennadam, C. Alexander, *Chem. Soc. Rev.* **2005**, *34*, 276–285.

[2] D. Roy, J. N. Cambre, B. S. Sumerlin, *Progress in Polymer Science* **2010**, *35*, 278–301.

[3] M. Mrinalini, S. Prasanthkumar, *ChemPlusChem* **2019**, *84*, 1103–1121.

[4] L. Li, W.-W. Yang, D.-G. Xu, *Journal of Drug Targeting* **2019**, *27*, 423–433.

[5] E. Kottelat, Z. Fabio, *Inorganics* **2017**, *5*, 24.

[6] T. Slanina, P. Šebej, *Photochem. Photobiol. Sci.* **2018**, *17*, 692–710.

[7] U. Schatzschneider, *Inorganica Chimica Acta* **2011**, *374*, 19–23.

[8] Q. Tang, H.-L. Zhang, Y. Wang, J. Liu, S.-P. Yang, J.-G. Liu, *J. Mater. Chem. B* **2021**, *9*, 4241–4248.

[9] S. H. C. Askes, G. U. Reddy, R. Wyrwa, S. Bonnet, A. Schiller, *J. Am. Chem. Soc.* **2017**, *139*, 15292–15295.

[10] S. Gläser, R. Mede, H. Görls, S. Seupel, C. Bohlender, R. Wyrwa, S. Schirmer, S. Dochow, G. U. Reddy, J. Popp, M. Westerhausen, A. Schiller, *Dalton Trans.* **2016**, *45*, 13222–13233.

[11] C. Bohlender, S. Gläser, M. Klein, J. Weisser, S. Thein, U. Neugebauer, J. Popp, R. Wyrwa, A. Schiller, *J. Mater. Chem. B* **2014**, *2*, 1454–1463.

[12] M. Klausen, M. Ucuncu, M. Bradley, *Molecules* **2020**, *25*, 5239.

[13] J. Ghorbani, D. Rahban, S. Aghamiri, A. Teymouri, A. Bahador, *Laser Therapy* **2018**, *27*, 293–302.

[14] S. Navarro, J. Fenoll, N. Vela, E. Ruiz, G. Navarro, *Journal of Hazardous Materials* **2009**, *172*, 1303–1310.

[15] W. Zhang, M. Gong, J. Yang, J. Gu, *Langmuir* **2021**, *37*, 8157–8166.

[16] Y. Ren, D. Guo, Z. Zhao, P. Chen, F. Li, J. Yao, H. Jiang, Y. Liu, *Chemical Engineering Journal* **2022**, *435*, 134832.

[17] M. C. DeRosa, R. J. Crutchley, *Coord. Chem. Rev.* **2002**, *233–234*, 351–371.

[18] *N Engl J Med* **2014**, *370*, 2542–2543.

[19] C. J. L. Murray, K. S. Ikuta, F. Sharara, L. Swetschinski, G. R. Aguilar, A. Gray, C. Han, C. Bisignano, P. Rao, E. Wool, *The Lancet* **2022**, *399*, 629–655.

[20] A. Iborra-Torres, A. N. Kulak, R. G. Palgrave, G. Hyett, *ACS Appl. Mater. Interfaces* **2020**, *12*, 33603–33612.

[21] Y. Dong, P. Wang, T. Wei, T. Zhou, M. Huangfu, Z. Wu, *Advanced Materials Interfaces* **2017**, *4*, 1700953.

[22] S. Bhattacharyya, S. R. Ali, M. Venkateswarulu, P. Howlader, E. Zangrando, M. De, P. S. Mukherjee, *J. Am. Chem. Soc.* **2020**, *142*, 18981–18989.

[23] A. K. Awasthi, S. Gupta, J. Thakur, S. Gupta, S. Pal, A. Bajaj, A. Srivastava, *Nanoscale* **2020**, *12*, 5021–5030.

[24] F.-X. Xiao, M. Pagliaro, Y.-J. Xu, B. Liu, *Chem. Soc. Rev.* **2016**, *45*, 3088–3121.

[25] J. J. Richardson, M. Björnmalm, F. Caruso, *Science* **2015**, *348*, aaa2491.

[26] M. Ghanadpour, F. Carosio, L. Wågberg, *Applied Materials Today* **2017**, *9*, 229–239.

[27] B. Wang, H. Liu, Z. Wang, S. Shi, K. Nan, Q. Xu, Z. Ye, H. Chen, *J. Mater. Chem. B* **2017**, *5*, 1498–1506.

[28] M. He, Q. Wang, W. Zhao, C. Zhao, *J. Mater. Chem. B* **2018**, *6*, 3904–3913.

[29] V. Mohanta, G. Madras, S. Patil, *ACS Appl. Mater. Interfaces* **2014**, *6*, 20093–20101.

[30] A. Das, S. Sengupta, J. Deka, A. M. Rather, K. Raidongia, U. Manna, *J. Mater. Chem. A* **2018**, *6*, 15993–16002.

[31] A. K. Gill, Sk. Riyajuddin, M. Alam, K. Ghosh, D. Patra, *European Polymer Journal* **2020**, *124*, 109455.

[32] W. A. Marmisollé, O. Azzaroni, *Nanoscale* **2016**, *8*, 9890–9918.

[33] S. Schastak, S. Ziganshyna, B. Gitter, P. Wiedemann, T. Claudepierre, *PLOS ONE* **2010**, *5*, e11674.

[34] B. Pucelik, J. M. Dąbrowski, in *Advances in Inorganic Chemistry* (Eds.: R. van Eldik, C.D. Hubbard), Academic Press, **2022**, pp. 65–108.

Workshop and Conferences Attended

1) “Synthesis and Evaluation of Photosensitization Properties of Iodo-functionalised Salicylideneimine-Boron Complexes”, Sanchita Shah and Prakash P. Neelakandan*, a poster presented at the 23rd CRSI-National Symposium in Chemistry, held at IISER Bhopal, Madhya Pradesh, India on 13-15 July, 2018.

2) Attended workshop on “Mass Spectrometry” organized by Sophisticated Analytical Instrumentation Facility, Panjab University, Chandigarh on 20-21 March, 2018.

3) “Synthesis and Evaluation of Photosensitization Properties of Iodo-functionalised Salicylideneimine-Boron Complexes”, Sanchita Shah and Prakash P. Neelakandan*, a poster presented at the 17th Prof. K.V. Thomas Endowment Seminar & Second International Symposium on New Trends in Applied Chemistry (NTAC-2019), held at Sacred Heart College, Thevara, Kerala, India during 14-15 January, 2019.

4) “Synthesis and Evaluation of Photosensitization Properties of Iodo-functionalised Salicylideneimine-Boron Complexes”, Sanchita Shah and Prakash P. Neelakandan*, a poster presented at a symposium on "Recent Advances in Organic and Bioorganic Chemistry (RAOBC), held at IISER Mohali, Punjab, India on 22-24 March, 2019.

5) “Iodo-functionalized Salicylideneimine-Boron Complexes as Photosensitization Agents for Water Purification and Anti-microbial Activity”, Sanchita Shah and Prakash P. Neelakandan*, a poster presented and talk delivered at the annual meeting, Chem@Nano 2021 of Energy and Environment Unit, Institute of Nanoscience and Technology, Mohali on 10-11 September, 2021.

List of Publications

1. Iodo-functionalized Salicylideneimine-Boron Complexes: Synthesis and Photosensitized Degradation of Organic Water Pollutants. **Sanchita Shah**, Ashima Bajaj, Abhishek Shibu, Md. Ehesan Ali*, and Prakash P. Neelakandan*, *Chem. Eur. J.*, **2018**, 24, 18788-18794.

2. Advances in the Supramolecular Chemistry of Tetracoordinate Boron-containing Organic Molecules into Organogels and Mesogens. **S Shah**, P Marandi, PP Neelakandan*, *Front. Chem.*, **2021**, 9, 2296-2646.

3. Sunlight-activatable ROS generator multilayer Salicylideneimine boron polymer film for anti-bacterial coatings. **Sanchita Shah**, Arshdeep Kaur, Pranjali Yadav, AsifKhan Shanavas, Prakash P. Neelakandan* and Debabrata Patra*, *J. Mater. Chem. B*, **2022**, 10, 9869-9877.

4. Multifunctional BODIPY embedded non-woven fabric for CO release and singlet oxygen generation. **Sanchita Shah**, Neeraj Naithani, Subash Chandra Sahoo, Prakash P. Neelakandan* and Nidhi Tyagi*, *J. Photochem. Photobiol. B, Biol*., **2023**, 239, 1011-1344.

5. Bromination versus Iodination: impact on aggregation, luminescence and photosensitization of triple BODIPY dye. Sanchita Shah, Neeraj Naithani and Prakash P. Neelakandan*, (manuscript communicated).

6. Asymmetric thiathiozole as solvatochromic, reversible and self- healing acid-base molecular switch (manuscript under preparation).